



HAL
open science

Interfaces et durabilité d'électrodes avancées pour l'énergie : IT-SOFC et SOEC

Jaroslav Sar

► **To cite this version:**

Jaroslav Sar. Interfaces et durabilité d'électrodes avancées pour l'énergie : IT-SOFC et SOEC. Matériaux. Université de Grenoble; Instituto superior técnico (Lisbonne), 2014. Français. NNT : 2014GRENI106 . tel-03227686

HAL Id: tel-03227686

<https://theses.hal.science/tel-03227686>

Submitted on 17 May 2021

HAL is a multi-disciplinary open access archive for the deposit and dissemination of scientific research documents, whether they are published or not. The documents may come from teaching and research institutions in France or abroad, or from public or private research centers.

L'archive ouverte pluridisciplinaire **HAL**, est destinée au dépôt et à la diffusion de documents scientifiques de niveau recherche, publiés ou non, émanant des établissements d'enseignement et de recherche français ou étrangers, des laboratoires publics ou privés.

THÈSE

Pour obtenir le grade de

DOCTEUR DE L'UNIVERSITÉ DE GRENOBLE

Spécialité : **Matériaux, Mécanique, Génie Civil, Electrochimie**

Arrêté ministériel : 7 août 2006

Et de

DOUTOR EM ENGENHARIA DE MATERIAIS, INSTITUTO SUPERIOR TECNICO, UNIVERSIDADE DE LISBOA

Présentée par

Jarosław SAR

Thèse dirigée par **Elisabeth DJURADO (FRANCE)** et
dirigée par **Amélia ALMEIDA (PORTUGAL)**

préparée au sein du **Laboratoire d'Electrochimie et de Physico-
chimie des Matériaux et des Interfaces (LEPMI)**
dans l'**École Doctorale Ingénierie – Matériaux Mécanique
Energétique Environnement Procédés Production (I-MEP2)**

Interfaces et durabilité d'électrodes avancées pour l'énergie (IT-SOFC et SOEC)

Thèse soutenue publiquement le **04 Novembre 2014**,
devant le jury composé de :

M. Olivier JOUBERT

Professeur, Ecole Polytechnique de l'Université de Nantes, Président

Mme Rose-Noëlle Vannier

Professeur, Ecole Nationale Supérieure de Chimie, Lille, Rapporteur

M. Jean-Paul VIRICELLE

Directeur de recherches, Ecole des Mines de St. Etienne, Rapporteur

Mme Elisabeth DJURADO

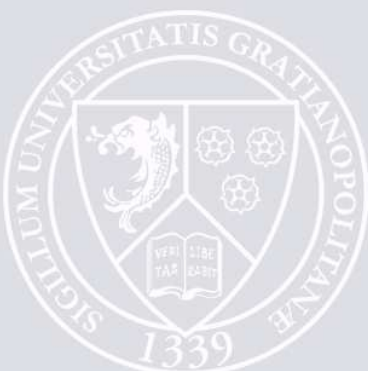
Professeur, Grenoble INP, Directeur de thèse (France)

Mme Amélia ALMEIDA

Professeur assistant, Departamento de Engenharia Quimica, Instituto
Superior Técnico, Lisbonne, Directeur de thèse (Portugal)

Mme Annabelle BRISSE

Doctor, European Institute for Energy Research, Karlsruhe,
Invitée (Allemagne)



Preface

In this place, I would like to thank to Prof. Elisabeth Djurado for supervising the work and be the director of the thesis. Thank you for all suggestions, ideas and discussions without which the completion of this work would not be possible. Thank you that you took care of the work and also that you were always helping me in Grenoble. MERCI !

I would like to thank to Prof. Amélia Almeida for supervising the work. Thank you for your helpful comments and discussion. Thank you that you took the responsibility for the project and for my stay in Lisbon. OBRIGADO !

I would like to thank to Dr. Annabelle Brisse for supervising the work during my stay in EIFER in Karlsruhe. MERCI (DANKE) !

I would like to thank to Prof. Laurent Dessemond (LEPMI-IES) for suggestions and discussion on electrochemical behavior of the oxygen electrode, impedance spectroscopy and many other things. I would like to say thanks to Prof. Christophe L. Martin (SIMAP-GPM2) for ideas and conversations on tomography and microstructural computings topics. Next thanks go to Prof. Rui Vilar (IST-ICEMS) for his comments on mechanical part. Thank to Dr. Josef Schefold (EIFER) for his help with experiments in the Fraunhofer Institute for Chemical Technology (Germany).

I would like to thank to Prof. Olivier Joubert (Ecole polytechnique de l'université de Nantes) that he agreed to be a director of the jury, Prof. Rose-Noëlle Vannier (ENSC Lille) and Prof. Jean-Paul Viricelle (Ecole des Mines de St Etienne) for being reviewers of the manuscript.

I would like to thank to LEPMI laboratory, especially to IES team with which I spent most of the time during thesis. The same feelings go to ICEMS team, EIFER team and Usigne team. Thank you for your help to overcome difficulties during my thesis.

Special thanks go to Rachel Martin and Frédéric Charlot CMTc (Consortium des Moyens Technologiques Communs) in Grenoble for carrying out FEG-SEM observations and FIB-SEM tomography.

Finally, I would like to thank to my colleague and real friend from the office 317 Guillaume Constantin for his help at each step on my PhD life. Thank you that you helped me to survive

in this barbarian country, for your good sense of humor, French lessons, car service and many, many things that happened on the way. Dziękuję !!!

Not less thanks belong to Olesia Danyliv, Marie Lachal, Liliana Canguero, Laurène Flandinet, Ania Wolnik, Carole Loable, Nicolas Bailly, Marc Zimmermann, Cheah Seng Kian, Luis Castanheira, Tomin Liu, Sahendra Pal Sharma, Alex Cunha, Bruno Nunes Tiago Ribeiro, friends from IDS-FunMat program and to all friends that I forgot to mention here. Thank you all for making PhD time unforgettable experience.

Chciałbym podziękować moim rodzicom i rodzeństwu za to, że pomagali mi na każdym kroku niezależnie czy byłem w Grenoble, w Lizbonie czy w Karlsruhe.

Na końcu, chciałbym podziękować Oli za to, że wspierała mnie na duchu przez te ciężkie trzy lata. To dzięki Tobie wytrwałem wszystkie podróże i problemy, dzięki za nieustanną motywację, pomoc naukową i otuchę. Dziękuję za wszystko !!!

Saint Martin d'Hères, 04 November 2014

Abstract (EN)

Interfaces and durability of advanced electrodes for energy (IT-SOFC and SOEC)

The objective of this PhD thesis is to fabricate advanced oxygen electrode based on $\text{Ce}_{0.9}\text{Gd}_{0.1}\text{O}_{1.95}$ (CGO) and $\text{La}_{0.6}\text{Sr}_{0.4}\text{Co}_{0.2}\text{Fe}_{0.8}\text{O}_{3-\delta}$ (LSCF) with graded and homogeneous composition onto yttria-stabilized zirconia (YSZ = 8 mol. % Y_2O_3 -doped ZrO_2) electrolyte using electrostatic spray deposition. A thin and dense layer of CGO was inserted between LSCF and YSZ to serve as a barrier diffusion layer. The novel microstructure with high porosity and large surface area is expected to improve the electrochemical performances. The electrical behavior of the electrode was investigated by impedance spectroscopy versus temperature in air. A detailed microstructural description was performed by 3D reconstructed model from FIB-SEM and X-ray nanotomography and related to electrical properties. The mechanical analysis was performed by microscratch and ultramicroindentation tests. Finally, durability tests were performed on the electrode with 45 cm^2 oxygen active area, up to 800 h at around $770 \text{ }^\circ\text{C}$, in full cell SOFC and SOEC configurations operating respectively in H_2 and $\text{H}_2/\text{H}_2\text{O}$ mixture.

Keywords: SOFC, SOEC, LSCF, CGO, coral microstructure, ESD, EIS, X-ray nanotomography, 3D reconstruction, ultra-microindentation.

Abstract (FR)

Interfaces et durabilité des électrodes de pointe pour l'énergie (PAC et EHT)

L'objectif de cette thèse concerne l'élaboration, par atomisation électrostatique, d'une électrode à oxygène à architecture innovante, basée sur un composite $\text{Ce}_{0.9}\text{Gd}_{0.1}\text{O}_{1.95}$ (CGO) - $\text{La}_{0.6}\text{Sr}_{0.4}\text{Co}_{0.2}\text{Fe}_{0.8}\text{O}_{3-\delta}$ (LSCF) possédant un gradient de composition ou une composition homogène. Cette électrode a été déposée sur un substrat de zircone yttrée (YSZ = 8 % mol. $\text{Y}_2\text{O}_3\text{-ZrO}_2$) sur laquelle a été intercalée au préalable une couche barrière mince et dense de CGO. Cette électrode possède une microstructure innovante, à porosité élevée permettant d'obtenir une grande surface active qui devrait conduire à l'amélioration des performances électrochimiques. Le comportement électrique de l'électrode a été étudié par spectroscopie d'impédance en fonction de la température et sous air. Une description microstructurale détaillée a été effectuée à l'aide d'un modèle de reconstruction 3D obtenu par MEB équipé d'une sonde ionique focalisée et par nanotomographie X. Ces propriétés microstructurales ont été reliées aux propriétés électriques. Les propriétés mécaniques et tribologiques de cette électrode composite ont été déterminées par des tests de microscratch et ultra-microindentation. Finalement, des tests de durabilité ont été effectués sur une électrode de grande taille possédant une surface active de 45 cm^2 jusqu'à 800 h à environ 770 °C , dans une cellule complète de configurations PAC et fonctionnant respectivement sous H_2 et un mélange $\text{H}_2/\text{H}_2\text{O}$.

Mots clés: PAC, EHT, LSCF, CGO, microstructure de type « corail », atomisation électrostatique, spectroscopie d'impédance, nanotomographie des rayons X, reconstruction 3D, ultra-microindentation.

Abstract (PT)

Interfaces e durabilidade de eléctrodos avançados para energia (IT-SOFC e SOEC)

O objectivo desta tese de Doutoramento é desenvolver eléctrodos de oxigénio avançados baseados em $\text{Ce}_{0.9}\text{Gd}_{0.1}\text{O}_{1.95}$ (CGO) e $\text{La}_{0.6}\text{Sr}_{0.4}\text{Co}_{0.2}\text{Fe}_{0.8}\text{O}_{3-\delta}$ (LSCF), homogéneos e com gradiente de composição, sobre electrólitos de zircónia estabilizada com ítria (YSZ = ZrO_2 dopada com 8 mol% Y_2O_3) utilizando deposição por pulverização electrostática. Uma camada fina e densa de CGO foi depositada entre o LSCF e a YSZ para atuar como barreira de difusão. Foi desenvolvida uma microestrutura com porosidade e área superficial muito elevadas de modo a obter um elevado desempenho electroquímico. O desempenho eléctrico do eléctrodo foi investigado por ensaios de espectroscopia de impedância em função da temperatura, realizados ao ar. Foi efectuada a descrição detalhada da microestrutura a partir de modelo 3D obtido por reconstrução de imagens de FIB-SEM e nanotomografia de raios X e relacionada com as propriedades eléctricas. O estudo do comportamento mecânico foi efectuado utilizando ensaios de riscagem e indentação instrumentados. Finalmente, foram efectuados ensaios de durabilidade em eléctrodo com 45 cm^2 de área ativa de oxigénio, até cerca de 800 h de operação a $770 \text{ }^\circ\text{C}$, em configurações de célula completa nos modos de SOFC e SOEC, com H_2 e mistura $\text{H}_2/\text{H}_2\text{O}$, respectivamente.

Palavras-chave: SOFC, SOEC, LSCF, CGO, Microestrutura em coral, ESD, EIS, nanotomografia de raios-X, reconstrução 3D, ultra-microindentação.

Table of contents

Motivations, objectives and structure of the PhD thesis	1
I. Introduction.....	7
I.1. Literature review	8
I.1.1. History and types of fuel cells	8
I.1.2. Solid Oxide Fuel Cells.....	10
I.1.2.1. Operation principles.....	10
I.1.2.2. Components	13
I.1.3. Solid Oxide Electrolyser Cells	22
I.1.3.1. Principle	22
I.1.3.2. Components	24
I.1.3.3. Degradation.....	24
I.1.4. Electrode microstructure and electrode/electrolyte interface	25
I.1.4.1. Oxygen reduction reaction.....	25
I.1.4.2. Compositional and microstructural optimization of LSCF cell performances	27
I.1.4.3. Air electrode/electrolyte interface	31
I.1.4.4. Morphological analysis by X-ray and focused ion-beam tomography.....	33
I.1.5. Mechanical properties of the electrode.....	37
I.2. Experimental	40
I.2.1. Electrostatic spray deposition.....	40
I.2.2. X-ray and focused ion-beam tomography	43
I.2.3. Impedance spectroscopy.....	44
I.2.4. Mechanical characterization	46
I.2.4.1. Instrumented indentation	47
I.2.4.2. Scratch test.....	49
I.3. References	51
II. Coral Microstructure of Graded CGO/LSCF Oxygen Electrode by Electrostatic Spray Deposition for Energy (IT-SOFC, SOEC)	69
II.1. Abstract.....	70
II.2. Introduction.....	71
II.3. Experimental	73

II.3.1. Coatings preparation	73
II.3.2. Coatings characterization	75
II.3.3. Electrochemical characterization	75
II.4. Results and discussion.....	76
II.4.1. Coatings characterization	76
II.4.2. Electrochemical characterization	80
II.5. Conclusions.....	81
II.6. References.....	83
III. Electrochemical properties of graded and homogeneous CGO-LSCF composite electrodes for IT-SOFC	87
III.1. Abstract.....	88
III.2. Introduction	88
III.3. Experimental.....	89
III.3.1. Oxygen electrode preparation	89
III.3.2.1. Cathode functional layer	90
III.3.2.2. Current collector layer.....	91
III.3.2. Microstructural characterization	91
III.3.2. Electrochemical characterization	92
III.4. Results and discussion	93
III.4.1. Microstructure.....	93
III.4.2. Electrochemical characterization	94
III.4.2.1. Series resistance	94
III.4.2.2. Polarization resistance.....	96
III.4.2.3. Isothermal agings	97
III.5. Conclusions	100
III.6. References	101
IV. 3D analysis of CGO-LSCF oxygen electrode for solid oxide fuel cells.....	105
IV.1. Abstract	106
IV.2. Introduction	107
IV.3. Experimental	108
IV.3.1. Deposition of CGO-LSCF coral microstructure.....	108
IV.3.2. Sample preparation for X-ray nanotomography	109
IV.3.3. X-ray nanotomography.....	109
IV.3.4. Data treatment.....	110

IV.3.5. PoroDict of GeoDict	110
IV.4. Results and discussion.....	110
IV.4.1. Microstructure by SEM	110
IV.4.2. 3D reconstruction of coral microstructure.....	111
IV.4.3. Microstructural analysis by PoroDict	113
IV.4.3.1. Open and closed porosity.....	113
IV.4.3.2. Specific surface area	117
IV.4.3.3. Percolation path	118
IV.4.3.4. Tortuosity factor.....	120
IV.4.4. Electrode polarization.....	121
IV.5. Conclusions	122
IV.6. References.	124
V. Mechanical properties on coral microstructure of CGO-LSCF oxygen electrode for SOFC and SOEC	129
V.1. Abstract.....	130
V.2. Introduction.....	130
V.3. Experimental.....	131
V.3.1. Electrode preparation	131
V.3.2. Mechanical characterization	133
V.3.2.1. Microscratch tests.....	133
V.3.2.2. Instrumented indentation tests.....	133
V.3.3. Microstructure analysis.....	133
V.4. Results and discussion	134
V.4.1. Microscratch tests	134
V.4.2. Instrumented microindentation tests	142
V.4.2.1. Indentation tests at 500 mN.....	142
V.4.2.2. Indentation tests at low loads: 2 – 40 mN	143
V.4.3. Calculation of the contact pressure	146
V.4.4. Comparison with powder pressing.....	148
V.5. Conclusions.....	149
V.6. References.....	151
VI. Durability test on coral CGO-LSCF with LSCF current collector working in SOFC and SOEC modes	153
VI.1. Abstract	154

VI.2. Introduction	154
VI.3. Experimental	156
VI.3.1. Oxygen electrode preparation.....	156
VI.3.2. Durability test in the SOFC and the SOEC modes.....	157
VI.3.3. Post-mortem microstructural observations	158
VI.4. Results and discussion.....	158
VI.4.1 SOFC mode	159
VI.4.1.1. Cell voltage degradation	159
VI.4.1.2. Cell resistance	160
VI.4.1.3. Influence of O ₂ gas flow change.....	163
VI.4.1.4. Influence of H ₂ gas flow change.....	165
VI.4.2. SOEC mode	167
VI.4.2.1. Cell voltage degradation	167
VI.4.2.2. Cell resistance	168
VI.4.2.3. Influence of O ₂ gas flow change.....	171
VI.4.2.4. Influence of H ₂ gas flow change.....	172
VI.4.3. Current-voltage behavior	173
VI.4.4. Post-mortem microstructural observations	174
VI.4.5. Discussion.....	177
VI.5. Conclusions	179
VI.6. References	181
General conclusions and prospect	187
Resumé (FR)	193

Motivations, objectives and structure of the PhD thesis

Motivations

The increasing consumption of energy and lack of fossil fuels force people to find new solutions. For the present situation the energy production is mainly focused on oil, coal and natural gas. The energy outlook released recently by US. Energy Information Administration showed that energy consumption should increase by 56 % in next 30 years (Fig. 1) [1]. Such high growth is expected mostly due to rising prosperity in developing countries like China, India and Brazil. In near future, the energy production more and more will concentrate on alternative sources of energy. However, energy should be produced in cheap and easy way without emission of harmful gases for human and the environment to compete with traditional sources of energy. One alternative option for heat and electrical energy productions are solid oxide fuel cells and solid oxide electrolysis cells [2].

The world continues to increase its demand for innovation in energy research, which is supported by increased government spending on energy and a rising number of worldwide researchers focusing efforts in this area [3]. Many energy-related research initiatives inherently require small-scale material analysis due to the micro- and nano-scale feature sizes in new and improved materials for energy innovation [4].

Working at intermediate temperature below 800 °C in solid oxide fuel cells (IT-SOFCs) would greatly decrease operation and fabrication expenses associated with interconnect materials, while improving their overall lifetime [5]. Unfortunately, detrimental phenomena such as electrolyte ohmic losses as well as electrode polarizations increase at lower temperature. One actual technological bolt in solid oxide electrolyser cells (SOECs) is the detachment of the anode where oxygen is produced [6-8]. To compensate the efficiency decrease in SOFCs and SOECs, alternative electrodes and electrolyte/electrode interfaces have to be evaluated.

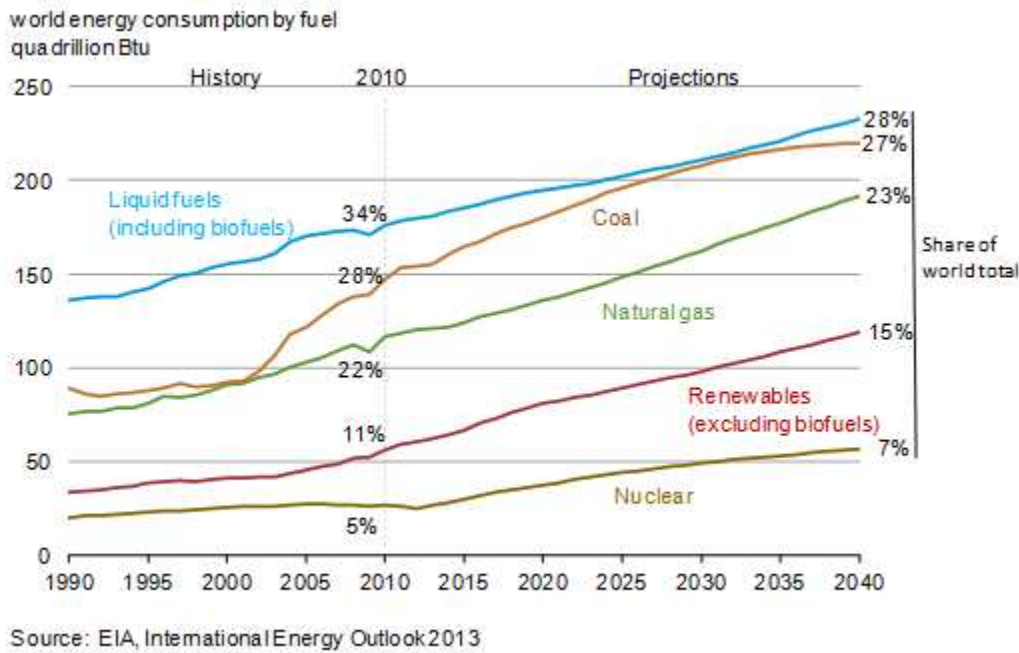


Fig. 1. World energy consumption by fuel quadrillion british thermal unit (Btu) [1].

This work is a part of the International Doctoral School in Functional Materials for Energy, Information Technology and Health (hereafter referred to as « IDS-FunMat ») which has been selected by the European Commission in the framework of the European Programme « ERASMUS MUNDUS II 2009-2013 ». IDS-FunMat combines a well-structured international doctoral education with high quality research work in leading laboratories from nine universities in five countries: University Louvain and University Liege (Belgium), University Waterloo (Canada), University Bordeaux 1, Grenoble INP, UPCM Paris (France), TU Darmstadt (Germany) and Instituto Superior Técnico (IST, Portugal). IDS-FunMat’s main objective is to implement doctoral programmes under co-supervision of at least two universities from two different countries and an Industry Partner.

The selected doctoral project is entitled “2011-08-EM Interfaces and durability of advanced electrodes for energy (Solid Fuel cells and Electrolysers) and is under the co-supervision of Pr. Elisabeth Djurado (supervising Grenoble INP) and Pr. Amélia Almeida (supervising IST). The two academic partners are Laboratoire d’Electrochimie et de Physico-Chimie des Matériaux et des Interfaces – LEPMI, UMR 5279 CNRS, Grenoble INP, Université de Savoie, Université Joseph Fourier in Grenoble, France and Instituto de Ciencia e Engenharia de Materiais e Superficies of Instituto Superior Technico (IST-ICEMS), Lisbon, Portugal. During the performance of the Doctoral Programme, research works have be carried out in collaboration with an industrial partner, Electricité de France – European Institute for Energy Research (EDF-EIfER), in Karlsruhe, Germany under Dr. Annabelle Brisse’s responsibility.

Objectives

The goal of this work is to fabricate a composite based on $\text{Ce}_{0.9}\text{Gd}_{0.1}\text{O}_{1.95}$ (CGO) and $\text{La}_{0.6}\text{Sr}_{0.4}\text{Co}_{0.2}\text{Fe}_{0.8}\text{O}_{3-\delta}$ (LSCF) as a porous and thin oxygen electrode film adherent to $(\text{ZrO}_2)_{0.92}(\text{Y}_2\text{O}_3)_{0.08}$ (YSZ) substrate by Electrostatic Spray Deposition (ESD), an innovative process, in order to improve durability in solid oxide fuel cells operating at intermediate temperature (IT-SOFC) and solid oxide electrolyser cells (SOEC). A thin and dense CGO barrier diffusion layer will be inserted between the electrolyte and the electrode.

The microstructure will be described by physical and chemical characterizations (Field Emission Gun-Scanning electron microscopy and energy-dispersive X-ray spectroscopy analyzer, FEG-SEM-EDS, X-ray diffraction, XRD) in LEPMI and CMTC (Consortium des Moyens Technologiques Communs, Grenoble INP), Grenoble. The particular investigation on electrode microstructure will be performed using FIB-SEM (Focused ion beam-SEM) and X-ray nanotomography at ESRF Grenoble (European Synchrotron Radiation Facility) and in collaboration with SIMaP laboratory (Grenoble INP).

Graded and homogeneous CGO-LSCF composites in half-cell configuration will be analyzed by Electrochemical Impedance Spectroscopy (EIS) to see the influence of compositions on the electrode polarization resistance. Furthermore, the interest of CGO insertion will be studied by EIS during durability tests in LEPMI, Grenoble. The mechanical analyses based on instrumented indentation and scratch tests will be performed in ICEMS laboratories in Lisbon. Finally, the oxygen electrode deposited on large scale will be tested in both SOFC and SOEC modes in full-cell configurations in EIFER in Karlsruhe.

This thesis summarizes results achieved during three years long through an European project between France, Portugal and Germany, with two academic partners (Grenoble INP and IST) and one industrial one (EDF-EIFER), respectively. Table 1 shows the mobility scheme during this PhD project. The total time spent in each parties was at least 6 months.

Table 1. Mobility scheme during PhD project.

PhD Year	Dates	Duration	Place
2011-2012	10/2011-06/2012	9 months	LEPMI, Grenoble
	07/2012-09/2012	3 months	ICEMS, Lisbon
2012-2013	10/2012-06/2013	9 months	LEPMI, Grenoble
	07/2013-09/2013	3 months	ICEMS, Lisbon
2013-2014	10/2013-11/2013	2 months	ICEMS, Lisbon
	12/2013	1 month	LEPMI, Grenoble
	01/2014-06/2014	6 months	EDF-ElFER, Karlsruhe
	07/2014-09/2014	3 months	LEPMI, Grenoble

Structure of the PhD thesis

The structure of the thesis is divided in chapters written in English and one large resume of the manuscript in French. The work starts with the motivations and the objectives of the work. An introduction consists of two parts: first in a literature review about SOFC, SOEC technologies, materials and specifications of the oxygen electrode. A second part of the introduction is devoted to a non-exhaustive description of some experimental techniques used in this work. The five following chapters (chapters II – VI) are written in a style of scientific articles. Each chapter contains an abstract, an introduction, an experimental part, a result part and a conclusion.

The objectives of chapter II are to create a graded porous and thin CGO-LSCF oxygen electrode for IT-SOFC and SOEC by ESD. Also, the microstructure has been investigated in order to observe porous morphology. Chapter III is focused on electrochemical characterization of the composite CGO-LSCF electrodes with graded and homogeneous compositions in two configurations: single corals with platinum mesh as a current collector and corals with additional screen-printed LSCF layer to serve as a current collector. Moreover, the durability test has been performed at 600 °C for 200 h. Chapter IV describes the coral microstructure by the microstructural parameters extracted from 3D model based on X-ray nanotomography. In addition, these parameters have been used to calculate the electrode resistance based on ALS (Adler-Lane-Steele) model. Chapter V is focused on mechanical behavior of the coral microstructure under mechanical loading. The microscratch and ultramicroindentation tests have been used to evaluate mechanical parameters such as hardness and Young's modulus. The objectives of Chapter VI are to perform durability test on

the full cell working in SOFC and SOEC modes. Post-mortem SEM observations have been carried out to explain the cell degradation.

The work in chapter II was presented in a form of a poster on the 5th International Conference on Fundamentals & Development of Fuel Cells at 16 – 18 April 2013 (FDFC 2013) in Karlsruhe, Germany. It got the best poster award in a category: Fuel Cells & Electrolyzers Materials. After the conference, the conference proceeding was selected to be published in *Fuel Cells – From Fundamentals to Systems* journal published by Wiley-VCH. The work in chapter III was presented in a form of an oral presentation on the 15th Topical Meeting of the International Society of Electrochemistry on Interfacial Electrochemistry at Atomic, Molecular and Nanoscale Domains from 27 – 30 April 2014 Niagara Falls, Canada. This part is going to be submitted in Journal of Power Sources.

The work in chapters IV – VI is prepared to be submitted in peer-reviewed journals.

The final part of the manuscript are general conclusions and prospect.

References

- [1] EIA. International Energy Outlook (IEO 2013), 2013.
- [2] D. Marinha, L. Dessemond, and E. Djurado, “Comprehensive Review of Current Developments in IT-SOFCs,” *Curr. Inorg. Chem.*, vol. 3, no. 1, pp. 2–22, 2013.
- [3] P. Piela and A. Czerwinski, “Review of fuel cell technology. Part II. Types of fuel cells.,” *Przem. Chem.*, vol. 85, no. 1, pp. 13–18, 2006.
- [4] C. Pianeses and M. Sorrentino, “Power control and optimalization,” *Proceedings of the Second Global Conference on Power Control and Optirnization; AIP Conf. Proc.; Bali, Indonesia, June 1-3, 2009*; vol. 1159, pp. 3–10, 2009.
- [5] J. A. Kilner and M. Burriel, “Materials for Intermediate-Temperature Solid-Oxide Fuel Cells,” *Annu. Rev. Mater. Res.*, vol. 44, pp. 365–393, 2014.
- [6] A. Hauch, S. H. Jensen, S. Ramousse, and M. Mogensen, “Performance and Durability of Solid Oxide Electrolysis Cells,” *J. Electrochem. Soc.*, vol. 153, no. 9, pp. A1741–A1747, 2006.
- [7] J. S. Herring, J. Obrien, C. Stoots, G. Hawkes, J. Hartvigsen, and M. Shahnam, “Progress in high-temperature electrolysis for hydrogen production using planar SOFC technology,” *Int. J. Hydrogen Energy*, vol. 32, no. 4, pp. 440–450, 2007.
- [8] A. V. Virkar, “Mechanism of oxygen electrode delamination in solid oxide electrolyzer cells,” *Int. J. Hydrogen Energy*, vol. 35, no. 18, pp. 9527–9543, 2010.

I. Introduction

I.1. Literature review

I.1.1. History and types of fuel cells

In 1839, C. F. Schönbein noticed current flowing between two different solutions: the first one containing water with dissolved hydrogen and the second containing water without hydrogen. These solutions were physically separated from one another by a membrane and connected by platinum wire [1]. Based on this experiment, W. R. Grove proposed the first fuel cell [2]. The cell consisted of beakers containing sulfuric acid solutions and tubes filled with water and either dissolved oxygen or hydrogen (Fig. I-1). The platinum wires were placed so that one end of each wire was immersed in the acid solution while the other was in the water-filled tube. He noticed two things, the constant current flow between the two wires and the increasing level of water in both tubes.

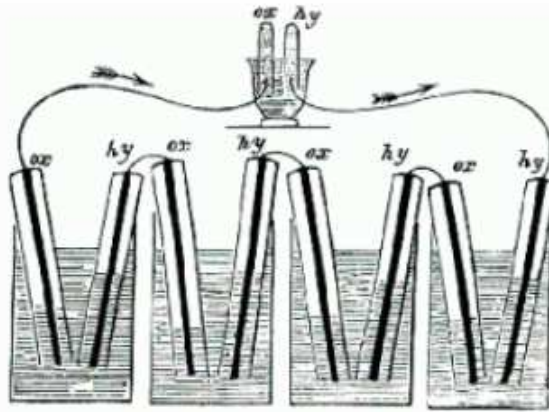


Fig. I-1. H₂-O₂ Fuel cell invented by W. R. Grove [2].

In 1889, Mond and Langer focused on the establishment of a prototype hydrogen-oxygen fuel cell that operated using industrial coal gas. They used a thin, perforated platinum electrode to increase gas adsorption. They noted high polarization losses at the oxygen electrode and a reduction of the cell efficiency was registered around 4 – 10 % after one operating hour [3]. Edward Nernst was responsible for truly advancing fuel cell technology in 1899. He discovered that the high electrical resistance of solid oxides can be significantly reduced by the addition of a solid oxide electrolyte such as doped zirconia [4]. In 1932, T. F. Bacon began a long term fuel cell program and 27 years later constructed a 5 kW alkaline fuel cell stack. Bacon's patents were used during World War II for British Royal Navy submarines. The discovery of solid oxide electrolytes by Nernst was the springboard for the creation of the first ceramic fuel cell by Baur and Preis in 1937 [5] which operated at 1000 °C. In the 1950s, research centers located at the Central Technical Institute in the Hage, Netherlands,

consolidation Coal Company in Pennsylvania and General Electric in Schenectady in New York developed a strong solid oxide fuel cell (SOFC) program. However, many problems such as high internal electrical resistance in the electrolyte, melting and short-circuiting due to semi conductivity almost stopped the research in its tracks. In the 1960s, fuel cells became a promising technology for the NASA space missions. These spacecraft required electricity to supply equipment, water for drinking as well as cooling and decent heat inside the spacecraft to keep astronauts alive. In the 1970s, the oil crisis also helped to encourage the development of fuel cells. The prices of natural gas and oil were so high that people started to look for alternative energy sources. The Westinghouse company achieved good cell performance using zirconium oxide and calcium oxide. Beginning in the 1950s and continuing into the 1990s, Westinghouse continued its research on solid oxide fuel cells. In 1997, the company demonstrated a test cell that worked for nearly 6 months (4035 hours). After this, the cell was redesigned and operation was resumed until a total of 12600 h of operating time was achieved. Indeed, the testing was halted not because the cell failed but rather the project had come to its end date. The efficiency of this cell in its final stage was 46 %, still a high value when compared with the average efficiency for typical combustion (34 %). The power achieved was 110 kW together with 65 kW provided by heat conversion. The ongoing research into SOFCs has fixed many problems but there is still much to be done to make fuel cells cheaper, more sustainable and more profitable. Current infrastructure is not prepared for future changes in production and distribution of electricity. On the other hand, the increasing cost of natural sources of energy, problems with decreasing amount of conventional fuels and instability in mining countries can accelerate fuel cell commercialization.

Types of fuel cells

Fuel cells can be classified by their operating temperature and by the electrolyte used in the cell. Details concerning the different types of fuel cells versus the electrolyte, the working temperature range, the fuel and applications are listed in Table I-1.

The principle behind how all fuel cells work is the same and consist in production of electrical energy directly from the electrochemical reaction between the fuel and oxygen. However, the choice of the electrolyte in the cell determines the working temperature and operating conditions.

Table I-1. Types of the fuel cells [6].

Type of fuel cell	Electrolyte	Working Temperature (°C)	Fuel	Applications
PEMFC	Polymer Membrane	70-110	H ₂ , CH ₃ COOH	Cars, mobile applications
AFC	KOH	100-250	H ₂	Planes, spacecraft
PAFC	H ₃ PO ₄	150-250	H ₂	Stationary applications
MCFC	(Na,K,Li) ₂ CO ₃	500-700	Hydrocarbons, H ₂	Cars, stationary applications
SOFC	(Zr,Y)O _{2-x}	700-1000	Hydrocarbons, H ₂	Cars, stationary applications

The working temperature limits the choice of the components such as electrode, electrolyte, interconnects and current collector materials as well as the fuel type used. Low temperature fuel cells (PEMFC, AFC, and PAFC) require pure hydrogen to be injected into the cell and the addition of a catalyst. For high temperature fuel cells (MCFC, SOFC) there is no need for an additional catalyst since the high temperatures facilitate the electrode reactions. Moreover, for these fuel cells, fuels other than pure H₂ can be used since it will be converted at high temperature inside the cell.

I.1.2. Solid oxide fuel cells

I.1.2.1. Operation principles

SOFCs are electrochemical devices that directly convert the chemical energy in various fuels into electrical energy and heat through oxidation by using a solid oxide as an electrolyte (oxygen anion conductor). The electrolyte also serves as a barrier preventing mixing of the fuel and oxidant streams. The working temperature of an SOFC typically ranges from 800 to 1000 °C due to the high activation energy required by the materials to attain suitable levels of charge transport and catalytic activity. Lower operation temperatures, down to 600 °C, would decrease the rate of chemical and mechanical degradations of SOFC components, thus decreasing operation and maintenance costs. In both cases, (high and low temperature) the working temperature allows for the use of different types of fuel such as pure hydrogen and hydrocarbons where internal reforming is included. The main advantage of SOFCs compared to other types of fuel cells is that a solid electrolyte is used, thus avoiding leaking and corrosion problems and rendering the two-phased system (gas-solid) highly stable.

Furthermore, no expensive catalysts are required. With respect to the other types of fuel cells, SOFCs attract greater interest due to their high energy-conversion efficiency and the possibility of recovering exhaust heat [7]–[10].

A single cell comprises a dense solid electrolyte in contact with a porous anode and cathode. These electrodes are placed in different atmospheres, the cathode in an oxidizing environment and the anode in reducing atmosphere. On the cathode side, oxygen gas is reduced to form the electrochemically active species, O^{2-} , that flows through the electrolyte. The electrochemical oxidation of the fuel (hydrogen, hydrocarbons, carbon monoxide or alcohols) with oxygen ions occurs on the anode side, liberating electrons in the process as well as water and heat. The electrolyte serves simultaneously as a selective charge transporter from the cathode to the anode and as physical barrier between the two atmospheres (Fig. I-2).

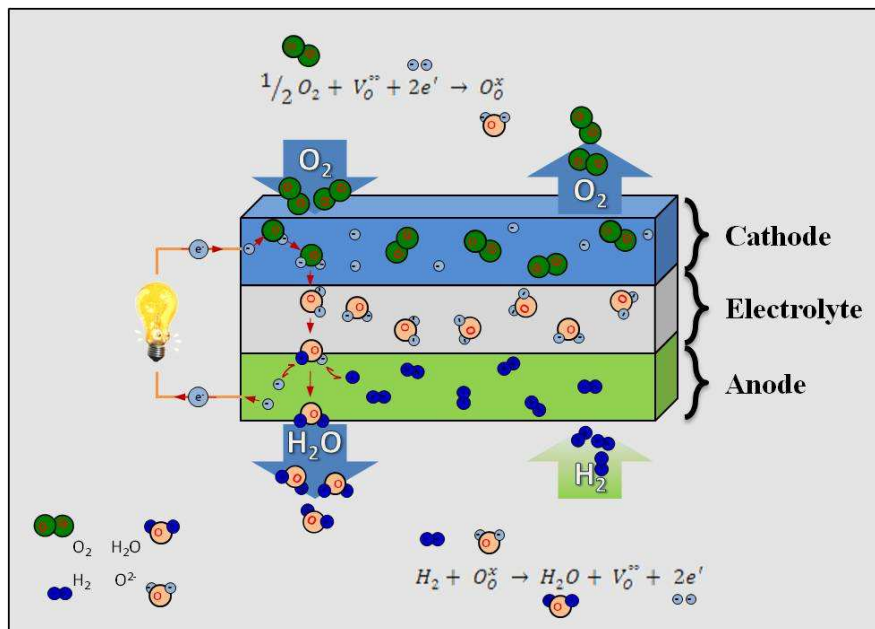


Fig. I-2. Schematic representation of an SOFC [11].

Reactions:

- anode side



- cathode side



- total reaction



The electromotive force E_r , or the reversible voltage, is described by Nernst equation:

$$E_r = E^0 + \frac{RT}{2F} \ln \left(\frac{p_{H_2} p_{O_2}^{1/2}}{p_{H_2O}} \right) \quad (I-4)$$

Where:

E^0 – reversible voltage at the standard state, V,

R – gas constant, $8.3144621(75) \text{ J.mol}^{-1}.\text{K}^{-1}$,

T – temperature, K,

F – Faraday constant, $9.64853365(21) \times 10^4 \text{ C.mol}^{-1}$,

$p_{H_2}, p_{H_2O}, p_{O_2}$ – respective partial pressures of hydrogen, water and oxygen gases, bar.

The real energy, E, is lower than E_r . The difference is due to ohmic voltage losses in the cell components and their interfaces, and by electrode polarization. The total polarization consists of cathode (η_c), anode (η_a) and electrolyte (IR) overpotentials. The final E of the cell is described as the following:

$$E = E_r - IR - \eta_a - \eta_c \quad (I-5)$$

The recent efforts in SOFC research are to diminish the total overpotentials. The cell shape, working temperature, pressure and materials used have the strongest influence on the polarization value.

Similar to molten carbonates, SOFCs require high temperatures to work efficiently. The waste heat can be used to heat-up buildings, support industrial processes or diverted to a standard generator for conversion into electricity. The efficiency of these cells range from 60 to 80 %. The applications of SOFCs are as stationary power plants or as energy sources in heavy vehicles. Many cell designs have been developed including tubular, planar, monolithic and single chamber [12]. The main differences between them are the current path inside the stack, the gas flow configuration and manifolding as well as the cell interconnectors [13]. The planar configuration is the most used in the research since the resistance can be lowered by decreasing the thickness of the components. These cells can be electrolyte-, anode- or cathode-supported, depending on the thickness of the components. In order to achieve commercially feasible productivity, the individual cells are combined into stacks using electrically-conductive gas-tight interconnectors to join the elements in series or in parallel. Fig. I-3 shows an example of stack arrangement on the basis of a planar SOFC concept.

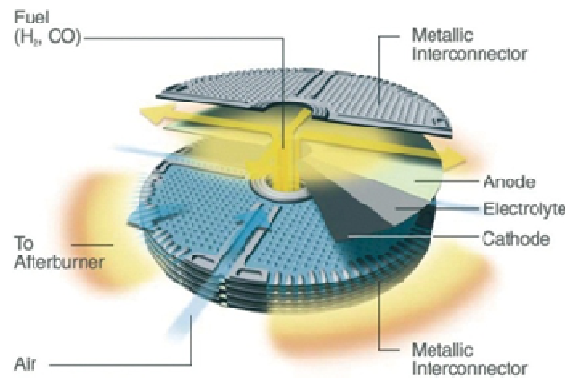


Fig. I-3. Planar SOFC stack design. Reprinted with permission from Hexis Ltd. [14].

In spite of the advantages with respect to the commercial electric power generation engines, practical application of SOFCs is still limited for the economical reasons, particularly as a result of the high costs of the component materials and fabrication methods.

II.1.2.2 Components

Anode

Regardless of the nature of the fuel (hydrogen or hydrocarbons), the anodic reaction occurs when oxygen ions arrive from the electrolyte and react with the oxidized fuel within the anode chamber, resulting in formation of water, electrons and heat. The reaction on the anode side is shown by the equation:



The reaction takes place at the triple phase boundaries (TPB), areas where the electrolyte (ion-conducting phase), the anode (electron-conducting phase) and the gaseous fuel meet. The anode must therefore be an adequate ionic and electronic conductor ($\sigma > 100 \text{ S.cm}^{-1}$). Classical fuel electrodes are usually a cermet composite of ceramic and metallic phases. The ceramic part is responsible for ionic conductivity, the transfer of oxygen anions from the electrolyte to the catalytically active locations. The role of metallic phase is to transfer electrons. The anode must fulfill the following requirements:

1. Porosity should be balanced to not deteriorate the electrochemical and mechanical performances but at the same time provide mechanical strength. Normally, porosity ranges between 30 – 40 %, supplying and distributing fuel and transporting away reaction products. The microstructure is optimized in order to have maximized percolation paths of ionic and electronic conduction, for optimum charge transport and maximized reaction surface areas.
2. Chemical stability in reducing atmosphere must not change composition during use.

3. Chemical and thermal compatibility with the electrolyte. The thermal expansion coefficients (TEC) of the electrolyte and anode should match to avoid mechanical stresses and cracking during heating/cooling cycles.
4. High catalytic oxidation of the hydrogen gas to H^+ .
5. Resistance to impurities in fuel. SOFCs can use different type of fuels, some of these fuels contain sulphur or carbon dioxide contaminants that can poison the microstructure.
6. Long term stability to avoid any coalescence of the metallic phase with temperature and time.

Typical material for the anode application is a nickel (Ni) – yttria stabilized zirconia (YSZ) metallic-ceramic composite (cermet) mostly in combination with a YSZ electrolyte. YSZ guarantees good oxygen conductivity and reduces thermal/chemical mismatch with the electrolyte. Moreover YSZ provides mechanical support for Ni particles and prevents coarsening of the metallic particles. At least 30 volume % of Ni is required to create effective electronic paths inside the cermet material. Nickel metal is not only chosen because of its cost effectiveness but also because it can be easily produced by co-sintering NiO and YSZ, followed by in-situ reduction of the nickel oxide. Metallic Ni has the good catalytic properties required to break H_2 bonds for fuel oxidation and/or reforming needs. Other metals, that may be used are copper, cobalt and noble metals. Copper has a lower propensity for coking and sulfur poisoning and is being considered as a replacement for Ni [15]. Other materials are currently being investigated as potential replacements for the Ni/YSZ combination. Mixed ionic-electronic conducting (MIEC) anode materials like $SrTiO_3$ - and $LaCrO_3$ -based compositions are particularly interesting due to their stability under reducing conditions. Improved conductivity and H_2 electroactivity of titanate-based oxides can be achieved with the addition of lanthanide dopants [16] and Mn and Ga on the B site [17]. Interesting results have been reported for $La_4Sr_8Ti_{11}Mn_{0.5}Ga_{0.5}O_{37.5}$ and $La_{0.4}Sr_{0.6}Ti_{1-x}Mn_xO_{3-x}$ compositions [18], [19], $La_xSr_{1-x}TiO_3$ [20], $Y_2O_3 - ZrO_2 - TiO_2$, $Sc_2O_3 - Y_2O_3 - ZrO_2 - TiO_2$ [21].

Electrolyte

In SOFCs, the electrolyte material must conduct oxygen ions from the cathode to the anode side. The best electrolyte candidates are materials with high ionic conductivity. Moreover, the electrolyte should be an insulator for electrons and should be stable under oxidizing and reducing conditions, between $1 - 10^{-18}$ atm of oxygen partial pressures. To maximize the ionic transport properties, large grain size (minimum grain boundary density) and maximum

density (gas tightness) are desirable. It must be gas-tight, to not allow fuel – oxygen mixing. Moreover, it cannot react chemically with either electrode, and their thermal expansion coefficients must be suitable.

Yttria stabilized zirconia (YSZ), 8 mol.% Y_2O_3 doped ZrO_2 , which crystallizes in the cubic fluorite structure (Fig. I-4), is widely used as a typical electrolyte for SOFCs. Common dopants such as Y_2O_3 , CaO , MgO , Sc_2O_3 and Yb_2O_3 are substituting for the host Zr^{4+} cations. The doping reaction is shown in the equation below using Kröger-Vink notation where the trivalent Y^{3+} cation substitutes with the Zr^{4+} ion, resulting in oxygen vacancies (Eq. I-7).

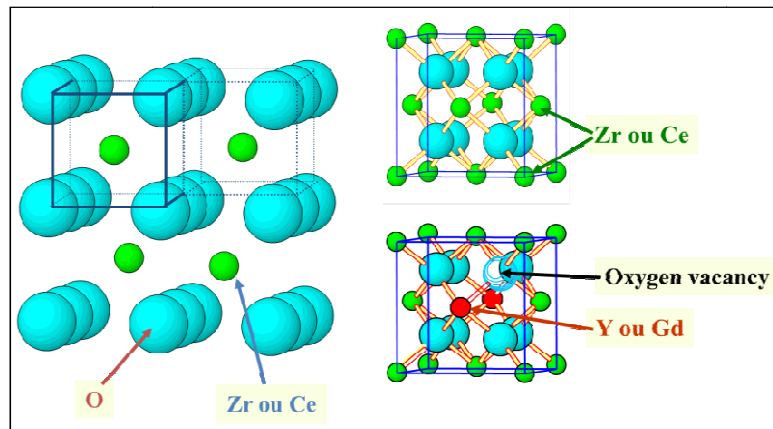
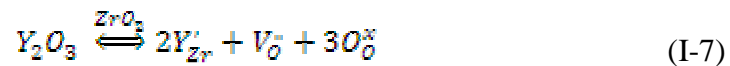


Fig. I-4. Cubic Fluorite YSZ.

Badwal et al. [22] showed that the ionic conductivity of yttria-stabilized zirconia is increased when the mol. % of Y_2O_3 is increased. The maximum ionic conductivity of 0.1 S.cm^{-1} at $1000 \text{ }^\circ\text{C}$ and 0.03 S.cm^{-1} at $800 \text{ }^\circ\text{C}$ is achieved at a dopant value of 8 – 10 % mol. % Y_2O_3 [23] after which the ionic conductivity severely drops (Fig. I-5). A dopant concentration that is too high leads to a phenomenon of association in between punctual defects, reducing their mobility and consequently diminishing the ionic conductivity [24]. As can be seen in Fig. I-5, the nature of the dopant must also be considered. Indeed it has been shown that when the dopant ionic radius has a close size mismatch to the ionic radius of the host, a larger ionic conductivity has been observed [25]. A larger mismatch leads to stresses in the crystalline lattice which can destabilize the crystalline structure leading to a phase transition.

YSZ possesses good mechanical and chemical properties for a broad range of temperatures and oxygen partial pressures. The commercial use of SOFC is limited by working temperature that is from 800 to $1000 \text{ }^\circ\text{C}$ due the highest oxygen ion conduction at this temperature range.

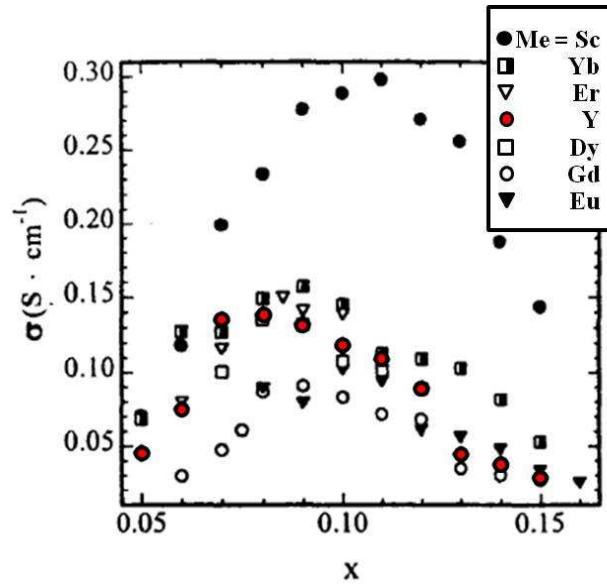


Fig. I-5. Variations in ionic conductivity at 1000°C for $(\text{ZrO}_2)_{1-x}(\text{Me}_2\text{O}_3)_x$ (Me = metal) with different Me content [23].

Since electrolytic performance of YSZ drops significantly with decreased working temperature, several alternatives to YSZ have been explored to reach larger ionic conductivity values at lower temperatures. Another group of potential candidates for SOFC electrolytes is based on perovskite lanthanum gallates (doped- LaGaO_3). Lanthanum can be partially substituted by Ca, Sr, Ba or other rare earth metals and gallium by In, Mg, Al or Zn. An example of such material is $(\text{La,Sr})(\text{Ga,Mg})\text{O}_{3-\delta}$ (LSGM), where both lanthanum and gallium are substituted by strontium and magnesium, respectively [26]. LSGM presents higher oxygen-ion conductivity in comparison with YSZ and can efficiently work at lower temperatures (650 – 800 °C) (Fig. I-6). Unfortunately, LSGM and another commonly used anode material, nickel oxide, can react giving rise to the formation of La-Ni-O insulating phases at the electrolyte/electrode interface leading to the deterioration of long term stability. The next promising material for electrolyte application is doped-ceria where the Ce^{4+} cation provides an open structure that facilitates O^{2-} migration. Ceria crystallizes into a fluorite structure type. The doped formula is $\text{Ce}(\text{M})\text{O}_{2-\delta}$, where M means rare earth or alkaline earth cations. Common doping cations are Gd or Sm with molar percentage of 10 – 30%. The doping reaction is similar to zirconia doping, in that Ce^{4+} cations are substituted by trivalent cations. As a result, oxygen vacancies are formed which enlarge the O^{2-} concentration. Sm-doped ceria shows the highest ionic conductivity but due to the cost of samarium and lack of the material, Gd is a priority before Sm. The advantage of CGO is a higher oxygen ion conductivity compared to YSZ ($2 \times 10^{-2} \text{ S}\cdot\text{cm}^{-1}$ for CGO [27], [28] and $8 \times 10^{-3} \text{ S}\cdot\text{cm}^{-1}$ for

YSZ [29] at 650 °C) and lower cost when compared with lanthanum gallate. The major drawback of CGO is that it must be used at temperatures above 650 °C. Under these conditions, doped cerium oxides present a strong reducibility at low oxygen partial pressures. Under reducing conditions, the electronic conductivity increases. Doped-CeO₂ is not mechanically stable under high oxygen chemical potential gradients [30].

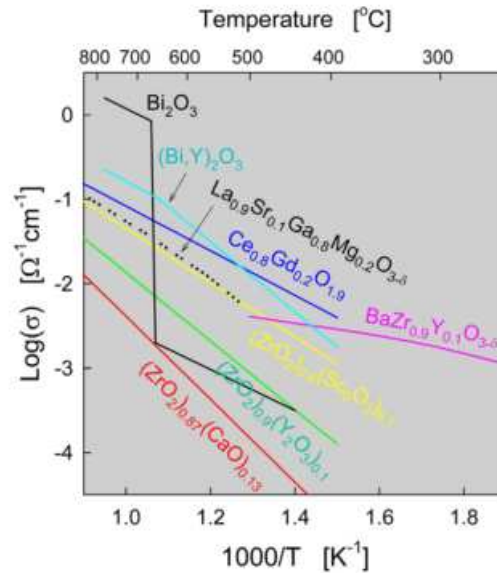


Fig. I-6. Conductivity for chosen electrolytes in SOFC [31].

A suitable candidate for an electrolyte application at lower temperatures could be Bi₂O₃ [32]. This material exists in its stable α -phase at room temperature where electronic conductivity predominates. The material transforms into the δ -phase when heating the α -phase from 730 to 825 °C (melting point). During cooling, the δ -phase is stable down to 650 °C where it transforms into the β -phase or down to 638 °C where it transforms into the γ -phase. All phases except α -Bi₂O₃, present high ionic conductivity. However, the δ -Bi₂O₃ phase is characterized by a conductivity three orders of magnitude higher than β -, and γ -phase. The range of usable temperatures for δ -Bi₂O₃ is increased by partial substituting of Bi by other elements. An exemplary material from the Bi₂O₃ group is Bi₄MeV₂O₁₁ commonly named BIMEVOX [33], [34] where the Me position is occupied by: Cu, Co, Y, Mg, Ti, Zr, Sc and others. The disadvantage of the material is its high reactivity with other electrode components and consequently greater polarization resistance. Moreover, BIMEVOX is easily reduced in low oxygen partial pressure and is characterized by higher thermal expansion coefficient than the rest of the cell components.

Another ion-conducting material is La₂Mo₂O₉ representing the so-called LAMOX family [35], [36]. LAMOX oxygen conductivity is higher than YSZ at intermediate temperature.

However, electrochemical and structural stability are still an issue. The hexavalent Mo is easily reducible at low oxygen partial pressures. Lanthanum molybdate is reduced in dilute hydrogen whereby there is a mixture of $\text{Mo}^{5+}/\text{Mo}^{6+}$ and creation of the $\text{La}_7\text{Mo}_7\text{O}_{30}$ phase and then decomposition [36]. In order to solve these problems, a wide range of substitutions in $\text{La}_2\text{Mo}_2\text{O}_9$ have been made. The most often substituting metals for La are Nd, Gd, Y while for Mo are W, In, Ge, Sb, Se and I. Doping increases mechanical and structural stability and anion conductivity. But still thermal expansion coefficients for materials from the LAMOX family are too high to be compatible with other electrodes.

The alternative materials for electrolyte are apatite-structured oxides. The chemical formula is $\text{A}_{10-x}(\text{BO}_4)_6\text{O}_{2\pm\delta}$. Materials like $\text{La}_{10-x}\text{Ge}_6\text{O}_{26+\delta}$ [37] and $\text{La}_{10-x}\text{Si}_6\text{O}_{26+\delta}$ [38], [39] are examples of such materials and present hexagonal structure. The ion conduction process runs differently compared to electrolytes based on fluorite and perovskite structures. In the apatite structure, the oxygen ion carriers are interstitial oxygen ions in contrast to oxygen vacancies. Apatites have higher oxygen-ion conductivity at lower temperature in comparison to YSZ. The material synthesis and sintering occur at very high temperatures ($> 1500\text{ }^\circ\text{C}$) making this material expensive and leading to general difficulty in obtaining high quality materials. Moreover, silica can diffuse into the electrode/electrolyte interface and block electrochemically active zones, thus reducing cell performance.

Cathode

The cathode is devoted to reducing the available oxygen molecules into oxygen ions, O^{2-} . Similar to the anode, this reaction must occur in the vicinity of TPB points. Consequently, electronic conductivity must be maximized and sufficient porosity is required to facilitate gas permeation. The microstructure of the cathode is therefore fundamental to enabling access of oxygen, electrons and ionic species between the cathode and the electrolyte, as well as expanding the number of TPB sites by increasing the total cathode surface area. The cathode must be stable in oxidizing environments and have high electrocatalytic activity for oxygen reduction.

Many materials can be used as an oxygen electrode in solid oxide fuel cells. Materials with a perovskite structure present catalytic and conductive performances and can be successfully used as an oxygen electrode in solid oxide cells (SOC). The classic perovskite formula is ABO_3 , where the A position is occupied by a large cation and the B position by a small one. Typical cations on the A site are La, Sr, Ba, Ca and Mn, Co, Fe, Ti, Zr on B site (Fig. I-7).

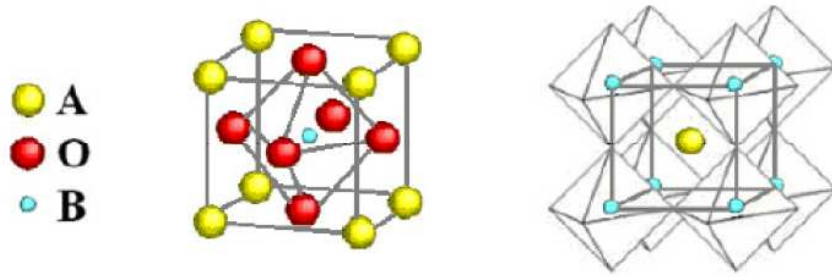


Fig. I-7. The ideal perovskite structure.

$\text{La}_{1-x}\text{Sr}_x\text{MnO}_3$ (LSM) is an example of the material with perovskite structure and is one of the best candidates for the electrode application in SOCs due to its high electronic conductivity at around 1000 °C [40]. Electronic conductivity drops with decreasing temperature below 900 °C and ionic conductivity is negligible. LSM is stable under oxidizing conditions but dissociates under $p\text{O}_2 < 10^{-14}$ at 1000 °C. LSM has a suitable TEC for use with YSZ electrolytes. The strontium content ranges between $0.2 < x < 0.3$. Strontium doping increases the electrical conductivity by increasing the $\text{Mn}^{4+}/\text{Mn}^{3+}$ ratio. However, Sr doping increases the reactivity between LSM and the most common electrolyte – YSZ. On the LSM/YSZ interface there is a creation of insulating phases such as $\text{La}_2\text{Zr}_2\text{O}_7$ and SrZrO_3 which are the origin of cell resistance increases and high polarization losses [41], [42]. The formation of insulating phases depends on the Sr/Zr ratio and is higher with a higher Sr/La ratio. LSM is a poor ionic conductor (very low oxygen self-diffusion coefficient $4 \times 10^{-14} \text{ cm}^2 \cdot \text{s}^{-1}$ at 900 °C [43]). The mechanism of oxygen reaction for the oxygen electrode in a solid oxide fuel cells is shown in Fig. I-8a.

The reaction in a pure electronic conductor does not occur on the whole electrode surface. The reaction consists of oxygen adsorption, diffusion of the oxygen along the surface to the contact area of the three phases called triple phase boundary (TPB). In that area, the oxygen species reduces to an oxygen anion by adopting electrons from conductor, incorporation into the electrolyte structure and finally transfer through the electrolyte bulk material. In such cases, the oxygen reaction highly depends on the density of TPBs, which are the only places where the oxygen can be transferred to the electrolyte.

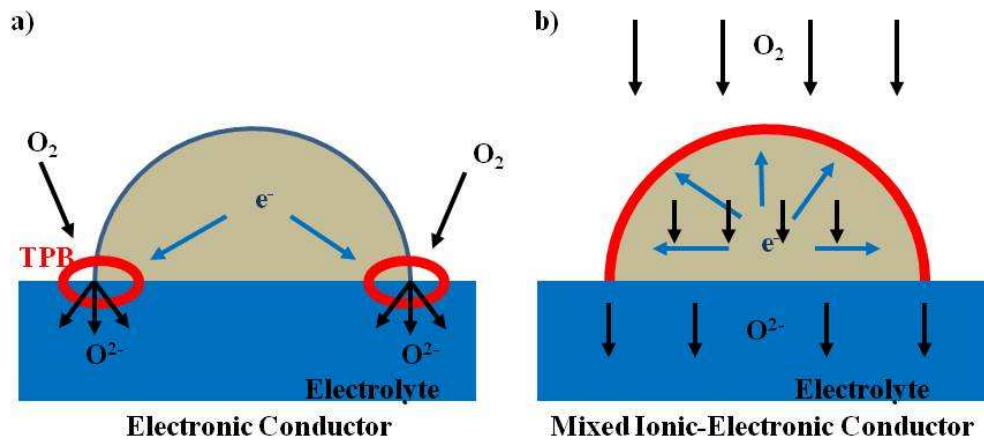


Fig. I-8. Sketch of the oxygen reaction electronic conductor (a) and mixed ionic-electronic conductor.

The reaction in a mixed ionic-electronic conductor (MIEC) is slightly different (Fig. I-8b). After adsorption of the oxygen onto the electrode surface, the oxygen diffusion to the TPB is not obligatory. In addition to diffusion at the TPB, oxygen can be reduced to an oxygen anion anywhere place on the conductor surface. Then the oxygen species incorporate into the electrode structure and transfer through the electrode bulk material to the electrolyte. After reaching the electrolyte/electrode interface, the oxygen anion may build-in into the electrolyte structure in vicinity of not only TPB but also of two-phase boundary point – 2PB. The total conductivity of a MIEC is a sum of the electronic and ionic conductivity. In this way, the reaction area is much larger compared to the electronic conductor.

The general effort in SOFC research is to decrease operation temperature from 1000 °C to values around 700 °C down to 500 °C in the so-called intermediate temperature solid oxide fuel cell (IT-SOFC) due to important economical and technological advantages. On one hand, high temperatures guarantee high reaction kinetics but on the other, working at high temperatures results in high operating costs, manufacturing costs, premature aging, and severely limits the available materials.

$La_{1-x}Sr_xCoO_{3-\delta}$ (LSC) became a potential material for cathodes especially at reduced temperatures [44], presenting both improved electronic and ionic conductivity in comparison with LSM at intermediate temperature ranges. The high Co content in LSC favors oxygen transport and catalytic properties [45]. However, with a higher cobalt content, the thermal expansion coefficient increases to $20.5 \times 10^{-6} K^{-1}$, $22.3 \times 10^{-6} K^{-1}$ and $25 \times 10^{-6} K^{-1}$ for x values equal to 0.4, 0.5 and 0.7, respectively [46]. Such high TEC values do not correspond with those from typical electrolytes consequently increasing mechanical stresses at the electrolyte interface. A solution to reduce thermal stresses is the substitution of Co by Fe, resulting in a composition in the form of $La_{1-x}Sr_xCo_{1-y}Fe_yO_{3-\delta}$ (LSCF) but electrical

conductivity is reduced. Similarly to LSM, the interaction between YSZ electrolyte and LSC is critical for cell stability and durability. Cobaltites easily react with zirconia. This reaction can be stopped with the insertion of ceria or LaGaO_3 as buffer layers.

A necessary compromise must be reached in terms of electrical conductivity and thermo-mechanical compatibility for potential IT-SOFC materials: $\text{La}_{0.6}\text{Sr}_{0.4}\text{Co}_{0.2}\text{Fe}_{0.8}\text{O}_{3-\delta}$ (LSCF6428). Fig. I-9 shows comparison of the total conductivity for different perovskite materials [47]. The graph shows that total conductivity for LSCF6428 is high and only $\text{La}_{0.7}\text{Sr}_{0.3}\text{CoO}_3$ (LSC) and $\text{La}_{0.7}\text{Sr}_{0.3}\text{Fe}_{0.6}\text{Ni}_{0.4}\text{O}_3$ (LSFN) have higher conductivity. For example, the LSCF6428 has been found to possess electrical conductivities of $350 - 400 \text{ S}\cdot\text{cm}^{-1}$ at 600°C [48], [49] and high ionic and electronic conductivity of 10^{-2} and $10^2 \text{ S}\cdot\text{cm}^{-1}$ at 800°C , respectively [50].

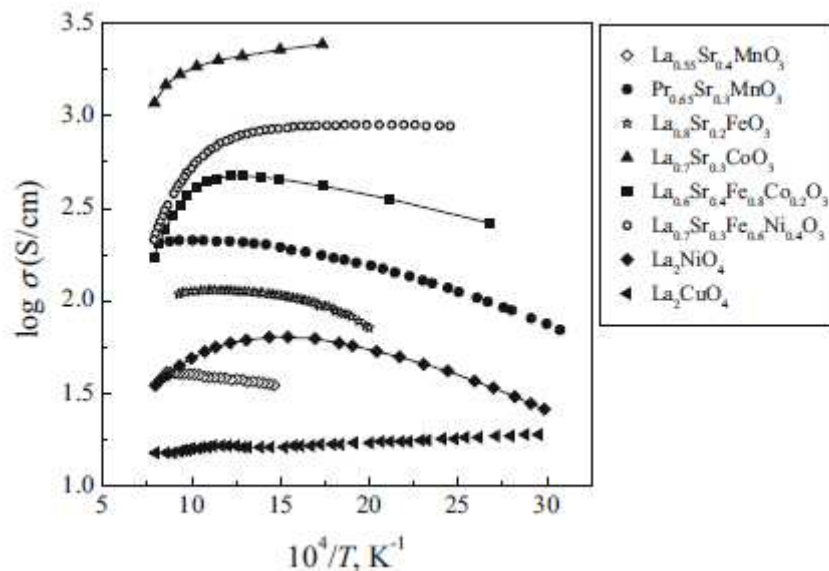


Fig. I-9. Comparison of the total conductivity for perovskite materials [47].

Nevertheless, LSCF reacts with YSZ electrolytes. As in the case of LSM, there is the formation of insulating phases ($\text{La}_2\text{Zr}_2\text{O}_7$ and SrZrO_3) [51] at the LSCF/YSZ interface, blocking the transfer of oxygen. To resolve the problem of lanthanum and strontium transfer into the electrolyte, LSCF and YSZ should be separated by a buffer layer. The best candidate is $\text{Ce}_{0.9}\text{Gd}_{0.1}\text{O}_{1.95}$ (CGO). CGO is a pure ionic conductor with a high oxygen mobility in oxygen, nitrogen and air at intermediate temperatures [52]. A dense layer of CGO can successfully prevent the migration of cations between an LSCF electrode and a YSZ electrolyte [53], [54]. It has been recently shown that a dense CGO layer as thin as 300 nm is sufficient to prevent strontium diffusion in between LSCF and CGO [55]. The LSCF electrode is also mechanically and chemically compatible with CGO electrolytes. Moreover,

CGO eliminates thermal mismatch of the average thermal expansion coefficients: $13.4 \times 10^{-6} \text{ K}^{-1}$ for CGO [30], $17.5 \times 10^{-6} \text{ K}^{-1}$ for LSCF [56] and $10.5 \times 10^{-6} \text{ K}^{-1}$ for YSZ [57].

I.1.3. Solid Oxide Electrolyser Cells

The use of hydrogen as energetic vector at a large scale is part of the actual context of sustainable energy development. High temperature electrolysis technology allows for massive hydrogen production without carbonaceous gas emission. The most effective fuel used in fuel cells is hydrogen. The chemical energy achieved for 1kg of hydrogen is 39.4 kWh which is three times higher than the those achieved from other fuels (13.1 kWh.kg^{-1} for liquid hydrocarbons). However, the high production costs, conditioning, distribution, transporting etc. outweigh energy efficiency. The solid oxide electrolyser cells are a type of solid oxide cell that uses the electrolysis process of water to create hydrogen. Solid oxide electrolyser cells (SOECs) consist of oxygen/air electrode (anode), steam/hydrogen electrode (cathode) and electrolyte [58].

I.1.3.1.Principle

SOECs are based on a ceramic oxide system generally working at $800 \text{ }^\circ\text{C}$ in order to provide sufficient ionic conduction of the electrolyte. The electrochemical reactions that take place in a solid oxide electrolyser cell are the inverse reactions to those that take place in a SOFC. Cell polarization is the opposite and the anode and cathode interchange their roles. In an SOEC, water acts as a reactant and is supplied to the cathode side of the cell. Oxygen ions are transported to the anode through the electrolyte, and hydrogen is produced in the cathode side (Fig. I-10) [59].

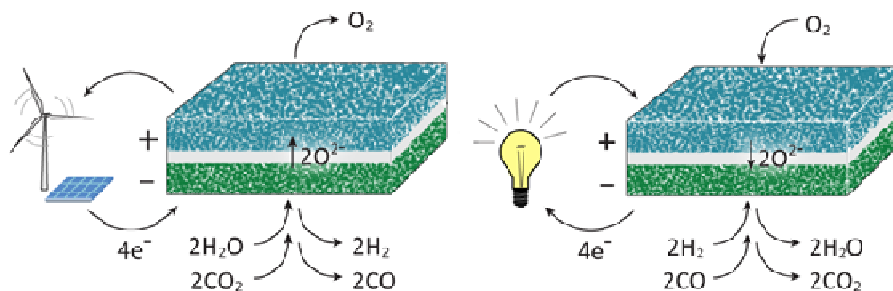


Fig. I-10. A solid oxide cell operated as an electrolysis cell (left) and as a fuel cell (right).

Reactions:

- anode side



- cathode side



The overall electrolysis reaction is shown in the equation below:



As a result of the reaction high purity hydrogen and oxygen are created.

On the cathode side, water is split using electrons, producing hydrogen gas and oxygen ions. Oxygen anions diffuse through the electrolyte to the anode where they give back electrons and create oxygen gas molecules. The electrolysis reaction is increasingly endothermic when the working temperature is increased (Fig. I-11). Part of the needed heat can be attained from the Joule heat produced by passage of the electrical current through the cell. This reduces H_2 production cost. The thermal potential at which the required heat for electrolysis is compensated by generated Joule heat is named thermoneutral potential.

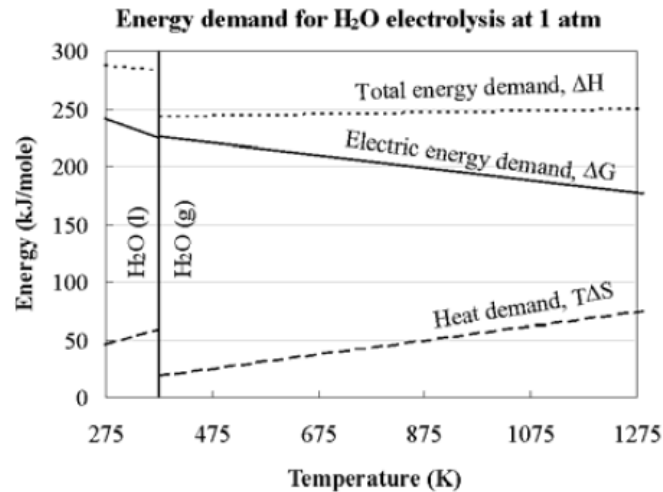


Fig. I-11. Thermodynamics of H_2O at a pressure of 1 atm [60].

The other main use for SOECs is the electrolysis of carbon dioxide. The electrolysis of CO_2 is shown in the equation below. As a result, carbon monoxide and oxygen are created.



Commonly, the electrolysis of steam and carbon dioxide are connected to generate a mixture of H_2 and CO (syngas) which is then used in the production of methane or methanol.

I.1.3.2. Components

Planar and tubular configurations of solid oxide electrolyzes are both being developed. Similarly to solid oxide fuel cells, the planar shape is advantageous mainly due to the lower total cell resistance. The requirements for cell components are similar to those for SOFCs. The electrolyte should be dense, gas-tight and should present a high ionic conductivity and good stability in the large oxygen partial pressure domain. The electrodes should be porous to supply and/or to distribute gaseous H_2O , H_2 , O_2 to the active zones. Moreover, electrodes should have high electrocatalytic activity and high electronic conductivity to provide sufficient current collecting. In fact, the common materials which are used for SOFCs are used but in reverse. The work of Hauch et al. [61] presented electrolysis in YSZ-metallic Ni/YSZ/YSZ-LSM – cathode/electrolyte/oxygen electrode, respectively. Other cathode materials can be samaria doped ceria with Ni-nanoparticles [62]. Instead of zirconia, ceria-based electrolytes can be used in SOECs [63], [64]. In terms of the oxygen electrode, $\text{La}_{0.8}\text{Sr}_{0.2}\text{FeO}_3$, $\text{La}_{0.8}\text{Sr}_{0.2}\text{CoO}_3$ [65], LSCF and lanthanum strontium copper ferrite [66] and others are an alternative to LSM. The set-up for SOECs is showed in Fig. I-12.

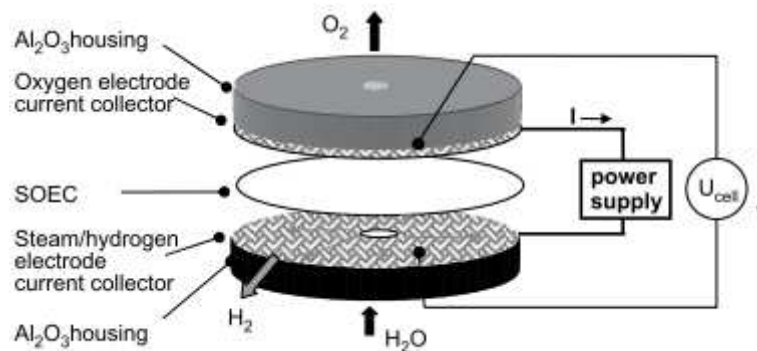


Fig. I-12. Experimental set-up of an SOEC [67].

I.1.3.3. Degradation

The long-term stability of SOECs has a crucial influence on commercialization of the technology. The lowest voltage degradation rates have been found to be around 1.7 %/1000 h after 3600 h and 3.8 %/1000 h for the total time of 9000 h testing at 800 °C with a current density of $-1.0 \text{ A}\cdot\text{cm}^{-2}$ [68]. Hauch et al. [69] reported degradation rate of 2 %/1000 h at 850 °C with a current density of $-0.5 \text{ A}/\text{cm}^2$ and 6 %/1000 h at 950 °C with a current density of $-1.0 \text{ A}\cdot\text{cm}^{-2}$. Degradation rates in a range of 10 %/1000 h were also reported [61], [69]–

[73]. The negative current density value of SOECs indicate the direction of the current flow that is opposite in relation to the current flow in SOFCs.

Degradation drops in cases where the cell stack is higher than a single cell. Stack degradation is caused mainly due to the degradation of the contact between interconnects and cells and provided impurities from tubing, interconnects and seals. The lowest voltage degradation for the stack was 1.5 %/1000 h at 800 °C under a current of -0.875 A.cm^{-2} where the steam-to-hydrogen conversion rate was 44 % [74]. Voltage drops between 3 and 5.6 %/1000 h were presented for 5 cell stacks under $-0.4 - 0.6 \text{ A.cm}^{-2}$ after total testing time of 4000 h [75], [76]. Zhang et al. [77] reported voltage degradation of 5.6 %/1000 h and 4.6 %/1000 h after 1100 h of testing for 5-10 cells in the stack operating under -0.25 and 0.32 A.cm^{-2} . Others degradation rates for the stacks were reported: 7 %/1000 h, -0.3 A.cm^{-2} [78] and 10 %/1000 h, -0.31 A.cm^{-2} [79].

Durability of the electrolyser cell depends on several parameters: operating temperature, current density, cell polarization, gas supply and steam-to-hydrogen conversion rate [80]. These parameters cause degradation of each cell components: oxygen/air electrode, electrolyte and hydrogen/steam electrode.

Oxygen electrode degradation has two main origins: formation of secondary phases and delamination of the air electrode. Secondary phases come from a reaction between Cr from the interconnect material (stainless steel) and the contact layer [81]. Products of the reaction block triple-phase boundary sites decreasing the active zone or directly forming insulating phases, increasing non-ohmic and ohmic resistances. The oxygen electrode delamination has been modeled by Virkar [73], and Jacobsen and Mogensen [82]. The origin of this delamination has been reported to be mainly due to the presence of high internal oxygen pressure inside the electrolyte but close to the electrolyte/oxygen electrode interface. The accumulated oxygen in the contact imperfections on the electrolyte/electrode interface facilitates detachment of the oxygen electrode.

I.1.4. Electrode microstructure and electrode/electrolyte interface

I.1.4.1. Oxygen Reduction Reaction Mechanism

Current development in fuel cells aims to reduce the total ohmic resistance. One solution for this issue is to decrease the thickness of the electrolyte and another one can be achieved by improving gas diffusivity on the oxygen side. The development of highly porous microstructure for the oxygen electrode guarantees easy access for oxygen gas to the oxygen

electrode and sufficient free electrochemically active space for the oxygen to be adsorbed, thus facilitating the oxygen reduction reaction (ORR). The oxygen transport for MIEC follows several elementary steps (Fig. I-13):

- 1) diffusion of oxygen from the gas to the electrode surface
- 2) adsorption of the oxygen on the electrode surface, moreover, the adsorped oxygen can stay in molecular form or dissociate
- 3) oxygen exchange redox reaction on the electrode surface, creation of the oxygen ion on the electrode surface

These three steps are similar for both (a) two-phase boundary (electrode/electrolyte) and (b) triple phase boundary (gas/electrode/electrolyte) mechanism. Next steps:

- 4 a) incorporation of the oxygen ion from electrode surface into the electrode structure by finding the oxygen vacancy
- 4 b) diffusion of the oxygen ion on the electrode surface to the TPB point
- 5 a) diffusion of the oxygen ion through the electrode bulk material to the interface between the electrode and the electrolyte
- 5 b) incorporation of the oxygen ion from the TPB point to the electrolyte structure
- 6 a) incorporation of the oxygen ion from the electrode structure to the electrolyte structure

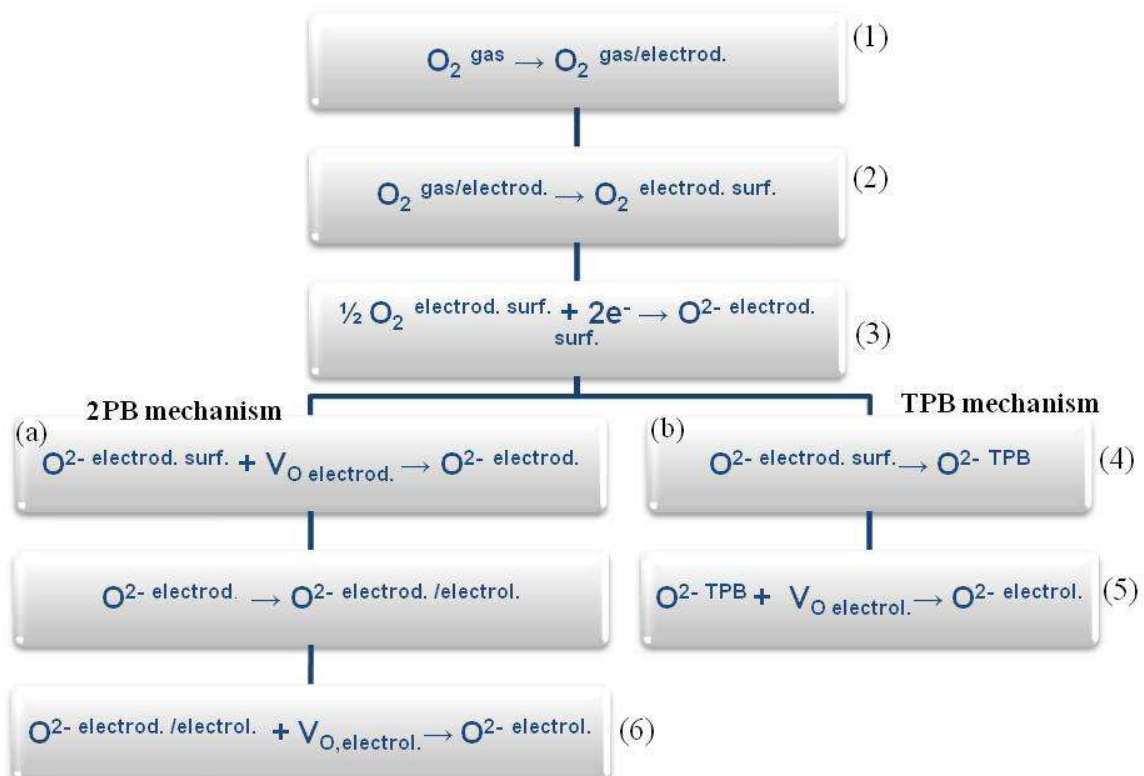


Fig. I-13. Simplified oxygen reduction reaction on the oxygen electrode side of the fuel cell [83].

It is worth mentioning that oxygen transfer in MIEC materials is mostly due to the sum of the 2PB and TPB mechanisms and it is difficult to distinguish which mechanism is dominating. For the case of the CGO-LSCF electrode, the reaction is no-longer limited by TPBs and can take place within the entire electrode volume. A highly porous oxygen electrode improves oxygen transport to the 2PB and TPB points whose quantity is enlarged by the microstructure morphology [84]. For more porous electrodes, electrochemical performance decreased due to bad contact with the interconnect and thus an insufficient supply of electrons to the electrode. When the electrode surface is discontinuous due to open porosity, the contact with the interconnect is only pointed and consequently the electro-conduction paths were cut off inside the electrode volume. As a result, 2TP and TPB points are not supported in electrons or the tortuosity of charge carrier path drastically increases. Another issue with the oxygen electrode microstructure is particle size. Smaller particles are characterized by higher surface area which favors enlargement of the active zone but additional boundaries are created for charge transfer [74], [85]. It is necessary to find a compromise which provides enhanced oxygen electrode performance.

I.1.4.2. Compositional and microstructural optimization of CGO-LSCF cells

Recent advances in the oxygen electrodes of IT-SOFC (and also SOEC) have resulted in very low polarization resistances. This was achieved mainly because of new material compositions as well as new microstructures. The lowest R_{pol} value of $0.023 \Omega \cdot \text{cm}^2$ at $600 \text{ }^\circ\text{C}$ was reported for $\text{La}_{0.6}\text{Sr}_{0.4}\text{CoO}_{3-\delta}$ (LSC) with a thickness of 200 nm, a mean grain size of 17 – 90 nm and porosity of up to 49 % with an additional screen-printed LSC current collector [86]. Such a low value was explained by the increased inner surface area and increased oxygen exchange reaction caused by the occurrence of cobalt rich local areas on the electrode surface.

The 20 molar % partial substitution of Co in LSC for Fe allowed produced R_{pol} values of $0.05 \Omega \cdot \text{cm}^2$ at $600 \text{ }^\circ\text{C}$ in LSCF (6482) [87]. On the one hand, the decrease in Co content leads to an increase in the polarization resistance. However, decreases in content reduce the TEC value of the electrode, reducing the thermal mismatch between electrode and electrolyte i.e. YSZ, CGO. Further substitution of Co leads to the investigation of LSCF (6428) material with a compromise between mechanical and electrical properties. The electrode resistance was found to vary between 0.73 and $6.94 \Omega \cdot \text{cm}^2$ at $600 \text{ }^\circ\text{C}$ in air [88]–[93]. The particular comparison of polarization resistance in revised publications is difficult due to different components fabrication techniques (electrostatic spray deposition [88], spray pyrolysis [89]–

[91], screen printing [92], [93]), film thickness (from nano-structured films to micro-structured films), sintering temperatures, film adhesion and the most important the microstructure. The influence of the microstructure on electrode performance was presented by Marinha et al. [88] on LSCF (6428) prepared by ESD. In this work, three LSCF microstructures called: dense, cracked and coral were fabricated under identical conditions. The best performances were noted for the open microstructures (cracked and coral), proving that porosity plays an important role of the microstructure.

As low R_{pol} as $0.13 \Omega \cdot \text{cm}^2$ at $600 \text{ }^\circ\text{C}$ were also measured with only 20 % Co content in LSCF (6428) by Marinha et al. [94]. Such a low value was possible in part due to the fabrication of the electrode with a large surface specific area using electrostatic spray deposition (ESD). The microstructure was characterized by columns that enhanced gas access to the electrode with additional nanostructured porosity inside the columns. An additional LSCF layer was screen-printed as a current collector. The area specific resistance (ASR) value corresponds to the lowest ASR values found in the reviewed literature at similar temperatures for the LSCF composition with 20 % Co-doping on the B site of the perovskite lattice.

CGO-LSCF electrode composite

The objective of this work is to fabricate a composite oxygen electrode with controlled composition and microstructure as an SOFC operating at intermediate temperatures and for solid oxide electrolyser cells. The electrode is based on two materials: a MIEC material (LSCF) and an ionic conductor (CGO). The CGO-LSCF composite has already been investigated by the variation of CGO weight percentage between 20 to 70 wt. % [92], [95]–[97]. The ASR for such an electrode was found to range from $0.17 \Omega \cdot \text{cm}^2$ to $0.60 \Omega \cdot \text{cm}^2$ at $600 \text{ }^\circ\text{C}$ with a CGO electrolyte [92], [95], [96]. ASR values of $0.33 \Omega \cdot \text{cm}^2$ and $1.00 \Omega \cdot \text{cm}^2$ at $600 \text{ }^\circ\text{C}$ have also been achieved for “non-protected” YSZ electrolyte [95], [97], respectively. Such a polarization effect is approximately six times lower than when LSM is used as the oxygen electrode. The lower ASR for the CGO electrolyte may indicate better electrochemical compatibility with the CGO-LSCF electrode in comparison with YSZ electrolytes. The ASR of the CGO-LSCF electrode deposited on the YSZ electrolyte with a thin CGO layer was measured to be $0.19 \Omega \cdot \text{cm}^2$ at $600 \text{ }^\circ\text{C}$ [95] which simply means that the CGO layer releases thermal and mechanical mismatch between the composite electrode and YSZ. The optimized composition of CGO and LSCF in the composite is still controversial. Different studies have shown the lowest ASR values for various compositional ratios of CGO-LSCF: 60/40 wt. % [92], 50/50 wt. % [95], 30/70 wt. % [96] and 50/50 wt. % [97]. The optimum

CGO addition of 36 % volume in relation to LSCF (6428) resulted in an ASR that was four times lower than other CGO additions, classifying this composition as a promising material for IT-SOFCs with CGO electrolytes [96]. Importantly, the inner distribution of each phase was not considered in these articles. The addition of CGO in the LSCF electrode volume presents several advantages. Firstly, CGO with its high ionic conductivity increases the ionic conductivity of the composite electrode. The oxygen transport can be illustrated by two mechanisms: diffusion through the bulk material described by a diffusion coefficient (D) and surface exchange described by surface exchange coefficient (k). The self-diffusion coefficient (D^*) determines the internal ionic transport that can take place even under equilibrium in the absence of concentration and/or chemical potential gradient. The higher D^* value indicates the higher degree of oxygen transfer through the conductor. The surface exchange coefficients characterize the ability of the material to exchange oxygen in the atmosphere and on the surface interface of the material. Both parameters can be extracted from an oxygen isotope diffusion profile using isotope exchange depth profiling (EDP) with secondary ion mass spectroscopy (SIMS) or from conductivity profiles from electrical conductivity relaxation experiments (ECR).

Table I-2. k and D^* values for CGO, LSCF and YSZ.

Material	k (cm.s⁻¹)	D^* (cm².s⁻¹)	Temperature (°C)	PO₂ (mbar)	Ref.
CGO	8x10 ⁻⁸	1x10 ⁻⁶	900	200	[98]
LSCF	5.51x10 ⁻⁶	4.18x10 ⁻⁸	800	880	[99]
YSZ	3x10 ⁻⁶	1x10 ⁻⁷	900	200	[100]

Table I-2. shows k and D^* values for CGO, LSCF and YSZ. CGO is characterized by a high oxygen self-diffusion coefficient and a low surface exchange coefficient compared to LSCF and YSZ. Esquirol et al. [99] investigated a composite electrode and proved that a composition of CGO and LSCF has a higher D^* and almost the same k value compared with a single LSCF electrode (Fig. I-14).

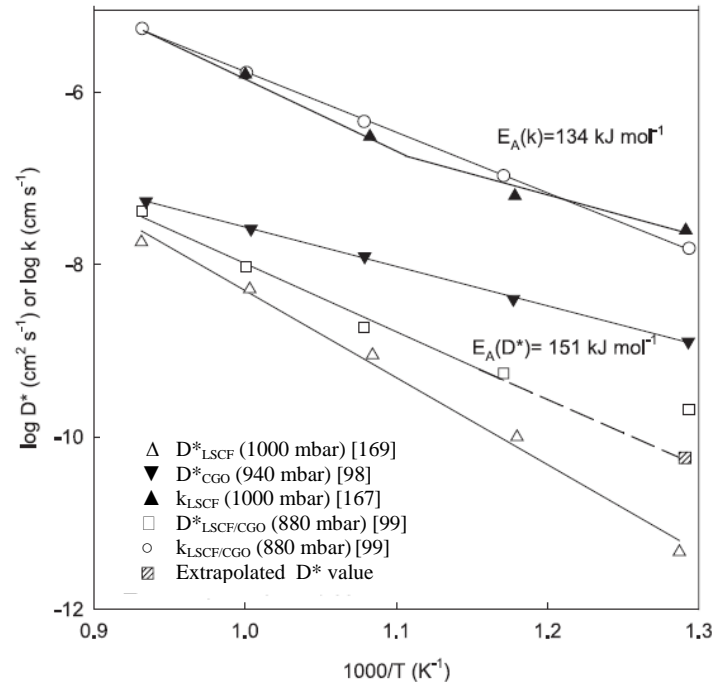


Fig. I-14. Arrhenius plots of the oxygen self-diffusion coefficient and the surface exchange coefficient for LSCF, CGO and LSCF/CGO composition [99].

The addition of CGO in the electrode volume increases the TPB length. As for the MIEC material, the oxygen charge transfer can occur throughout the bulk electrode material, the charge transfer via TPB area being still dominating. The composite electrode of CGO-LSCF shows better electrochemical performance compared with a single LSCF electrode. However the distribution of each phase in the electrode volume may have a predominant effect on its properties. Improper design (in terms of microstructure, composition and distribution of each phase) of the electrode makes electrocatalytic activity, thermomechanical and chemical stability worse. To attain the most effective properties, the region close to the electrolyte should be rich in CGO since it serves as the electrolyte in the electrode volume. At the same time, the top part of the electrode should be rich in LSCF since it provides electrons for the ORR and it is catalytically active for the ORR. After the oxygen incorporation into top LSCF electrode part, its diffusion through the electrode should be accelerated by the presence of CGO. Based on above, it was assumed that a gradient composition of CGO and LSCF would improve the electrode properties. The graded composite combines the ionic properties of CGO with the mixed ionic-electronic and electrocatalytic properties of LSCF and still manages to keep the electrode porosity at relatively high levels, facilitating oxygen gas penetration. The fine nanostructuring effect on the CGO-LSCF composite is promising for the improvement of the electrode performance. The preparation however of the graded electrode

is only possible by using the proper preparation process. Until recently, there have been many papers concerning the CGO-LSCF composite electrode, none however are working with a composite with gradient of CGO-LSCF components.

I.1.4.3. Air electrode/electrolyte interface

The interface between the air electrode and the YSZ electrolyte plays an important role not only for electrochemical properties but also for mechanical properties of the fuel cell. The electrochemical reactions take place preferably around the interface. There is also a concentration of stresses caused by possible thermal expansion mismatch. If thermal stresses overcome the electrode adhesion to the electrolyte then the coating cracks and delaminates. In such a case, the electrochemically active area decreases, the oxygen reduction reaction can take place in a limited area increasing the polarization and ohmic losses. The study by Park et al. [101] has shown that when the TEC of the electrode and the electrolyte differ by more than $7 \times 10^{-6} \text{ K}^{-1}$ the degradation of power density of a single cell after 500 h was $7.7 \text{ \%} \cdot \text{kh}^{-1}$ at $600 \text{ }^\circ\text{C}$ in an SOFC. Moreover, it was estimated that 10 % of the area delaminated within the first 500 h of operation. Nevertheless, the research focused on TECs allowed matching components with similar thermal expansions. The other major problem is the chemical reactivity in between the electrode and the electrolyte leading to secondary phases created during cell fabrication and/or operation.

In general, there are two main reasons for oxygen electrode deterioration and both originate at the electrode/electrolyte interface. The first one is based on the reactivity at the electrode/electrolyte contact where insulating phases can be formed. Depending on the air electrode material there were noticeable different secondary phases such as $\text{La}_2\text{Zr}_2\text{O}_7$ for the electrode rich in La. Moreover, there was the local accumulation of cations from electrode material which destroy the cell. One solution to avoid this chemical reactivity is to coat a thin and dense layer of CGO in between YSZ and LSCF. This CGO barrier diffusion layer can block the cationic diffusion and the formation of secondary phases [54], [102]–[104]. Han et al. [105] introduced dense CGO as a Sr-diffusion barrier layer of $0.5 \text{ }\mu\text{m}$ in thickness by physical vapor deposition (PVD) on the top of a $1 \text{ }\mu\text{m}$ thick YSZ electrolyte and noticed that ohmic resistance dropped by one order of magnitude in comparison with $10 \text{ }\mu\text{m}$ YSZ electrolyte with a $5 \text{ }\mu\text{m}$ thick screen-printed CGO layer. Constantin et al. [106] has shown that a dense CGO layer, fabricated by RF magnetron sputtering between LSCF6428 and YSZ, as thin as 110 nm , was sufficient to delay Sr^{2+} migration. Indeed, the electrolyte and the cathode

polarization resistances were strongly decreased to $40 \text{ } \Omega \cdot \text{cm}^2$ and $0.1 \text{ } \Omega \cdot \text{cm}^2$, respectively. After 550 h, a low series resistance variation was observed with the addition of the CGO layer due to better contact and improved ionic collection between LSCF and YSZ. The relative R_{pol} variation was strongly reduced to reach a minimal value of 57 % when the CGO layer was only $0.11 \text{ } \mu\text{m}$ thick. The relative R_{pol} variation for LSCF/YSZ without CGO layer was 694 %. These electrochemical impedance data were consistent with X-ray microanalysis where Sr^{2+} migration was only detected at the LSCF/YSZ interface. The barrier diffusion layer plays a role in this interlayer, the dense CGO fully covers the YSZ surface improving the adhesion of the electrode to the electrolyte. The high inner surface area and nanostructuring effect have a significant influence on the electrochemical performance. CGO is chemically compatible with both YSZ and LSCF. However, CGO and YSZ form a solid solution at $1300 \text{ } ^\circ\text{C}$, in which Ce and Gd cations diffuse and incorporate into the YSZ structure [55], [107]–[109]. A $(\text{YSZ})_{1-x}(\text{CGO})_x$ solid solution has a lower conductivity than each component itself. From this reason, the deposition and sintering should be carried out at temperatures below the solidus line.

The second reason for deterioration of cell performance is oxygen electrode delamination, mostly occurring in SOECs [110]–[112]. The origin of this degradation comes from accumulation of the oxygen in the electrolyte near the oxygen electrode. When this occurs, regions of high oxygen pressure may cause failure and detachment of the electrode along the interface. Chen et al. [113] have developed LSM with the addition of CGO nanoparticles as an oxygen electrode for high temperature electrolysis. The role of the nanoparticles is to raise the electrochemical activity for the transport of oxygen ions from the electrode. Additionally, the presence of CGO inhibits the delamination of the electrode leading to a decrease of internal high oxygen pressure due to the presence of CGO. For the case of the LSM/CGO composite, LSM impregnated with CGO acts as a MIEC electrode in which CGO is responsible for the oxygen oxidation reaction and LSM for the electronic transfer pathway. The other way to reduce high internal oxygen pressure is to use an electrolyte with a higher electronic conductivity. The solution was modeled by Virkar [73]. In general, the electronic conductivity of the electrolyte used in SOFC and SOEC is very small. Even small changes in the electrolyte electronic conductivity cause changes orders of magnitude in size in oxygen partial pressure close to the electrolyte/electrode interface.

A durability test of 9000 h performed in SOEC mode on a cell consisted of LSCF-CGO-YSZ-Ni/YSZ showed several degradation causes [114]. Post-mortem SEM and EDX investigations showed grain surfaces structuring in the electrolyte, void formation along grain boundaries,

horizontally aligned pores at the YSZ/CGO interface, mass transport and formation of a dense layer at the YSZ/CGO interface. Moreover, in the LSCF oxygen electrode the migration of cations and re-crystallization of the LSCF in the electrochemically active area was detected. For these reasons, the cell voltage increased 3 % every 1000 h. However, it was not possible to classify the influence of each process on the total degradation rate. Considering cell impedance spectra, an increase was noticed in the ohmic (at high-frequency resistance above 3000 Hz), in the non-ohmic (at frequencies above 300 Hz) and a minor increase in the low-frequencies (0.1 – 10 Hz) contributions.

The coverage of the electrolyte by the oxygen electrode also has an important influence on the electrochemical properties. For the case of an oxygen electrode made of purely electron conducting material, the electrode/electrolyte interface should not be fully covered by the electrode material since the number of TPBs would be decreased. However the poor electrode/electrolyte contact becomes a nucleation site for crack creation. For mixed ionic-electronic conductors, the whole YSZ electrolyte surface can be covered with a diffusion barrier layer to eliminate crack formation and propagation. Moreover, the larger surface for oxygen diffusion from the bulk electrode to the electrolyte is achieved when the electrode fully covers the electrolyte.

Adhesion between the electrolyte and the oxygen electrode has an influence on oxygen transfer. In order to ensure good electrode/electrolyte contact, a dense LSCF layer with a thickness of 200 nm was deposited by pulsed laser deposition (PLD) serving as the functional layer and followed by a porous LSCF layer with a thickness of 53 μm by screen-printing serving as the current collecting layer [115]. The polarization resistance was reduced from 0.7 to 0.2 $\Omega\cdot\text{cm}^2$ at 600 $^\circ\text{C}$ by introducing a dense nano-scaled LSCF to the screen-printed LSCF. Such a low R_{pol} was explained by the improvement in adhesion, a larger oxygen incorporation in the electrode structure transfers through the dense LSCF functional layer. For the case of the LSCF, the oxygen percolation path is expected to be larger than for the porous one.

I.1.4.4. Morphology analysis by X-ray and focused ion beam-scanning electron beam (FIB-SEM) tomography

The microstructures of the oxygen electrode, fuel electrode and interfaces between electrode and electrolyte are currently being investigated by many researchers. Recently, X-ray nanotomography and focused FIB-SEM have appeared as powerful tools to investigate the microstructure in 3D. In the last few years, both techniques have been improved to increase

the resolution but still FIB-SEM has a higher resolution (~10 nm) which is mainly limited by the thickness of milled layer. For X-ray nanotomography, the resolution is around 32 nm but can be improved using a brighter X-ray source. However, FIB-SEM technique is usually focused on quantitative analysis of individual solid phase fractions since for X-ray the contrast is too low and not sufficient especially for nano-structured composites.

The difference between both techniques is in the sectioning. For X-ray tomography, X-rays are used to create a single cross section at each degree while rotating the specimen. FIB with a dual beam gun uses electrons to create a section picture and then ions (usually Ga) to mill the specimen to see the deeper structure. After sectioning, slices are combined into a stack that is then used for three-dimensional reconstruction. One disadvantage of FIB-SEM is that it is destructive. FIB requires physically milling the material away, X-ray nanotomography is non-destructive and can be followed by further sintering or aging tests.

Information such as surface area, open/closed porosity, pore size distribution, tortuosity, triple-phase boundaries, and percolation path can be extracted from the 3D model and used to explain the relation between electrode structure and performance. Researchers are focused on three dimensional reconstruction and microstructure quantifications on LSM/YSZ composite electrode [116]–[118], LSCF electrode [88], [119]–[122], NiO/YSZ fuel electrode [123]–[127].

Table I-3. Microstructural characterization of an LSM-YSZ electrode obtained using X-ray nanotomography and FIB-SEM [116].

Parameters and phases	X-ray nanotomography	FIB-SEM
Mean phase diameter (μm)		
Pore	0.34	0.27
YSZ	0.27	0.28
LSM	0.42	0.40
Volume fraction		
Pore	0.34	0.34
YSZ	0.32	0.33
LSM	0.34	0.33
Contiguity (%)		
Pore	99.6	99.8
YSZ	99.8	99.4
LSM	98.2	94.3

Nelson et al. [116] used both FIB-SEM and X-ray nanotomography to characterize microstructure of an LSM-YSZ electrode using a resolution of 45 nm and below. A comparison of mean phase diameter, volume fraction and contiguity of phases was reported (Table I-3). The total interfacial area for pore-LSM, for LSM-YSZ and for pore-LSM achieved basing on X-ray nanotomography and on FIB-SEM was similar, the difference between the areas were lower than 10%. Despite the different resolutions (45 nm for X-ray nanotomography and 30 nm for FIB-SEM nanotomography) both techniques showed similar microstructural parameters to directly describe the oxygen electrode.

3D microstructural analysis is usually related to impedance spectroscopy measurements. Composites made from LSM/YSZ with compositions ranging from 30 to 70 wt. % of LSM were studied by Wilson et al. [117]. FIB-SEM nanotomography with a pixel size lower than 50 nm was used to investigate variations in TPB lengths, interfacial curvatures, phase volume fraction and phase tortuosity while changing ratios of LSM to YSZ. All electrode composites were designed to have porosity volume fraction of 50 %. The tortuosity of the YSZ phase varied from 2.5 for 30 wt. % of LSM to 6.5 for 70 wt. % of LSM. The lowest polarization resistance was achieved for an electrode with 50 wt. % YSZ, when the tortuosity was equal to 3.5. The high overpotential for other compositions was explained by the low intra-connectivity of the LSM phase for case of the low LSM content composite and by the low YSZ phase tortuosity for the case of the low YSZ content composite. The pore phase connectivity was 100 % for all compositions, the lowest YSZ phase connectivity was 94 % for 70 wt. % LSM increasing to 100 % for the other compositions. Finally, the LSM phase connectivity linearly decreased as the LSM content in the electrode decreased. For a composition below 40 wt. % LSM, the intra-connectivity drastically dropped down to < 60 % [117].

An increase in electrode polarization resistance for $\text{La}_{0.8}\text{Sr}_{0.2}\text{Co}_{0.2}\text{Fe}_{0.8}\text{O}_{3-\delta}$ electrodes on YSZ sintered at 850, 950 and 1100 °C has been reported by Gostovic et al. [120]. Based on FIB, a three-dimension model of the cathode for SOFC was reconstructed with a x-y resolution of 3 nm and z direction sectioning of 20 nm. Information about porosity, surface area, tortuosity, pore size and TPBs were correlated with the data from electrochemical impedance spectroscopy. The lowest cathode polarization of $0.65 \text{ } \Omega \cdot \text{cm}^2$ at 700 °C was achieved for samples sintered at 850 °C and was explained by several microstructural parameters. Samples sintered at 850 °C were characterized by the highest surface area per volume of $9.3 \text{ } \mu\text{m}^{-1}$ in relation to $8.8 \text{ } \mu\text{m}^{-1}$ and $7.2 \text{ } \mu\text{m}^{-1}$ for samples sintered at 950 and 1100 °C, respectively.

Moreover, the effective O₂ diffusion through the electrode was found to be decreased when the volume fraction of porosity to tortuosity ratio was increased from 0.087 to 0.097 and to 0.116 for samples sintered at 850, 950 and 1100 °C, respectively. Finally, the sample sintered at lowest temperature presented the highest TPB length of TPB length/area of $3.2 \pm 1.6 \mu\text{m}^{-1}$. Similarly to Gostovic et al. [120], FIB-SEM on LSCF (6428) electrodes together with electrochemical measurements proved that larger oxygen surface areas have led to lower electrode polarization resistances as presented by Marinha et al. [88]. In their work, the electrode-pore interfacial areas normalized by the cross-sectional area of the support were found to be 2.0, 24.7 and 28.2 for dense, cracked and coral microstructures, respectively. The area specific polarization resistance values, measured by impedance spectroscopy at 600 °C in air using Pt grids (3600 mesh.cm² for current collection), were found to decrease from 6.23 to the lowest value of 0.82 Ω.cm² corresponding to samples with higher surface areas for the coral microstructure. Moreover, the material and microstructural parameters were used to calculate the polarization resistance and impedance response in the Adler-Lane-Steele (ALS) model [128]. The trend in modelled resistance values was in an agreement with measured impedance values. The higher values for the denser one were explained by underestimation of the pore-electrode surface area due to the resolution limit of the FIB-SEM method.

The image post-processing has an influence on extracted geometrical properties. Wrongly chosen levels of the grayscale threshold, media filter radius and smoothing filters can significantly change the measured values of porosity, surface area, electronic conductivity and diffusivity values. Gunda et al. [129] calculated that improper image analysis caused variations in the electrode porosity of 33 % and in the internal surface area of 25 %. In another work, Joos et al. [121] used two algorithms (Otsu, Mean) to mathematically define a ‘true’ grayscale threshold level and its influence on surface area, volume/porosity fraction and tortuosity extracted based on FIB-SEM tomography of an LSCF oxygen electrode. They found that thresholding did not affect the surface area while the porosity fraction and the tortuosity strongly depended on it.

I.1.5. Mechanical properties of the electrode

Solid oxide fuel cells and electrolysis cells are weakly investigated from mechanical point of view. Nevertheless, the mechanical stability of the cell components is an important issue. The existing works are few and based on different approaches. Stresses in the cell can arrive from manufacturing process, oxygen activity gradients, redox cycling, external mechanical load and not homogeneous distribution of the temperature during working. Different TECs of components lead to not identical material expansions and to thermal stresses. The magnitude of stresses depends mainly on material properties, operating conditions and the cell design [130].

The other question is the mechanical stability of a SOFC/SOEC stack. The following effects can affect the mechanical behavior, diminish electrochemical properties or even kill the stack:

- Variations or not homogeneous distribution of the electrical load
- Aggressive environment
- Coarsening of the electrolyte microstructure
- Creation of pores
- Local modifications of the composition
- Creation of insulating phases on electrode-electrolyte interface
- Phase transformations

There are some research groups working on the mechanical failure mechanism of cell stacks by modeling approaches. Nakujo et al. [131] used thermo-electrochemical model and Weibull statistics [132] to study the influence of various aspects such as assembly, electrical load shutdown, phases heat-up/cool down, current-voltage characterization and dynamic operation. The probability of mechanical failure of SOFC stacks has been calculated and procedures to reduce it by controlling the operation conditions have been proposed. The failure of gas-diffusion layers, interconnect and other cell components was estimated [133], [134]. Laurencin et al. [135] investigated the risk of failure due to residual stresses and cracks arose during manufacturing. A numerical tool was used to estimate the stress state and cell degradation during operation for the planar cell configuration. The thermal stresses distribution can be characterized by finite element analysis (FEA) [136]–[138]. Lin et al. [137] used FEA to model stresses in planar SOFC stacks including the effect of glass-ceramic seals. The approach in the work of Anandakumar et al. [136] was different. They used FEA to model thermal stresses and the probability of failure in cells of NiO-YSZ/YSZ with single

LSM and NiO-YSZ/YSZ with functionally graded CGO-LSCF. The results have shown that the lowest probability of failure occurs for a functionally graded SOFC.

An performed a study of $(\text{Pr}_{0.7}\text{Sr}_{0.3})\text{MnO}_{3\pm\delta}/8\text{YSZ}$ oxygen electrode before and after a 1000 h durability test at 1000 °C using indentation, plate tensile tests, four-point bending, ball-on-ring and pressure-on-ring tests [138].

However, these studies used conventional macro-scale testing methods that require large volume samples and machining operations, and do not allow assessing material properties but sample (coating and substrate) properties instead. The investigation of mechanical properties of cell components is not without difficulties. The small size of electrode (from few to dozens μm) requires micro- or nano-scale techniques able to tests small volumes of material and with little or no specific sample preparation. The use of micro- or nano-indentation testing methods to evaluate the mechanical properties of this type of materials has been attempted by several authors.

Xiang et al. [139] used nanoindentation to determine the hardness and elastic modulus of a non-reduced NiO-YSZ hydrogen electrode in a half-cell configuration and proposes a method to determine these properties based on the work of indentation modified approach.

Li et al. [140] measured the elastic modulus and nano-hardness for a wide range of CGO-LSCF composites as materials for IT-SOFC, using indentation. The pellets and bars were created by pressing and sintering a mixture of CGO and LSCF powders. Such samples were mounted in epoxy resin and polished to achieve flat surface for indentation. Densities were measured with Archimedes method and were in the range 94 to 98 % of the theoretical density. Such high densities indicated low porosity fraction in the samples; however, the preparation of the electrode for SOFC does not allow achieving such high densities. The values obtained for elastic modulus were 119 – 153 GPa and 8.9 – 10.8 GPa for the hardness. Elastic modulus and the hardness changed almost linearly with density.

However, most of these studies are performed on materials with porosity levels under 30 % and since porosity has been demonstrated to have a huge influence on mechanical properties, the results cannot be extrapolated to materials with higher porosity.

Meille et al. [141] showed that the mechanical behavior in compression of alumina with porosity between 30 – 75 vol.% transited from brittle failure to a more damageable behavior as the relative porosity increases above 60 %. The mechanical properties of materials with high porosity could be described by models developed for cellular materials. These properties are modeled using the properties and description of the solid phase as an assembly of walls and struts in a periodic microstructure [142], [143]. Though the porosity of the coral

microstructure developed in the present work is compatible with a cellular structure, its morphology is more typical of a columnar structure in which periodicity is hardly recognized.

I.2. Experimental

I.2.1. Electrostatic spray deposition (ESD)

Electrostatic spray deposition is one of the most promising chemical deposition methods for fabricating porous electrodes as well as dense electrolytes in solid oxide cells due to its simplicity and low costs (Fig. I-15). Nowadays, many oxide materials have been deposited by ESD: NiO/Gd₂O₃-doped CeO₂ [144], La_{1-x}Sr_xCo_{1-y}Fe_yO_{3-δ} [145], La_{0.9}Sr_{0.1}Ga_{0.8}Mg_{0.2}O_{2.87} [146], La_{0.6}Sr_{0.4}Co_{0.2}Fe_{0.8}O_{3-δ} [147], a composition of Sr-doped LaMnO₃ and Y₂O₃ stabilized ZrO₂ [148] for the electrode applications and doped-ZrO₂ [149], [150], Ce_{0.9}Gd_{0.1}O_{1.95} [55], [146], [151] for the electrolyte applications. In general, a liquid precursor solution is pumped by the syringe pump into a stainless steel nozzle at a constant flow rate. An electrical field generates an aerosol and directs it towards the substrate. During the flight, the solvent partially evaporate from the droplets. Droplets dry and decompose to create a solid layer that adheres to the substrate surface. A proper concentration of precursor salts in the solution guarantees a good stoichiometry of the components in the deposited layer. Deposition is carried out at relatively low temperatures ranging from 300 to 400 °C. A typical ESD setup (Fig. I-15) consists of a syringe pump, a syringe, a needle, a heating plate, a high voltage power supplier and a substrate. A precursor solution is kept in a syringe which is connected to a needle by silicon tubing. A syringe pump presses onto the syringe at a constant rate causing the solution to flow. A heating plate is surrounded by isolating material to provide the best thermal control of the substrate. Moreover, the substrate temperature is calibrated by a K-type thermocouple without the aerosol.

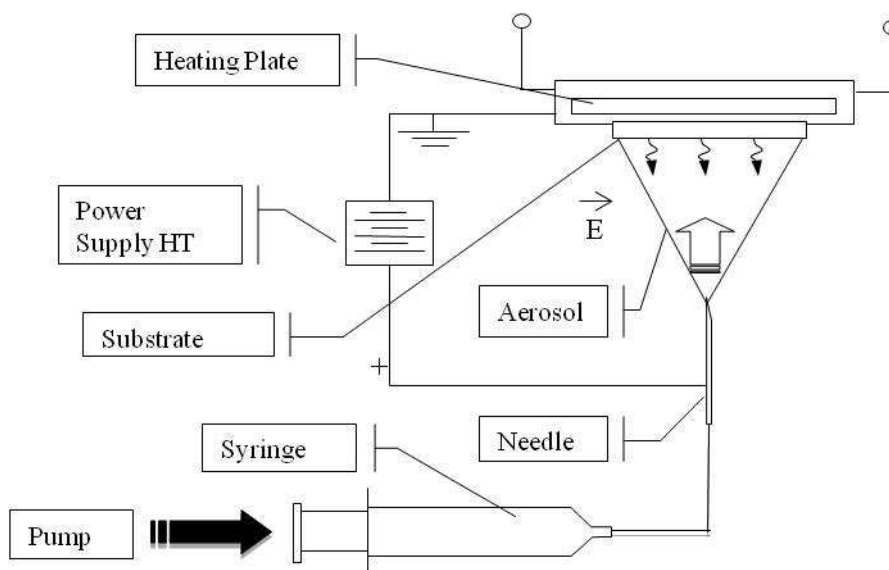


Fig. I-15. ESD setup.

The first step of the deposition is the atomization of the precursor solution. The electrostatic field applied between the positively charged needle and the grounded substrate polarizes the solution on the needle tip and creates the jet-cone called a Taylor cone. The next step is the formation of a spray. The atomized solution moves inside the Taylor cone to the top of the cone. In that point, the electrostatic force is equal or higher than the surface tension of the solution and causes spreading (Fig. I-16). The spray is aimed at the heated substrate. During the flight, the droplets shrink from their initial size to their final size when reaching the target.

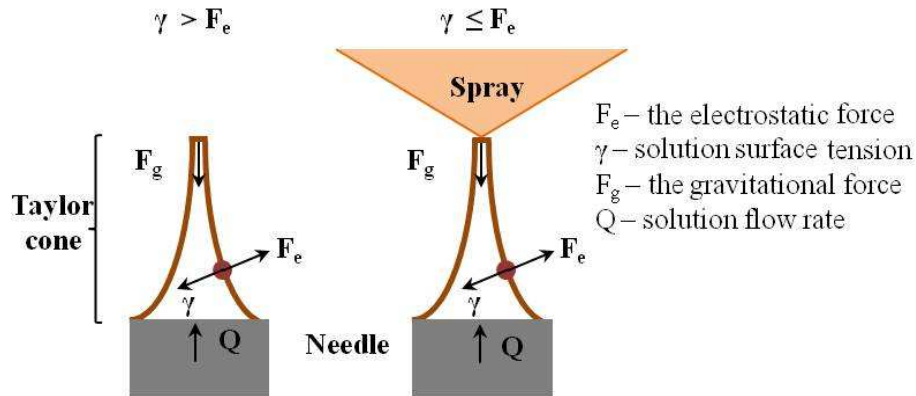


Fig. I-16. Schema of the atomization during electrostatic spray deposition.

The main advantage of ESD is that one can obtain a wide variety of microstructures with good homogeneity and reproducibility. In principle, the microstructure and thickness of the coating depends on the droplet size which can range from a few nanometers to approximately 100 μm [152]. According to literature, studies have been focused on the electrohydrodynamic parameters that have an influence on the size of the droplets in this cone-jet. Gañan-Calvo et al. [153] presented an equation where the droplets size (d) is correlated to the solution density (ρ), vacuum permeability (ϵ_0) (equal to $8.85 \times 10^{-12} \text{ F.m}^{-1}$), flow rate (Q), solution surface tension (γ) and solution electrical conductivity (σ), as the following:

$$d \sim \left(\frac{\rho \epsilon_0 Q^3}{\gamma \sigma} \right)^{\frac{1}{6}} \quad (\text{I-12})$$

The solvent is important as it influences the quality of the aerosol and droplet size. In this regard, relatively low surface tension and viscosity are required and conductivity values of the solution may vary between 10^{-8} and $10^{-1} \text{ S.cm}^{-1}$. One fundamental characteristic is the boiling point which limits the possible film morphologies [154]. In addition to these parameters from the Gañan-Calvo's equation, the process conditions (nozzle-to-substrate distance, deposition time, substrate temperature) also have an influence on the coating microstructure.

In general, the substrate temperature, the nozzle-to-substrate distance and the flow rate significantly change the microstructure of the coating. These three parameters have the strongest influence on the size of the droplets when they impact the surface of the substrate. When large droplets arrive at the surface and are still liquid, they tend to spread on the surface and dry. Such mechanism leads to the formation of a dense, reticular or cracked coating. If small droplets are used, they are completely dry when reach the substrate then they are electrically attracted by the closest curvatures on the surface of the substrate and create wide open porous microstructures [155].

The microstructure of the deposited layer is a consequence of the physicochemical properties of the precursor solution combined with the deposition conditions.

The vast majority of film morphologies may be obtained in conditions when the droplets are still liquid upon impact. In this situation, the droplets will dry and solidify in any of the configurations illustrated in Fig. I-17a resulting in film microstructures ranging from dense (Fig. I-17a-3) to reticulated (Fig. I-17a-6). The particular case of reticulation occurs whenever the simultaneous spreading and drying solidify the droplet at the moment it reaches maximum spreading [156]. Dense films require adequate amounts of liquid in the droplets in order to avoid cracking due to stresses generated during drying.

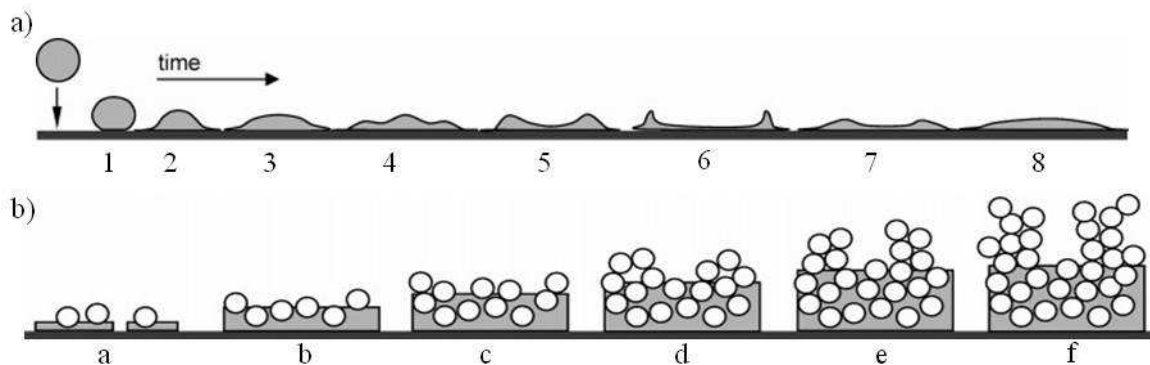


Fig. I-17. Spreading of a liquid droplet on a smooth surface (a) and film growth using solid particles [155].

Authorized reprinting. Copyright 2005 American Chemical Society.

After droplets of a given size are generated at the nozzle, other effects come into play causing droplets to undergo dynamic changes in size due to solvent evaporation occurring during the flight between the nozzle and the heated substrate. In this regard, the effect of parameters such as solution boiling point, nozzle-to-substrate distance and substrate temperature must be taken into account when considering the desired morphology.

A wide variety of $\text{La}_{0.6}\text{Sr}_{0.4}\text{Co}_{0.2}\text{Fe}_{0.8}\text{O}_{3-\delta}$ microstructures ranging from dense to porous, with particular features such as reticulation and micro-porosity, were obtained by varying the ESD

deposition parameters: nozzle-to-substrate distance, solution flow rate and substrate temperature. The correlation between deposition parameters and resulting microstructures was systematically studied and put into evidence in Marinha's PhD thesis [6].

I.2.2. X-ray and focused ion-beam tomography

New tomography technique characterization using X-ray and focused ion beam allows for a detailed three-dimensional characterization of the microstructure. These are powerful tools that provide new insight into the ORR and anodic reactions as a function of microstructural parameters. First, the materials of interest must be sectioning into a stack of 2D pictures with detailed information about microstructure. These images are then aligned and reconstructed to produce a 3D model. The sectioning in X-ray tomography is due to the 180 °C rotation and collection of projection images series, while FIB-SEM pictures are taken by scanning the surface with electrons, creating an image, and then milling the surface away with ions to reveal a surface at a greater depth. Image analysis is used to remove artifacts, to segment and to process the images [157].

The sample size is greatly dependent on whether or not X-ray or FIB-SEM tomography is used. The X-ray tomography setup allows analysis of large samples as well as small samples in comparison with SEM where the sample size is limited by the chamber size. However, the larger the sample, the lower the resolution. Nevertheless, the preparation of small samples is complex. The most common preparation is cutting and polishing of the impregnated sample to the required dimensions. The impregnation by epoxy resin helps keep the material together and avoids detachment of material. However, the impregnation itself may cause fractures of the fragile material and may trap air bubbles inside the structure, creating artifacts. To achieve a 25 nm resolution in nanotomography, the recommended sample size is 100 μm x 100 μm x 5 mm. To ensure the right size, the sample was alternatively cut, infiltrated by resin and polished down to the required dimensions from each sample's side. The investigation of the porous coating of the dense ceramics leads to different X-ray absorption rates, thus leading noises especially at the interface. The alternative method for sample preparation is to cut accurate sizes by FIB however this is expensive and time-consuming.

Sample preparation for FIB-SEM is simpler. It often requires infiltrating sample with resin and polishing. The sample has the size allowance since the right spot can be observed before tomography. Imaging must be conducted under the vacuum. The resin is not transparent to electrons and the deeper part of the sample is not visible before starting the milling.

The nanotomography was performed at the nano-imaging end station (ID22NI beamline) of the European Synchrotron Radiation Facilities (ESRF) in Grenoble. A schematic of the tomography setup with marked characteristic distances (D1 – distance from focal plane to sample, D2 – sample-to-detector distance) is presented in Fig. I-18.

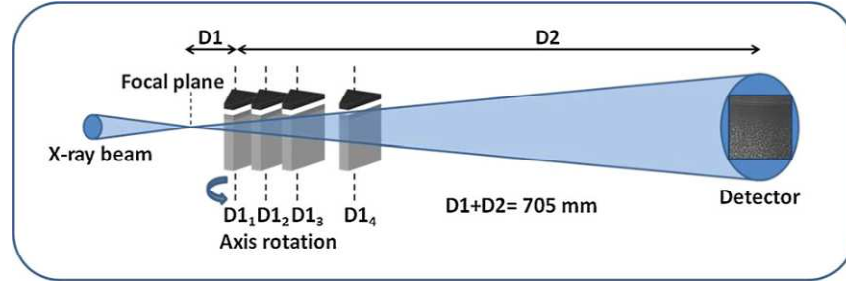


Fig. I-18. Schema of holotomography setup at the ID22NI beamline in the ESRF, D1 indicates distance between focal plane and the sample and D2 sample-to-detector distance [158].

The principle of holotomography is described elsewhere [159], [160]. The beam energy was fixed to 29.6 keV with a 1.6 % bandwidth. The required beam time for four samples including scanning time, sample mounting and positioning was 24 h. Achieved images were four tomographic scans with different sample-to-detector distances used to create a stack of data. The further operations require following steps: correction of the image distortion, resizing and alignment of the individual radiographs, phase retrieval calculation and tomographic reconstruction [158].

I.2.3. Impedance spectroscopy

Based on [161], [162].

Impedance spectroscopy is a technique based on a response of an electrochemical system to an applied sinusoidal perturbation (potential or current) for a wide range of frequencies at low magnitude. The frequency range allows one to measure and recognize several electrochemical reactions (charge transfer activation, ion and electron transport, gas diffusion, electrolyte resistance, etc...) that take place within different frequency ranges. In general, by applying a sinusoidal potential, the current response will also be sinusoidal with the same frequency but shifted in phase and reduced in amplitude by the sample's resistance. According to Ohm's law, the impedance of the system is given by:

$$Z(\omega) = \frac{V(t)}{I(t)} = \frac{V_0 \exp(j\omega t)}{I_0 \exp(j\omega t - \varphi)} = |Z| \exp(j\varphi) = Z' + jZ'' \quad (\text{I-13})$$

Where:

ω – radial frequency, as a function of frequency (f), $\omega = 2\pi f$

$Z(\omega)$ – complex impedance as a function of radial frequency (ω)

$V(t), I(t)$ – potential signal and current signal as a function of time (t)

V_0, I_0 , – amplitudes of the potential and current

$|Z|$ – impedance module

φ – phase shift between potential signal and current response

j – imaginary number $j^2 = -1$

Z', Z'' – real (resistance) and imaginary (reactance) part of impedance

Impedance spectroscopy data are commonly presented on a Nyquist plot where the real part is on the X-axis and the imaginary part on Y-axis. Bode plots are also commonly used where the first line is a relation between $\log(|Z|) - \log(f)$ and the second line is $\log(\varphi) - \log(f)$. Processes that occur during impedance spectroscopy can be represented as electrical circuit elements.

Common circuit elements and their impedance relationships are presented below:

- Resistor (R - resistance) $Z_R = R$ (I-14)

- Inductor (L - inductance) $Z_L = j \omega L$ (I-15)

- Capacitor (C - capacitance) $Z_C = \frac{1}{j \omega C}$ (I-16)

- Constant phase element (CPE) $Z_{CPE} = \frac{1}{C_o(j \omega)^p}$ (I-17)

Constant phase element is a more complex element and cannot be described by R, L or C. It consists of a pseudo-capacity (C_o) and an exponent (p) that ranges between $-1 \leq p \leq 1$. When $p \rightarrow 1$, the element becomes an ideal capacitor, as $p \rightarrow 0$ it becomes an ideal resistor and when $p \rightarrow -1$ it becomes an ideal inductor. CPE is used to describe the imperfection of standard elements mainly due to system inhomogeneity or the dispersion of physical property value.

However, very few electrochemical cells can be well explained by single equivalent circuit elements. Most must be modeled as a sum of single elements connected in serial and parallel combinations. Herein lies the difficulty with electrochemical impedance spectroscopy (EIS), one spectrum can be described by many equivalent circuit models. It is necessary to understand and predict what kinds of processes occur in the electrochemical system to simulate and fit the model. Different physical-chemical processes in the system during impedance have different dwell times thus the response of the system depends on the frequency. The validity of the equivalent circuit model can be checked by comparing the

element frequencies to different electrochemical processes. The impedance spectrum for a ceramic material is presented on Fig. I-19.

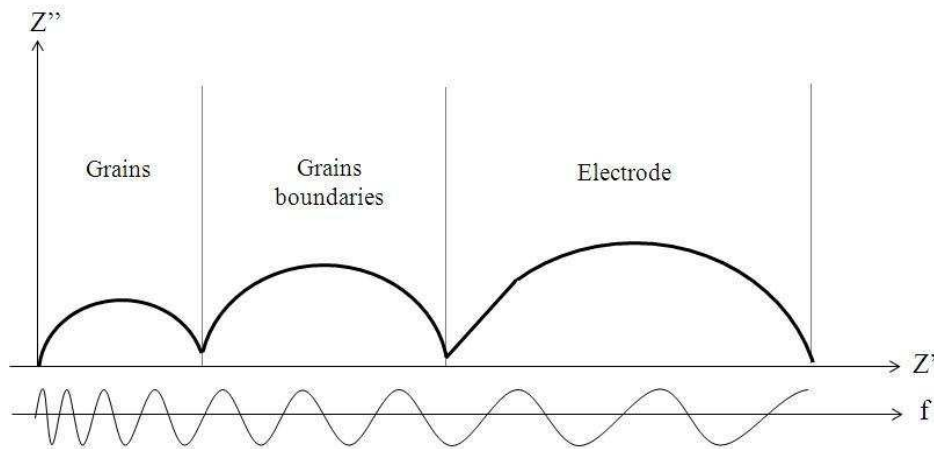


Fig. I-19. Characteristic impedance spectrum for a ceramic electrochemical cell.

Fig. I-19 shows three regions, the first in the high frequency domain is related to grains (bulk properties), the second region at intermediate frequency range refers to the microstructure (grains boundaries, pores, secondary phases, etc...) and the last one in the low frequency range relates to the electrode reaction itself [163]. Oxygen transfer can be thoroughly investigated by electrochemical impedance spectroscopy.

I.2.4. Mechanical characterization

ESD deposited electrodes were characterized for mechanical strength using indentation and scratch testing. One of the requirements for the oxygen electrode is a high resistance to mechanical stresses that could occur during cell operation and especially at the electrode-electrolyte interface that may cause degradation of the cell or even compromise its integrity. Mechanical stresses originate from various sources: differences in thermal expansion between the various components, pressure applied to ensure good contact and from the weight of the stack itself. Stresses depend on material properties but also on process variables and use conditions. As mentioned in the literature review, work is being done on the assessment of mechanical properties of materials used in SOFC, the stacks and also on their probability of failure. However, most of the studies and model predictions are based on relatively dense materials (porosity levels under 30 %). In materials with very high levels of porosity most of the well-known mechanical property models for cellular materials may apply. Most of these models are based on the existence of a periodic structure of cells with a known mechanism of deformation under loading: elastic deformation followed by buckling and bending of cell walls, densification and fracture due to rupture of cells [141], [142]. Nevertheless, the non-

cellular and non-periodic nature of the structure of the film developed in the current work may lead to a different micromechanical response.

The objective of this work is to investigate the mechanical properties and micromechanical behavior of the coral microstructure of CGO-LSCF composite film developed. Since the use of conventional macro-scale testing methods is not compatible with the very thin and fragile films deposited by ESD in the present work, the mechanical characterization was done using micro-scale methods.

Intensive research has been carried out in the last two decades on the use of indentation and scratch testing methods to evaluate the mechanical properties of thin films and coatings. Standard tests have been developed (ASTM E2546, ISO 14577, ASTM C1624, ISO 1071) and these methods are now currently used. In the present work, instrumented indentation and scratch tests performed at very low loads have been used to assess the mechanical properties of the materials developed, in an attempt to understand the respective deformation and fracture behavior under loading.

I.2.4.1. Instrumented indentation

Indentation testing allows determining the hardness (H) of a material [164], [165]. In principle, an indenter with a specific shape of a specific material indents a sample material under an accurately controlled force and for a specific amount of time. After removal of the indenter the material recovers partially its deformation and is left with a residual impression (indentation) on the surface that can be measured by optical or atomic force microscopy. This is the basis of a standard indentation test that allows determining the hardness of a material through the ratio of the applied load and the measurement of the projected area of the residual indentation. However, in instrumented indentation the equipment is provided with a depth sensing system and the applied load is registered as a function of the penetration depth, thus enabling the measurement of the loading and unloading response of the material during the test. This type of test allows not only determining the hardness of the material but also elastic properties (like the Young's modulus), creep, fracture toughness, etc...

The most commonly used indentation tip geometries are spheres, pyramids (Vickers, Berkovich, Knoop indenters) or cones.

Typical indentation testing can be described by the following steps:

- a) Indenter is pressed into sample with controlled test force (loading), penetration depth is recorded

- b) The force is maintained for a specific dwell time
- c) Indenter is removed from the sample leaving an indenter-shaped expression (unloading)
- d) The contact area may be determined optically by measuring the indentation diagonals or using the penetration depth and indenter material and shape.

Hardness, H , is a function of the test force (P) and the projected area of the indentation (A) (Eq. I-18):

$$H = \frac{P}{A} \quad (\text{I-18})$$

Depending on the indenter used, the equation for the contact area calculation may vary.

Different types of indenters may be used (sphere, cone, pyramids). In the present case a Berkovich indenter was used, which is a diamond three-sided pyramid, with a phase angle of 65.03° and the same real surface area to depth ratio as Vickers indenter [165]. The tip radius for a typical new Berkovich indenter is about 50 – 100 nm and it usually increases to about 200 nm with use. For this type of indenter the projected area (A) is related to the contact depth (h_c) as:

$$A \approx 24.5 h_c^2 \quad (\text{I-19})$$

with:

$$h_c = h_m - 0.75 \frac{P_{max}}{S} \quad (\text{I-20})$$

where P_{max} , h_m , S are the maximum load and the respective depth and the contact stiffness, respectively.

Fig. I-20 shows a load-displacement typical curve of an elastic-plastic solid. An indentation made using a Berkovich tip can be observed in the top left corner of Fig. I-20. As the initial region of the unloading curve corresponds to the material's elastic recovery, the respective tangent is the contact stiffness (S) (Eq. I-21).

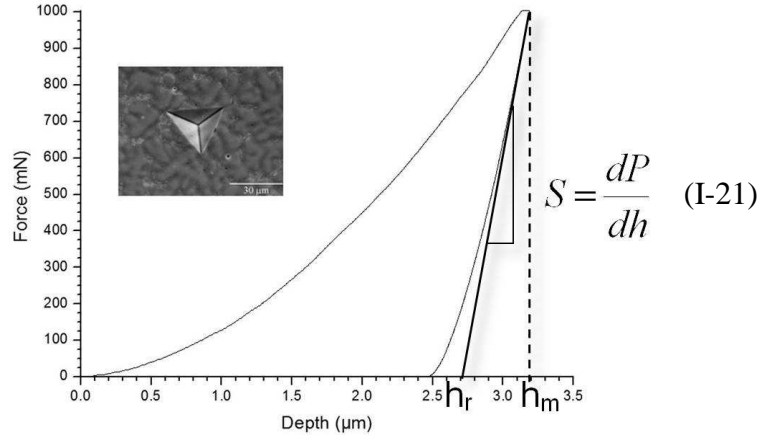


Fig. I-20. Load-displacement curve for an elastic-plastic solid. Top left corner: indentation made with a Berkovich indenter [166].

The response of the material during unloading allows determining the reduced Young's modulus (E^*) from the contact area and the stiffness (S):

$$E^* = \frac{1}{2} \frac{dP}{dh} \frac{\sqrt{\pi}}{\sqrt{A}} \quad (\text{I-22})$$

However, since the stiffness includes the deformation of the sample and the machine, the reduced elastic modulus obtained includes contributions from the indenter (E_{ind}) and the specimen (E_{mat}). Knowing the Poisson's ratios for the indenter (ν_{ind}) and specimen (ν_{mat}) the materials elastic modulus may be determined using Eq. I-23:

$$\frac{1}{E^*} = \frac{1-\nu_{ind}^2}{E_{ind}} + \frac{1-\nu_{mat}^2}{E_{mat}} \quad (\text{I-23})$$

Usually, the contribution from the indenter to the reduced modulus is low, however in micro- and nano-indentation tests performed at very low loads, it becomes significant and the correction is required.

I.2.4.2. Scratch tests

The scratch test is a standard method used to characterize the mechanical strength (adhesion and cohesion) of a coating/substrate system [167], [168]. In principle, a stylus (indenter made of diamond or hard metal) is moved across a coating surface with a constant or linearly increasing load for a specified distance. During motion, the normal force (F_n) and tangential friction force (F_t) as well as the depth profile are recorded. Often, the scratch tester is equipped with an acoustic emission sensor to detect produced sound during testing resulting from coating damage. The critical load (F_c) (minimum load required to produce coating damage) is determined by variations in the normal and tangential (friction) forces applied to

the sample, acoustic emission or optical and scanning electron microscopy. During scratch testing, cracks concentrate at defect sites in the coating or in the coating-substrate interface causing coating failure. Failure may be cohesive or adhesive. Cohesive failure is caused by tensile stresses behind the indenter, leading to through-thickness cracking. When through-thickness cracks reach the coating-substrate interface they usually propagate along the interface. If these through cracks meet other through-thickness cracks it results in coating spallation. Adhesive failure occurs due to compressive stresses and leads to coating separation from the substrate by buckling or chipping.

Hardness can be evaluated from scratch tests performed at a constant normal load. The hardness is then given from the relation between the normal force (P) and the width of the scratch (W) (Eq. I-24):

$$H = k \frac{P}{W^2} \quad (\text{I-24})$$

However, if the constant, k , is unknown, hardness can be obtained by comparison to a reference material with a known hardness value (H_{ref}):

$$H_S = H_{Ref} \frac{P_S}{P_{Ref}} \left(\frac{W_{Ref}}{W_S} \right)^2 \quad (\text{I-25})$$

where S and Ref correspond to sample and reference material, respectively.

I.3. References

- [1] C. F. Schönbein, “On the voltaic polarization of certain solid and fluid substances,” *Philosophical Mag. J.*, vol. 3, no. 14, pp. 43–45, 1839.
- [2] W. R. Grove, “On a gaseous voltaic battery,” *Philosophical Mag. J.*, vol. 21, no. 140, pp. 417–420, 1842.
- [3] M. L. Mond and C. Langer, “A new Form of Gas Battery,” *Proc. R. Soc. London*, vol. 46, pp. 296–304, 1889.
- [4] W. Nernst, “Material for electronic-lamp glowers. US Patent 685730,” 1899.
- [5] E. Baur and H. Preis, “Über Brennstoff-Kelten Mit Festleitern,” *Zeitschrift für Elektrochemie*, vol. 43, pp. 727–732, 1937.
- [6] D. Marinha, “Nouvelles électrodes à architecture contrôlée pour piles à combustible à oxydes solides fonctionnant à température intermédiaire,” PhD Thesis, Grenoble INP, 2010.
- [7] S. Park, J. M. Vohs, and R. J. Gorte, “Direct oxidation of hydrocarbons in a solid-oxide fuel cell,” *Nature*, vol. 404, pp. 265–267, 2000.
- [8] K. Eguchi, H. Kojo, T. Takeguchi, R. Kikuchi, and K. Sasaki, “Fuel flexibility in power generation by solid oxide fuel cells,” *Solid State Ionics*, vol. 152–153, pp. 411–416, 2002.
- [9] S. C. Singhal, “Solid oxide fuel cells for stationary, mobile, and military applications,” *Solid State Ionics*, vol. 152–153, pp. 405–410, 2002.
- [10] O. Yamamoto, “Solid oxide fuel cells: fundamental aspects and prospects,” *Electrochim. Acta*, vol. 45, pp. 2423–2435, 2000.
- [11] G. Constantin, “Interfaces et durabilité d’un cœur de pile à combustible à oxyde solide fonctionnant à température intermédiaire,” PhD Thesis, Grenoble INP, 2012.

- [12] T. Hibino, H. Tsunekawa, S. Tanimoto, and M. Sano, "Improvement of a Single-Chamber Solid-Oxide Fuel Cell and Evaluation of New Cell Designs," *J. Electrochem. Soc.*, vol. 147, no. 4, pp. 1338–1343, 2000.
- [13] N. Minh, "Solid oxide fuel cell technology – features and applications," *Solid State Ionics*, vol. 174, no. 1–4, pp. 271–277, 2004.
- [14] Hexis Ltd., "http://www.hexis.com/downloads/HEXIS_Zellstapel_e.jpg,".
- [15] X.-F. Ye, S. R. Wang, J. Zhou, F. R. Zeng, H. W. Nie, and T. L. Wen, "Assessment of the performance of Ni-yttria-stabilized zirconia anodes in anode-supported Solid Oxide Fuel Cells operating on H₂-CO syngas fuels," *J. Power Sources*, vol. 195, no. 21, pp. 7264–7267, 2010.
- [16] T. Takahashi, H. Iwahara, and T. Arao, "High oxide ion conduction in sintered oxides of the system Bi₂O₃-Y₂O₃," *J. Appl. Electrochem.*, vol. 5, pp. 187–195, 1975.
- [17] S. Tao and J. T. S. Irvine, "Discovery and characterization of novel oxide anodes for solid oxide fuel cells.," *J. Chem. Res.*, vol. 4, no. 2, pp. 83–95, 2004.
- [18] S. W. Tao and J. T. S. Irvine, "A redox-stable efficient anode for solidoxide fuel cells," *Nat. Mater.*, vol. 2, pp. 320–323, 2003.
- [19] S. W. Tao and J. T. S. Irvine, "Synthesis and characterization of (La_{0.75}Sr_{0.25})Cr_{0.5}Mn_{0.5}O_{3-δ}, a redox-stable efficient perovskite anode for SOFCs," *J. Electrochem. Soc.*, vol. 151, no. 2, pp. A252–A259, 2004.
- [20] J. Cheng, "Synthesis of La_xSr_{1-x}TiO₃ anode materials by SOL-GEL auto-combustion method," *J. Chil. Chem. Soc.*, vol. 57, no. 1, pp. 969–971, 2012.
- [21] S. Tao and J. T. S. Irvine, "Optimization of Mixed Conducting Properties of Y₂O₃-ZrO₂-TiO₂ and Sc₂O₃-Y₂O₃-ZrO₂-TiO₂ Solid Solutions as Potential SOFC Anode Materials," *J. Solid State Chem.*, vol. 165, no. 1, pp. 12–18, 2002.
- [22] S. P. S. Badwal, "Zirconia-based solid electrolytes: microstructure, stability and ionic conductivity," *Solid State Ionics*, vol. 52, pp. 23–32, 1992.

- [23] O. Yamamoto, Y. Arachi, H. Sakai, Y. Takeda, N. Imanishi, Y. Mizutani, M. Kawai, and Y. Nakamura, “Zirconia Based Oxide Ion Conductors for Solid Oxide Fuel Cells,” *Ionics*, vol. 4, pp. 403–408, 1998.
- [24] J. W. Fergus, “Electrolytes for solid oxide fuel cells,” *J. Power Sources*, vol. 162, no. 1, pp. 30–40, 2006.
- [25] J. A. Kilner, “A study of oxygen ion conductivity in doped non-stoichiometric oxides,” *Solid State Ionics*, vol. 6, pp. 237–252, 1982.
- [26] T. Yamada, N. Chitose, H. Eto, M. Yamada, K. Hosoi, N. Komada, T. Inagaki, F. Nishiwaki, K. Hashino, H. Yoshida, M. Kawano, S. Yamasaki, and T. Ishihara, “Application of Lanthanum Gallate Based Oxide Electrolyte in Solid Oxide Fuel Cell Stack,” *Adv. Solid Oxide Fuel Cells III*, vol. 28, no. 4, pp. 79–89, 2009.
- [27] D. Pérez-Coll, P. Núñez, J. R. Frade, and J. C. C. Abrantes, “Conductivity of CGO and CSO ceramics obtained from freeze-dried precursors,” *Electrochim. Acta*, vol. 48, no. 11, pp. 1551–1557, 2003.
- [28] B. C. H. Steele, “Appraisal of $Ce_{1-y}Gd_yO_{2-y/2}$ electrolytes for IT-SOFC operation at 500°C,” *Solid State Ionics*, vol. 129, pp. 95–110, 2000.
- [29] M. Han, X. Tang, H. Yin, and S. Peng, “Fabrication, microstructure and properties of a YSZ electrolyte for SOFCs,” *J. Power Sources*, vol. 165, no. 2, pp. 757–763, 2007.
- [30] V. V. Kharton, F. M. Figueiredo, L. Navarro, E. N. Naumovich, A. V. Kovalevsky, A. A. Yaremchenko, A. P. Viskup, A. Carneiro, F. M. B. Marques, and J. R. Frade, “Ceria-based materials for solid oxide fuel cells,” *J. Mater. Sci.*, vol. 36, pp. 1105–1117, 2001.
- [31] S. M. Haile, “Fuel cell materials and components,” *Acta Mater.*, vol. 51, no. 19, pp. 5981–6000, 2003.
- [32] A. A. Yaremchenko, V. V. Kharton, E. N. Naumovich, and A. A. Tonoyan, “Stability of δ -Bi₂O₃-based solid electrolytes,” *Mater. Res. Bull.*, vol. 35, pp. 515–520, 2000.

- [33] F. Abraham, J. Boivin, G. Mairesse, and G. Nowogrocki, “The bimevox series: A new family of high performances oxide ion conductors,” *Solid State Ionics*, vol. 40–41, pp. 934–937, 1990.
- [34] S. J. Skinner and J. A. Kilner, “Oxygen ion conductors,” *Mater. Today*, vol. 6, no. 3, pp. 30–37, 2003.
- [35] S. Georges, F. Goutenoire, O. Bohnke, M. C. Steil, S. J. Skinner, H. Wiemhöfer, and P. Lacorre, “The LAMOX Family of Fast Oxide-Ion Conductors: Overview and Recent Results,” *J. New Mater. Electrochem. Syst.*, vol. 7, pp. 51–57, 2004.
- [36] F. Goutenoire, R. Retoux, E. Suard, and P. Lacorre, “Ab Initio Determination of the Novel Perovskite-Related Structure of $\text{La}_7\text{Mo}_7\text{O}_{30}$ from Powder Diffraction,” *J. Solid State Chem.*, vol. 142, pp. 228–235, 1999.
- [37] D. Marrero-López, P. Díaz-Carrasco, J. Peña-Martínez, J. C. Ruiz-Morales, and J. R. Ramos-Barrado, “Lanthanum Germanate-Based Apatites as Electrolyte for SOFCs,” *Fuel Cells*, vol. 11, no. 1, pp. 65–74, 2011.
- [38] H. Gasparyan, S. Neophytides, D. Niakolas, V. Stathopoulos, T. Kharlamova, V. Sadykov, O. Van der Biest, E. Jothinathan, E. Louradour, J.-P. Joulin, and S. Bebelis, “Synthesis and characterization of doped apatite-type lanthanum silicates for SOFC applications,” *Solid State Ionics*, vol. 192, no. 1, pp. 158–162, 2011.
- [39] H. Yoshioka, T. Mitsui, A. Mineshige, and T. Yazawa, “Fabrication of anode supported SOFC using plasma-sprayed films of the apatite-type lanthanum silicate as an electrolyte,” *Solid State Ionics*, vol. 181, no. 37–38, pp. 1707–1712, 2010.
- [40] B. Steele, “Materials for IT-SOFC stacks 35 years R&D: the inevitability of gradualness?,” *Solid State Ionics*, vol. 134, no. 1–2, pp. 3–20, 2000.
- [41] H. Yokokawa, T. Horita, N. Sakai, M. Dokiya, and T. Kawada, “Thermodynamic representation of nonstoichiometric lanthanum manganite,” *Solid State Ionics*, vol. 86–88, pp. 1161–1165, 1996.

- [42] J. A. M. Van Roosmalen and E. H. P. Cordfunke, “Chemical reactivity and interdiffusion of (La,Sr)MnO₃ and (Zr,Y)O₂, solid oxide fuel cell cathode and electrolyte materials,” *Solid State Ionics*, vol. 52, pp. 303–312, 1992.
- [43] S. Carter, A. Selcuk, R. J. Chater, J. Kajda, J. A. Kilner, and B. C. H. Steele, “Oxygen transport in selected nonstoichiometric perovskite-structure oxides,” *Solid State Ionics*, vol. 56, pp. 597–605, 1992.
- [44] S. B. Adler, J. A. Lane, and B. C. H. Steele, “Fundamental issues in modeling of mixed-conductors (A rebuttal to comments on ‘electrode kinetics of porous mixed-conducting oxygen electrodes’),” *J. Electrochem. Soc.*, vol. 144, no. 5, pp. 1884–1890, 1997.
- [45] D. Marinha, L. Dessemond, and E. Djurado, “Comparison of Electrochemical Performances of Electrosprayed LSCF Cathode Films for IT-SOFCs for Different Morphologies and Cobalt Contents,” *ECS Trans.*, vol. 35, no. 1, pp. 2283–2294, 2011.
- [46] H. Ullmann, N. Trofimenko, F. Tietz, D. Stover, and A. Ahmad-Khanlou, “Correlation between thermal expansion and oxide ion transport in mixed conducting perovskite-type oxides for SOFC cathodes,” *Solid State Ionics*, vol. 138, pp. 79–90, 2000.
- [47] E. V. Tsipis and V. V. Kharton, “Electrode materials and reaction mechanisms in solid oxide fuel cells: a brief review,” *J. Solid State Electrochem.*, vol. 12, no. 11, pp. 1367–1391, 2008.
- [48] J. W. Stevenson, I. Armstrong, R. D. Carneim, L. I. Pederson, and W. J. Weber, “Electrochemical Properties of Mixed Conducting Perovskites (M = Sr, Ba, Ca),” *J. Electrochem. Soc.*, vol. 143, no. 9, pp. 2722–2729, 1996.
- [49] L. Tai, M. M. Nasrallah, H. U. Anderson, D. M. Sparlin, and S. R. Sehlin, “Structure and electrical properties of La_{1-x}Sr_xCo_{1-y}Fe_yO₃. Part 1. The system La_{0.8}Sr_{0.2}Co_{1-y}Fe_yO₃,” *Solid State Ionics*, vol. 76, no. 3–4, pp. 259–271, 1995.
- [50] Y. Teraoka, H. M. Zhang, K. Okamoto, and N. Yamazoe, “Mixed ionic-electronic conductivity of La_{1-x}Sr_xCo_{1-y}Fe_yO_{3-δ} perovskite-type oxides,” *Mater. Res. Bull.*, vol. 23, no. 1, pp. 51–58, 1988.

- [51] G. C. Kostoglouidis, G. Tsiniarakis, and C. Ftikos, “Chemical reactivity of perovskite oxide SOFC cathodes and yttria stabilized zirconia,” *Solid State Ionics*, vol. 135, pp. 529–535, 2000.
- [52] E. Ruiz-Trejo, J. D. Sirman, Y. M. Baikov, and J. A. Kilner, “Oxygen ion diffusivity, surface exchange and ionic conductivity in single crystal Gadolinia doped Ceria,” *Solid State Ionics*, vol. 113–115, pp. 565–569, 1998.
- [53] S. Uhlenbruck, T. Moskalewicz, N. Jordan, H.-J. Penkalla, and H. P. Buchkremer, “Element interdiffusion at electrolyte–cathode interfaces in ceramic high-temperature fuel cells,” *Solid State Ionics*, vol. 180, no. 4–5, pp. 418–423, 2009.
- [54] T. Nguyen, K. Kobayashi, T. Honda, Y. Iimura, K. Kato, a Neghisi, K. Nozaki, F. Tappero, K. Sasaki, and H. Shirahama, “Preparation and evaluation of doped ceria interlayer on supported stabilized zirconia electrolyte SOFCs by wet ceramic processes,” *Solid State Ionics*, vol. 174, no. 1–4, pp. 163–174, 2004.
- [55] G. Constantin, C. Rossignol, J.-P. Barnes, and E. Djurado, “Interface stability of thin, dense CGO film coating on YSZ for solid oxide fuel cells,” *Solid State Ionics*, vol. 235, pp. 36–41, 2013.
- [56] L. W. Tai, M. M. Nasrallah, H. U. Andreson, D. M. Sparlin, and S. R. Sehlin, “Structure and electrical properties of $\text{La}_{1-x}\text{Sr}_x\text{Co}_{1-y}\text{Fe}_y\text{O}_3$. Part 2. The system $\text{La}_{1-x}\text{Sr}_x\text{Co}_{0.2}\text{Fe}_{0.8}\text{O}_3$,” *Solid State Ionics*, vol. 2738, no. 94, pp. 273–283, 1995.
- [57] H. Hayashi, T. Saitou, N. Maruyama, H. Inaba, K. Kawamura, and M. Mori, “Thermal expansion coefficient of yttria stabilized zirconia for various yttria contents,” *Solid State Ionics*, vol. 176, no. 5–6, pp. 613–619, 2005.
- [58] A. Züttel, A. Borgschulte, and L. Schlapbach, *Hydrogen as a future energy carrier*. Weinheim: Wiley-VHC Verlag GmbH & Co., 2008.
- [59] M. A. Laguna-Bercero, “Recent advances in high temperature electrolysis using solid oxide fuel cells: A review,” *J. Power Sources*, vol. 203, pp. 4–16, 2012.

- [60] W. Donitz and E. Erdle, “High-temperature electrolysis of water vapor-status of development and perspectives for application,” *Int. J. Hydrogen Energy*, vol. 10, no. 5, pp. 291–295, 1985.
- [61] A. Hauch, S. D. Ebbesen, S. H. Jensen, and M. Mogensen, “Highly efficient high temperature electrolysis,” *J. Mater. Chem.*, vol. 18, no. 20, pp. 2331–2340, 2008.
- [62] H. Uchida, N. Osada, and M. Watanabe, “High-Performance Electrode for Steam Electrolysis Mixed Conducting Ceria-Based Cathode with Highly-Dispersed Ni Electrocatalysts,” *Electrochem. Solid-State Lett.*, vol. 7, no. 12, pp. A500–A502, 2004.
- [63] K. Eguchi, T. Hatagishi, and H. Arai, “Power generation and steam electrolysis characteristics of an electrochemical cell with a zirconia- or ceria-based electrolyte,” *Solid State Ionics*, vol. 2738, no. 96, pp. 1245–1249, 1996.
- [64] B. Zhu, I. Albinsson, C. Anderson, K. Borsand, M. Nilsson, and B.-E. Mellander, “Electrolysis Studies Based on Ceria-based Composites,” *Electrochem. commun.*, vol. 8, pp. 495–498, 2006.
- [65] W. Wang, Y. Huang, S. Jung, J. M. Vohs, and R. J. Gorte, “A Comparison of LSM, LSF, and LSCo for Solid Oxide Electrolyzer Anodes,” *J. Electrochem. Soc.*, vol. 153, pp. A2066–A2070, 2006.
- [66] D. A. Marina, L. R. Pederson, M. C. Williams, G. W. Coffey, K. D. Meinhardt, C. D. Nguyen, and E. C. Thomsen, “Electrode Performance in Reversible Solid Oxide Fuel Cells,” *J. Electrochem. Soc.*, vol. 154, pp. B452–B459, 2007.
- [67] A. Brisse, J. Schefold, and M. Zahid, “High temperature water electrolysis in solid oxide cells,” *Int. J. Hydrogen Energy*, vol. 33, no. 20, pp. 5375–5382, 2008.
- [68] J. Schefold, A. Brisse, and F. Tietz, “Nine Thousand Hours of Operation of a Solid Oxide Cell in Steam Electrolysis Mode,” *J. Electrochem. Soc.*, vol. 159, no. 2, pp. A137–A144, 2012.
- [69] A. Hauch, S. D. Ebbesen, S. H. Jensen, and M. Mogensen, “Solid Oxide Electrolysis Cells: Microstructure and Degradation of the Ni/Yttria-Stabilized Zirconia Electrode,” *J. Electrochem. Soc.*, vol. 155, no. 11, pp. B1184–B1193, 2008.

- [70] J. R. Mawdsley, J. David Carter, A. Jeremy Kropf, B. Yildiz, and V. a. Maroni, “Post-test evaluation of oxygen electrodes from solid oxide electrolysis stacks,” *Int. J. Hydrogen Energy*, vol. 34, no. 9, pp. 4198–4207, 2009.
- [71] J. S. Herring, J. Obrien, C. Stoots, G. Hawkes, J. Hartvigsen, and M. Shahnam, “Progress in high-temperature electrolysis for hydrogen production using planar SOFC technology,” *Int. J. Hydrogen Energy*, vol. 32, no. 4, pp. 440–450, 2007.
- [72] A. Hauch, S. H. Jensen, S. Ramousse, and M. Mogensen, “Performance and Durability of Solid Oxide Electrolysis Cells,” *J. Electrochem. Soc.*, vol. 153, no. 9, pp. A1741–A1747, 2006.
- [73] A. V. Virkar, “Mechanism of oxygen electrode delamination in solid oxide electrolyzer cells,” *Int. J. Hydrogen Energy*, vol. 35, no. 18, pp. 9527–9543, 2010.
- [74] V. N. Nguyen, Q. Fang, U. Packbier, and L. Blum, “Long-term tests of a Jülich planar short stack with reversible solid oxide cells in both fuel cell and electrolysis modes,” *Int. J. Hydrogen Energy*, vol. 38, no. 11, pp. 4281–4290, 2013.
- [75] J. Schefold, A. Brisse, M. Zahid, J. P. Ouweltjes, and J. U. Nielsen, “Long Term Testing of Short Stacks with Solid Oxide Cells for Water Electrolysis,” *ECS Trans.*, vol. 35, no. 1, pp. 2915–2927, 2011.
- [76] J. Schefold, A. Brisse, and M. Zahid, “Long Term Testing of Solid Oxide Fuel Cell Stacks with Yttria Stabilised Zirconia Electrolyte in the H₂O Electrolysis Mode,” *ECS Trans.*, vol. 28, no. 11, pp. 357–367, 2010.
- [77] X. Zhang, J. E. O’Brien, R. C. O’Brien, J. J. Hartvigsen, G. Tao, and G. K. Housley, “Improved durability of SOEC stacks for high temperature electrolysis,” *Int. J. Hydrogen Energy*, vol. 38, no. 1, pp. 20–28, 2013.
- [78] M. Zahid, J. Schefold, and A. Brisse, *High Temperature Water Electrolysis Using Planar Solid Oxide Fuel Cell Technology: a Review. In: Hydrogen and Fuel Cells Fundamentals, Technologies an Applications*, PD Stolten. Weinheim, Germany: Wiley-VHC Verlag GmbH & Co. KGaA, pp. 227–242, 2010.

- [79] J. E. O'Brien, M. G. McKellar, E. a. Harvego, and C. M. Stoots, "High-temperature electrolysis for large-scale hydrogen and syngas production from nuclear energy – summary of system simulation and economic analyses," *Int. J. Hydrogen Energy*, vol. 35, no. 10, pp. 4808–4819, 2010.
- [80] R. Knibbe, A. Hauch, J. Hjelm, S. D. Ebbesen, and M. Mogensen, "Durability of Solid Oxide Cells," *Green*, vol. 1, pp. 141–169, 2011.
- [81] V. I. Sharma and B. Yildiz, "Degradation Mechanism in $\text{La}_{0.8}\text{Sr}_{0.2}\text{CoO}_3$ as Contact Layer on the Solid Oxide Electrolysis Cell Anode," *J. Electrochem. Soc.*, vol. 157, no. 3, pp. B441–B448, 2010.
- [82] T. Jacobsen and M. Mogensen, "The Course of Oxygen Partial Pressure and Electric Potentials across an Oxide Electrolyte Cell," *ECS Trans.*, vol. 13, no. 26, pp. 259–273, 2008.
- [83] A. Ringuede and J. Fouletier, "Oxygen reaction on strontium-doped lanthanum cobaltite dense electrodes at intermediate temperatures," *Solid State Ionics*, vol. 139, pp. 167–177, 2001.
- [84] S. Shimizu, T. Yamaguchi, Y. Fujishiro, and M. Awano, "Effect of microstructure on the conductivity of porous $(\text{La}_{0.8}\text{Sr}_{0.2})_{0.99}\text{MnO}_3$," *J. Ceram. Soc. Japan*, vol. 117, no. 8, pp. 895–898, 2009.
- [85] M. J. Jørgensen, S. Primdahl, C. Bagger, and M. Mogensen, "Effect of sintering temperature on microstructure and performance of LSM – YSZ composite cathodes," *Solid State Ionics*, vol. 139, pp. 1–11, 2001.
- [86] J. Hayd, L. Dieterle, U. Guntow, D. Gerthsen, and E. Ivers-Tiffée, "Nanoscaled $\text{La}_{0.6}\text{Sr}_{0.4}\text{CoO}_{3-1}$ as intermediate temperature solid oxide fuel cell cathode: Microstructure and electrochemical performance," *J. Power Sources*, vol. 196, no. 17, pp. 7263–7270, 2011.
- [87] L. Baqué, A. Caneiro, M. S. Moreno, and A. Serquis, "High performance nanostructured IT-SOFC cathodes prepared by novel chemical method," *Electrochem. commun.*, vol. 10, no. 12, pp. 1905–1908, 2008.

- [88] D. Marinha, L. Dessemond, J. S. Cronin, J. R. Wilson, S. A. Barnett, and E. Djurado, “Microstructural 3D Reconstruction and Performance Evaluation of LSCF Cathodes Obtained by Electrostatic Spray Deposition,” *Chem. Mater.*, vol. 23, no. 24, pp. 5340–5348, 2011.
- [89] D. Beckel, U. Muecke, T. Gyger, G. Florey, A. Infortuna, and L. Gauckler, “Electrochemical performance of LSCF based thin film cathodes prepared by spray pyrolysis,” *Solid State Ionics*, vol. 178, no. 5–6, pp. 407–415, 2007.
- [90] A. Esquirol, N. P. Brandon, J. A. Kilner, and M. Mogensen, “Electrochemical Characterization of $\text{La}_{0.6}\text{Sr}_{0.4}\text{Co}_{0.2}\text{Fe}_{0.8}\text{O}_3$ Cathodes for Intermediate-Temperature SOFCs,” *J. Electrochem. Soc.*, vol. 151, no. 11, p. A1847, 2004.
- [91] C.-S. Hsu and B.-H. Hwang, “Microstructure and Properties of the $\text{La}_{0.6}\text{Sr}_{0.4}\text{Co}_{0.2}\text{Fe}_{0.8}\text{O}_3$ Cathodes Prepared by Electrostatic-Assisted Ultrasonic Spray Pyrolysis Method,” *J. Electrochem. Soc.*, vol. 153, no. 8, pp. A1478–A1483, 2006.
- [92] Y. Leng, S. Chan, and Q. Liu, “Development of LSCF–GDC composite cathodes for low-temperature solid oxide fuel cells with thin film GDC electrolyte,” *Int. J. Hydrogen Energy*, vol. 33, no. 14, pp. 3808–3817, 2008.
- [93] A. Mai, V. Haanappel, S. Uhlenbruck, F. Tietz, and D. Stover, “Ferrite-based perovskites as cathode materials for anode-supported solid oxide fuel cells. Part I. Variation of composition,” *Solid State Ionics*, vol. 176, no. 15–16, pp. 1341–1350, 2005.
- [94] D. Marinha, J. Hayd, L. Dessemond, E. Ivers-Tiffée, and E. Djurado, “Performance of $(\text{La,Sr})(\text{Co,Fe})\text{O}_{3-x}$ double-layer cathode films for intermediate temperature solid oxide fuel cell,” *J. Power Sources*, vol. 196, pp. 5084–5090, 2011.
- [95] W. Wang and M. Mogensen, “High-performance lanthanum-ferrite-based cathode for SOFC,” *Solid State Ionics*, vol. 176, no. 5–6, pp. 457–462, 2005.
- [96] V. Dusastre and J. A. Kilner, “Optimisation of composite cathodes for intermediate temperature SOFC applications,” *Solid State Ionics*, vol. 126, pp. 163–174, 1999.

- [97] E. P. Murray, M. J. Sever, and S. A. Barnett, “Electrochemical performance of (La,Sr)(Co,Fe)O₃–(Ce,Gd)O₃ composite cathodes,” *Solid State Ionics*, vol. 148, pp. 27–34, 2002.
- [98] P. S. Manning, J. D. Sirman, and J. A. Kilner, “Oxygen self-diffusion electrolytes and surface exchange studies of oxide having the fluorite structure,” *Solid State Ionics*, vol. 93, pp. 125–132, 1997.
- [99] A. Esquirol, J. Kilner, and N. Brandon, “Oxygen transport in La_{0.6}Sr_{0.4}Co_{0.2}Fe_{0.8}O_{3-δ} / Ce_{0.8}Ge_{0.2}O_{2-x} composite cathode for IT-SOFCs,” *Solid State Ionics*, vol. 175, pp. 63–67, 2004.
- [100] P. S. Manning, J. D. Sirman, R. A. De Souza, and J. A. Kilner, “The kinetics of oxygen transport in 9.5 mol % single crystal yttria stabilised zirconia,” *Solid State Ionics*, vol. 100, pp. 1–10, 1997.
- [101] K. Park, S. Yu, J. Bae, H. Kim, and Y. Ko, “Fast performance degradation of SOFC caused by cathode delamination in long-term testing,” *Int. J. Hydrogen Energy*, vol. 35, no. 16, pp. 8670–8677, 2010.
- [102] K. Kobayashi, I. Takahashi, M. Shiono, and M. Dokiya, “Supported Zr(Sc)O₂ SOFCs for reduced temperature prepared by electrophoretic deposition,” *Solid State Ionics*, vol. 152–153, pp. 591–596, 2002.
- [103] A. Mai, V. Haanappel, F. Tietz, and D. Stover, “Ferrite-based perovskites as cathode materials for anode-supported solid oxide fuel cells. Part II. Influence of the CGO interlayer,” *Solid State Ionics*, vol. 177, pp. 2103–2107, 2006.
- [104] D. Wang, J. Wang, C. He, Y. Tao, C. Xu, and W. G. Wang, “Preparation of a Gd_{0.1}Ce_{0.9}O_{2-δ} interlayer for intermediate-temperature solid oxide fuel cells by spray coating,” *J. Alloys Compd.*, vol. 505, no. 1, pp. 118–124, 2010.
- [105] F. Han, R. Mücke, T. Van Gestel, A. Leonide, N. H. Menzler, H. Peter, and D. Stöver, “Novel high-performance solid oxide fuel cells with bulk ionic conductance dominated thin-film electrolytes,” *J. Power Sources*, vol. 218, pp. 157–162, 2012.

- [106] G. Constantin, C. Rossignol, P. Briois, A. Billard, L. Dessemond, and E. Djurado, “Efficiency of a dense thin CGO buffer layer for solid oxide fuel cell operating at intermediate temperature,” *Solid State Ionics*, vol. 249–250, pp. 98–104, 2013.
- [107] H. Mitsuyasu, Y. Nonaka, K. Eguchi, and H. Arai, “TEM Observation of Reaction at the Interface between Yttria-Doped Ceria and Yttria-Stabilized Zirconia,” *J. Solid State Chem.*, vol. 129, no. 1, pp. 74–81, 1997.
- [108] N. M. Sammes and Z. Cai, “Ionic conductivity of ceria/yttria stabilized zirconia electrolyte materials,” *Solid State Ionics*, vol. 100, pp. 39–44, 1997.
- [109] A. Tsoga, A. Gupta, A. Naoumidis, and P. Nikolopoulos, “Gadolinia-doped ceria and yttria stabilized zirconia interfaces: regarding their application for SOFC technology,” *Acta Mater.*, vol. 48, no. 18–19, pp. 4709–4714, 2000.
- [110] A. V. Virkar, “Theoretical analysis of the role of interfaces in transport through oxygen ion and electron conducting membranes,” *J. Power Sources*, vol. 147, pp. 8–31, 2005.
- [111] A. Momma, T. Kata, Y. Kaga, and S. Nagata, “Polarization Behavior of High Temperature Electrolysis Cells (SOEC),” *J. Ceram. Soc. Japan*, vol. 105, no. 5, pp. 369–373, 1997.
- [112] J. Guan, N. Minh, B. Ramamurthi, J. Ruud, J.-K. Hong, P. Riley, and D. Weng, “High Performance Flexible Reversible Solid Oxide Fuel Cell,” *GE Global Research Center Report DE-FC36e04GO14351*, 2007.
- [113] K. Chen, N. Ai, and S. Ping, “Development of (Gd,Ce)O₂ -Impregnated (La,Sr)MnO₃ Anodes of High Temperature Solid Oxide Electrolysis Cells,” *J. Electrochem. Soc.*, vol. 157, no. 11, pp. P89–P94, 2010.
- [114] F. Tietz, D. Sebold, A. Brisse, and J. Schefold, “Degradation phenomena in a solid oxide electrolysis cell after 9000 h of operation,” *J. Power Sources*, vol. 223, pp. 129–135, 2013.
- [115] N. Hildenbrand, B. A. Boukamp, P. Nammensma, and D. H. A. Blank, “Improved cathode / electrolyte interface of SOFC,” *Solid State Ionics*, vol. 192, no. 1, pp. 12–15, 2011.

- [116] G. J. Nelson, W. M. Harris, J. J. Lombardo, J. R. Izzo, W. K. S. Chiu, P. Tanasini, M. Cantoni, J. Van herle, C. Comninellis, J. C. Andrews, Y. Liu, P. Pianetta, and Y. S. Chu, “Comparison of SOFC cathode microstructure quantified using X-ray nanotomography and focused ion beam–scanning electron microscopy,” *Electrochem. commun.*, vol. 13, no. 6, pp. 586–589, 2011.
- [117] J. R. Wilson, J. S. Cronin, A. T. Duong, S. Rukes, H.-Y. Chen, K. Thornton, D. R. Mumm, and S. Barnett, “Effect of composition of (La_{0.8}Sr_{0.2}MnO₃–Y₂O₃-stabilized ZrO₂) cathodes: Correlating three-dimensional microstructure and polarization resistance,” *J. Power Sources*, vol. 195, no. 7, pp. 1829–1840, 2010.
- [118] J. R. Wilson, A. T. Duong, M. Gameiro, H.-Y. Chen, K. Thornton, D. R. Mumm, and S. a. Barnett, “Quantitative three-dimensional microstructure of a solid oxide fuel cell cathode,” *Electrochem. commun.*, vol. 11, no. 5, pp. 1052–1056, 2009.
- [119] C. Yang, A. Coffin, and F. Chen, “High temperature solid oxide electrolysis cell employing porous structured (La_{0.75}Sr_{0.25})_{0.95}MnO₃ with enhanced oxygen electrode performance,” *Int. J. Hydrogen Energy*, vol. 35, no. 8, pp. 3221–3226, 2010.
- [120] D. Gostovic, J. R. Smith, D. P. Kundinger, K. S. Jones, and E. D. Wachsman, “Three-Dimensional Reconstruction of Porous LSCF Cathodes,” *Electrochem. Solid-State Lett.*, vol. 10, no. 12, pp. B214–B217, 2007.
- [121] J. Joos, T. Carraro, A. Weber, and E. Ivers-Tiffée, “Reconstruction of porous electrodes by FIB/SEM for detailed microstructure modeling,” *J. Power Sources*, vol. 196, no. 17, pp. 7302–7307, 2010.
- [122] K. Matsuzaki, N. Shikazono, and N. Kasagi, “Three-dimensional numerical analysis of mixed ionic and electronic conducting cathode reconstructed by focused ion beam scanning electron microscope,” *J. Power Sources*, vol. 196, no. 6, pp. 3073–3082, 2011.
- [123] J. Laurencin, R. Quey, G. Delette, H. Suhonen, P. Cloetens, and P. Bleuet, “Characterisation of Solid Oxide Fuel Cell Ni–8YSZ substrate by synchrotron X-ray nano-tomography: from 3D reconstruction to microstructure quantification,” *J. Power Sources*, vol. 198, pp. 182–189, 2011.

- [124] G. J. Nelson, K. N. Grew, J. R. Izzo, J. J. Lombardo, W. M. Harris, A. Faes, A. Hessler-Wyser, J. Van herle, S. Wang, Y. S. Chu, A. V. Virkar, and W. K. S. Chiu, “Three-dimensional microstructural changes in the Ni–YSZ solid oxide fuel cell anode during operation,” *Acta Mater.*, vol. 60, no. 8, pp. 3491–3500, 2012.
- [125] N. Vivet, S. Chupin, E. Estrade, a. Richard, S. Bonnamy, D. Rochais, and E. Bruneton, “Effect of Ni content in SOFC Ni-YSZ cermets: A three-dimensional study by FIB-SEM tomography,” *J. Power Sources*, vol. 196, no. 23, pp. 9989–9997, 2011.
- [126] J. R. Wilson, M. Gameiro, K. Mischaikow, W. Kalies, P. W. Voorhees, and S. A. Barnett, “Three-Dimensional Analysis of Solid Oxide Fuel Cell Ni-YSZ Anode Interconnectivity,” *Microsc. Microanal.*, vol. 15, no. 1, pp. 71–77, 2009.
- [127] J. R. Wilson, J. S. Cronin, and S. a. Barnett, “Linking the microstructure, performance and durability of Ni-yttria-stabilized zirconia solid oxide fuel cell anodes using three-dimensional focused ion beam–scanning electron microscopy imaging,” *Scr. Mater.*, vol. 65, no. 2, pp. 67–72, 2011.
- [128] S. B. Adler, J. A. Lane, and B. C. H. Steele, “Electrode Kinetics of Porous Mixed-Conducting Oxygen Electrodes,” *J. Electrochem. Soc.*, vol. 143, no. 11, pp. 3554–3564, 1996.
- [129] N. S. K. Gunda, H.-W. Choi, A. Berson, B. Kenney, K. Karan, J. G. Pharoah, and S. K. Mitra, “Focused ion beam-scanning electron microscopy on solid-oxide fuel-cell electrode: Image analysis and computing effective transport properties,” *J. Power Sources*, vol. 196, no. 7, pp. 3592–3603, 2011.
- [130] A. Selimovic, M. Kemm, T. Torisson, and M. Assadi, “Steady state and transient thermal stress analysis in planar solid oxide fuel cells,” *J. Power Sources*, vol. 145, pp. 463–469, 2005.
- [131] A. Nakajo, J. Kuebler, A. Faes, U. F. Vogt, H. Ju, L. Chiang, S. Modena, J. Van, and T. Hocker, “Compilation of mechanical properties for the structural analysis of solid oxide fuel cell stacks . Constitutive materials of anode-supported cells,” *Ceram. Int.*, vol. 38, pp. 3907–3927, 2012.

- [132] W. Weibull, “A statistical theory of the strength of materials,” *Proc. R. Swedish Inst. Eng. Reserach*, vol. 151, pp. 1–45, 1939.
- [133] A. Nakajo, F. Mueller, J. Brouwer, J. Van, and D. Favrat, “Mechanical reliability and durability of SOFC stacks . Part I: Modelling of the effect of operating conditions and design alternatives on the reliability,” *Int. J. Hydrogen Energy*, vol. 37, no. 11, pp. 9249–9268, 2012.
- [134] A. Nakajo, F. Mueller, J. Brouwer, J. Van, and D. Favrat, “Mechanical reliability and durability of SOFC stacks . Part II: Modelling of mechanical failures during ageing and cycling,” *Int. J. Hydrogen Energy*, vol. 37, no. 11, pp. 9269–9286, 2012.
- [135] J. Laurencin, G. Delette, F. Lefebvre-Joud, and M. Dupeux, “A numerical tool to estimate SOFC mechanical degradation: Case of the planar cell configuration,” *J. Eur. Ceram. Soc.*, vol. 28, pp. 1857–1869, 2008.
- [136] G. Anandakumar, N. Li, A. Verma, P. Singh, and J. Kim, “Thermal stress and probability of failure analyses of functionally graded solid oxide fuel cells,” *J. Power Sources*, vol. 195, no. 19, pp. 6659–6670, 2010.
- [137] C. Lin, T. Chen, Y. Chyou, and L. Chiang, “Thermal stress analysis of a planar SOFC stack,” *J. Power Sources*, vol. 164, pp. 238–251, 2007.
- [138] K. An, “Mechanical properties and electrochemical durability of solid oxide fuel cells,” PhD Thesis, Virginia Polytechnic Institute and State University, 2003.
- [139] Z. Xiang, W. Fenghui, H. Jianye, and L. Tiejun, “Determining the mechanical properties of solid oxide fuel cell by an improved work of indentation approach,” *J. Power Sources*, vol. 201, pp. 231–235, 2012.
- [140] N. Li, A. Verma, A. Smirnova, and P. Singh, “Measurement of Mechanical properties of LSCF - GDC Composite SOFC Cathode,” *Am. Ceram. Soc. Meet.*, FL, USA, 2010.
- [141] S. Meille, M. Lombardi, J. Chevalier, and L. Montanaro, “Mechanical properties of porous ceramics in compression: On the transition between elastic, brittle, and cellular behavior,” *J. Eur. Ceram. Soc.*, vol. 32, no. 15, pp. 3959–3967, 2012.

- [142] L. J. Gibson and M. F. Ashby, *Cellular solids: structures and properties (S.S.S. Series)*. Cambridge University Press, 1988.
- [143] M. Scheffler and P. Colombo, *Cellular ceramics, structure, manufacturing, properties and applications*, 1st Editio. Wiley, 2005.
- [144] B.-H. Hwang, C.-L. Chang, C.-S. Hsu, and C.-Y. Fu, “Electrostatic spray deposition of NiO/CGO films,” *J. Phys. D. Appl. Phys.*, vol. 40, no. 11, pp. 3448–3455, 2007.
- [145] I. Taniguchi, R. C. Van Landschoot, and J. Schoonman, “Fabrication of $\text{La}_{1-x}\text{Sr}_x\text{Co}_{1-y}\text{Fe}_y\text{O}_3$ thin films by electrostatic spray deposition,” *Solid State Ionics*, vol. 156, pp. 1 – 13, 2003.
- [146] I. Taniguchi, R. C. Van Landschoot, and J. Schoonman, “Electrostatic spray deposition of $\text{Gd}_{0.1}\text{Ce}_{0.9}\text{O}_{1.95}$ and $\text{La}_{0.9}\text{Sr}_{0.1}\text{Ga}_{0.8}\text{Mg}_{0.2}\text{O}_{2.87}$ thin films,” *Solid State Ionics*, vol. 160, no. 3–4, pp. 271–279, 2003.
- [147] D. Marinha, C. Rossignol, and E. Djurado, “Influence of electrospraying parameters on the microstructure of $\text{La}_{0.6}\text{Sr}_{0.4}\text{Co}_{0.2}\text{Fe}_{0.8}\text{O}_{3-\delta}$ films for SOFCs,” *J. Solid State Chem.*, vol. 182, no. 7, pp. 1742–1748, 2009.
- [148] A. Princivalle and E. Djurado, “Nanostructured LSM/YSZ composite cathodes for IT-SOFC: A comprehensive microstructural study by electrostatic spray deposition,” *Solid State Ionics*, vol. 179, no. 33–34, pp. 1921–1928, 2008.
- [149] R. Neagu, D. Perednis, a Princivalle, and E. Djurado, “Zirconia coatings deposited by electrostatic spray deposition. Influence of the process parameters,” *Surf. Coatings Technol.*, vol. 200, no. 24, pp. 6815–6820, 2006.
- [150] R. Neagu, D. Perednis, a Princivalle, and E. Djurado, “Influence of the process parameters on the ESD synthesis of thin film YSZ electrolytes,” *Solid State Ionics*, vol. 177, no. 19–25, pp. 1981–1984, 2006.
- [151] C. Rossignol, B. Roman, G. D. Benetti, and E. Djurado, “Elaboration of thin and dense CGO films adherent to YSZ by electrostatic spray deposition for IT-SOFC applications,” *New J. Chem.*, vol. 35, no. 3, pp. 716–723, 2011.

- [152] A. Jaworek and A. T. Sobczyk, “Electrospraying route to nanotechnology: An overview,” *J. Electrostat.*, vol. 66, no. 3–4, pp. 197–219, 2008.
- [153] A. M. Gañan-Calvo, J. Davila, and A. Barrero, “Current and droplet size in the Electrspraying of Liquids. Scaling laws,” *J. Aerosol Sci.*, vol. 28, no. 2, pp. 249–275, 1997.
- [154] C. Chen, E. M. Kelder, J. J. M. van der Put, and J. Schoonman, “Morphology control of thin LiCoO₂ films fabricated using the electrostatic spray deposition (ESD) technique,” *J. Mater. Chem.*, vol. 6, no. 5, pp. 765–771, 1996.
- [155] R. Neagu, D. Perednis, and E. Djurado, “Initial Stages in Zirconia Coatings Using ESD,” *Chem. Mater.*, vol. 17, no. 4, pp. 902–910, 2005.
- [156] R. Neagu, “Elaboration de films minces d’électrolyte par une technique innovante: l’atomisation électrostatique.,” PhD Thesis, Grenoble INP, 2005.
- [157] “[http://imagej.nih.gov/ij/.](http://imagej.nih.gov/ij/)”
- [158] J. Villanova, P. Cloetens, H. Suhonen, J. Laurencin, F. Usseglio-Viretta, E. Lay, G. Delette, P. Bleuet, D. Jauffres, D. Roussel, A. Z. Lichtner, and C. L. Martin, “Multi-scale 3D imaging of absorbing porous materials for solid oxide fuel cells,” *J. Mater. Sci.*, vol. 49, pp. 5626–5634, 2014.
- [159] “LEPMI Spring School Mai 2012 on ‘Electrochimie des Céramiques.’”
- [160] G. Martinez-Criado, R. Tucoulou, P. Cloetens, P. Bleuet, S. Bohic, J. Cauzid, I. Kieffer, E. Kosior, S. Laboure, S. Petitgirard, A. Rack, J. A. Sans, J. Segura-Ruiz, H. Suhonen, J. Susini, and J. Villanova, “Status of the hard X-ray microprobe beamline ID22 of the European Synchrotron Radiation Facility,” *J. Synchrotron Radiat.*, vol. 19, pp. 10–18, 2012.
- [161] A. Hammou and S. Georges, *Electrochimie des Solides: exercices corrigés avec rappels de cours*. EDP Sciences, 2011.
- [162] P. Cloetens, W. Ludwig, J. Baruchel, D. Van Dyck, J. Van Landuyt, J. P. Guigay, and M. Schlenker, “Holotomography: Quantitative phase tomography with micrometer

- resolution using hard synchrotron radiation x rays,” *Appl. Phys. Lett.*, vol. 75, no. 19, pp. 2912–2914, 1999.
- [163] J. R. Macdonald, “Impedance Spectroscopy,” *Ann. Biomed. Eng.*, vol. 20, pp. 289–305, 1992.
- [164] W. C. Oliver and G. M. Pharr, “Measurement of hardness and elastic modulus by instrumented indentation: Advances in understanding and refinements to methodology,” *J. Mater. Res.*, vol. 19, no. 1, pp. 1–20, 2003.
- [165] A. C. Fischer-Cripps, *Nanoindentation (Mechanical Engineering Series)*, Third Edit. Springer, 2011.
- [166] M. Teixeira, C. Loable, A. Almeida, O. Florencio, J. C. S. Frernandes, and R. Vilar, “Combinatorial laser-assisted development of novel Ti-Ta alloys for biomedical applications,” *ICALEO 2013 - 32nd Int. Congr. Apl. Lasers Electro-Optics*, FL, USA, pp. 34–42, 2013.
- [167] S. Kuiry, “Advanced Scratch Testing for Evaluation of Coatings,” *Bruker Nano surfaces Division, Tribology and Mechanical Testing*, 2012.
- [168] B. Mell and G. Bégin, “Scratch adhesion testing of compact disc coating,” *NANOVEA*, pp. 1–10, 2010.
- [169] S. J. Benson, “PhD thesis, Department Materials, Imperial College,” PhD Thesis, Imperial College, 1999.

II. Coral Microstructure of Graded CGO/LSCF Oxygen Electrode by Electrostatic Spray Deposition for Energy (IT-SOFC, SOEC)

J. Sar, F. Charlot, A. Almeida, L. Dessemond, and E. Djurado, *Fuel Cells*, vol. 14, no. 3, pp. 357–363, 2014, doi : 10.1002/fuce.201300146

Coral Microstructure of Graded CGO/LSCF Oxygen Electrode by Electrostatic Spray Deposition for Energy (IT-SOFC, SOEC)

J. Sar^{1,3}, F. Charlot², A. Almeida³, L. Dessemond¹, E. Djurado^{1,*}

¹ Laboratoire d'Electrochimie et de Physico-Chimie des Matériaux et des Interfaces – LEPMI, UMR 5279 CNRS, Grenoble INP, Université de Savoie, Université Joseph Fourier, 1130 Rue de la Piscine, B.P. 75, 38402 St. Martin d'Hères, France

² Consortium des Moyens Technologiques Communs – CMTC, Grenoble INP, 1260 Rue de la Piscine, B.P. 75, 38402 St. Martin d'Hères, France

³ Dep. Eng. Quimica, Instituto Superior Tecnico, Av. Rovisco Pais, Torre Sul, 1049-001 Lisboa, Portugal

**Elisabeth.Djurado@lepmi.grenoble-inp.fr*

II.1. Abstract

The goal of this work was to fabricate a composite based on $\text{Ce}_{0.9}\text{Gd}_{0.1}\text{O}_{1.95}$ (CGO) and $\text{La}_{0.6}\text{Sr}_{0.4}\text{Co}_{0.2}\text{Fe}_{0.8}\text{O}_{3-\delta}$ (LSCF) as a porous and thin oxygen electrode film adherent to $(\text{ZrO}_2)_{0.92}(\text{Y}_2\text{O}_3)_{0.08}$ (YSZ) substrate by Electrostatic Spray Deposition (ESD) in order to improve durability in solid oxide fuel cells operating at intermediate temperature (IT-SOFC) and solid oxide electrolyser cells (SOEC). A simultaneous gradient in composition and in porosity of CGO/LSCF coatings has been successfully obtained by choosing proper deposition parameters and physicochemical properties of the precursor solution. Detailed microstructural characterization was made by SEM and completed with 3D focused ion beam-scanning electron microscope (FIB-SEM) tomography. The graded composition rich in CGO close to YSZ and rich in LSCF at the electrode surface has been investigated by Energy Dispersive X-ray Spectroscopy (EDS) through line profile of coral microstructure. Only cubic CGO and cubic LSCF perovskite were detected by XRD in deposited coatings after heat treatment at 900 °C for 2 h.

Keywords: SOFC, SOEC, Electrostatic Spray Deposition, CGO, LSCF, Graded Composition, FIB-SEM Tomography.

II.2. Introduction

The increasing world's energy consumption demands to create an advanced technology for diversified energy supply and reduce pollution. High-temperature solid oxide cells (SOCs) can be reversibly operated as electrolyser cells (SOECs) for water splitting or syngas production [1] and as fuel cells (SOFCs). SOCs are used to produce energy created directly from electrochemical processes between oxygen and fuel which can be hydrogen, hydrocarbons or ethanol, named Solid Oxide Fuel Cells (SOFCs). The global researches on SOFCs focus on improving the cells properties by lowering operating temperatures from above 900 °C to below 700 °C in so called Intermediate Temperature Solid Oxide Fuel Cells (IT-SOFCs).

Intermediate temperatures help to increase overall lifetime and reduce operation and fabrication costs. However, electrolyte ohmic losses and electrode polarizations of the cell are increased. Consequently, new materials have to be provided to follow investigation at lower temperatures. In general, materials for SOFCs are $\text{La}_{1-x}\text{Sr}_x\text{MnO}_{3-x}$ (LSM) as an oxygen electrode, yttria-stabilized zirconia (YSZ = 8 mol % Y_2O_3 -doped ZrO_2) as an electrolyte and cermet composition of Ni/YSZ as a hydrogen electrode. In IT-SOFC, alternative materials to LSM electronic conductors are Mixed Ionic and Electronic Conductors (MIEC) such as $\text{La}_{0.6}\text{Sr}_{0.4}\text{Co}_{0.2}\text{Fe}_{0.8}\text{O}_{3-\delta}$ (LSCF). Perovskite LSCF presents high electrical conductivity of 350-400 Scm^{-1} at 600 °C [2], [3] and high ionic and electronic conductivity of 10^{-2} and 10^2Scm^{-1} at 800 °C, respectively [4]. Unfortunately, LSCF reacts with the most popular electrolyte material YSZ to create insulating phases ($\text{La}_2\text{Zr}_2\text{O}_7$ and SrZrO_3) [5]. To avoid diffusion of lanthanum and strontium to electrolyte, it is necessary to separate them by creation of barrier diffusion layer. As it was reported, dense $\text{Ce}_{0.9}\text{Gd}_{0.1}\text{O}_{1.95}$ (CGO) is a potential barrier diffusion layer in between LSCF electrode and YSZ electrolyte [6], [7]. Moreover, CGO has high oxygen ion mobility at intermediate temperatures [8]. Furthermore, LSCF and CGO are mechanically and chemically compatible. CGO overcomes thermal stresses between LSCF and YSZ which average thermal expansion coefficients value $13.4 \times 10^{-6} \text{K}^{-1}$, $17.5 \times 10^{-6} \text{K}^{-1}$ and $10.5 \times 10^{-6} \text{K}^{-1}$, respectively [9]–[11]. Additionally, application of original composition of graded CGO-LSCF in electrode can impede diffusion from LSCF to YSZ.

Apart from components materials, morphology has a great influence on the fuel cells properties. Porous electrode microstructure enhances oxygen exchange rates. Microporosity and tortuosity expand reactive surface area for oxygen to penetrate material, and create places for oxygen to be adhered and ionized [12]. To understand well properties of porous microstructure, quantity and distribution of porosity as well as tortuosity have to be defined.

Due to important role of the surface in electrochemical reactions it is necessary to select proper deposition method to achieve needed microstructure in investigated layers.

Electrostatic spray deposition (ESD) is an innovative method to produce porous as well as dense coatings. Fundamentally, droplets in a form of aerosol are created by atomization of precursor solution and are targeted to a heated substrate when the high voltage is applied between the nozzle and the substrate. Depositions are carried out in relatively low temperatures ranging from 300 to 400 °C. During droplets flight caused by electrical field, solvents evaporate to create solid layer with good adhesion to the grounded substrate. A wide variety of microstructures with good homogeneity can be formed depending on the process parameters (nozzle-to-substrate distance, deposition time, substrate temperature, solution flow rate) and the precursor solution physico-chemical properties (boiling point, conductivity, surface tension, etc...) which were studied in our laboratory and it was reported in others publications [13]. The droplet size (d) in the spray is correlated to solution density (ρ), vacuum permeability (ϵ_0) (equal to $8.85 \times 10^{-12} \text{ F.m}^{-1}$), flow rate (Q), solution surface tension (γ) and solution electrical conductivity (σ) regarding to Gañan-Calvo's equation (Eq. (II-1)) [14]. Equation (II-2) presents Gañan-Calvo's relation including units.

$$d \sim \left(\frac{\rho \epsilon_0 Q^3}{\gamma \sigma} \right)^{\frac{1}{6}} \quad (\text{II-1})$$

$$[m] \sim \left(\frac{[kg.m^{-3}][F.m^{-1}]([m^3.s])^3}{[N.m^{-1}][S.m^{-1}]} \right)^{\frac{1}{6}} \quad (\text{II-2})$$

The microstructure of the deposited layer is the result of the interaction between droplets with a given liquid content and the combined effects of spreading and drying rates determined by the substrate temperature at the moment of impact. The advantages of the method are simplicity of the equipment, overall low cost, a good control of the microstructure of the coatings with a good adhesion and a low deposition temperature compare to traditional depositions. Moreover the quantity of precursors and solvents used during deposition is small. This work reports the fabrication of graded porous and thin CGO-LSCF electrode for SOFCs and SOECs deposited on dense YSZ electrolyte by ESD process. The investigation of the microstructure in terms of controlled porous morphology is presented and completed with 3D focused ion beam-scanning electron beam (FIB-SEM) tomography.

II.3. Experimental

II.3.1. Coatings preparation

Gradient in composition of $\text{La}_{0.6}\text{Sr}_{0.4}\text{Co}_{0.2}\text{Fe}_{0.8}\text{O}_{3-\delta}$ (LSCF) and $\text{Ce}_{0.9}\text{Gd}_{0.1}\text{O}_{1.95}$ (CGO) layers were deposited on homemade YSZ substrates. YSZ substrates were prepared in the shape of disks, 19 mm in diameter and 1 mm thick from TZ-8Y powder (8 mol. % Y_2O_3 - ZrO_2 , Tosoh Corporation), isostatically pressed at 250 MPa for 5 min. and sintered in air at 1450 °C for 2 h to get dense pellets (98 % of the theoretical density). The as-densified pellets were rectified to become parallel and then polished to guarantee a smooth uniform surface before deposition.

Two LSCF and CGO solutions were prepared with a total salt concentration equal to 0.02 mol.L^{-1} . The precursor solution of LSCF consisted of lanthanum nitrate hexahydrate ($\text{La}(\text{NO}_3)_3 \cdot 6\text{H}_2\text{O}$, Rectapur Prolabo, 99.5 %), strontium chloride hexahydrate ($\text{SrCl}_2 \cdot 6 \text{H}_2\text{O}$, Strem Chemicals, 99 %), cobalt nitrate hexahydrate ($\text{Co}(\text{NO}_3)_2 \cdot 6\text{H}_2\text{O}$, Merck, 99 %) and iron (III) nitrate nonahydrate ($\text{Fe}(\text{NO}_3)_3 \cdot 9\text{H}_2\text{O}$, Sigma Aldrich, 99.99 %). Salts were weighted to achieve proper stoichiometry of $\text{La}_{0.6}\text{Sr}_{0.4}\text{Co}_{0.2}\text{Fe}_{0.8}\text{O}_{3-\delta}$ solution. In the same way $\text{Ce}_{0.9}\text{Gd}_{0.1}\text{O}_{1.95}$ solution was based on cerium nitrate hexahydrate ($\text{Ce}(\text{NO}_3)_3 \cdot 6\text{H}_2\text{O}$, Rectapur Prolabo, 99.5 %) and gadolinium nitrate ($\text{Gd}(\text{NO}_3)_2$, Aldrich, 99.99 %). Adequate amounts of salts were dissolved in distilled water and ethanol ($\text{C}_2\text{H}_5\text{OH}$, Sigma-Aldrich, 99.8 %) in 5:1 volume ratio to create LSCF precursor solution; diethylene glycol monobutyl ether, well known as butyl carbitol ($\text{CH}_3(\text{CH}_2)_3(\text{OC}_2\text{H}_4)_2\text{OH}$, Acros Organics, 99 %) and ethanol in 4:1 volume ratio for CGO precursor solution. The films were deposited by electrostatic spray deposition using vertical setup (Fig. II-1).

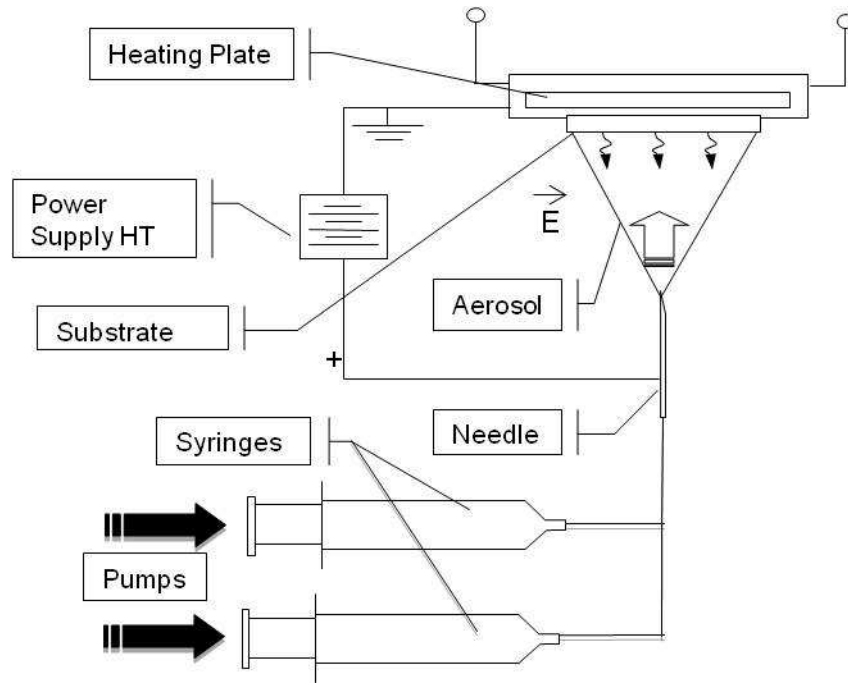


Fig. II-1. Schema of the ESD setup for gradient LSCF/CGO deposition.

Depositions were made at a 35 mm nozzle-to-substrate distance. Two syringes pumps (Sage M361) with separated pipes were set to simultaneously provide two separate precursor solutions. In order to create graded composition, the flow rate of LSCF varied from 0 to 1 mL.h⁻¹ (Q_{LSCF}), while the flow rate of CGO varied from 1 to 0 mL.h⁻¹ (Q_{CGO}). Flow rates were changed with 0.1 mL.h⁻¹ step in every 15 min. The last part of the depositions was carried out using only LSCF solution with flow rate equal to 1 mL.h⁻¹ for 30 min. A total flow rate was kept constant to 1 mL.h⁻¹. The values of solutions flow rates during deposition time are described in Table II-1. The substrate temperature was kept stable at 400 °C, obtained after temperature calibration by K-type thermocouple. This value referred to as the surface of the substrate facing the spray. A positive high voltage from 7 to 11 kV was applied between the nozzle and the grounded substrate to atomize the precursor solutions and to get a stable cone-jet. The complete deposition time was 3 h.

Table II-1. Variation of precursor solutions flow rates during the deposition.

$Q_{CGO} / \text{mL.h}^{-1}$	1	0.9	0.8	0.7	0.6	0.5	0.4	0.3	0.2	0.1	0
$Q_{LSCF} / \text{mL.h}^{-1}$	0	0.1	0.2	0.3	0.4	0.5	0.6	0.7	0.8	0.9	1
CGO / mol %	100	90	80	70	60	50	40	30	20	10	0
Progressive time / h	0.25	0.5	0.75	1	1.25	1.5	1.75	2	2.25	2.5	3

II.3.2. Coatings characterization

Microstructure morphology observations were investigated on samples post-annealed at 900 °C for 2 h in air using scanning electron microscopy with field emission guns, FEG-SEM, (ZEISS Ultra 55) operating at the voltage equal to 3 kV and working distance 7 mm. A platinum layer was deposited on each sample to avoid charging of observed area.

Quantitative analysis was carried out using line profile method on Energy Dispersive X-ray Spectroscopy (EDS) combined to FEG-SEM microscopy. Sample was put inside plastic holder, filled up by the mixture of EpoFix Resin and EpoFix Hardener (Struers) and kept one day for bonding. After that, outer parts of the sample were cut and the sample was polished and prepared for observation.

X-ray powder diffraction was performed on samples post-annealed at 900 °C for 2 h in air using a Panalytical X'Pert Pro MPD diffractometer in the Bragg–Brentano geometry from 20° to 120° in 2θ (0.017° in 2θ step with Cu K α radiation $\lambda = 1.5418 \text{ \AA}$). Phases were identified using EVA software.

FIB-SEM tomography was done using a dual column focus ion beam (FIB) (Ga) – field emission gun scanning electron microscopy FEG-SEM NVISION 40 from Carl ZEISS. A sequence of slices were obtained after using a 30 kV 0.700 nA ion beam energy. Images were collected using secondary electrons detector (SE) and backscattered electrons detector (BSE) with the accelerating electron voltage of 1.5 kV to get two types of pictures on each slice. Two samples were prepared: sample with 40 nm.pixel⁻¹ in x-y-z resolution and sample mounted in the resin with 20 nm.pixel⁻¹ in x-y-z resolution.

II.3.3. Electrochemical characterization

The electrochemical performances of coral microstructure of CGO/LSCF composite electrode were investigated by Electrochemical Impedance Spectroscopy. Measurements were done in three-electrode configuration, where CGO/LSCF coating with area of around 2.0 cm² served as the working electrode (WE). On the opposite side of the YSZ substrate, there was painted symmetrically to WE platinum paste to serve as the counter electrode (CE). The reference electrode (RE) was painted platinum paste around the substrate. Platinum grids with 3600 mesh were used as current collectors for WE and CE. All electrodes were connected to the external electric circuit by using platinum wires with a diameter of 0.2 mm. Investigation was performed between 550 and 700 °C in air at open circuit voltage (OCV) using Solartron (SI 1280B) potentiostat/galvanostat frequency response analyzer with a frequency range of 0.01 Hz to 20 kHz.

II.4. Results and discussion

II.4.1. Coatings characterization

A systematic study of the influence of deposition parameters on the microstructure of pure $\text{La}_{0.6}\text{Sr}_{0.4}\text{Co}_{0.2}\text{Fe}_{0.8}\text{O}_{3-\delta}$ films deposited by ESD on CGO substrates was previously reported in our group by Marinha et al. [13]. The morphology of the coatings was controlled by varying the nozzle-to-substrate distance, the precursor solution flow rate and the substrate temperature leading to different droplet sizes which impact the heated substrate. Consequently, the spreading and drying of the droplets on the substrate are fully dependent on the droplets size leading to different microstructures. The correlation between the studied parameters and droplet size is significantly dependent on the different stages of the deposition: flow rate determines the initial droplet size, the nozzle-to-substrate distance and temperature determine the dynamic change of the droplet size during the flight. As far as distance and temperature parameters are increased, drier droplets will be formed due to a larger evaporation rate of the droplets to lead to porous films. Basically, droplets in which solvents start to evaporate are electrostatically attracted by the closest curvatures on the substrate. This mechanism is called a preferential landing [15]. By changing the solvent composition, the layer morphology may also be modified. Indeed, the droplet size is mainly dependent on the solution electrical conductivity (σ) using low surface tension (γ) in order to get a stable cone-jet mode regarding to Gañan-Calvo's equation (Eq. II-1) [14]. ESD deposition parameters such as distance nozzle-to substrate of 35 mm, a total solution flow rate of $1 \text{ mL}\cdot\text{h}^{-1}$ and substrate temperature of $400 \text{ }^\circ\text{C}$ were chosen to create coral microstructure with high reproducibility to prepare CGO/LSCF composite with comparison to the previous data for the obtaining of pure LSCF [13]. When using 83 vol.% H_2O and 17 vol.% EtOH as the solvent, σ is equal to about $50 \text{ }\mu\text{S}\cdot\text{cm}^{-1}$ and is high enough to favor the formation of small droplets.

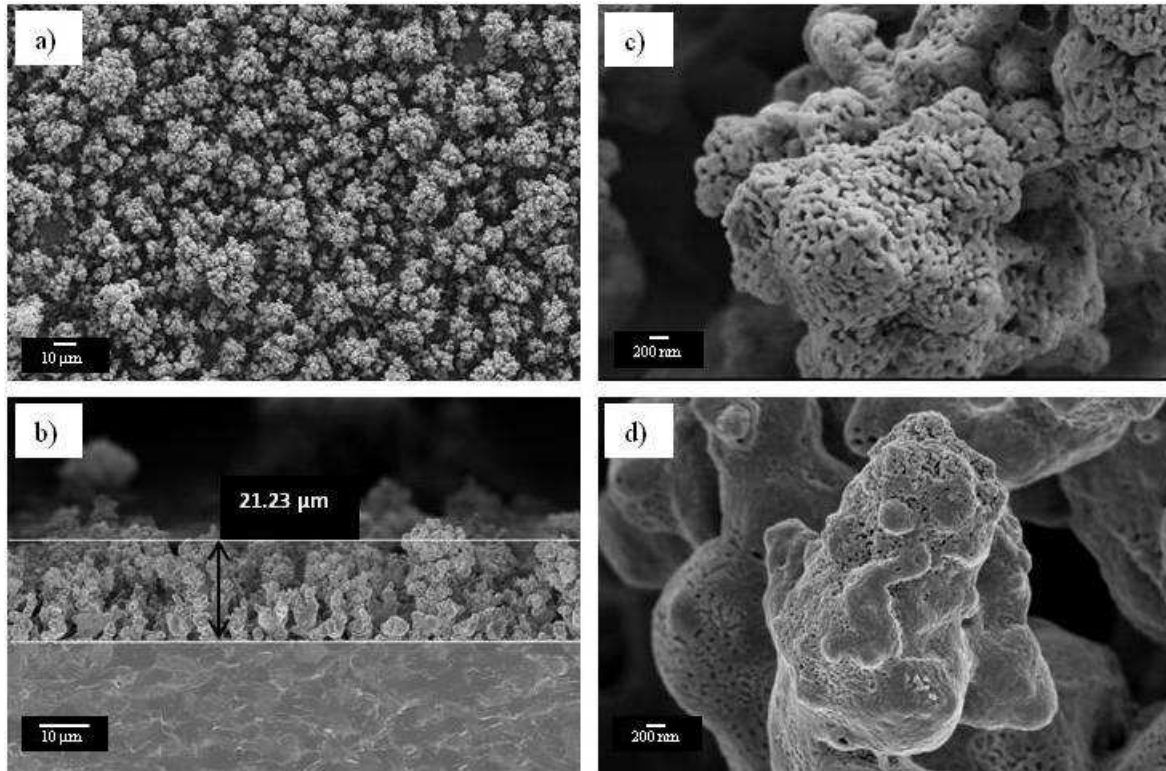


Fig. II-2. FEG-SEM pictures of gradient CGO/LSCF films deposited on YSZ pellets for 3h at 400°C with a constant total flow rate of 1 mL.h⁻¹ and nozzle-to-substrate distance of 35 mm using ESD technique, surface magnifications – 500x (a), 20kx (c) and cross section magnifications – 1kx (b), 20kx (d).

It is worth to mention that a selected longer deposition time of 3h has also resulted in an increased roughness with comparison to laboratory previous work [13]. The creation of a porous graded CGO/LSCF coating with high surface area, referred to as a coral microstructure has been obtained (Fig. II-2). FEG-SEM micrographs show the presence of corals in deposited layers ~20-30 μm in thickness (Fig. II-2b) with two micrometric and nanometric porosities. Typically, the microscopic pores create very high surface area visible on Fig. II-2a. Due to precursor solution simultaneously boiling and drying, deposited particules are very small and stick to itself and create second scale porosity – nanoporosity, which can be observed on high magnification pictures (Fig. II-2c and 2d).

Additionally, SEM images have shown good adhesion of CGO/LSCF film on YSZ whereas the deposition temperature is quite low (Fig. II-2b). FIB-SEM images were scanned on the cross section of CGO/LSCF films deposited on YSZ, unmounted with 40 nm pixel size and mounted in epoxy resin with 20 nm pixels size (Fig. II-3). A good adhesion between the coating and the substrate is presented in the complete volume of the sample (Fig. II-3a). Moreover, images of sample mounted in epoxy resin have shown micrometric and very thin nanometric porosity not only on the surface, but also inside the corals (Fig. II-3b). A large

part of the inner pores are connected to the surrounding and leads to an increasing surface area with large percolation paths.

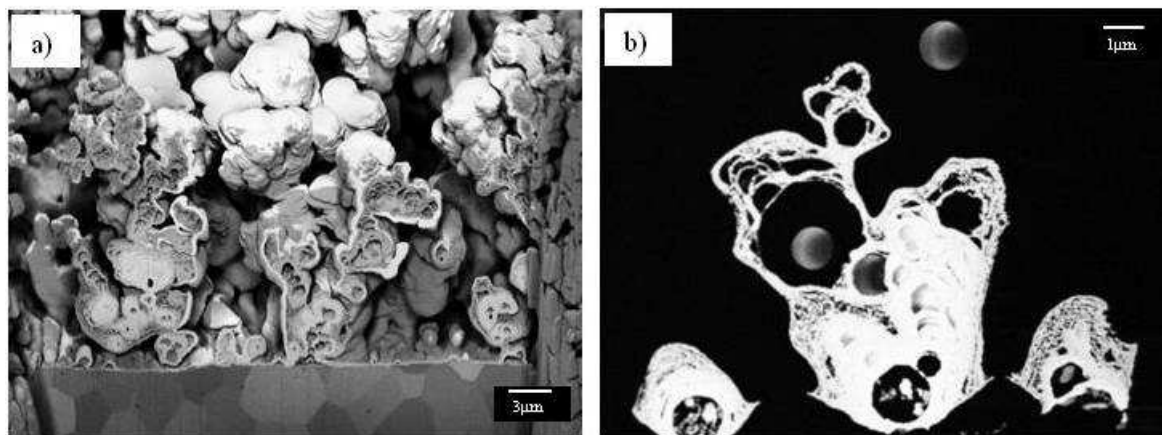


Fig. II-3. FIB-SEM pictures made on cross section of gradient CGO/LSCF films: CGO/LSCF layer with YSZ substrate with 40 nm pixel^{-1} size (a) and CGO/LSCF layer, sample mounted in epoxy resin with 20 nm pixel^{-1} size (b).

The CGO/LSCF gradient in composition was controlled by a progressive modification of the flow rates of precursor solutions during the deposition time [16] keeping constant the total flow rate of 1 mL.h^{-1} in order to get a similar average droplet size. Such configurations have provided continuous change of the composition in one layer, termed a graded CGO/LSCF composition. Fig. II-4 shows quantitative elemental analysis made through oxygen electrode layer cross section by EDS-SEM, starting from the LSCF surface and reaching YSZ pellet. Quantity of LSCF elements is decreased and quantity of CGO elements is increased while EDS analysis is reaching the substrate.

Moreover, providing with pure CGO precursor solution at the beginning of deposition, guarantees dense and very thin (100 nm) CGO film which is very important for two reasons. It plays a main role as a barrier diffusion layer against LSCF elements diffusion to YSZ avoiding chemical reactivity. Moreover, higher electrical performances can be achieved for porous LSCF electrodes when the electrolyte was first coated by a LSCF thin ($< 60 \text{ nm}$) and dense interlayer as reported by M. Prestat et al. [17]. LSCF interlayer was characterized by great diffusivity which was explained by many grain boundaries in the dense layer nanostructure [17].

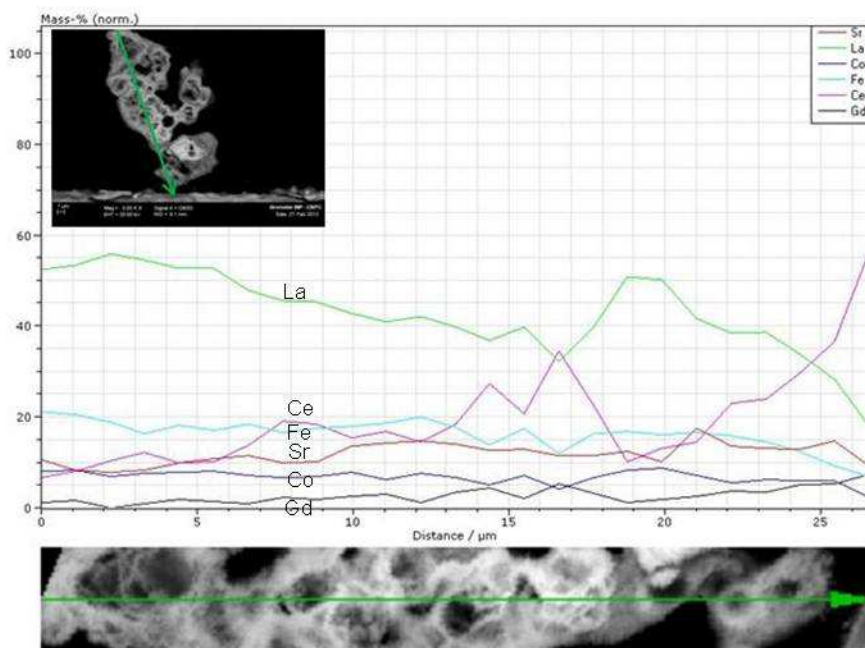


Fig. II-4. EDS-SEM quantitative analysis of graded CGO/LSCF films deposited on YSZ pellet for 3 h at 400 °C with a constant total flow rate of 1 mL.h⁻¹ and nozzle-to-substrate distance of 35 mm using ESD technique.

Profile line passing through the layer and especially through the corals is not a straight line. Decreasing of CGO and increasing of LSCF elements tendencies in the EDS result was mainly because of fact that corals do not grow in vertical order but grow according to the preferential landing. Different morphologies are obtained if complete solvent evaporation occurs during flight, in which case the solute particles precipitate into solid particles. Because the surface of these particles is charged, they are electrostatically attracted towards points in the substrate with higher curvatures. This effect is termed preferential landing and leads to the formation of branched structures resembling corals. This same coral growth mechanism has been published in zirconia coating focusing on the initial stages by ESD [18], [19]. Moreover, corals are hollow inside and EDS profile is not going through continuous materials leading to values with large incertitude.

As-deposited coatings were found amorphous. After sintering at 900 °C for 2 h in air [20], two CGO and YSZ crystalline phases have been detected by XRD (Fig. II-5). Additionally, neither secondary phases nor impurities were noticed. It was reported [10], [21]–[23] that perovskite $\text{La}_{1-x}\text{Sr}_x\text{Co}_{1-y}\text{Fe}_y$ (where x, y change from 0 to 1), structure can either be orthorhombic, cubic or rhombohedral. Even small differences in LSCF composition like $\text{La}_{0.75}\text{Sr}_{0.25}\text{Co}_{0.2}\text{Fe}_{0.8}\text{O}_{3-\delta}$ or $\text{La}_{0.46}\text{Sr}_{0.54}\text{Co}_{0.2}\text{Fe}_{0.8}\text{O}_{3-\delta}$ lead to changes of crystallization phase from orthorhombic to rhombohedral respectively [24].

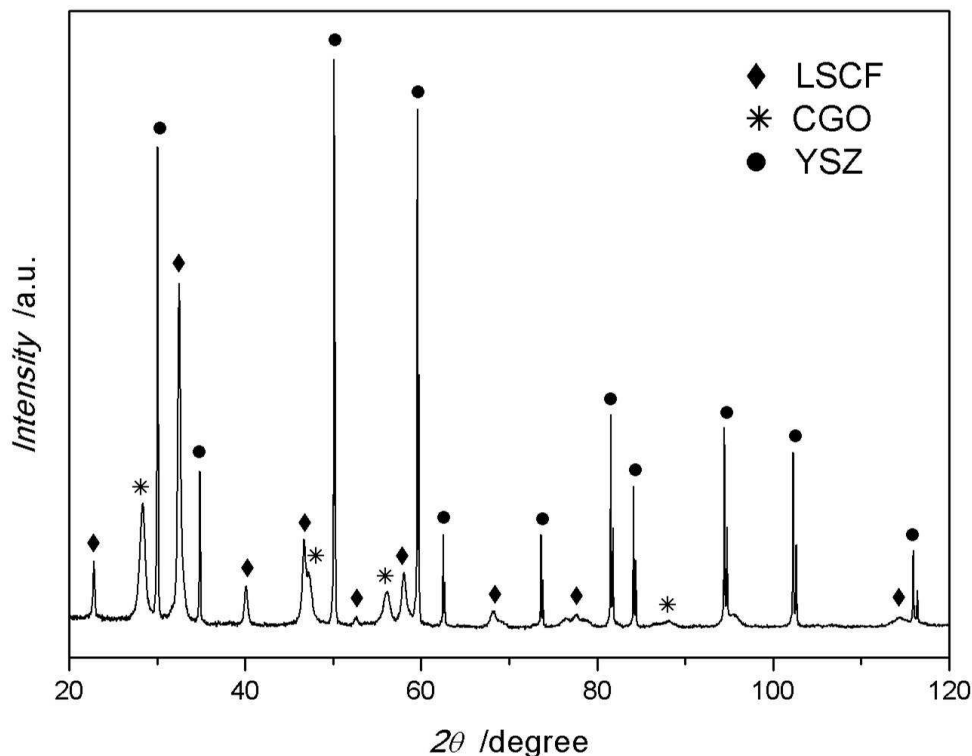


Fig. II-5. XRD pattern of a gradient CGO/LSCF layer deposited on YSZ by ESD; (•) YSZ, (*) CGO and (♦) LSCF.

II.4.2. Electrochemical characterization

Fig. II-6 shows electrode polarization resistance values in a range of 550 – 700 °C presented in Arrhenius plot. The activation energy, derived from Arrhenius equation, was found to be 1.31 eV what is in good agreement with E_a published for CGO/LSCF composite [25]–[32] and pure LSCF electrode [26], [27], [29], [33], [34].

Area specific resistance (ASR) value was equal to $66 \Omega \cdot \text{cm}^2$ at 600 °C (Fig. II-6). However, it is extremely difficult to make comparison of ASR to already reported values even if the stoichiometry of CGO and LSCF is the similar. One should be kept in mind, that preparation method, sintering temperature and duration have influence on the microstructure and thus on electrochemical performances. A concrete comparison can be made to the work of Marinha et al. [34] where oxygen electrode presents similar coral microstructure, but still ASR is $0.82 \Omega \cdot \text{cm}^2$ at 600 °C what is 80 times lower than the value presented in this work. Such great difference is hard to explain even keeping in mind that they did deposition of pure LSCF coating on CGO substrate with the electrode area of 0.5 cm^2 in comparison here to deposition of graded CGO/LSCF electrode on YSZ with the electrode area of 2.3 cm^2 . CGO ionic and LSCF electronic phases may not fully percolate in such fine nano-structuring. As an example, if some LSCF particles are completely embedded by CGO particles, a loss of percolation

should be expected. In such a case, some regions become electrochemically inactive within the electrode leading to an increase of the polarization resistance. One may also anticipate a loss of contact in between CGO and LSCF due to the presence of traces of additional phases not detectable experimentally. Specifically for coral microstructure the top part of the coating is rough. This roughness limits contact with current supplier therefore decreases current collecting. Electrochemical data did not show any additional resistance due the formation of an insulating phase such as $\text{La}_2\text{Zr}_2\text{O}_7$ and SrZrO_3 , what simply indicates that CGO barrier diffusion layer efficiently separate LSCF from YSZ.

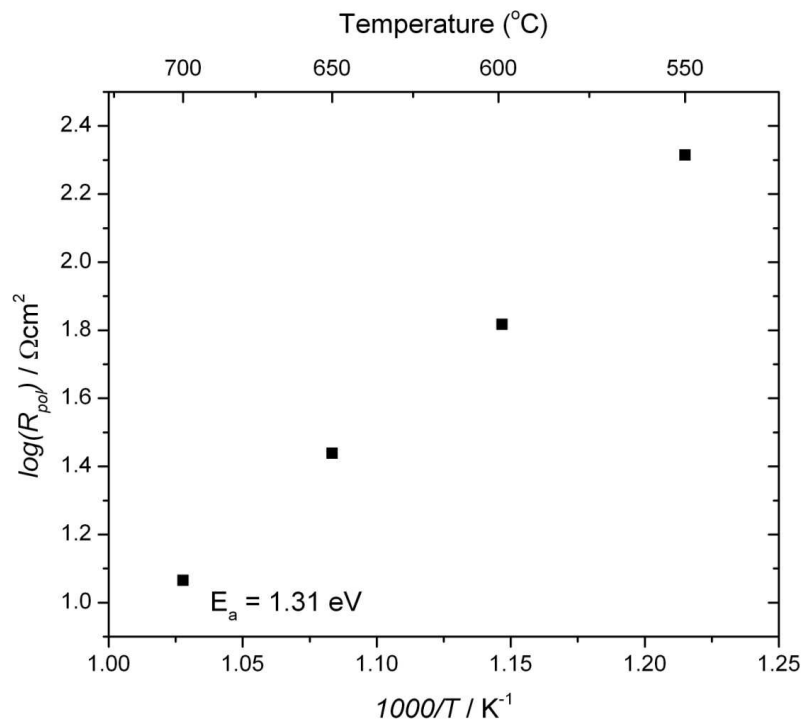


Fig. II-6. Electrode polarization resistances versus the reciprocal temperature.

II.5. Conclusions

This work demonstrates for the first time, that graded CGO/LSCF porous films were successfully deposited on YSZ substrate by electrostatic spray deposition to be used as oxygen electrode in intermediate temperature solid oxide fuel cells and solid oxide electrolyser cells. ESD is an interesting method to produce innovative porous electrode films with good reproducibility. A simultaneous gradient in composition was obtained by applying two precursor solutions (CGO and LSCF) with different flow rates in one unique coating. The combination of precursor solutions physico-chemical parameters with deposition conditions

has led to the obtaining of two scale porosities: nano-porous and micro-porous in so-called coral microstructure. The successful producing of coral microstructure with high surface area due to micro- and nanoporosity gives a positive expectation for optimizing electrochemical reactions and transport efficiency for the oxygen electrode purpose. No reactivity between LSCF and YSZ was detected by XRD after annealing at 900 °C for 2 h in air with the presence of CGO and LSCF phases in the electrode layer. 3D reconstruction based on FIB-SEM tomography and porosity computing is in progress to better understand the coral microstructure.

First electrochemical impedance spectroscopy results were presented in order to show the role of the chemical gradation in the electrical performances of this original porous CGO/LSCF electrode. ASR values are relatively high comparing to others works. Further electrochemical analysis is now in progress to improve electrode polarization resistance by printing additional LSCF current functional layer to unanimously decide the influence of graded composition.

Acknowledgement

The project is a part of International Doctoral School in Functional Materials for Energy, Information Technology, and Health in the framework of the European Programme ‘Erasmus Mundus II 2009-2013’. The work is financed by IDS-FunMat Consortium to perform a doctoral programme and entitled ‘*Interfaces and durability of advanced electrodes for energy (Solid Oxide Fuel Cells and Electrolysers)*’ – n°2011-08.

II.6. References

- [1] A. Hauch, S. H. Jensen, S. Ramousse, and M. Mogensen, “Performance and Durability of Solid Oxide Electrolysis Cells,” *J. Electrochem. Soc.*, vol. 153, no. 9, pp. 1741–1747, 2006.
- [2] J. W. Stevenson, I. Armstrong, R. D. Carneim, L. I. Pederson, and W. J. Weber, “Electrochemical Properties of Mixed Conducting Perovskites (M = Sr, Ba, Ca),” *J. Electrochem. Soc.*, vol. 143, no. 9, pp. 2722–2729, 1996.
- [3] L. W. Tai, M. M. Nasrallah, H. U. Andreson, D. M. Sparlin, and S. R. Sehlin, “Structure and electrical properties of $\text{La}_{1-x}\text{Sr}_x\text{Co}_{1-y}\text{Fe}_y\text{O}_3$. Part 2. The system $\text{La}_{1-x}\text{Sr}_x\text{Co}_{0.2}\text{Fe}_{0.803}$,” *Solid State Ionics*, vol. 2738, no. 94, pp. 273–283, 1995.
- [4] Y. Teraoka, H. M. Zhang, K. Okamoto, and N. Yamazoe, “Mixed ionic-electronic conductivity of $\text{La}_{1-x}\text{Sr}_x\text{Co}_{1-y}\text{Fe}_y\text{O}_{3-\delta}$ perovskite-type oxides,” *Mater. Res. Bull.*, vol. 23, no. 1, pp. 51–58, 1988.
- [5] G. C. Kostogloudis, G. Tsiniarakis, and C. Ftikos, “Chemical reactivity of perovskite oxide SOFC cathodes and yttria stabilized zirconia,” *Solid State Ionics*, vol. 135, pp. 529–535, 2000.
- [6] S. Uhlenbruck, T. Moskalewicz, N. Jordan, H.-J. Penkalla, and H. P. Buchkremer, “Element interdiffusion at electrolyte–cathode interfaces in ceramic high-temperature fuel cells,” *Solid State Ionics*, vol. 180, no. 4–5, pp. 418–423, 2009.
- [7] T. Nguyen, K. Kobayashi, T. Honda, Y. Iimura, K. Kato, a Neghisi, K. Nozaki, F. Tappero, K. Sasaki, and H. Shirahama, “Preparation and evaluation of doped ceria interlayer on supported stabilized zirconia electrolyte SOFCs by wet ceramic processes,” *Solid State Ionics*, vol. 174, no. 1–4, pp. 163–174, 2004.
- [8] E. Ruiz-Trejo, J. D. Sirman, Y. M. Baikov, and J. A. Kilner, “Oxygen ion diffusivity, surface exchange and ionic conductivity in single crystal Gadolinia doped Ceria,” *Solid State Ionics*, vol. 113–115, pp. 565–569, 1998.

- [9] V. V. Kharton, F. M. Figueiredo, L. Navarro, E. N. Naumovich, A. V. Kovalevsky, A. A. Yaremchenko, A. P. Viskup, A. Carneiro, F. M. B. Marques, and J. R. Frade, “Cerium-based materials for solid oxide fuel cells,” *J. Mater. Sci.*, vol. 36, pp. 1105–1117, 2001.
- [10] L. Tai, M. M. Nasrallah, H. U. Anderson, D. M. Sparlin, and S. R. Sehlin, “Structure and electrical properties of $\text{La}_{1-x}\text{Sr}_x\text{Co}_{1-y}\text{Fe}_y\text{O}_3$. Part 1. The system $\text{La}_{0.8}\text{Sr}_{0.2}\text{Co}_{1-y}\text{Fe}_y\text{O}_3$,” *Solid State Ionics*, vol. 76, no. 3–4, pp. 259–271, 1995.
- [11] F. Tietz, “Thermal Expansion of SOFC Materials,” *Ionics (Kiel)*, vol. 5, pp. 129–139, 1999.
- [12] B. Kenney and K. Karan, “Engineering of microstructure and design of a planar porous composite SOFC cathode: A numerical analysis,” *Solid State Ionics*, vol. 178, no. 3–4, pp. 297–306, Feb. 2007.
- [13] D. Marinha, C. Rossignol, and E. Djurado, “Influence of electrospraying parameters on the microstructure of $\text{La}_{0.6}\text{Sr}_{0.4}\text{Co}_{0.2}\text{Fe}_{0.8}\text{O}_{3-\delta}$ films for SOFCs,” *J. Solid State Chem.*, vol. 182, no. 7, pp. 1742–1748, 2009.
- [14] A. M. Gañan-Calvo, J. Davila, and A. Barrero, “Current and droplet size in the Electrospraying of Liquids. Scaling laws,” *J. Aerosol Sci.*, vol. 28, no. 2, pp. 249–275, 1997.
- [15] C. Rossignol, B. Roman, G. D. Benetti, and E. Djurado, “Elaboration of thin and dense CGO films adherent to YSZ by electrostatic spray deposition for IT-SOFC applications,” *New J. Chem.*, vol. 35, no. 3, pp. 716–723, 2011.
- [16] A. Princivalle and E. Djurado, “Nanostructured LSM/YSZ composite cathodes for IT-SOFC: A comprehensive microstructural study by electrostatic spray deposition,” *Solid State Ionics*, vol. 179, no. 33–34, pp. 1921–1928, 2008.
- [17] M. Prestat, A. Infortuna, S. Korrodi, S. Rey-Mermet, P. Muralt, and L. J. Gauckler, “Oxygen reduction at thin dense $\text{La}_{0.52}\text{Sr}_{0.48}\text{Co}_{0.18}\text{Fe}_{0.82}\text{O}_{3-\delta}$ electrodes. Part II: Experimental assessment of the reaction kinetics,” *J. Electroceramics*, vol. 18, no. 1–2, pp. 111–120, 2007.

- [18] R. Neagu, D. Perednis, and E. Djurado, “Initial Stages in Zirconia Coatings Using ESD,” *Chem. Mater.*, vol. 17, no. 4, pp. 902–910, 2005.
- [19] C. Chen, E. M. Kelder, J. J. M. van der Put, and J. Schoonman, “Morphology control of thin LiCoO₂ films fabricated using the electrostatic spray deposition (ESD) technique,” *J. Mater. Chem.*, vol. 6, no. 5, pp. 765–771, 1996.
- [20] A. Muchtar, N. a. Hamid, N. Muhamad, and W. R. W. Daud, “Sintering Effects on LSCF Cathodes for Intermediate Temperature Solid Oxide Fuel Cells (IT-SOFCs),” *Adv. Mater. Res.*, vol. 139–141, no. 3, pp. 141–144, 2010.
- [21] S. Hashimoto, Y. Fukuda, M. Kuhn, K. Sato, K. Yashiro, and J. Mizusaki, “Oxygen nonstoichiometry and thermo-chemical stability of La_{0.6}Sr_{0.4}Co_{1-y}Fe_yO_{3-δ} (y=0.2, 0.4, 0.6, 0.8),” *Solid State Ionics*, vol. 181, no. 37–38, pp. 1713–1719, 2010.
- [22] H. Kruidhof, H. J. M. Bouwmeester, R. H. E. Doorn, and A. J. Burggraaf, “Influence of order-disorder transitions on oxygen permeability through selected nonstoichiometric perovskite-type oxides,” *Solid State Ionics*, vol. 63–65, pp. 816–822, 1993.
- [23] F. Prado, N. Grunbaum, A. Caneiro, and A. Manthiram, “Effect of La³⁺ doping on the perovskite-to-brownmillerite transformation in Sr_{1-x}La_xCo_{0.8}Fe_{0.2}O_{3-δ} (0 ≤ x ≤ 0.4),” *Solid State Ionics*, vol. 167, no. 1–2, pp. 147–154, 2004.
- [24] Y. J. Gu, Z. N. Yang, Y. B. Chen, H. Q. Liu, H. K. Wu, L. Chen, M. Wang, L. L. Zuo, X. W. Huang, X. B. Liu, W. G. Wei, C. Lu, Y. Hu, Z. Guo, and Z. W. Hu, “Structural Analysis of Multiphase La_{1-x}Sr_xCo_{1-x}Fe_xO_{3-δ},” *Adv. Mater. Res.*, vol. 177, pp. 74–77, 2011.
- [25] B. F. Angoua and E. B. Slamovich, “Single solution spray pyrolysis of La_{0.6}Sr_{0.4}Co_{0.2}Fe_{0.8}O_{3-δ} – Ce_{0.8}Gd_{0.2}O_{1.9} (LSCF–CGO) thin film cathodes,” *Solid State Ionics*, vol. 212, pp. 10–17, 2012.
- [26] D. Beckel, U. Muecke, T. Gyger, G. Florey, a Infortuna, and L. Gauckler, “Electrochemical performance of LSCF based thin film cathodes prepared by spray pyrolysis,” *Solid State Ionics*, vol. 178, no. 5–6, pp. 407–415, 2007.

- [27] V. Dusastre and J. A. Kilner, “Optimisation of composite cathodes for intermediate temperature SOFC applications,” *Solid State Ionics*, vol. 126, pp. 163–174, 1999.
- [28] Y. Leng, S. Chan, and Q. Liu, “Development of LSCF–GDC composite cathodes for low-temperature solid oxide fuel cells with thin film GDC electrolyte,” *Int. J. Hydrogen Energy*, vol. 33, no. 14, pp. 3808–3817, 2008.
- [29] E. P. Murray, M. J. Sever, and S. A. Barnett, “Electrochemical performance of (La,Sr)(Co,Fe)O₃–(Ce,Gd)O₃ composite cathodes,” *Solid State Ionics*, vol. 148, pp. 27–34, 2002.
- [30] J. Nielsen, T. Jacobsen, and M. Wandel, “Impedance of porous IT-SOFC LSCF:CGO composite cathodes,” *Electrochim. Acta*, vol. 56, no. 23, pp. 7963–7974, 2011.
- [31] S. Wang, T. Kato, S. Nagata, T. Kaneko, N. Iwashita, T. Honda, and M. Dokiya, “Electrodes and performance analysis of a ceria electrolyte SOFC,” *Solid State Ionics*, vol. 153, pp. 477–484, 2002.
- [32] W. Wang and M. Mogensen, “High-performance lanthanum-ferrite-based cathode for SOFC,” *Solid State Ionics*, vol. 176, no. 5–6, pp. 457–462, 2005.
- [33] C.-S. Hsu and B.-H. Hwang, “Microstructure and Properties of the La_{0.6}Sr_{0.4}Co_{0.2}Fe_{0.8}O₃ Cathodes Prepared by Electrostatic-Assisted Ultrasonic Spray Pyrolysis Method,” *J. Electrochem. Soc.*, vol. 153, no. 8, pp. A1478–A1483, 2006.
- [34] D. Marinha, L. Dessemond, J. S. Cronin, J. R. Wilson, S. a. Barnett, and E. Djurado, “Microstructural 3D Reconstruction and Performance Evaluation of LSCF Cathodes Obtained by Electrostatic Spray Deposition,” *Chem. Mater.*, vol. 23, no. 24, pp. 5340–5348, 2011.

III. Electrochemical properties of graded and homogeneous CGO-LSCF composite electrodes for IT-SOFC

Electrochemical properties of graded and homogeneous CGO-LSCF composite electrodes for IT-SOFC

Jarosław Sar^{1,2}, Laurent Dessemond^{1,2}, Elisabeth Djurado^{1,2*}

¹ Univ. Grenoble Alpes, LEPMI, F-38000 Grenoble France

² CNRS, LEPMI, F-38000 Grenoble France

**Elisabeth.Djurado@lepmi.grenoble-inp.fr*

III.1. Abstract

Graded and homogeneous CGO-LSCF composite electrodes deposited by Electrostatic Spray Deposition on YSZ substrate were studied with and without screen-printed LSCF current collector. Impedance spectroscopy measurements were performed in air at open circuit potential at temperature range of 450 to 700 °C and during isothermal treatments at 600 °C for 200 h and at 800 °C for 12 h to estimate the relevance of such oxygen electrode for intermediate temperature solid oxide fuel cells (IT-SOFCs). A thin and dense CGO layer was firstly deposited to avoid any chemical reaction between LSCF and YSZ. No significant increase of the polarization resistance was evidenced during isothermal test at 600 °C for 200 h, proving a good stability of the electrode. Using a LSCF current collector layer (CCL) the polarization resistance decreased by 1.5 order of magnitude compared to samples with single cathode functional layer (CFL). The electrochemical results did not unanimously indicate which composition presents lower polarization effects.

Keywords: IT-SOFC, CGO-LSCF, Composite electrode, Electrostatic spray deposition, Impedance spectroscopy.

III.2. Introduction

The global research is focused on finding cheap and clean energy. Solid oxide fuel cell (SOFC) is a promising technology for production of pure electric energy with zero CO₂ emissions. However, working at temperature of 1000 °C yields high costs for the application and decreases the life span. The great opportunity comes with so called intermediate temperature SOFC (IT-SOFC) operating below 700 °C. The most common electrode

materials are LSM-YSZ composite and Ni-YSZ cermet and are not suitable at intermediate temperatures range due to increased overpotentials and high electrolyte ohmic losses. $\text{La}_{0.6}\text{Sr}_{0.4}\text{Co}_{0.2}\text{Fe}_{0.8}\text{O}_{3-\delta}$ (LSCF) can successfully replace LSM as a cathode material in IT-SOFCs. Moreover, undesirable reaction between LSCF and YSZ [1]–[4] can be eliminated by insertion of a dense $\text{Ce}_{0.9}\text{Gd}_{0.1}\text{O}_{2-\delta}$ (CGO) barrier diffusion layer [5]–[7]. CGO is chemically compatible and mechanically with LSCF and YSZ because of close thermal expansion coefficients [8]–[10] at the intermediate temperature. The electrode based on CGO-LSCF composite, presents mixed ionic-electronic conductivity together with catalytic properties from LSCF and enlarged ionic conductivity by CGO.

The other issue influencing the SOFC performances is the electrode microstructure. Electrostatic spray deposition (ESD) is a cheap and versatile technique to create dense or porous coatings with a good adhesion to the substrate. In general, precursor solution is atomized to a spray when the high voltage is set between the nozzle with precursor solution and the heated substrate. Droplets inside the spray dry during the flight and create solid coating on the grounded substrate. Deposition is controlled by process parameters (nozzle-to-substrate distance, deposition time, substrate temperature, solution flow rate) and the precursor solution physico-chemical properties (boiling point, conductivity, surface tension, etc...). Deposition is performed at relatively low temperature (300 – 400 °C) combined with post-annealing at temperatures lower than 1000 °C.

This work describes preparation and electrochemical characterization of composite electrodes built of $\text{Ce}_{0.9}\text{Gd}_{0.1}\text{O}_{2-\delta}$ (CGO) and $\text{La}_{0.6}\text{Sr}_{0.4}\text{Co}_{0.2}\text{Fe}_{0.8}\text{O}_{3-\delta}$ (LSCF) with a coral microstructure (high porosity for gas access) deposited on 8 mol.% $\text{Y}_2\text{O}_3\text{-ZrO}_2$ (YSZ) pellet by ESD. A thin and dense CGO layer was firstly deposited on YSZ in order to separate LSCF and YSZ. Homogeneous and graded compositions of CGO-LSCF mixture throughout composite electrodes were studied in order to see the interest of CGO insertion on the performances. Moreover, the relevance of screen printed LSCF current collector onto coral microstructure was also investigated.

III.3. Experimental

III.3.1. Oxygen electrode preparation

Two types of electrode were investigated: 1) single-layered: CGO-LSCF composite as a cathode functional layer (CFL) without any current collector layer, 2) double-layered: CGO-LSCF composite as a CFL and a screen-printed LSCF current collector layer (CCL).

III.3.1.1. Cathode functional layer

Coral CGO-LSCF composites were deposited on homemade YSZ disk shaped substrates, 19 mm in diameter and 1 mm thick. Dense electrolyte pellets were polished to provide smooth and uniform surface before the deposition. LSCF and CGO solution were prepared with a total salt concentration of 0.02 mol.L⁻¹. The precursor solution of LSCF consisted of lanthanum nitrate hexahydrate (La(NO₃)₃·6H₂O, Rectapur Prolabo, 99.5 %), strontium chloride hexahydrate (SrCl₂·6H₂O, Strem Chemicals, 99 %), cobalt nitrate hexahydrate (Co(NO₃)₂·6H₂O, Merck, 99 %) and iron (III) nitrate nonahydrate (Fe(NO₃)₃·9H₂O, Sigma Aldrich, 99.99 %), weighted to achieve proper stoichiometry of La_{0.6}Sr_{0.4}Co_{0.2}Fe_{0.8}O_{3-δ} solution. The precursor solution of Ce_{0.9}Gd_{0.1}O_{1.95} was based on cerium nitrate hexahydrate (Ce(NO₃)₃·6H₂O, Rectapur Prolabo, 99.5 %) and gadolinium nitrate (Gd(NO₃)₂, Aldrich, 99.99 %). Salts were dissolved in distilled water and ethanol (C₂H₅OH, Sigma-Aldrich, 99.8 %) in a 5:1 volume ratio to create LSCF precursor solution, and in diethylene glycol monobutyl ether (butyl carbitol (CH₃(CH₂)₃(OC₂H₂)₂OH, Acros Organics, 99 %) and ethanol in a 4:1 volume ratio to create CGO precursor solution.

Depositions by ESD were carried out in air at a 35 mm nozzle-to-substrate distance (Table III-1) by using two syringes pumps (Sage M361) with separated pipes to simultaneously provide two precursor solutions. Thus, graded and homogeneous CGO-LSCF composite electrodes were prepared. The deposition procedure consisted of two successive steps: 1) deposition of a thin CGO buffer layer, 2) deposition of CGO and LSCF. A graded composition was deposited by varying the flow rate of LSCF precursor solution from 0 to 1 mL.h⁻¹ (Q_{LSCF}), while the flow rate of CGO was varied from 1 to 0 mL.h⁻¹ (Q_{CGO}). Flow rates were changed with 0.1 mL.h⁻¹ step in every 15 min (Table III-2).

Table III-1. ESD deposition parameters.

T (°C)	d (mm)	Q_{total} (mLh⁻¹)	t (h)	V (kV)
400	35	1	3	7-11

A homogeneous composition was deposited by keeping flow rates of CGO and LSCF precursor solutions equal to 0.5 mL.h⁻¹, e.g. a total flow rate equal to 1 mL.h⁻¹ (Table III-2). The substrate temperature was kept stable at 400 °C, calibrated before the deposition by K-type thermocouple. A positive high voltage applied during the deposition ranged from 7 to 11 kV. Layer was deposited in a disk shape with a diameter of ~ 17 mm. After the deposition, all

CGO-LSCF electrodes were annealed at 900 °C for 2 h with a heating/cooling rate of 3 °C.min⁻¹ in air.

Table III-2. Variation of the solutions flow rates during deposition to create graded composition [11].

$Q_{CGO} / \text{mL.h}^{-1}$	1	0.9	0.8	0.7	0.6	0.5	0.4	0.3	0.2	0.1	0
$Q_{LSCF} / \text{mL.h}^{-1}$	0	0.1	0.2	0.3	0.4	0.5	0.6	0.7	0.8	0.9	1
CGO / mol %	100	90	80	70	60	50	40	30	20	10	0
Progressive time / h	0.25	0.5	0.75	1	1.25	1.5	1.75	2	2.25	2.5	3

III.3.1.2. Current collector layer

Current collector layers were screen printed either at Ecole Nationale Supérieure des Mines de Saint-Etienne (ENSMSE) in France and or at Karlsruhe Institute of Technology (KIT) in Germany, respectively. Thus, the samples will be referenced hereafter by ENSMSE or KIT. Samples referred to as LEPMI presented CGO-LSCF coral microstructure without current collector layer.

The CCLs from ENSMSE were circular with a diameter of ~ 17 mm accurately matched to the coral structure. For these samples, the screen printing was carried out only on one face of the YSZ pellet. Four successive printings, each dried for 15 min at 115 °C in air, were performed to achieve a total current collector thickness of 45 µm. Then, the CCLs were heated up at high temperature in air to sinter the layer and remove binders from the layer. To completely debind organic components, a heating rate was 0.5 °C.min⁻¹ up to 600 °C, after this stage a heating up to 900 °C was performed with a rate of 3.0 °C.min⁻¹ and followed by a final cooling to the room temperature at 3.0 °C.min⁻¹. The CCLs from KIT were screen printed in both faces of the electrolyte substrate with 10 x 10 mm² area. The printed layer thickness was 45 µm. After printing, samples were dried at 60 °C for 12 h and then kept at 300 °C for an hour in order to burn out the binder.

III.3.2. Microstructural characterization

Microstructure morphology was observed using scanning electron microscopy with field emission guns, FEG-SEM, (ZEISS Ultra 55). A platinum layer was deposited on each sample to avoid charging of observed area. Surface and cross sections of single and doubled layer electrodes were observed before and after electrochemical measurements.

III.3.3. Electrochemical characterization

Impedance Spectroscopy was used to characterize CGO-LSCF composite electrodes in air. The sample configurations are showed on Fig. III-1.

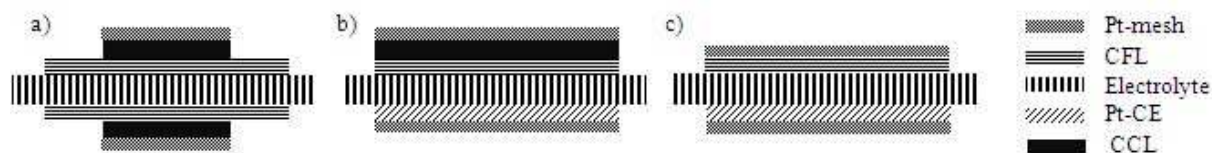


Fig. III-1. Sample configurations: a) symmetrical for KIT samples, b) ENSMSE sample and c) for LEPMI samples.

The upper part of the electrode was connected with a platinum mesh (Heraeus, mesh 3600) of accurate size as a function of the sample ($10 \times 10 \text{ mm}^2$ or 17 mm in diameter) (Fig. III-1). Considering the symmetrical cells from KIT, impedance measurements were performed in a two-electrode configuration. The electrical characterization of samples from ENSMSE was carried out in a three-electrode configuration, using CGO-LSCF composites as the working electrode (WE). Platinum paste (Metalor) was painted symmetrically opposite to the WE to serve as the counter electrode (CE). The reference electrode was painted as a ring around the YSZ pellet. Platinum paste was annealed at 800 °C for 1 h in air. Similar measurements were performed on single-layered CGO-LSCF composite electrodes (referenced as LEPMI) to study the effect of the LSCF current collector on the recorded responses (Fig. III-1). Same surface areas from WE and CE were chosen to improve the reliability of impedance measurements. The electrochemical response of CGO-LSCF composite electrodes was investigated in air between 450 and 800 °C at open circuit potential (OCP) using a Solartron potentiostat/galvanostat frequency response analyzer (SI 1280B) within a frequency range of 0.01 Hz to 20 kHz and between 250 and 650 °C at OCP using a Hewlett Packard Impedance Analyser (4192A) with a frequency range of 5 Hz to 13 MHz. The magnitude of the AC signal was chosen lower than 50 mV to ensure the linearity of the recorded responses. The isothermal stability tests were carried out at 600 °C for 200 h and at 800 °C for 12 h in air, respectively.

III.4. Results and discussion

III.4.1. Microstructure

The ESD parameters were chosen in order to create highly porous microstructure called coral microstructure previously studied for single layered LSCF electrode [11], [12]. The deposition parameters were used to enlarge the solvent evaporation processes during the droplet flight by increasing nozzle-to-substrate distance and the substrate temperature while lowering the precursor solution flow rate in order to yield smaller droplets drying faster. Droplets are electrostatically attracted by the closest curvatures on the substrate surface or on already deposited particles. This process is called preferential landing [13]. Finally, accumulation of the material on the YSZ pellet generates porous structure presented in Fig. III-2. Thickness varies from 15 to 25 μm . High magnification pictures (Fig. III-2b and d) showed nanoscale porosity on the corals surface. Detailed information of the coral microstructure with graded CGO-LSCF composition can be found elsewhere [11].

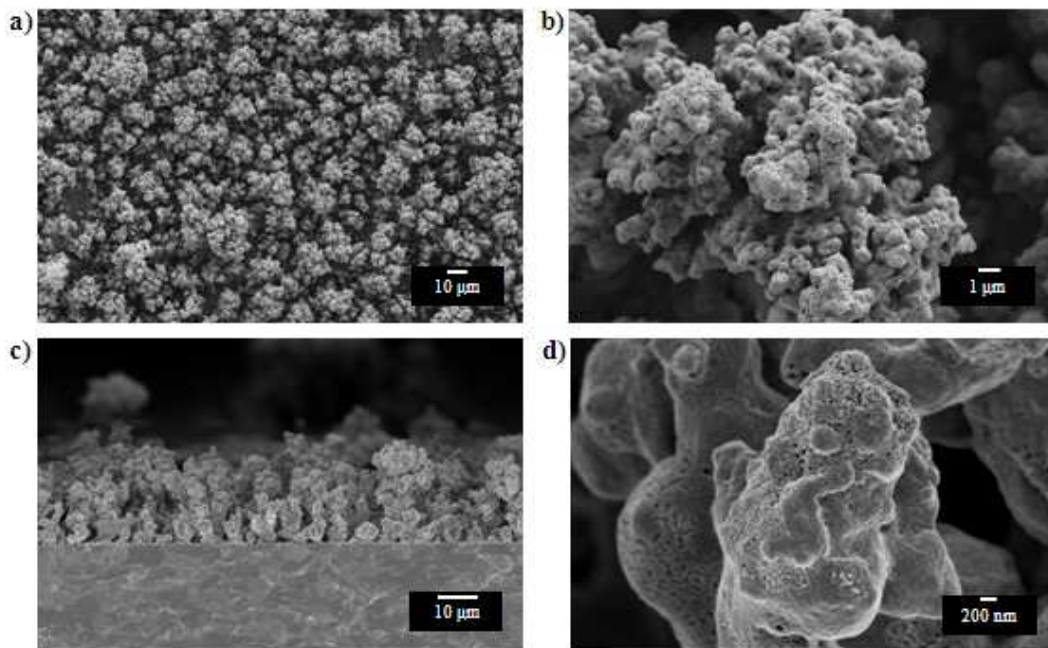


Fig. III-2. Pictures of CGO-LSCF coral microstructure sample before electrochemical characterization, a), b) surface views and c), d) cross section views [11].

A good contact between CFL and CCL was observed using FEG-SEM. The CCL surface is much flatter than coral. Fig. III-3 shows the interface between a coral CGO-LSCF layer and a current collector layer screen printed in ENSMSE and KIT. It can be observed that CCL penetrates through the coral microstructure. However, there is still some gap providing active

zones for oxygen transport. Depending on the spot, the thickness of the functional layer is ranging from 5 to 10 μm . The top part of corals is fully penetrated and consequently, it is hard to recognize elements of corals.

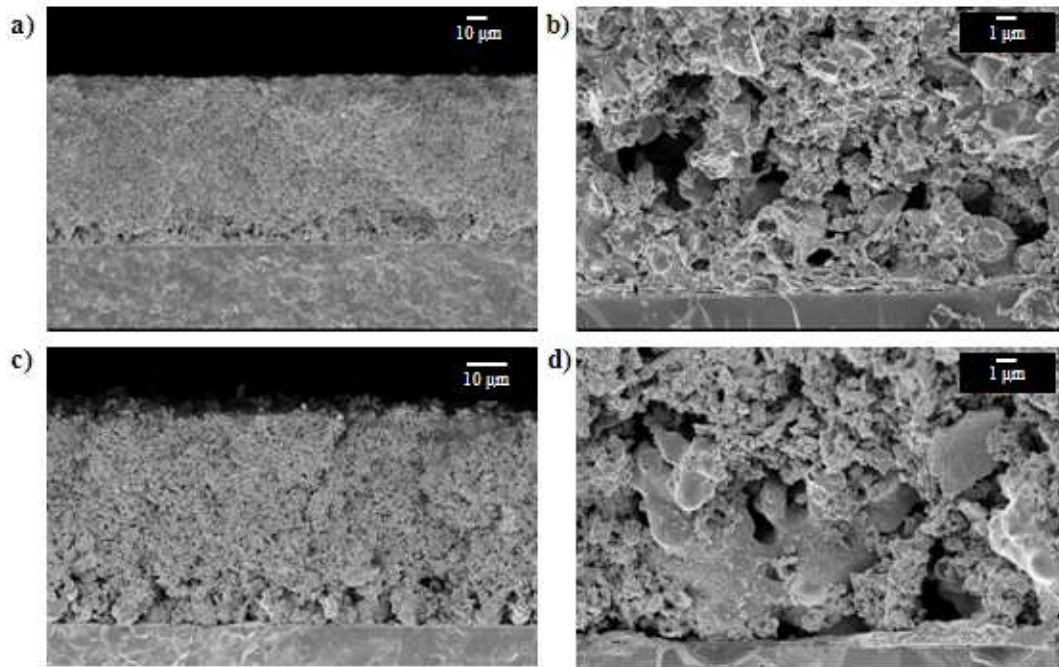


Fig. III-3. Cross section pictures showing coral CGO-LSCF layer with LSCF current collector layer screen printed in a), b) ENSMSE, c), d) KIT.

III.4.2. Electrochemical Characterization

III.4.2.1. Series resistance

Regardless of the sample configuration (Fig. III-1), one can deduce the electric response of YSZ grains and internal interfaces from impedance measurements performed below 450 °C in a two-electrode configuration between WE and CE. In the chosen experimental conditions, the impedance diagram is always composed of two contributions referenced as HF and LF for high and low frequencies, respectively. As shown in Fig. III-4, the apex frequencies of both contributions belong to two well separated families. The capacitance of the HF contribution ranges between 2×10^{-11} and 1×10^{-10} $\text{F}\cdot\text{cm}^{-2}$ and the capacitance of the LF response varies between 8×10^{-9} and 2×10^{-7} $\text{F}\cdot\text{cm}^{-2}$. At this stage, the HF contribution can be related to the ionic transport within YSZ grains. The LF contribution represents the blocking effect of charge carriers at grain boundaries in polycrystalline YSZ and at internal interfaces.

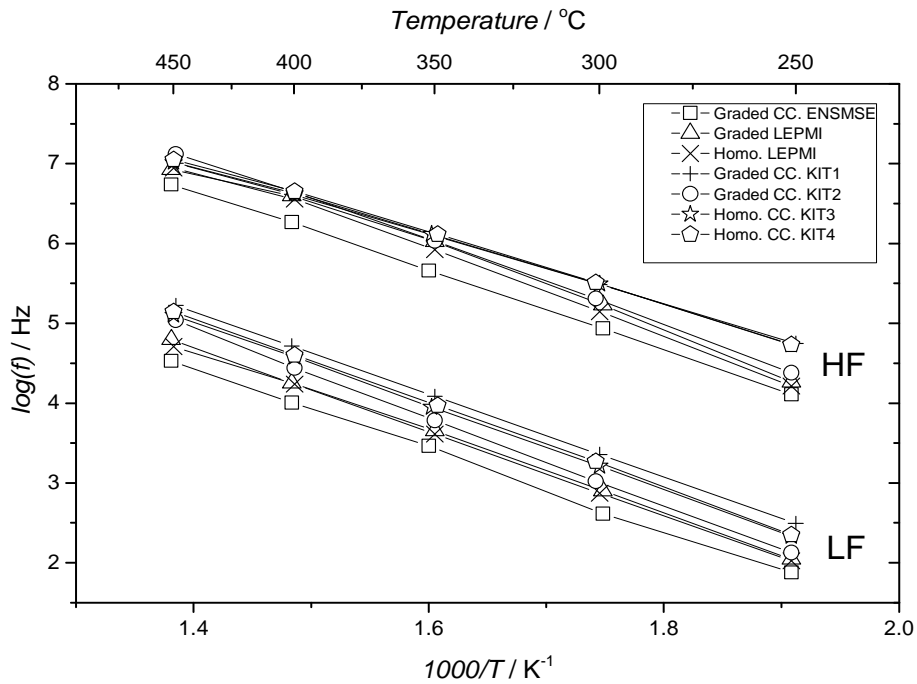


Fig. III-4. Arrhenius plots of the apex frequencies for HF and LF contributions.

Between 250 and 450 °C, the activation energy of the total conductivity (which is proportional to the opposite of the series resistance R_s), calculated from linear dependencies in Arrhenius plots (Fig. III-5) varies from 0.78 to 1.01 eV, in agreement with literature data [14]-[16]. The recorded variations on total conductivity are not mainly due to microstructure differences in sintered pellets since these pellets were elaborated from the same batch of powder. These variations are likely to originate from heterogeneous distributions of current lines [17] and cannot be related to poor contacts between the platinum grid and LSCF current collector [18]. Indeed, if one refers to the flatness of the CCL (Fig. III-3) and the roughness of the CFL (Fig. III-2), one could anticipate a high contact area between the platinum grid and current collector, and thus a more homogeneous distribution of current lines throughout the CFL. The higher conductivity values recorded for graded electrodes (samples ENSMSE and KIT2) support this assumption. Nevertheless, some values deduced from measurements performed with a screen printed LSCF layer (samples KIT1 and KIT4, for instance) are nearly similar to those recorded without any CCL (samples LEPMI). At this stage, the differences are likely to be due to constriction of current lines at the electrode/electrolyte interface or at internal interfaces between CGO and LSCF [19].

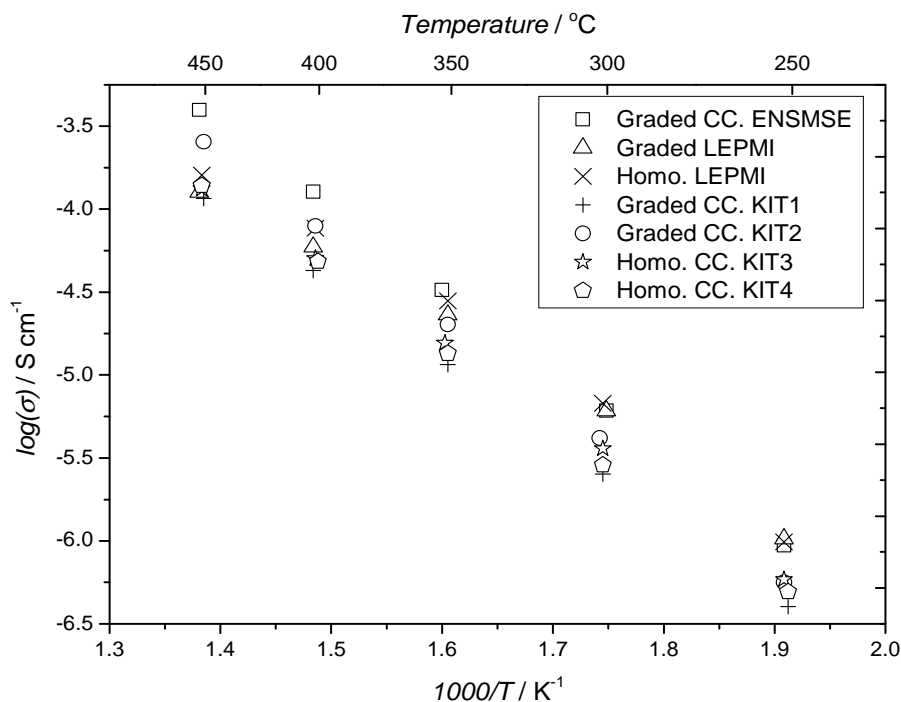


Fig. III-5. Arrhenius plots of the total conductivity.

III.4.2.2. Polarization resistance

Fig. III-6 shows Arrhenius plots of the polarization resistance R_{pol} for all electrodes. By assuming a linear dependence of R_{pol} versus the reciprocal temperature, one can calculate the corresponding activation energy. Between 450 and 700 °C, the activation energy varies between 1.1 and 1.4 eV. These values are in the range of those reported for pure LSCF [20]-[24] and CGO-LSCF composites [25]-[29]. The first peculiar feature is that adding a LSCF screen printed CCL significantly improves the electrochemical performances of coral functional layer. For instance, the polarization resistance of graded and homogeneous CGO-LSCF composite electrodes decreases by a factor of 20 and 60 at 600 °C, respectively, which agrees with the results of a previous study [30]. This result indicates that the electrochemical active area of the CFL is enlarged by using an appropriate current collector, yielding a more homogeneous distribution of current lines in the LSCF-based electrode. Another peculiar feature is that grading of the composition in the CFL does not significantly improve the polarization resistance for a given current collector. For all KIT samples, R_{pol} varies between 1.3 and 2.3 $\Omega \cdot \text{cm}^2$ at 600 °C (Fig. III-6). For a graded CGO-LSCF electrode, R_{pol} is slightly lower when using a CCL printed in KIT. This could be related to the more porous morphology of the layer yielding a better access for the gas phase to the active sites (Fig. III-3).

It is worth noting that such resistance values are close to some previously reported in the literature [20],[25],[26] but do not correspond to the lowest ones for CGO-LSCF composite electrodes [21],[27],[29]. But one must keep in mind that comparison with literature data is rather complicated because of different electrode microstructures and particle sizes. Nevertheless, the lowest as-measured R_{pol} is twice higher than that recorded for a pure LSCF coral electrode, deposited by ESD on a CGO pellet, using a CCL printed in KIT ($0.6 \Omega \cdot \text{cm}^2$ at $600 \text{ }^\circ\text{C}$) [30]. At this stage, the origin of the recorded difference remains still unclear. This could be due to low contacts between CGO and LSCF particles in the electrode volume.

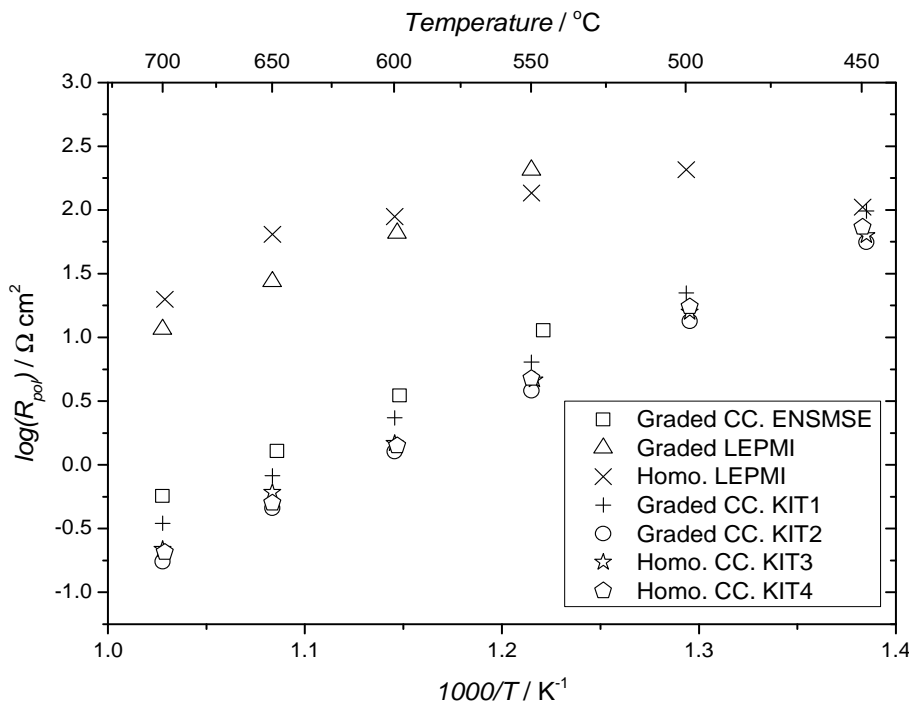


Fig. III-6. Arrhenius plots of the polarization resistance.

III.4.2.3. Isothermal agings

In order to check the stability of investigated electrodes, both series and polarization resistance were recorded during isothermal tests at $600 \text{ }^\circ\text{C}$ for 200 h in air. The corresponding results are shown in Fig. III-7. No significant variation of the series resistance R_s was recorded within the experimental accuracy. R_s varies only between 1 and 6 % after 200 h. This suggests that internal interfaces are not altered in the chosen experimental conditions. This also indicates the effectiveness of the CGO interlayer deposited on YSZ before depositing CGO-LSCF composites. The polarization resistance of a graded electrode from

ENSMSE increases by 27 % for 200 h (Fig. III-7). Since R_{pol} remains nearly unchanged for the sample without any CCL, the recorded increase is not likely to be due to any degradation of the CFL microstructure. For samples from KIT, the highest increase is only of 5 % for a graded electrode while the polarization resistance even decreases for homogeneous electrodes (up to 39 % after 200 h). A similar monotonic decrease of R_{pol} was reported by Marinha et al. [30] for a pure coral LSCF electrode at 600 °C during 140 h in air. The decrease of the polarization resistance can be explained by a partial sintering between CFL and CCL during isothermal ageing.

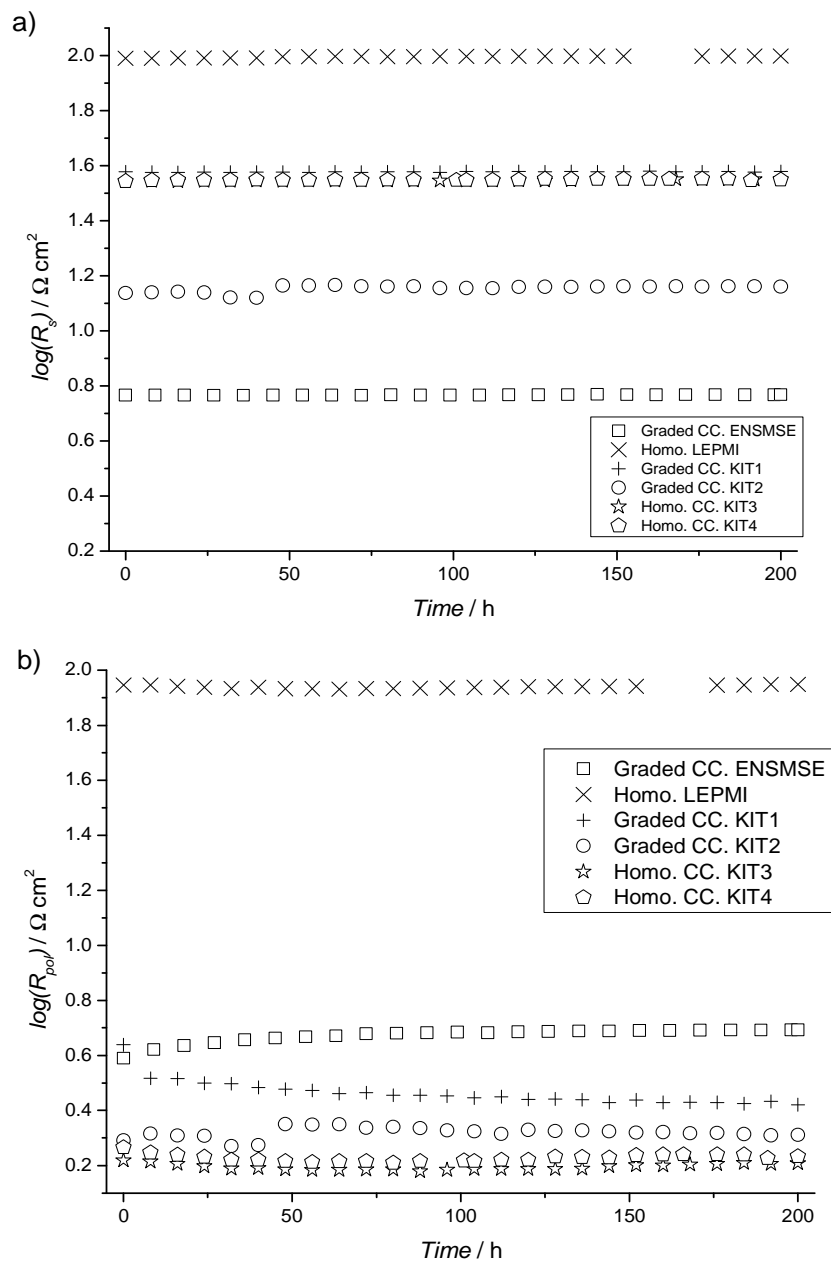


Fig. III-7. a) Series resistance and b) polarization resistance versus ageing time at 600 °C in air.

To go further in the characterization of the stability of composite electrodes, a subsequent annealing at 800 °C for 12 h in air was performed after isothermal ageing at 600 °C. This was carried out only for two electrodes (Fig. III-8). In agreement with the responses at 600 °C, the series resistance is not altered at a higher temperature, further suggesting a good thermal stability on internal interfaces. For both electrodes, the polarization resistance increases at high temperature, but the variation is lower than 20 %. It is worth mentioning that the lowest increase is recorded for the homogeneous electrode which rather well agrees with the behaviours evidenced at 600 °C (Fig. III-7).

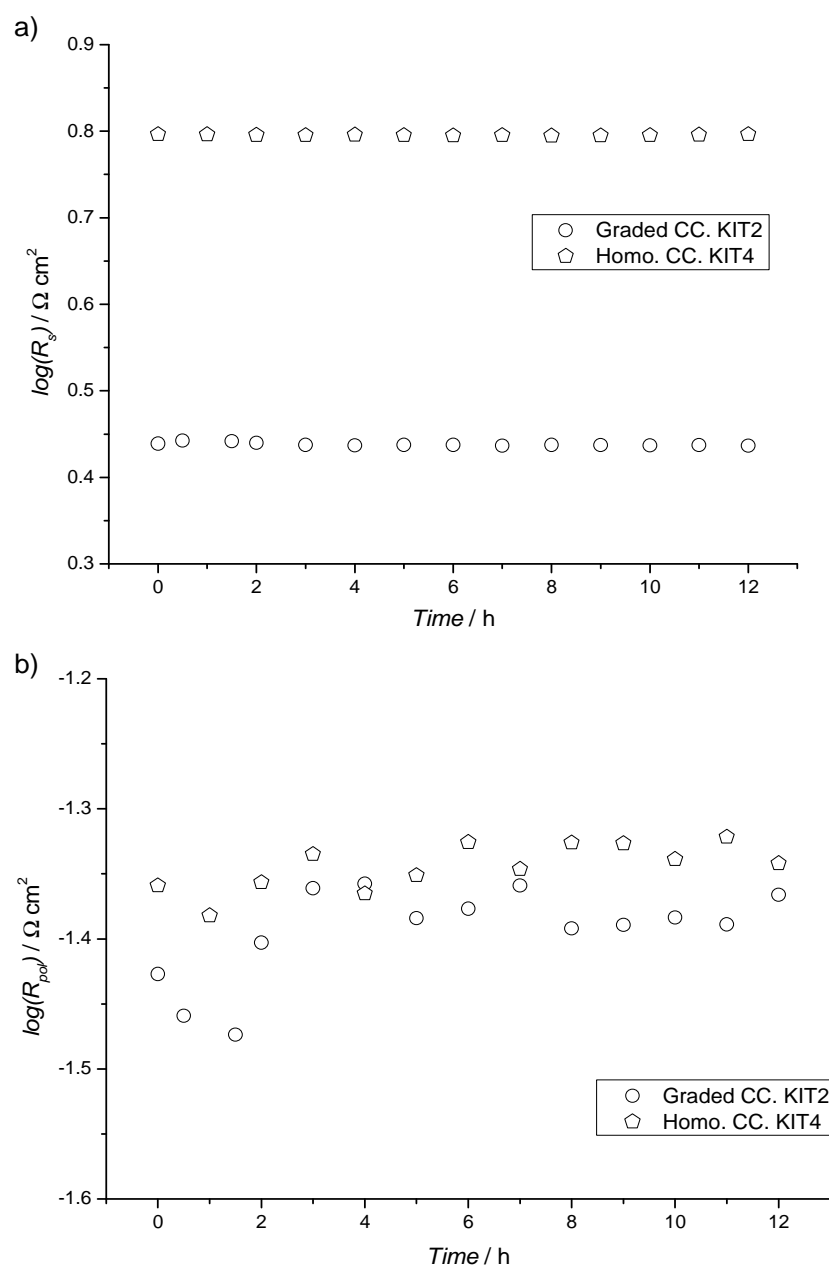


Fig. III-8. a) Series resistance and b) polarization resistance versus ageing time at 800 °C in air.

III.5. Conclusions

Homogeneous and graded compositions of CGO-LSCF oxygen electrode were successfully deposited on YSZ substrate by ESD. The isothermal tests carried out at 600 °C for 200 h and 800 °C for 12 h did not show any high increase of the polarization resistance. The dense CGO buffer layer can effectively impede ion migration between LSCF and YSZ and can stop creation of inhibitors for oxygen transfer. The lowest R_{pol} values were achieved for the samples with LSCF current collector layer, where the minimum ASR value at 600 °C of $1.3 \Omega \cdot \text{cm}^2$, which is 1.5 order of magnitude lower than that the one without CCL. Flat and homogeneous surface of the screen-printed layer improves current collecting. However, the polarization resistance of CGO-LSCF composites remains higher than that of a pure LSCF electrode. It means that presence of CGO in the cathode volume does not improve electrode performances. Moreover, the electrochemical datas do not allow distinguishing the influence of the composition on the electrochemical processes. R_{pol} values for graded and homogeneous composition lie too close to each other to unanimously discriminate which composition is more appreciated.

Acknowledgments

The authors would like to thank to the International Doctoral School in Functional Materials for Energy, Information Technology, and Health in the framework of the European Programme ‘Erasmus Mundus II 2009-2013’ for financial support. We thank M. Rieu (ENSMSE) and J. Hayd (KIT) for LSCF current collector screen-printing.

III.6. References

- [1] G. C. Kostoglou, G. Tsiniarakis, and C. Ftikos, “Chemical reactivity of perovskite oxide SOFC cathodes and yttria stabilized zirconia,” *Solid State Ionics*, vol. 135, pp. 529–535, 2000.
- [2] M. Sase, D. Ueno, K. Yashiro, A. Kaimai, T. Kawada, and J. Mizusaki, “Interfacial reaction and electrochemical properties of dense (La,Sr)CoO_{3-δ} cathode on YSZ (1 0 0),” *J. Phys. Chem. Solids*, vol. 66, no. 2–4, pp. 343–348, 2005.
- [3] H. Y. Tu, Y. Takeda, N. Imanishi, and O. Yamamoto, “Ln_{0.4}Sr_{0.6}Co_{0.8}Fe_{0.2}O_{3-δ} (Ln = La, Pr, Nd, Sm, Gd) for the electrode in solid oxide fuel cells,” *Solid State Ionics*, vol. 117, pp. 277–281, 1999.
- [4] L. Kindermann, D. Das, H. Nickel, and K. Hilpert, “Chemical compatibility of the LaFeO₃ base perovskites (La_{0.6}Sr_{0.4})_zFe_{0.8}M_{0.2}O_{3-δ} (z = 1, 0.9; M = Cr, Mn, Co, Ni) with yttria stabilized zirconia,” *Solid State Ionics*, vol. 89, pp. 215–220, 1996.
- [5] T. Nguyen, K. Kobayashi, T. Honda, Y. Iimura, K. Kato, A. Neghisi, K. Nozaki, F. Tappero, K. Sasaki, and H. Shirahama, “Preparation and evaluation of doped ceria interlayer on supported stabilized zirconia electrolyte SOFCs by wet ceramic processes,” *Solid State Ionics*, vol. 174, no. 1–4, pp. 163–174, 2004.
- [6] S. Uhlenbruck, T. Moskalewicz, N. Jordan, H.-J. Penkalla, and H. P. Buchkremer, “Element interdiffusion at electrolyte–cathode interfaces in ceramic high-temperature fuel cells,” *Solid State Ionics*, vol. 180, no. 4–5, pp. 418–423, 2009.
- [7] G. Constantin, C. Rossignol, J.-P. Barnes, and E. Djurado, “Interface stability of thin, dense CGO film coating on YSZ for solid oxide fuel cells,” *Solid State Ionics*, vol. 235, pp. 36–41, 2013.
- [8] V. V. Kharton, F. M. Figueiredo, L. Navarro, E. N. Naumovich, A. V. Kovalevsky, A. A. Yaremchenko, A. P. Viskup, A. Carneiro, F. M. B. Marques, and J. R. Frade, “Ceria-based materials for solid oxide fuel cells,” *J. Mater. Sci.*, vol. 36, pp. 1105–1117, 2001.

- [9] H. Hayashi, T. Saitou, N. Maruyama, H. Inaba, K. Kawamura, and M. Mori, “Thermal expansion coefficient of yttria stabilized zirconia for various yttria contents,” *Solid State Ionics*, vol. 176, no. 5–6, pp. 613–619, 2005.
- [10] L. Tai, M. M. Nasrallah, H. U. Anderson, D. M. Sparlin, and S. R. Sehlin, “Structure and electrical properties of $\text{La}_{1-x}\text{Sr}_x\text{Co}_{1-y}\text{Fe}_y\text{O}_3$. Part 1. The system $\text{La}_{0.8}\text{Sr}_{0.2}\text{Co}_{1-y}\text{Fe}_y\text{O}_3$,” *Solid State Ionics*, vol. 76, no. 3–4, pp. 259–271, 1995.
- [11] J. Sar, F. Charlot, A. Almeida, L. Dessemond, and E. Djurado, “Coral Microstructure of Graded CGO/LSCF Oxygen Electrode by Electrostatic Spray Deposition for Energy (IT-SOFC, SOEC),” *Fuel Cells*, vol. 14, no. 3, pp. 357–363, 2014.
- [12] D. Marinha, C. Rossignol, and E. Djurado, “Influence of electro spraying parameters on the microstructure of $\text{La}_{0.6}\text{Sr}_{0.4}\text{Co}_{0.2}\text{Fe}_{0.8}\text{O}_{3-\delta}$ films for SOFCs,” *J. Solid State Chem.*, vol. 182, no. 7, pp. 1742–1748, 2009.
- [13] C. Rossignol, B. Roman, G. D. Benetti, and E. Djurado, “Elaboration of thin and dense CGO films adherent to YSZ by electrostatic spray deposition for IT-SOFC applications,” *New J. Chem.*, vol. 35, no. 3, pp. 716–723, 2011.
- [14] S. P. S. Badwal, “Zirconia-based solid electrolytes: microstructure, stability and ionic conductivity,” *Solid State Ionics*, vol. 52, pp. 23–32, 1992.
- [15] S. Hui, J. Roller, S. Yick, X. Zhang, C. Decès-Petit, Y. Xie, R. Maric, and D. Ghosh, “A brief review of the ionic conductivity enhancement for selected oxide electrolytes,” *J. Power Sources*, vol. 172, no. 2, pp. 493–502, 2007.
- [16] M. Filal, C. Petot, M. Mokchah, C. Chateau, and J. L. Carpentier, “Ionic conductivity of yttrium-doped zirconia and the ‘composite effect’,” *Solid State Ionics*, vol. 80, pp. 27–35, 1995.
- [17] M. Prestat, A. Infortuna, S. Korrodi, S. Rey-Mermet, P. Mural, and L. J. Gauckler, “Oxygen reduction at thin dense $\text{La}_{0.52}\text{Sr}_{0.48}\text{Co}_{0.18}\text{Fe}_{0.82}\text{O}_{3-\delta}$ electrodes. Part II: Experimental assessment of the reaction kinetics,” *J. Electroceramics*, vol. 18, no. 1–2, pp. 111–120, 2007.

- [18] E. J. Abram, D. C. Sinclair, and A. R. West, “Electrode-Contact Spreading Resistance Phenomena in Doped-Lanthanum Gallate Ceramics,” *J. Electroceramics*, vol. 7, pp. 179–188, 2001.
- [19] J. Fleig and J. Maier, “The Influence of Laterally Inhomogeneous Contacts on the Impedance of Solid Materials: A Three-Dimensional Finite-Element Study,” *J. Electroceramics*, vol. 1, no. 1, pp. 73–89, 1997.
- [20] V. Dusastre and J. A. Kilner, “Optimisation of composite cathodes for intermediate temperature SOFC applications,” *Solid State Ionics*, vol. 126, pp. 163–174, 1999.
- [21] E. P. Murray, M. J. Sever, and S. A. Barnett, “Electrochemical performance of (La,Sr)(Co,Fe)O₃–(Ce,Gd)O₃ composite cathodes,” *Solid State Ionics*, vol. 148, pp. 27–34, 2002.
- [22] D. Beckel, U. Muecke, T. Gyger, G. Florey, A. Infortuna, and L. Gauckler, “Electrochemical performance of LSCF based thin film cathodes prepared by spray pyrolysis,” *Solid State Ionics*, vol. 178, no. 5–6, pp. 407–415, 2007.
- [23] C.-S. Hsu and B.-H. Hwang, “Microstructure and Properties of the La_{0.6}Sr_{0.4}Co_{0.2}Fe_{0.8}O₃ Cathodes Prepared by Electrostatic-Assisted Ultrasonic Spray Pyrolysis Method,” *J. Electrochem. Soc.*, vol. 153, no. 8, pp. A1478–A1483, 2006.
- [24] D. Marinha, L. Dessemond, J. S. Cronin, J. R. Wilson, S. a. Barnett, and E. Djurado, “Microstructural 3D Reconstruction and Performance Evaluation of LSCF Cathodes Obtained by Electrostatic Spray Deposition,” *Chem. Mater.*, vol. 23, no. 24, pp. 5340–5348, 2011.
- [25] J. Nielsen, T. Jacobsen, and M. Wandel, “Impedance of porous IT-SOFC LSCF:CGO composite cathodes,” *Electrochim. Acta*, vol. 56, no. 23, pp. 7963–7974, 2011.
- [26] B. F. Angoua and E. B. Slamovich, “Single solution spray pyrolysis of La_{0.6}Sr_{0.4}Co_{0.2}Fe_{0.8}O_{3-δ}–Ce_{0.8}Gd_{0.2}O_{1.9} (LSCF–CGO) thin film cathodes,” *Solid State Ionics*, vol. 212, pp. 10–17, 2012.

- [27] Y. Leng, S. Chan, and Q. Liu, “Development of LSCF–GDC composite cathodes for low-temperature solid oxide fuel cells with thin film GDC electrolyte,” *Int. J. Hydrogen Energy*, vol. 33, no. 14, pp. 3808–3817, 2008.
- [28] S. Wang, T. Kato, S. Nagata, T. Kaneko, N. Iwashita, T. Honda, and M. Dokiya, “Electrodes and performance analysis of a ceria electrolyte SOFC,” *Solid State Ionics*, vol. 153, pp. 477–484, 2002.
- [29] W. Wang and M. Mogensen, “High-performance lanthanum-ferrite-based cathode for SOFC,” *Solid State Ionics*, vol. 176, no. 5–6, pp. 457–462, 2005.
- [30] D. Marinha, J. Hayd, L. Dessemond, E. Ivers-Tiffée, and E. Djurado, “Performance of (La,Sr)(Co,Fe)O_{3-x} double-layer cathode films for intermediate temperature solid oxide fuel cell,” *J. Power Sources*, vol. 196, pp. 5084–5090, 2011.

IV. 3D analysis of CGO-LSCF oxygen electrode for solid oxide cells

3D analysis of CGO-LSCF oxygen electrode for solid oxide cells

Jaroslav Sar^{1,2}, Ozden Celikbilek^{1,2}, Julie Villanova⁴, Laurent Dessemond^{1,2}, Christophe L. Martin³, Elisabeth Djurado^{1,2*}

¹ Univ. Grenoble Alpes, LEPMI, F-38000 Grenoble, France;

² CNRS, LEPMI, F-38000 Grenoble, France;

³ Univ. Grenoble Alpes, CNRS, SIMaP, F-38000 Grenoble, France

⁴ ESRF – The European Synchrotron, CS 40220,
F-38043 Grenoble Cedex 9, France

**Elisabeth.Djurado@lepmi.grenoble-inp.fr*

IV.1. Abstract

Notwithstanding the importance of material composition, microstructure also plays a significant role in performances of solid oxide cells. X-ray nanotomography with a voxel size of 25 nm was used to image the microstructure of a CGO-LSCF composite oxygen electrode obtained by electrostatic spray deposition (ESD). The stack of data after image processing was used to create a 3D model. Two volumes were selected from the 3D model and microstructural parameters such as porosity, surface area, percolation path and tortuosity were computed in order to quantify the microstructure. The influence of the applied threshold values on the parameters was investigated. Comparison of these parameters with previously reported data has shown significant differences. The porosity of CGO-LSCF oxygen electrode varied from 67 to 87 vol.%. Such a high porosity level makes this ESD microstructure unique. The microstructural parameters were used to determine the electrode polarization by ALS model. Model polarization resistance was in an agreement with experimental data.

Keywords: Solid oxide cells, CGO-LSCF, nanotomography, oxygen electrode, coral microstructure, electrostatic spray deposition, 3D reconstruction.

IV.2. Introduction

Solid oxide cells (SOCs) are a potential clean technology for energy production as solid oxide fuel cells (SOFCs) and for water splitting or syngas production as solid oxide electrolyser cells (SOECs). Moreover, SOCs can reversibly operate in both fuel cells and electrolysis modes providing electrical energy or gaseous hydrogen. Mixed ionic and electronic conductor (MIEC) material such as $\text{La}_{0.6}\text{Sr}_{0.4}\text{Co}_{0.2}\text{Fe}_{0.8}\text{O}_{3-\delta}$ (LSCF) [1]–[3] has generated much interest as an alternative to the widely used $\text{La}_{1-x}\text{Sr}_x\text{MnO}_{3-x}$ (LSM), an oxygen electrode in SOC. LSCF exhibits much higher ionic and electronic conductivities than LSM due to relatively sparse surface oxygen vacancies and is a preferred oxygen electrode material for intermediate temperature SOFC applications [4]–[6]. The insertion of a thin and dense $\text{Ce}_{0.9}\text{Gd}_{0.1}\text{O}_{1.95}$ (CGO) barrier diffusion layer [7], [8] in between the YSZ electrolyte and LSCF electrode avoids the creation of insulating phases [9]. Papers have shown that electrochemical properties of the LSCF electrode can be improved by introducing CGO in the electrode bulk to increases the ionic conductivity [10]–[13].

The development of the oxygen electrode for solid oxide cells should not only focused on new materials but should also rely on the improvement of the electrode microstructure [14]. The electrochemical performances, the reactions and the processes occurring during the cell operation are strongly related to the microstructure [15]. Parameters such as porosity, surface area, percolation path and tortuosity are the most typical parameters to consider in order to accurately describe the morphology of the electrode. 2D and 3D microstructural reconstructions are well suited for their determination. The optical microscopy is advantageously replaced by advanced techniques based on X-rays and electrons emission. X-ray tomography and scanning electron microscopy (SEM) combined with focused ion beam (FIB) tomography differ from each other. The main differences are (i) the destruction of the sample during the FIB analysis. The ion beam in FIB-SEM mills the material then slices it to get deeper sections. Thus the sample is repeatedly destroyed. X-ray tomography is a non-destructive technique in which X-rays get through the tested material and the reconstruction is made on detected projections. (ii) the typical volume that can be reconstructed with FIB/SEM is much smaller ($10 \times 10 \times 10 \mu\text{m}^3$) with as low as 10 nm voxel resolution [16] than the volume with X-ray nanotomography where a volume of $50 \times 50 \times 100 \mu\text{m}^3$ with a 50 nm voxel resolution can be expected. Both techniques are complementary for a complete analysis of the electrode morphology. However since the size of the large pores that dictate gas flow properties are typically larger than 10 μm in the electrode material, X-ray nanotomography seems to be more appropriated. For example, nano-tomography has been used recently to

reconstruct a commercial cermet anode (Ni-8YSZ) and to compute porosity and tortuosity parameters [17].

The microstructural characteristics have been determined recently by X-ray nanotomography on LSCF [18], [19], LSCF-SDC [20], LSM-YSZ [21], CGO-LSM [22] oxygen electrodes and Ni-8YSZ hydrogen electrode [17], [23].

In this work X-ray nanotomography was used to get a 3D model of a graded CGO-LSCF oxygen electrode deposited by electrostatic spray deposition for application in solid oxide cells. The image analysis was performed on the stack volumes in order to prepare it for the computing. The microstructural parameters such as porosity, surface area, percolation path and tortuosity were extracted and calculated using PoroDict module of GeoDict software [24]. The software determines open and closed pores volume percentages which sum gives the total porosity volume percentage. Open pores are described as extensive networks of interconnected pores while isolated pores as closed pores. Surface area is estimated by a statistical approach and not by simply adding up the voxel surface. Percolation path is determined as the shortest possible path that maximum diameter of a spherical particle can travel through the matter. Tortuosity is defined as the ratio of pore effective path length from one to another sample side to the sample length [25]. The influence of threshold values on these parameters was investigated. Adler-Lane-Steele (ALS) model [26] was used to determine the electrode polarization (R_{pol}) based on the microstructural parameters achieved from nanotomography. Modeled R_{pol} was compared to experimental electrode resistance from Electrochemical impedance spectroscopy (EIS).

IV.3. Experimental

IV.3.1. Deposition of CGO-LSCF coral microstructure

The composite with a gradient in composition of $Ce_{0.9}Gd_{0.1}O_{1.95}$ (CGO) and $La_{0.6}Sr_{0.4}Co_{0.2}Fe_{0.8}O_{3-\delta}$ (LSCF) oxygen electrode was deposited on a YSZ disk shape substrate by Electrostatic Spray Deposition (ESD) [27]. The homemade substrate was 19 mm in diameter and 1 mm thick. Two precursor solutions were prepared to have a concentration of 0.02 mol.L^{-1} based on nitrate and chloride salts. The salts were dissolved in a mixture of butyl carbitol and ethanol in 4:1 volume ratio for CGO solution and in a mixture of distilled water and ethanol in 5:1 volume ratio for LSCF solution. The deposition was performed at a 35 mm nozzle-to-substrate distance. CGO barrier diffusion layer was deposited as a first step of the deposition. Graded composition was achieved by varying the precursor solution flow rates but keeping the total flow rate stable to 1 mL.h^{-1} . The substrate temperature was fixed at $400 \text{ }^{\circ}\text{C}$.

As-deposited coatings were found amorphous by X-ray diffraction and then sintered at 900 °C for 2 h. The detailed description of the graded CGO-LSCF oxygen electrode deposition can be found elsewhere [27].

IV.3.2. Sample preparation for X-ray nanotomography

The YSZ disk was coated by a 20 µm thick graded CGO-LSCF composite. The whole was embedded in a mixture of EpoFix Resin and EpoFix Hardener (Struers) in a volume ratio of 8:1. Due to the very absorbent properties of the materials, it is necessary to obtain thin samples (typically less than 250 µm). Thus, after bonding, the sample was alternately cut and polished to obtain a needle shape. The final sample had a height of 5 mm with a cross section of around 100 x 100 µm. This sample was glued to the metallic support allowing rotation during the nanotomography at ESRF (The European Synchrotron Radiation Facilities).

IV.3.3. X-ray nanotomography

The experiment was performed at nano-imaging end station ID22NI of the ESRF in Grenoble. A schematic of the holotomography setup is presented in Fig. IV-1.

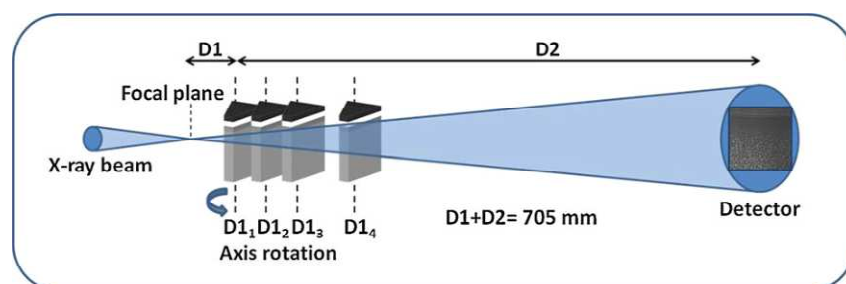


Fig. IV-1. Schematic of the holotomography setup at the ID22NI beamline in ESRF. D1 indicates distance between focal plane and the sample and D2 sample-to-detector distance [21].

The detailed principle of holotomography is described elsewhere [28], [29]. The beam energy was fixed to 29.6 keV with a bandwidth of 1.6 %. The required beam time for one sample including scanning time, sample mounting and positioning was 6 h. Distance between focal plane and the sample (D1) was varied from 24 to 300 mm. The resolution was ranging from 25 to 320 nm leading to the determination of the field of view from 50 to 650 µm, by varying the position of D1. Achieved images were four tomographic scans with different sample-to-detector distances used to create a stack of data. Subsequent processing required the following steps: correction of the image distortion, resizing and alignment of the individual radiographs, phase retrieval calculation and tomographic reconstruction [21].

IV.3.4. Data treatment

The stack of data acquired right after nanotomography required further treatment to be ready for microstructural parameters analysis. It was necessary to remove noises and artifacts that unavoidably come with nanotomography. Defects in the data stack originated from the strong difference between absorption indexes of dense YSZ substrate and highly porous CGO-LSCF oxygen electrode. Moreover, local melting of the resin may have occurred due to the use of a high X-ray energy. The microstructural parameter calculations were performed for two selected small scale reconstructions. Two selected volumes were described as volume 1 and volume 2. The next step was consisted of applying the median filter and three different threshold values to each volume. All data treatment was performed using a public software for image processing and analysis in Java ImageJ [30].

IV.3.5. PoroDict of GeoDict

PoroDict module of GeoDict software was used to estimate various microstructural parameters from three-dimensional porous models. Porosity (open and closed), specific surface area, percolation path and tortuosity factor were computed [25].

IV.4. Results and discussion

IV.4.1. Microstructure by SEM

The graded CGO-LSCF composite oxygen electrode was successfully deposited on a YSZ substrate by ESD. The layer presented highly porous microstructure called coral microstructure previously reported for single LSCF electrode [31]. The thickness of CGO-LSCF layer was varied from 15 to 25 μm . SEM observations (Fig. IV-2) showed two-scale porosities. The large pores between corals were micronic in size and are the main contribution of the composite porosity. High magnification micrographs (Fig. IV-2b and d) demonstrate the existence of some nanoscale porosity on the corals surface. A detailed description of the CGO-LSCF graded composition can be found elsewhere [27].

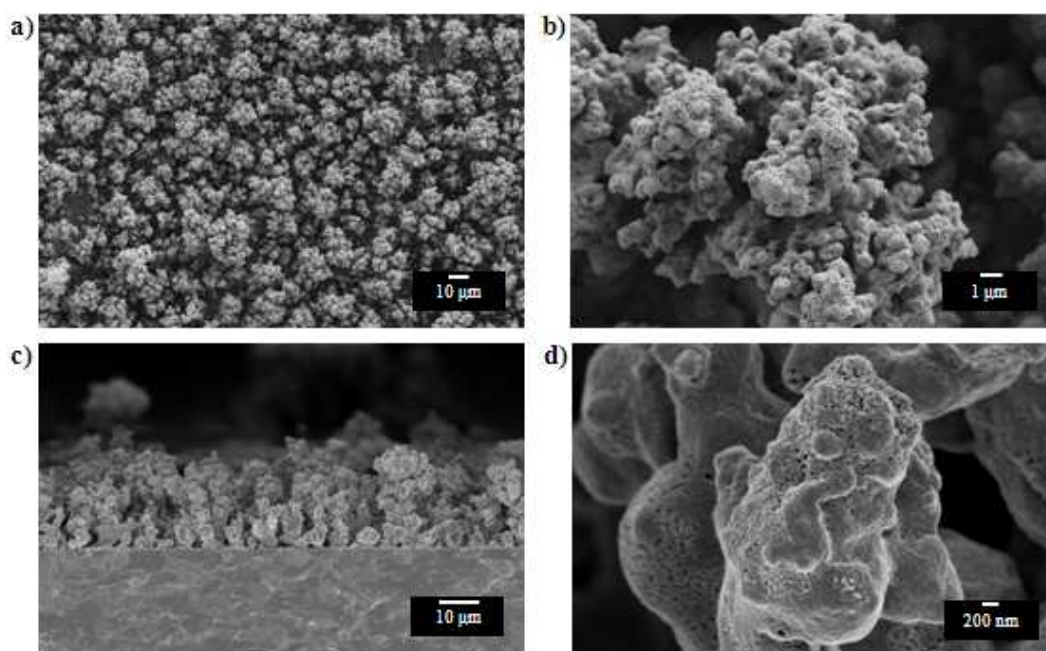


Fig. IV-2. Pictures of CGO-LSCF coral microstructure sample before electrochemical characterization, a), b) surface views and c), d) cross section views [27].

IV.4.2. 3D reconstruction of coral microstructure

A tomography reconstruction stack file was successfully achieved after X-ray nanotomography with a voxel size of 25 nm and a field of view of approximately 50 μm . The separation of CGO, LSCF and YSZ phases on a 3D model was not possible due to a similar phase modulation. Images collected during nanotomography presented strong contrast only between two features discriminated as solid (CGO-LSCF or YSZ) and pores. The reconstructed volume 1 and volume 2 are presented in Fig. IV-3 and Fig. IV-4, respectively.

Table IV-1. Dimensions and volume of the volumes

Volume	Dimensions (x x y x z – μm)	Volume (μm^3)
1	22.5 x 13.8 x 16.5	5123.3
2	14.1 x 9.4 x 15.8	2094.1

The size of volume 1 was 898 x 550 x 661 pixel and 564 x 376 x 631 pixel for volume 2. The rescaled dimensions and volumes of volume 1 and volume 2 are presented in Table IV-1. The first selected volume was larger in all dimensions and the three dimensional reconstructed volume showed two corals without the substrate. The second selected volume presented just one full coral and some small portions of other coral top parts. Moreover, almost all the

volume bottom portion was covered by the substrate enlarging the matter volume. Interestingly, it was found that all corals were hollow. The empty space between corals was considered as porosity and was added to the total pore volume.

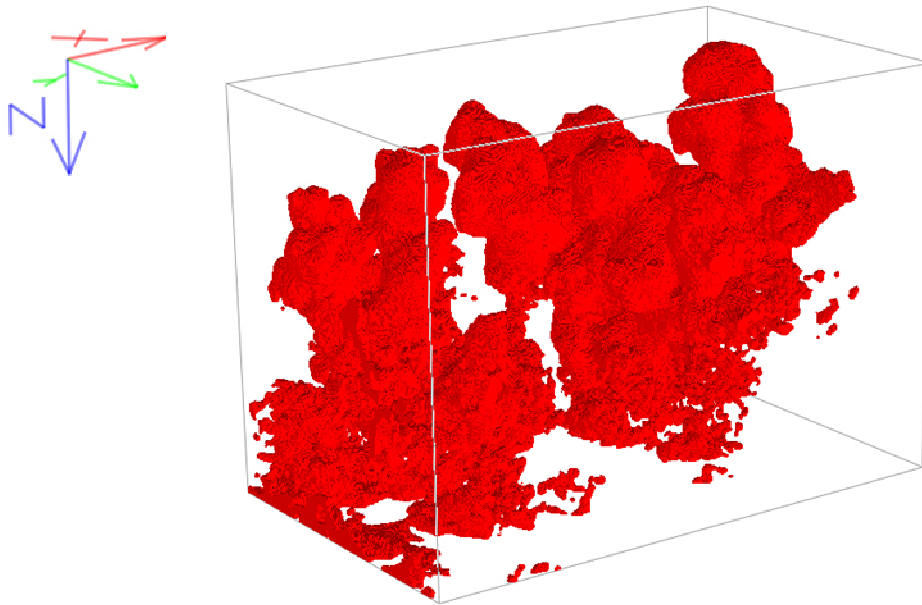


Fig. IV-3. Three dimensional reconstructed volume of volume 1.

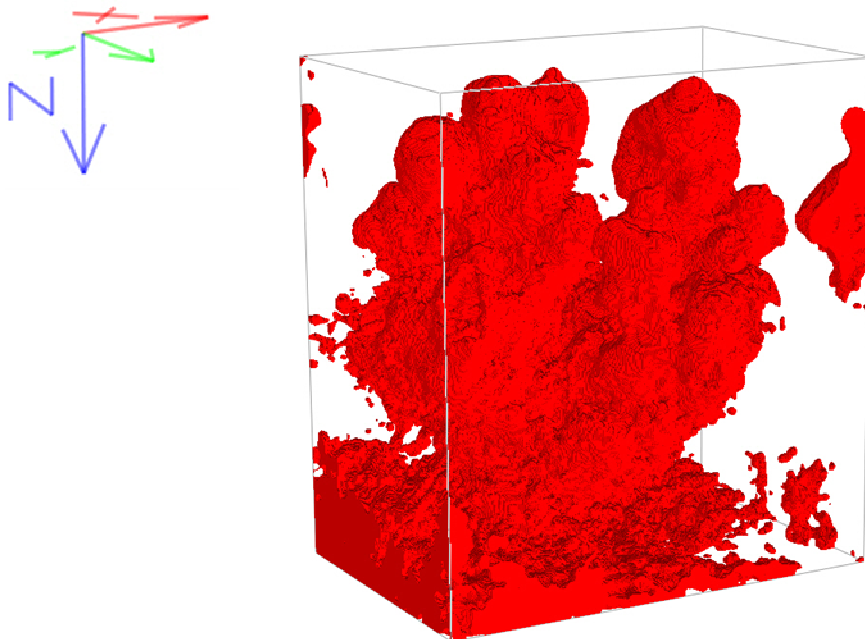


Fig. IV-4. Three dimensional reconstructed volume of volume 2.

IV.4.3. Microstructure analysis by PoroDict

The data treatment has a significant influence on the quantification of microstructural parameters such as porosity, specific surface area, tortuosity and percolation path. However, it is worth noting that each coral is different in relation to its height, width and porosity. Thus each selected volume is unique. Standardization and comparison of the volumes to each other is difficult.

Two volumes were chosen from the stack containing 1919 slices. The selected volumes did not overlap. Each individual image was built of pixels in different grayscale levels described in values from 0 (black) to 255 (white). Such an image cannot be used to distinguish the microstructural parameters. It is necessary to perform a segmentation stage called thresholding to assign pixel (voxel) as a pore or as solid [32]. In order to study the influence of thresholding on porosity, three thresholding values were selected for the same volume of interest. The ‘correct’ threshold value was chosen based on the best match with a simple observation of the microstructure. This value was complemented by two others by simply adding and subtracting a reasonable deviation. The threshold levels of volumes are summarized in Table IV-2.

Table IV-2. Different threshold levels applied to the volumes.

Volume	Threshold level		
1	110	120	130
2	116	123	131

IV.4.3.1. Open and closed porosities

Porosity is an important microstructural parameter since it affects the oxygen electrode mechanical and electrochemical properties. In terms of oxygen electrode, isolated pores referred to as closed pores are undesirable for the oxygen reduction reaction. They are trapped inside corals and remain inactive for oxygen transfer via the electrode. Moreover, mechanical strength is reduced and electronic and ionic percolation paths are increased. Fig. IV-5 shows variations of the open and closed porosities for volume 1 and volume 2 in relations to the threshold value. The total porosity (sum of open and closed porosities) was at least 80 vol.% for volume 1 and 67 vol.% for volume 2. The difference between porosities of the selected volumes was 12 %. This difference was stable for all threshold values. This indicates that it arises from the specification of each volume and not from the data treatment. For both

volumes, the closed porosity did not exceed a limit of 0.7 vol.%. Importantly, such a low value for the closed porosity indicates that the hollow parts of corals are connected to the large pores surrounding corals and should not be considered as closed pores. The closed porosity can be considered as negligible. volume 1 had higher open porosity and lower closed porosity in comparison with volume 2. Fig. IV-5 indicates that for both volumes, the open porosity is decreasing with increasing threshold values while closed porosity is increasing with increasing threshold values. This tendency may be interpreted by the fact that for higher threshold value, more pixels are assigned to the solid, thus decreasing the calculated porosity. Reversely, for closed porosity the solid fraction was getting thicker with increasing threshold since more pixels were selected as solid and trap the pixels assigned as pores inside the material.

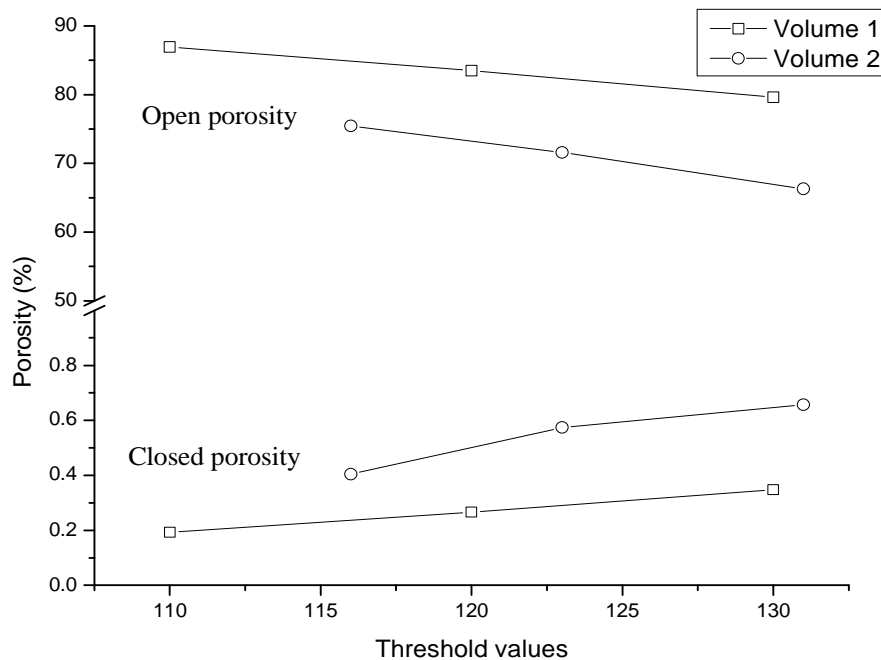


Fig. IV-5. Open and closed porosities for volume 1 and 2 for different threshold values.

The variations of the open and the closed porosity in relation to the volume height are shown in Fig. IV-6 and Fig. IV-7. The lowest open porosity was noticed at the coral height of almost 13 μm for all threshold values for volume 1 (Fig. IV-6). It is in accordance with the coral shape in the selected volume presented in Fig. IV-3. At such height the material/pore ratio is the highest. Still, the variation of the open porosity against the volume height is rather small (approximately 4 vol.%). This confirms that corals are very porous, all along their heights. The closed porosity was found negligible at the bottom of the volume (below 11.5 μm). Above 11.5 μm , the closed porosity increased to the highest value at the height of approximately 13 μm . Above this height the closed porosity was decreasing again. The closed

porosity percentage seemed to increase with the solid fraction. At 13 μm the material concentration was the highest together with the highest concentration of pores trapped inside the material.

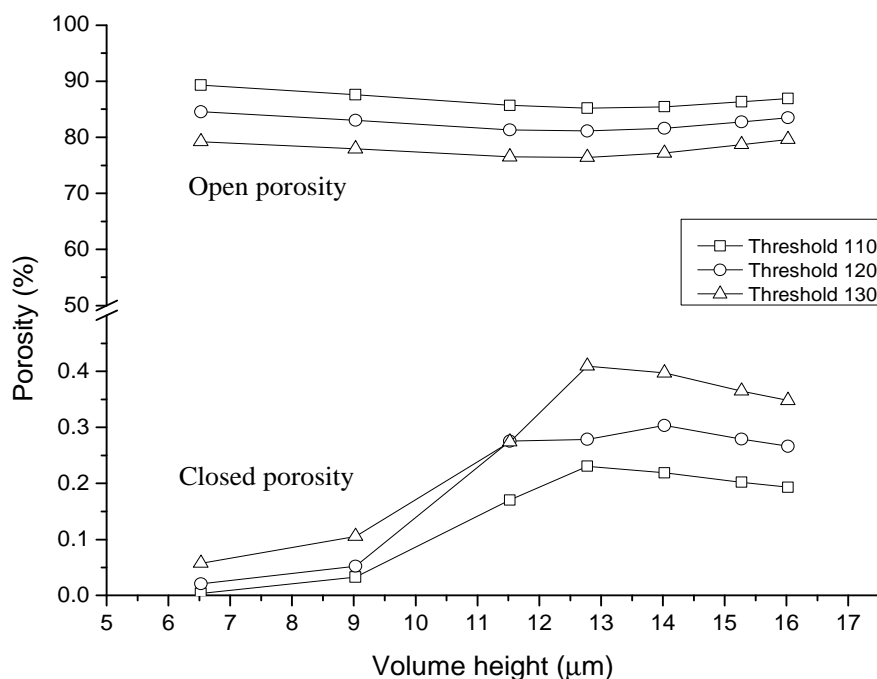


Fig. IV-6. Open and closed porosity changes for volume 1 in relation to the volume height for threshold values of 110, 120 and 130.

The shapes of the corals are different in volume 1 and 2 (Fig. IV-4). On volume 2 the extensive presence of the substrate on the bottom induces relatively small porosity values. Below 1 μm height the porosities are 44, 35 and 24 vol.% for the threshold values of 116, 123 and 131, respectively (Fig. IV-7). Moreover, the porosity at each height was consistently lower for all threshold values in comparison with volume 1. The open porosity was increasing with increasing height for all threshold values.

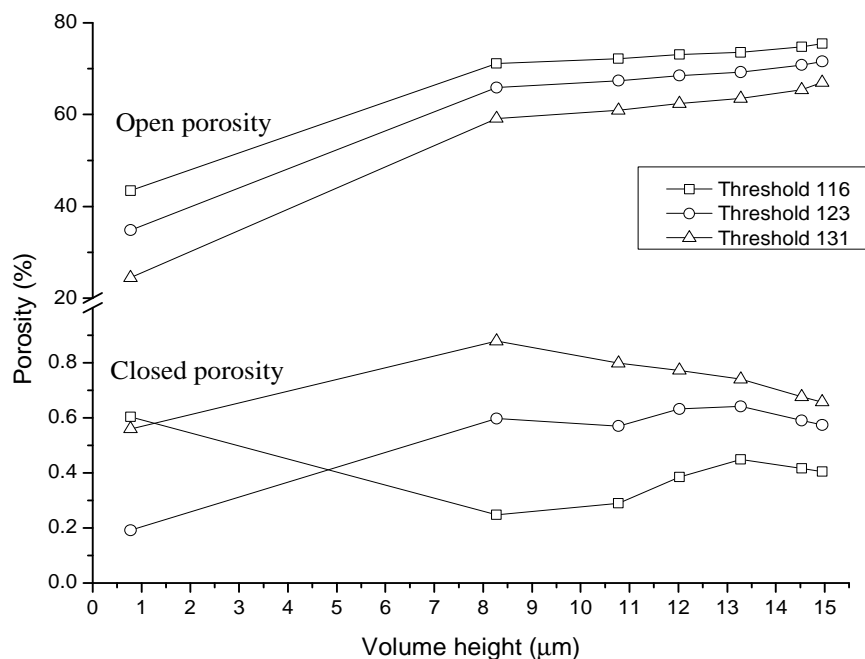


Fig. IV-7. Open and closed porosity changes for volume 2 in relation to the volume height for threshold values of 116, 123 and 131.

Thresholding did not change the tendencies of the porosity evolution regarding the volume height but had an influence especially on the number of pixels assigned as solid or as pore.

The high porosity level for the CGO-LSCF coral electrode can be compared to the porosity level for the LSCF coral electrode published previously by Marinha et al. [15] using the same ESD process. The porosity in both microstructures was the result of simultaneous macro- and nano-porosities. The macro-porosity in the order of micrometer scale was characterizing the space between corals and the large pores inside the corals. The nano-scale porosity was observed on the internal and external coral surfaces. Pores smaller than 25 nm may exist inside the coral or on its surface. However, they were not detected by nanotomography due to the limited resolution. It is worth mentioning that the porosity measured here is much higher than the porosity for the oxygen electrode published in the literature. For example, porosity of around 34 vol.% and 50 vol.% for LSM-YSZ [33], [34], 50 vol.% for LSM [35], 22 vol.% and 48 vol.% for LSCF [36], [37], and 5 – 10 vol.% for LSCF-SDC composite electrode [20] were reported in the literature. The comparison of the oxygen electrodes microstructures whose porosities vary more than 30 vol.% is challenging.

IV.4.3.2. Specific surface area

The specific surface area (SSA) values were calculated as the ratio of the surface area to the volume of a selected volume. The algorithm used in PoroDict to estimate surface area is based on statistical methods and not only on voxel surface calculation. A larger surface area leads to an increase in the number of sites for the oxygen reduction reaction. SSA was slightly increasing with threshold value for the volumes (Fig. IV-8). SSA for volume 2 was higher by 20 % than for volume 1. The calculated specific surface areas vary from 0.56 to 0.83 μm^{-1} which is small in comparison to previously published data for other oxygen electrodes [34], [36]–[38]. For instance, a composite of LSM-YSZ exhibited SSA of 3.0 – 4.5 μm^{-1} [34] and of 7.2 – 9.3 μm^{-1} [36] and LSCF electrode of 6.6 – 9.3 μm^{-1} [37], [38]. The difference can be explained not only by specification of the microstructure and preparation technique but also by method of calculation. In this work, the empty space between corals was considered as pores thus decreasing the specific surface area. The particular comparison of the oxygen electrode/pore interface surface area normalized by the cross-sectional area of the support calculated in this work can be done with the LSCF coral microstructure deposited by Marinha et al. [15]. In their work, the normalized surface area for coral sample was more than twice higher than the one presented here.

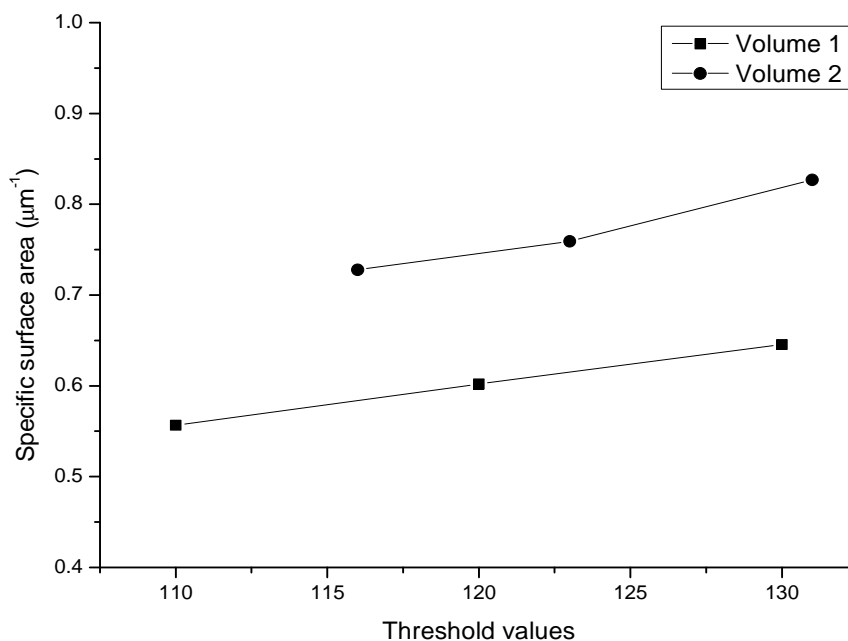


Fig. IV-8. Specific surface area for the volumes for different threshold values.

IV.4.3.3. Percolation path

The percolation path describes the shortest path for a spherical particle to travel through the whole sample in a given direction. The percolation path was calculated from the top of the coral microstructure to the bottom (dense YSZ substrate). The percolation path of the electrode material indicates both the electronic percolation path to electrochemically active zones and percolation path of the oxygen ion through the electrode. The electronic percolation is predominant and supports all electrode volume. The oxygen ion percolation path should be short to facilitate oxygen transfer through the electrode [39]. The percolation path calculation was determined at height of 16.03 μm and of 12.78 μm for volume 1 and at 14.95 μm and 12.20 μm for volume 2. Fig. IV-9 shows percolation paths calculated for volume 1 at different threshold values, the horizontal lines indicate the height of the volume. Percolation paths were just a little longer than the height of the volume. This means that the percolation paths were almost a straight line from the top to the bottom of the selected volume. Furthermore, the threshold value did not have any influence on the percolation path length. Table IV-3 shows the maximum diameter of the spherical particle that can move through the percolation path for volume 1. A particle diameter larger than 8 μm means that a rather thick percolation path exists for all threshold values.

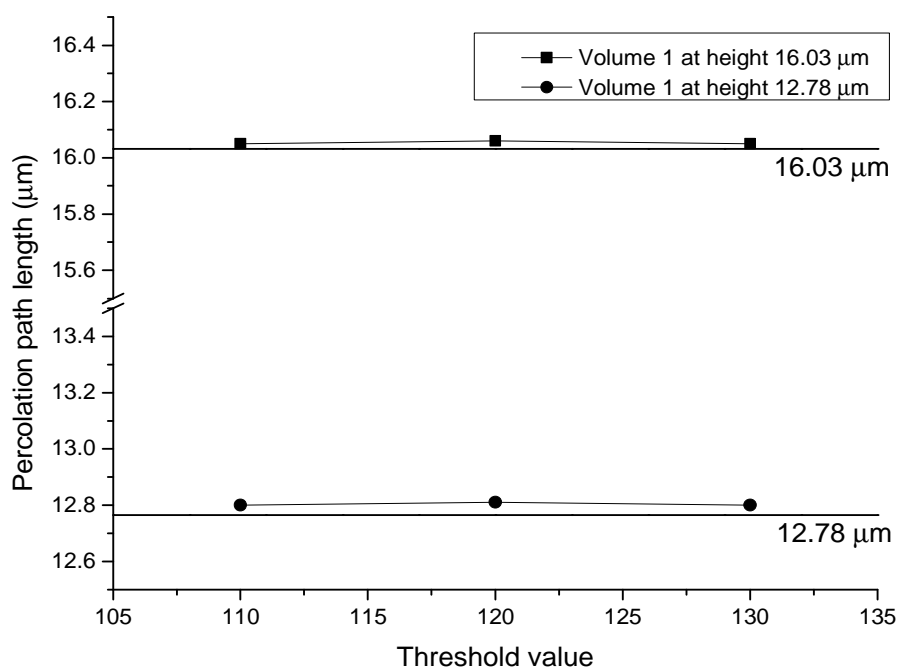


Fig. IV-9. Percolation path length for volume 1 at the volume height of 16.03 μm and 12.78 μm for different threshold values.

Table IV-3. Maximum diameter of a spherical particle that can move through the percolation path calculated at 16.03 and 12.78 μm heights for volume 1.

Area height (μm)	Diameter of particle (μm) for threshold of:		
	110	120	130
16.03	8.7	8.5	8.3
12.78	8.7	8.5	8.3

The percolation path length for volume 2 is presented in Fig. IV-10. The height, width and length of volume 2 are lower than these of volume 1. This is the reason for selecting smaller heights at which percolation paths were calculated for volume 2, as compared to volume 1. Percolation paths were clearly higher than the volume heights. The percolation path lengths had almost the same value for the threshold values of 123 and 131. The highest porosity recorded for threshold value of 116 led to an increase of the percolation path length. The path length was around 11 – 15 % longer in comparison with higher threshold values. A low threshold value caused path breaking at some point and required to find other way for the path. Table IV-4 shows the maximum diameter of the sphere that can move through the percolation path for volume 2. Diameters for the particle were around 2 μm , four times lower than for volume 1. It means that the percolation path was much thinner than percolation paths for volume 1.

Table IV-4. Maximum diameter of a spherical particle that can move through the percolatin path calculated at 14.95 and 12.20 μm heights for volume 2.

Area height (μm)	Diameter of particle (μm) for threshold of:		
	116	123	131
14.95	2.2	2.0	1.7
12.20	2.2	2.0	1.7

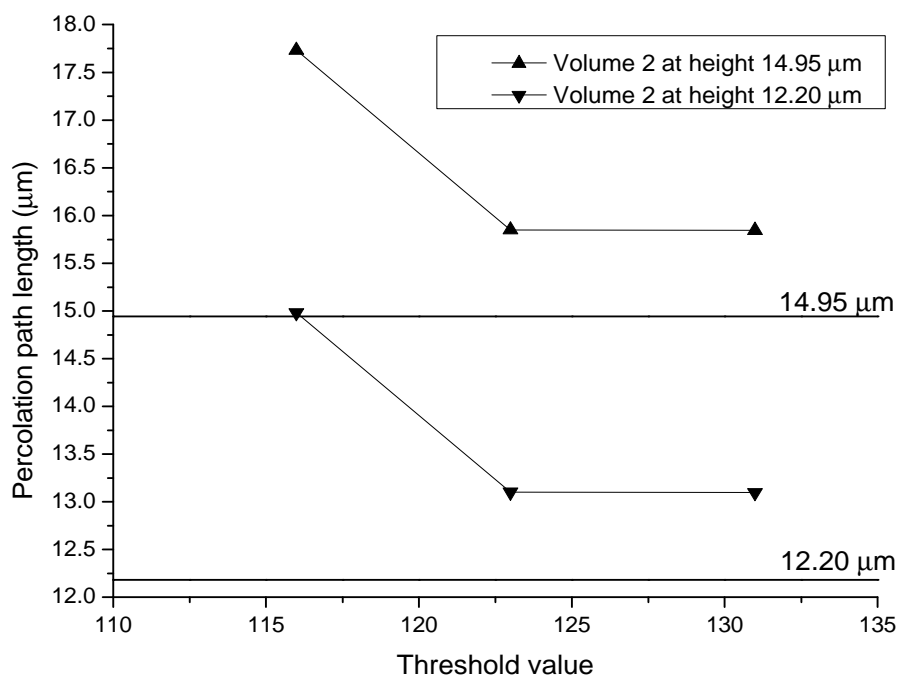


Fig. IV-10. Percolation path length for volume 2 at the volume height of 14.95 μm and 12.20 μm for different threshold values.

IV.4.3.4. Tortuosity factor

Usually, tortuosity is defined as the ratio of the effective path length divided by the length of the sample. The higher the ratio, the longer the length of the path is for a particle to pass from one side to another side. In this work the tortuosity is described as a pore tortuosity. The tortuosity was calculated in x-, y- and z-directions because oxygen can diffuse to the oxygen electrode from all three directions. The tortuosity factors in relation to the threshold value for volume 1 and 2 are presented in Fig. IV-11. Volume 2 exhibits higher tortuosity factors in all directions than volume 1. The tortuosity factors varied from 1.1 to 1.3 for volume 1 and from 1.3 to 1.4 for volume 2. The tendencies of increasing factors with the threshold values were in accordance with the coarsening of the material volume. Higher threshold values are at the origin of a larger volume fraction thus the effective path length for one oxygen gas molecule as an example, was getting longer to encircle the material. The highest calculated factor was in y- and the lowest in z-direction for volume 1. In case of volume 2, the highest factor was in the z-direction while the lowest was in x-direction. Nevertheless the representative volumes, the calculated tortuosity factors were lower than factors of 1.6 for LSM-YSZ [34] and of 2.7 and 2.0 for LSCF [36], [37] electrodes that can be found in the literature. Low tortuosity factors indicated easy oxygen gas access to the microstructure and short gas channels through the microstructure to electrochemically active zones.

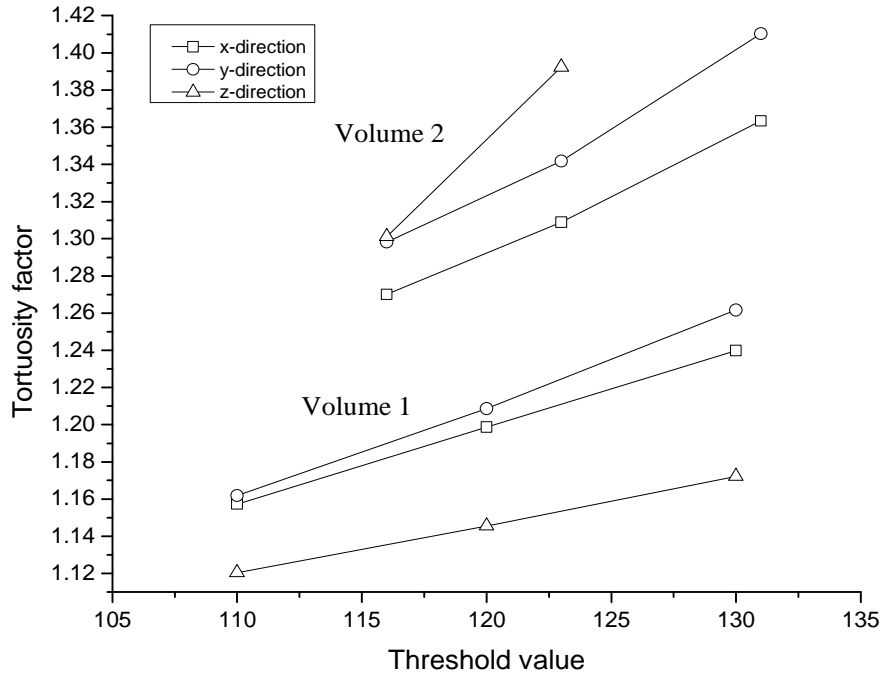


Fig. IV-11. Tortuosity factors for volume 1 and 2 in x-, y- and z-direction for different threshold values.

IV.4.4. Electrode polarization

ALS model describes the polarization resistance based on the material and the microstructural parameters (Eq. IV-1) [26]. Tortuosity factor τ , porosity fraction ε , and specific surface area a , where calculated by PoroDict module.

$$R_{pol} = \frac{RT}{2F^2} \left(\sqrt{\frac{\tau}{(1-\varepsilon)a D^* k C_0^2}} \right) \quad (IV-1)$$

The parameters were chosen for threshold value of 120 for volume 1 and threshold value of 123 for volume 2 as these values were the ‘correct’ threshold values. The tortuosity factors for R_{pol} calculation were used as average factor from x-, y- and z-directions. The parameters values are listed in Table IV-5.

Table IV-5. The microstructural parameters used for R_{pol} calculation for volume 1 and 2.

Volume	τ (-)	a (μm^{-1})	ε (-)
1	1.19	0.60	0.84
2	1.35	0.76	0.72

The surface exchange coefficient, k , and the self-diffusion coefficient, D^* , were taken from Esquirol et al. [40] and were equal to $1.9 \times 10^{-8} \text{ cm.s}^{-1}$ and $6.3 \times 10^{-11} \text{ cm}^2.\text{s}^{-1}$, respectively at

500 °C for CGO-LSCF composite. The oxygen concentration, C_o , measured by Fukuda et al. [41] was $0.084 \text{ mol.cm}^{-3}$ at 500 °C for LSCF composition and was used in the equation. Polarization resistances of 132 and $95 \text{ } \Omega.\text{cm}^2$ were calculated for volume 1 and 2 at 500 °C. The polarization resistance measured for homogeneous CGO-LSCF oxygen electrode at open circuit potential at the same temperature by EIS was $208 \text{ } \Omega.\text{cm}^2$ (see Chapter III). The difference between these values could be explained by additional contribution at high frequency range coming from the charge transfer on the electrode/electrolyte interface which is not included in ALS model.

IV.5. Conclusions

In this work, the coral microstructure of graded CGO-LSCF oxygen electrode for SOC was examined. 3D models were reconstructed based on the X-ray nanotomography data collected at ESRF Grenoble (ID22NI). The microstructural parameters such as open and closed porosity, specific surface area, percolation path and tortuosity factor were computed by PoroDict module of GeoDict software. Moreover, the variation of those parameters was discussed. The total porosity was much higher than those reported in the literature. Specific surface area and tortuosity factor were relatively low. One should keep in mind that the coral microstructure has a unique morphology and a fair comparison with other microstructures is difficult. The microstructural parameters presented here are meaningful only for the volume that was taken into consideration. Based on the two volumes, it is hard to generalize and to propose parameters that could describe the coral microstructure as a whole since the two selected volumes show just few corals. Still, we believe that the present study offers a useful view of these complex coral structures. The electrode resistance calculated from ALS model was coherent to experimental value achieved from EIS for CGO-LSCF composite with homogeneous microstructure.

Due to the specification of the coral microstructure, highly porous corals deposited on dense ceramic substrate, the presented work was complex. The sample preparation for nanotomography took much longer than typical LSM-YSZ electrodes. Moreover, on each preparation step the chance for sample failure was high. The nanotomography itself provided a lot of artifacts to the stack of data mainly due to a strong contrast between porous electrode and dense electrolyte. Imperfections could not be completely removed from the stack. Finally, the comparison of the microstructural parameters to those in the literature was challenging.

Acknowledgments

The authors thank the IDS-FunMat consortium for the financial support in the framework of the European Programme ‘Erasmus Mundus II 2009-2013’. Dr. P. Lhuissier and Dr. D. Jauffrès from the Laboratoire SIMaP, Univ. Grenoble Alpes are acknowledged for their input in the image analysis.

IV.6. References

- [1] J. W. Stevenson, I. Armstrong, R. D. Carneim, L. I. Pederson, and W. J. Weber, “Electrochemical Properties of Mixed Conducting Perovskites (M = Sr, Ba, Ca),” *J. Electrochem. Soc.*, vol. 143, no. 9, pp. 2722–2729, 1996.
- [2] L. Tai, M. M. Nasrallah, H. U. Anderson, D. M. Sparlin, and S. R. Sehlin, “Structure and electrical properties of $\text{La}_{1-x}\text{Sr}_x\text{Co}_{1-y}\text{Fe}_y\text{O}_3$. Part 1. The system $\text{La}_{0.8}\text{Sr}_{0.2}\text{Co}_{1-y}\text{Fe}_y\text{O}_3$,” *Solid State Ionics*, vol. 76, no. 3–4, pp. 259–271, 1995.
- [3] Y. Teraoka, H. M. Zhang, K. Okamoto, and N. Yamazoe, “Mixed ionic-electronic conductivity of $\text{La}_{1-x}\text{Sr}_x\text{Co}_{1-y}\text{Fe}_y\text{O}_{3-\delta}$ perovskite-type oxides,” *Mater. Res. Bull.*, vol. 23, no. 1, pp. 51–58, 1988.
- [4] M. E. Lynch, Q. Yang, W. Qin, J.-J. Choi, M. Liu, and K. Blinn, “Enhancement of $\text{La}_{0.6}\text{Sr}_{0.4}\text{Co}_{0.2}\text{Fe}_{0.8}\text{O}_{3-\delta}$ durability and surface electrocatalytic activity by $\text{La}_{0.85}\text{Sr}_{0.15}\text{MnO}_{3\pm\delta}$ investigated using a new test electrode platform,” *Energy Enviromental Sci.*, vol. 4, pp. 2249–2258, 2011.
- [5] S. J. Skinner, “Recent advances in Perovskite-type materials for solid oxide fuel cell cathodes,” *Int. J. Inorg. Mater.*, vol. 3, pp. 113–121, 2001.
- [6] D. J. L. Brett, A. Atkinson, N. P. Brandon, and S. J. Skinner, “Intermediate temperature solid oxide fuel cells,” *Chem. Soc. Rev.*, vol. 37, no. 8, pp. 1568–1578, 2008.
- [7] S. Uhlenbruck, T. Moskalewicz, N. Jordan, H.-J. Penkalla, and H. P. Buchkremer, “Element interdiffusion at electrolyte–cathode interfaces in ceramic high-temperature fuel cells,” *Solid State Ionics*, vol. 180, no. 4–5, pp. 418–423, 2009.
- [8] T. Nguyen, K. Kobayashi, T. Honda, Y. Iimura, K. Kato, A. Neghisi, K. Nozaki, F. Tappero, K. Sasaki, and H. Shirahama, “Preparation and evaluation of doped ceria interlayer on supported stabilized zirconia electrolyte SOFCs by wet ceramic processes,” *Solid State Ionics*, vol. 174, no. 1–4, pp. 163–174, 2004.
- [9] G. C. Kostogloudis, G. Tsiniarakis, and C. Ftikos, “Chemical reactivity of perovskite oxide SOFC cathodes and yttria stabilized zirconia,” *Solid State Ionics*, vol. 135, pp. 529–535, 2000.

- [10] Y. Leng, S. Chan, and Q. Liu, “Development of LSCF–GDC composite cathodes for low-temperature solid oxide fuel cells with thin film GDC electrolyte,” *Int. J. Hydrogen Energy*, vol. 33, no. 14, pp. 3808–3817, 2008.
- [11] W. Wang and M. Mogensen, “High-performance lanthanum-ferrite-based cathode for SOFC,” *Solid State Ionics*, vol. 176, no. 5–6, pp. 457–462, 2005.
- [12] V. Dusastre and J. A. Kilner, “Optimisation of composite cathodes for intermediate temperature SOFC applications,” *Solid State Ionics*, vol. 126, pp. 163–174, 1999.
- [13] E. P. Murray, M. J. Sever, and S. A. Barnett, “Electrochemical performance of (La,Sr)(Co,Fe)O₃–(Ce,Gd)O₃ composite cathodes,” *Solid State Ionics*, vol. 148, pp. 27–34, 2002.
- [14] B. Kenney and K. Karan, “Engineering of microstructure and design of a planar porous composite SOFC cathode: A numerical analysis,” *Solid State Ionics*, vol. 178, no. 3–4, pp. 297–306, 2007.
- [15] D. Marinha, L. Dessemond, J. S. Cronin, J. R. Wilson, S. A. Barnett, and E. Djurado, “Microstructural 3D Reconstruction and Performance Evaluation of LSCF Cathodes Obtained by Electrostatic Spray Deposition,” *Chem. Mater.*, vol. 23, no. 24, pp. 5340–5348, 2011.
- [16] J. R. Wilson, J. S. Cronin, and S. A. Barnett, “Linking the microstructure, performance and durability of Ni-yttria-stabilized zirconia solid oxide fuel cell anodes using three-dimensional focused ion beam–scanning electron microscopy imaging,” *Scr. Mater.*, vol. 65, no. 2, pp. 67–72, 2011.
- [17] J. Laurencin, R. Quey, G. Delette, H. Suhonen, P. Cloetens, and P. Bleuet, “Characterisation of Solid Oxide Fuel Cell Ni–8YSZ substrate by synchrotron X-ray nano-tomography: from 3D reconstruction to microstructure quantification,” *J. Power Sources*, vol. 198, pp. 182–189, 2011.
- [18] E. Lay-Grindler, J. Laurencin, J. Villanova, I. Kieffer, F. Usseglio-Viretta, T. Le Bihan, P. Bleuet, A. Mansuy, and G. Delette, “Degradation Study of La_{0.6}Sr_{0.4}Co_{0.2}Fe_{0.8}O₃

- Solid Oxide Electrolysis Anode after High Temperature Electrolysis Operation,” *ECS Trans.*, vol. 57, no. 1, pp. 3177–3187, 2013.
- [19] X. Chen, C. Jin, L. Zhao, L. Zhang, C. Guan, L. Wang, Y. Song, C. Wang, and J. Wang, “Study on the Cr deposition and poisoning phenomenon at $(\text{La}_{0.6}\text{Sr}_{0.4})(\text{Co}_{0.2}\text{Fe}_{0.8})\text{O}_{3-\delta}$ electrode of solid oxide fuel cells by transmission X-ray microscopy,” *Int. J. Hydrogen Energy*, vol. in Press, p. <http://dx.doi.org/10.1016/j.ijhydene.2014.07.112>, 2014.
- [20] Y. Guan, X. Pan, G. Liu, Z. Liang, S. Chen, X. Zhang, Y. Xiong, Y. Tian, and C. Xia, “Analysis of impact of sintering temperature on microstructure of LSCF-SDC composite cathodes using nano-CT,” *Proc. Int. Soc. Opt. Photonics*, vol. 8851, p. 885112, 2013.
- [21] J. Villanova, P. Cloetens, H. Suhonen, J. Laurencin, F. Usseglio-Viretta, E. Lay, G. Delette, P. Bleuet, D. Jauffres, D. Roussel, A. Z. Lichtner, and C. L. Martin, “Multi-scale 3D imaging of absorbing porous materials for solid oxide fuel cells,” *J. Mater. Sci.*, vol. 49, pp. 5626–5634, 2014.
- [22] R. Bjørk, V. Esposito, E. M. Lauridsen, P. S. Jørgensen, J. L. Fife, K. B. Andersen, S. P. V Foghmoes, and N. Pryds, “In situ characterization of delamination and crack growth of a CGO – LSM multi-layer ceramic sample investigated by X-ray tomographic microscopy,” *J. Eur. Ceram. Soc.*, vol. 34, no. 12, pp. 3019–3025, 2014.
- [23] G. J. Nelson, K. N. Grew, J. R. Izzo, J. J. Lombardo, W. M. Harris, A. Faes, A. Hessler-Wyser, J. Van herle, S. Wang, Y. S. Chu, A. V. Virkar, and W. K. S. Chiu, “Three-dimensional microstructural changes in the Ni–YSZ solid oxide fuel cell anode during operation,” *Acta Mater.*, vol. 60, no. 8, pp. 3491–3500, 2012.
- [24] “<http://www.geodict.de/>.” .
- [25] J. Becke, R. Westerteiger, and A. Wiegmann, *GeoDict User’s Guide Release # 3*. 2008, pp. 145–163.

- [26] S. B. Adler, J. A. Lane, and B. C. H. Steele, “Electrode Kinetics of Porous Mixed-Conducting Oxygen Electrodes,” *J. Electrochem. Soc.*, vol. 143, no. 11, pp. 3554–3564, 1996.
- [27] J. Sar, F. Charlot, A. Almeida, L. Dessemond, and E. Djurado, “Coral Microstructure of Graded CGO/LSCF Oxygen Electrode by Electrostatic Spray Deposition for Energy (IT-SOFC, SOEC),” *Fuel Cells*, vol. 14, no. 3, pp. 357–363, 2014.
- [28] P. Cloetens, W. Ludwig, J. Baruchel, D. Van Dyck, J. Van Landuyt, J. P. Guigay, and M. Schlenker, “Holotomography: Quantitative phase tomography with micrometer resolution using hard synchrotron radiation x rays,” *Appl. Phys. Lett.*, vol. 75, no. 19, pp. 2912–2914, 1999.
- [29] G. Martinez-Criado, R. Tucoulou, P. Cloetens, P. Bleuet, S. Bohic, J. Cauzid, I. Kieffer, E. Kosior, S. Laboure, S. Petitgirard, A. Rack, J. A. Sans, J. Segura-Ruiz, H. Suhonen, J. Susini, and J. Villanova, “Status of the hard X-ray microprobe beamline ID22 of the European Synchrotron Radiation Facility,” *J. Synchrotron Radiat.*, vol. 19, pp. 10–18, 2012.
- [30] “[http://imagej.nih.gov/ij/.](http://imagej.nih.gov/ij/)”
- [31] D. Marinha, C. Rossignol, and E. Djurado, “Influence of electrospraying parameters on the microstructure of $\text{La}_{0.6}\text{Sr}_{0.4}\text{Co}_{0.2}\text{Fe}_{0.8}\text{O}_{3-\delta}$ films for SOFCs,” *J. Solid State Chem.*, vol. 182, no. 7, pp. 1742–1748, 2009.
- [32] L. O’Gorman, M. J. Sammon, and M. Seul, *Practical Algorithms for Image Analyses*, Cambridge University Press. 2008.
- [33] G. J. Nelson, W. M. Harris, J. J. Lombardo, J. R. Izzo, W. K. S. Chiu, P. Tanasini, M. Cantoni, J. Van herle, C. Comninellis, J. C. Andrews, Y. Liu, P. Pianetta, and Y. S. Chu, “Comparison of SOFC cathode microstructure quantified using X-ray nanotomography and focused ion beam–scanning electron microscopy,” *Electrochem. commun.*, vol. 13, no. 6, pp. 586–589, 2011.
- [34] J. R. Wilson, J. S. Cronin, A. T. Duong, S. Rukes, H.-Y. Chen, K. Thornton, D. R. Mumm, and S. Barnett, “Effect of composition of $(\text{La}_{0.8}\text{Sr}_{0.2}\text{MnO}_3\text{--Y}_2\text{O}_3\text{-stabilized}$

- ZrO₂) cathodes: Correlating three-dimensional microstructure and polarization resistance,” *J. Power Sources*, vol. 195, no. 7, pp. 1829–1840, 2010.
- [35] N. S. K. Gunda, H.-W. Choi, A. Berson, B. Kenney, K. Karan, J. G. Pharoah, and S. K. Mitra, “Focused ion beam-scanning electron microscopy on solid-oxide fuel-cell electrode: Image analysis and computing effective transport properties,” *J. Power Sources*, vol. 196, no. 7, pp. 3592–3603, 2011.
- [36] D. Gostovic, J. R. Smith, D. P. Kundinger, K. S. Jones, and E. D. Wachsman, “Three-Dimensional Reconstruction of Porous LSCF Cathodes,” *Electrochem. Solid-State Lett.*, vol. 10, no. 12, pp. B214–B217, 2007.
- [37] J. Joos, T. Carraro, A. Weber, and E. Ivers-Tiffée, “Reconstruction of porous electrodes by FIB/SEM for detailed microstructure modeling,” *J. Power Sources*, vol. 196, no. 17, pp. 7302–7307, 2010.
- [38] K. Matsuzaki, N. Shikazono, and N. Kasagi, “Three-dimensional numerical analysis of mixed ionic and electronic conducting cathode reconstructed by focused ion beam scanning electron microscope,” *J. Power Sources*, vol. 196, no. 6, pp. 3073–3082, 2011.
- [39] A. S. Martinez and J. Brouwer, “Percolation modeling investigation of TPB formation in a solid oxide fuel cell electrode–electrolyte interface,” *Electrochim. Acta*, vol. 53, no. 10, pp. 3597–3609, 2008.
- [40] A. Esquirol, J. Kilner, and N. Brandon, “Oxygen transport in La_{0.6}Sr_{0.4}Co_{0.2}Fe_{0.8}O_{3-δ} / Ce_{0.8}Ge_{0.2}O_{2-x} composite cathode for IT-SOFCs,” *Solid State Ionics*, vol. 175, pp. 63–67, 2004.
- [41] Y. Fukuda, S. Hashimoto, K. Sato, K. Yashiro, and J. Mizusaki, “High Temperature Defect Equilibrium, Solid State Properties and Crystal Structure of La_{0.6}Sr_{0.4}Co_{1-y}Fe_yO_{3-δ} (y=0.2, 0.4, 0.6, 0.8) for Cathode of Solid Oxide Fuel Cells,” *ECS Trans.*, vol. 25, no. 2, pp. 2375–2380, 2009.

V. Mechanical tests of coral microstructure of CGO-LSCF oxygen electrode for SOFC and SOEC

Mechanical tests on coral microstructure of CGO-LSCF oxygen electrode for SOFC and SOEC

Jaroslav Sar^{1,2,3}, Amélia Almeida^{3*}, Laurent Dessemond^{1,2}, Elisabeth Djurado^{1,2}.

¹ Univ. Grenoble Alpes, LEPMI, F-38000 Grenoble, France;

² CNRS, LEPMI, F-38000 Grenoble, France;

³ Dep. Eng. Quimica, Instituto Superior Tecnico, Av. Rovisco Pais, Torre Sul, 1049-001 Lisboa, Portugal

**Amelia.Almeida@ist.utl.pt*

V.1. Abstract

The goal of this work is to investigate mechanical properties of CGO-LSCF composite as a potential oxygen electrode for SOFC and SOEC. The electrode is characterized by highly porous morphology called coral microstructure. The mechanical behavior was analyzed by scratch and ultramicroindentation tests. Instead of fracturing and detachment as a typical behavior for a brittle material under loading, corals break in three-stage regime under loading similarly to powder densification. Firstly, the top part of corals are broken and fall down on the surface, then the material is compacting into an increasingly denser layer, and finally, in the material is almost fully compacted. The same breaking mechanism was found for both tests. The mechanical parameters such as hardness and Young's modulus were determined in each regime by ultramicroindentation test. The image analysis showed a porosity decrease from 60 to 5 vol.% during loading. The parameters values were increasing with decreasing level of the porosity in the coating during the mechanical tests.

Keywords: Solid oxide fuel cells (SOFC), Solid oxide electrolysis cells (SOEC), Oxygen electrode, scratch test, indentation test, mechanical properties.

V.2. Introduction

Nowadays, fuel cells technologies are mainly focused on hydrogen production as a potential fuel (Solid Oxide Electrolyser Cells) as well as on production of the electricity directly from electrochemical reaction between fuel and oxygen (Solid Oxide Fuel Cells). The current

research in solid oxide cells focuses on the reduction of the total resistance of the cell. It can be achieved by reducing the electrolyte thickness, since the cell resistance is proportional to the electrolyte thickness (distance for oxygen ions to transfer from one side of the cell to the other). However, requirements for the electrolyte limit further decreasing of the thickness. The electrolyte has to be dense to avoid fuel-oxygen mixing. The further decrease of the cell resistance by increasing the oxygen gas diffusivity, requires the development of new oxygen electrodes with highly porous microstructures. An example of such microstructure is a coral microstructure characterized by a two-scale porosity level in which macroscopic porosity exists between corals and nanoscale porosity on the corals surface and inside corals, increasing the total available surface area. Such porosity facilitates, on one hand, the adsorption process and provides a high active zone for oxygen reduction reaction. On the other hand, a total volume porosity of 75 % decreases the mechanical strength of the electrode. In highly porous materials (above 50 vol.% porosity) the mechanical properties are controlled by the distribution of the solid phase unlike denser materials (below 50 vol.% porosity) where the mechanical properties are controlled by the presence of isolated pores [1]. During cell operation, the mechanical stresses on the electrode result from: the differences between components thermal expansion, the mechanical loads applied to ensure a good contact of the cell components and, especially for the stack, its own weight. For example, the reduction of the most common fuel electrode material nickel oxide to metallic nickel leads to an important shrinkage of the electrode volume. The oxygen electrode has a minor influence on the stress, but its mechanical failure (delamination, cracking) cuts the ionic and electronic conduction paths. The mechanical properties of the oxygen electrode may be evaluated by the materials hardness, elastic modulus and thermal compatibility. In this work, the mechanical properties of a CGO-LSCF oxygen electrode with a coral microstructure developed by Electrostatic Spray Deposition were investigated using micro-scratch and ultramicroindentation tests. The mechanical behavior of this material was evaluated and the mechanisms of material deformation under loading were analyzed.

V.3. Experimental

V.3.1. Electrode preparation

Coral microstructure of CGO-LSCF composite was deposited by electrostatic spray deposition on a homemade YSZ substrate in a disk form with a diameter of 19 mm. Precursor solutions were prepared based on: lanthanum nitrate hexahydrate ($\text{La}(\text{NO}_3)_3 \cdot 6\text{H}_2\text{O}$), strontium chloride hexahydrate ($\text{SrCl}_2 \cdot 6\text{H}_2\text{O}$), cobalt nitrate hexahydrate ($\text{Co}(\text{NO}_3)_2 \cdot 6\text{H}_2\text{O}$) and iron (III)

nitrate nonahydrate ($\text{Fe}(\text{NO}_3)_3 \cdot 9\text{H}_2\text{O}$) for $\text{La}_{0.6}\text{Sr}_{0.4}\text{Co}_{0.2}\text{Fe}_{0.8}\text{O}_{3-\delta}$ solution and cerium nitrate hexahydrate ($\text{Ce}(\text{NO}_3)_3 \cdot 6\text{H}_2\text{O}$) and gadolinium nitrate ($\text{Gd}(\text{NO}_3)_2$) for $\text{Ce}_{0.9}\text{Gd}_{0.1}\text{O}_{1.95}$ solution. Adequate amounts of salts to prepare a total concentration of 0.02 mol.L^{-1} were dissolved in distilled water and ethanol in 5:1 volume ratio to create LSCF precursor solution; diethylene glycol monobutyl ether, well known as butyl carbitol ($\text{CH}_3(\text{CH}_2)_3(\text{OC}_2\text{H}_2)_2\text{OH}$) and ethanol in 4:1 volume ratio for CGO precursor solution. Fig. V-1 presents schema of the ESD setup.

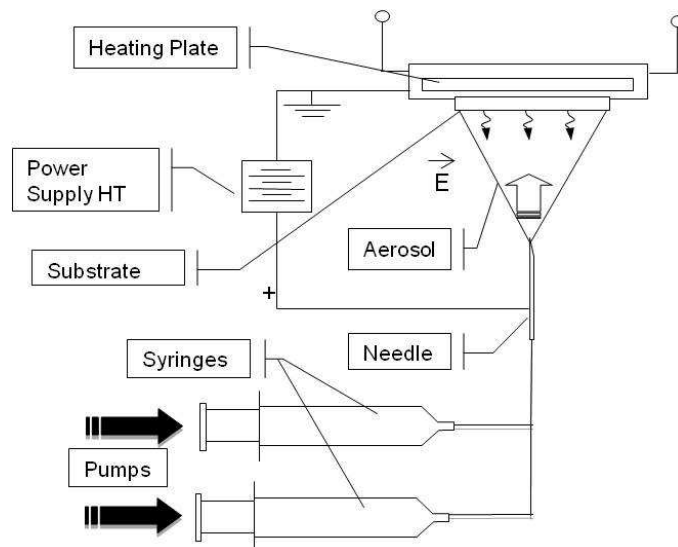


Fig. V-1. Schema of the ESD setup used for coral CGO-LSCF deposition

The deposition parameters are listed in the Table III-1. There were prepared graded and homogeneous composition of CGO and LSCF by changing flow rates of precursor solutions. The deposition was divided in three steps. Firstly, deposition of single CGO to create a barrier diffusion layer, then deposition either graded or homogeneous composition of CGO-LSCF and finally deposition of LSCF. The substrate temperature was $400 \text{ }^\circ\text{C}$ calibrated by thermocouple. The positive high voltage applied between the nozzle and the grounded substrate ranges from 7 to 11 kV. The deposited coating was in a shape of disk with a diameter of 17 mm. After the deposition, the heat treatment was performed at $900 \text{ }^\circ\text{C}$ for 2 h with a rate of $3 \text{ }^\circ\text{C.min}^{-1}$ in air.

The particular microstructural description of coral microstructure can be found in Chapter II [2] together with electrochemical properties of homogeneous and graded CGO-LSCF corals Chapter III.

V.3.2. Mechanical characterization

V.3.2.1. Microscratch tests

The microscratch tests were performed in EMPA – Swiss Federal Laboratories for Materials Science and Technology, Thun, Switzerland using a MTS XP Nanoindenter equipment. The indenter used was a WC sphere with a diameter of 0.5 mm. The tests were made on the top surface of the samples glued to the holder using silver paste. In order to try to assess the coating-substrate adhesion resistance, some preliminary tests were carried out under progressive loads up to 40 N, along a distance of 5 mm. To investigate the mechanical behaviour at microscale the scratch tests were made under progressive loading from 0 to 50 N, to 200 mN along a distance of 1 mm and to 500 mN along a distance of 5 mm, at a speed of $10 \mu\text{m}\cdot\text{s}^{-1}$.

V.3.2.2. Instrumented indentation tests

Ultramicroindentation tests were performed with a Shimadzu DUH211S ultramicroindenter using a Berkovich indenter. The tests were made on the top surface of the samples, using a load-creep-unload-creep cycle. The creep stages had a duration of 15 s. Initially, the tests were carried out up to a maximum force of 500 mN. At least 5 tests were carried out in different regions of the sample and the results presented are the average of those measurements.

The indentation hardness was determined from indentation depth according to Eq. I-18. The elastic modulus was determined from the unloading part of the load-displacement curves, based on the contact stiffness and the indenter depth. The results for hardness and Young's modulus presented are the average of 5 measurements.

V.3.3. Microstructure analysis

After the indentation and scratch tests the surface of the samples was analyzed by FEG-SEM in order to characterize the morphology of the structural features produced that will allow understanding the mechanisms of materials deformation and fracture occurring

Image analysis was performed on several images in different regions along the scratch length using imageJ software package [3], [4].

V.4. Results and discussion

V.4.1. Microscratch tests

A full scratch performed using progressive loading up to a maximum force of 40 N is presented in Fig. V-2. The width of the scratch increased progressively as the load increases. Contrary to the expectations, no fracture of the coating was observed and it was not possible to determine the coating/substrate adhesive resistance. Instead, it is clearly visible from SEM images (Fig. V-3) that since very early stages of scratching (relatively low values of normal force), there is a relatively smooth compact layer of material that forms and that becomes smoother and less porous towards the end of the scratch in the high load regions. The beginning of the scratch (region A in Fig. V-2) is formed of aggregated particles of the coral structure fractured by the tip during contact. As the load increases, this particles aggregate even more and start to form a relatively dense layer which porosity rapidly decreases originating a densified coating that does not fracture nor detach form the substrate, at least up to the maximum load used (40 N).

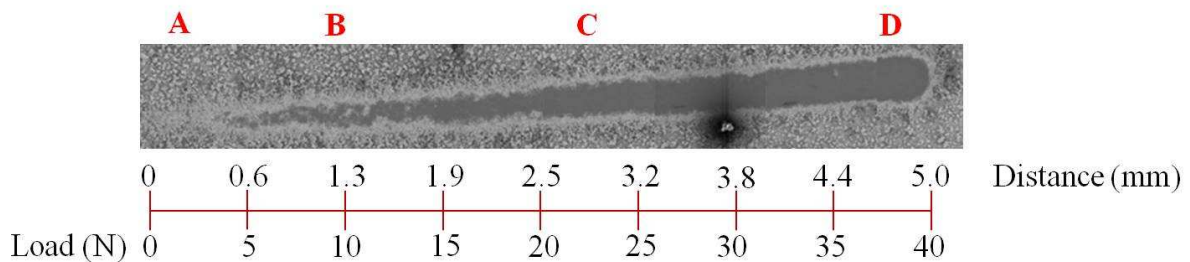


Fig. V-2. Scratch made with progressive loading up to 40 N.

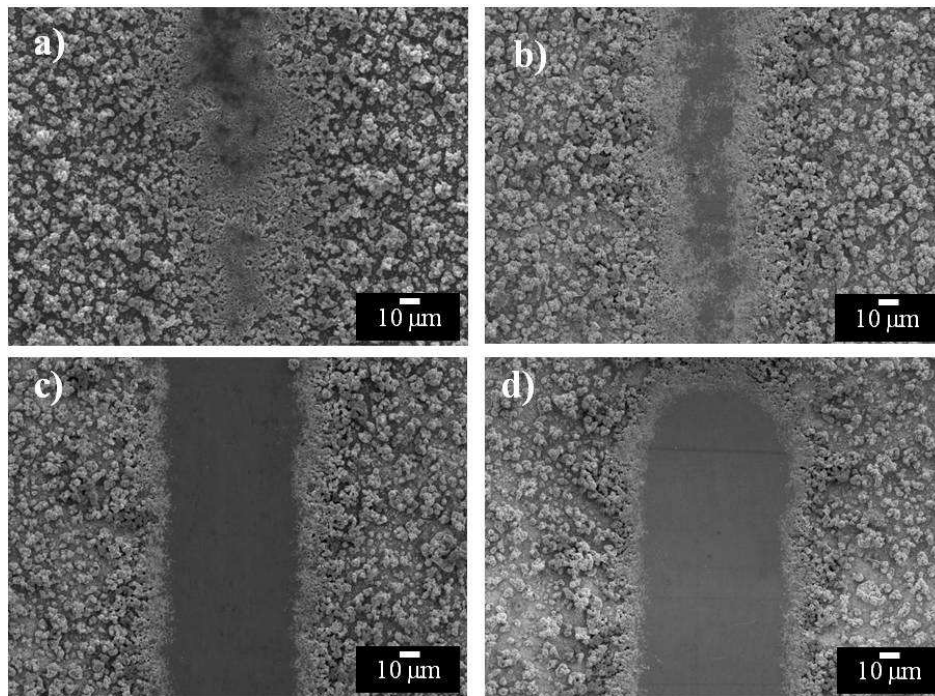


Fig. V-3. Evolution of coating structure along the scratch length made with increasing load up to 40 N of Fig V-2; a) region A; b) Region B; c) region C; d) region D.

This is confirmed by EDS analysis results performed at the end of the scratches (region D) that showed that the scratch contains La (Fig. V-4b) and Sr (Fig. V-4c) and a negligible amount of Zr (Fig. V-4d), what indicates that the coating material is still present in the scratch. The scratch test did not remove the coral film from the YSZ substrate, but pressed it into a compacted layer, instead, demonstrating the absence of brittle fracture behavior that is commonly observed in ceramic materials.

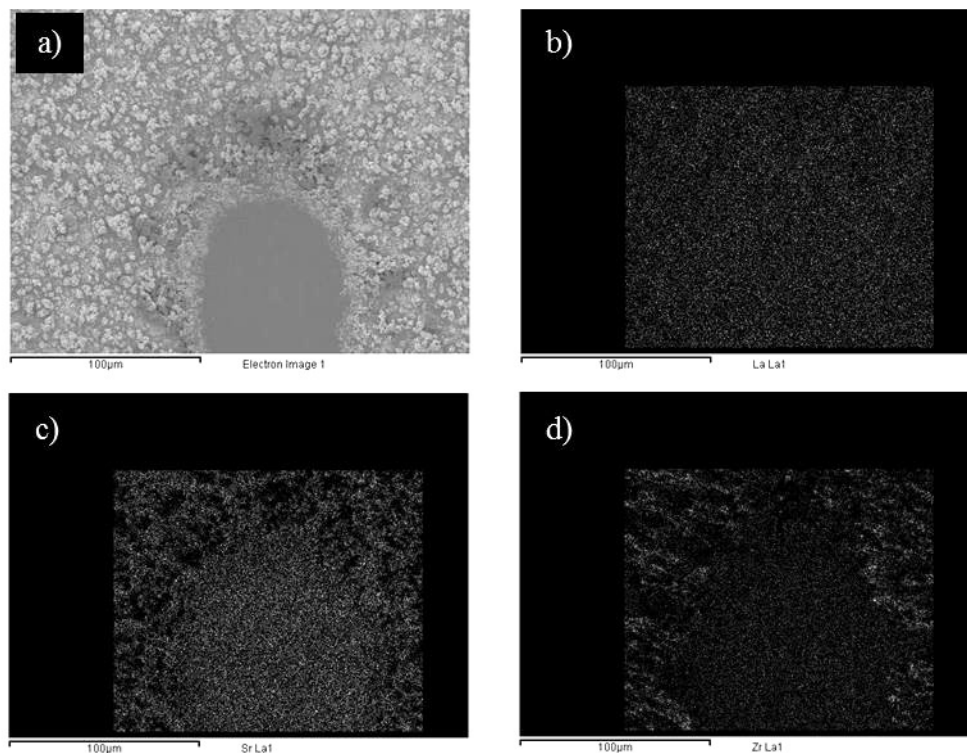


Fig.V-4. EDS mapping at the end (40 N side) of the scratch performed with a progressive load up to 40 N: a) SEM image; b) La (La_1) distribution map; c) Sr ($Sr La_1$) distribution map and d) Zr ($Zr La_1$) distribution map.

In order to try to understand the behavior of the coating before compaction microscratch tests were also carried out at significantly lower maximum loads.

A displacement depth-distance curve obtained for tests carried out up to a maximum load of 500 mN is presented in Fig. V-5. Though there is some variability of the results obtained in scratches made in different regions of the sample (also due to heterogeneity in the sample structure), all curves present evolution of the displacement depth along the length. Three regions can be distinguished corresponding to different slopes in the curve.

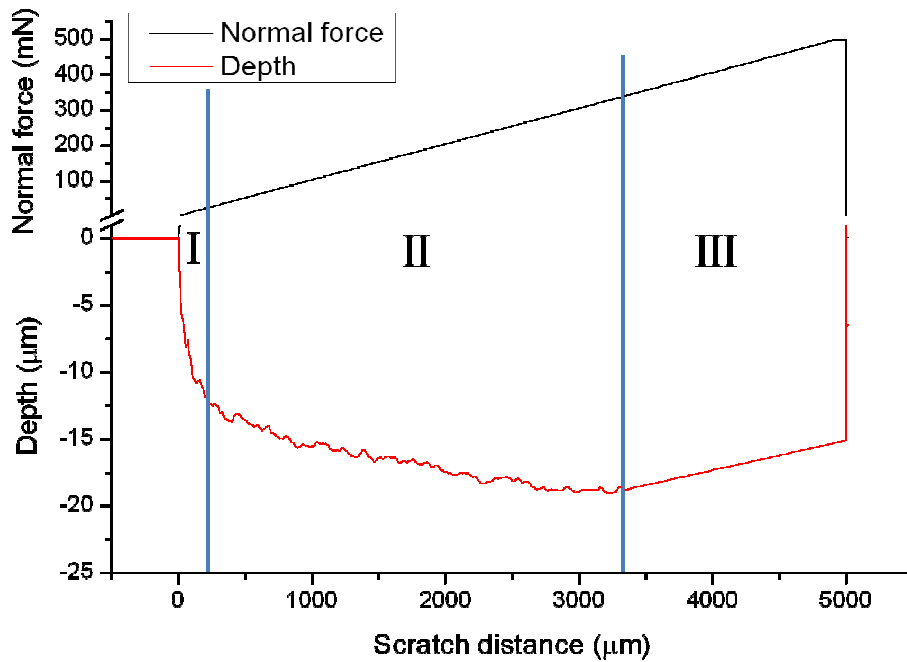


Fig. V-5. Depth and normal force variation with scratch distance in test made with progressive loading from 0 to 500 mN.

Though the limits of each region vary from test to test, in all cases region I occurs in the 0 – 400 μm of the scratch length to up where the force reaches about 40 mN while the depth increases up to 10-14 μm . It is characterized by a sharp increase of depth in a small scratch distance. Region II is characterized by a smoother increase of the depth. This region extends up to about 3340 μm of the scratch length, corresponding to normal forces around 340 mN and maximum depths of 14-19 μm .

Table V-1. Values of scratch length, force and depth for the three regions detected during scratching with progressive loading from 0 to 500 mN.

Region	Scratch length (μm)	Force (mN)	Depth (μm)
I	0 – 400	0 – 42	0 – 14
II	400 – 3340	42 – 340	14 – 19
III	3340 – 5000	340 – 500	19 – 15

This region corresponds to the densification stage following region I. In region III, the scratch distance and force continue to increase up to the final values of 5000 μm and 500 mN, respectively, before unloading. In this region the depth decreases from the maximum value attained at the end of region II to about 15 μm . This last region corresponds most probably to a high level of material densification where material build up in front of the scratch tip occurs. This effect is not observed in scratch tests carried out at lower loads, where a continuous increase in the depth is observed with increasing load along the scratch length (Fig. V-6). This confirms that material pile-up in front of the tip occurs only in region III after considerable densification of the material and that this region starts at loads higher than 200 mN. Table V-1 lists values of scratch length, force and depth for the three regions during scratching with progressive loading from 0 to 500 mN.

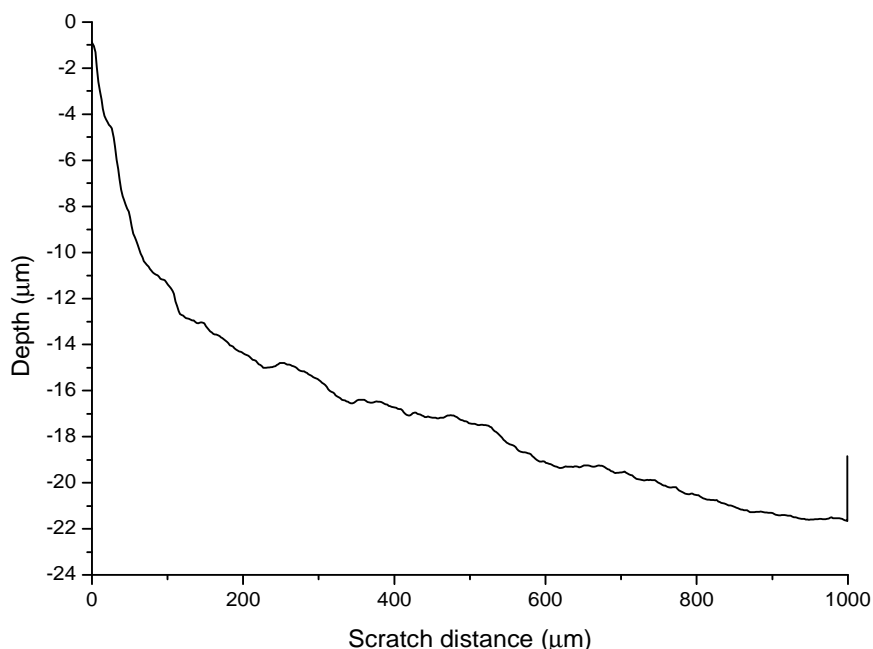


Fig. V-6. Depth variation with scratch distance during microscratch test with progressive loading from 0 to 200 mN.

The FEG-SEM observation of the surface of the scratches in each region has allowed understanding the mechanism involved in each of them. Images of the scratch in region I are presented in Fig. V-7. The material in this region presents very little damage and most of the corals seem intact. However, the high magnification images show that some of these corals (probably the tallest) have fractured and their top surface show the open porosity characteristic of its inner structure. Some cracks are even observed in the base of surrounding corals. The indenter is far from the substrate and touches only the tops of a few corals. Broken

parts of corals fall down on the surrounding area. Since the density of the material at the top part of corals is low, despite the force being very low, it results in a relatively high contact pressure at those tips that easily breaks the corals. This occurs even for very small loads between 0 – 10 mN. In this case, the increase in force is small and the depth increases rapidly.

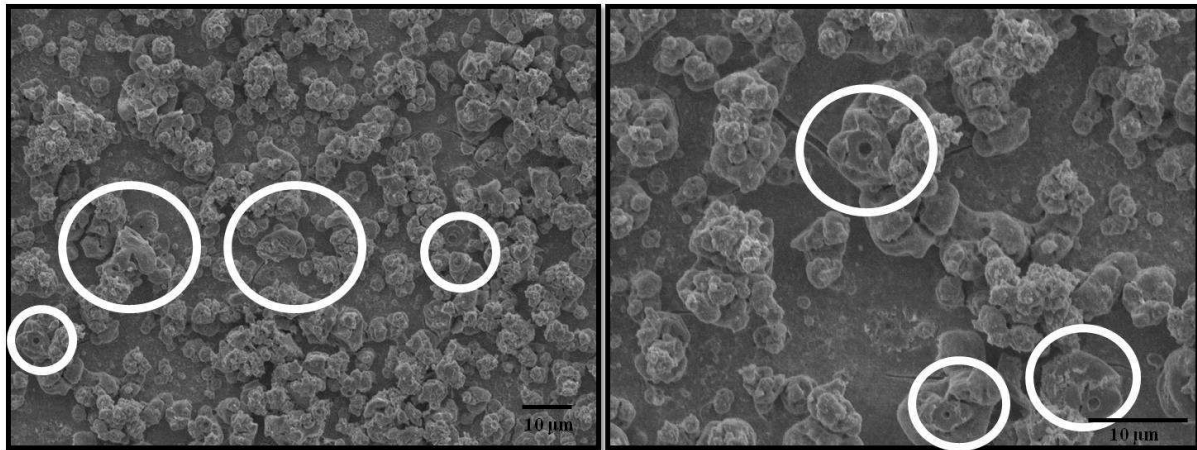


Fig. V-7. FEG-SEM pictures at the beginning of region I formed during a microscratch test up to 500 mN.

Further loading leads to fracture of some corals (some closer to the top, others closer to the base as seen in Fig. V-7) and the fractured fragments start filling the empty spaces in the structure. Fracture of the corals continues as observed in the serrations present in the curve that correspond to the several coral fracture events that occur. As the density of the material becomes larger in this region (due to the fractured fragments), the indenter starts compacting the material into an increasingly denser layer. In this compacting stage the force increases in less pronounced than in region I due to a higher fraction of material under the contact tip. Fig. V-8 shows FEG-SEM pictures of the surface of the scratch in region II, where compacted fragments can be clearly seen.

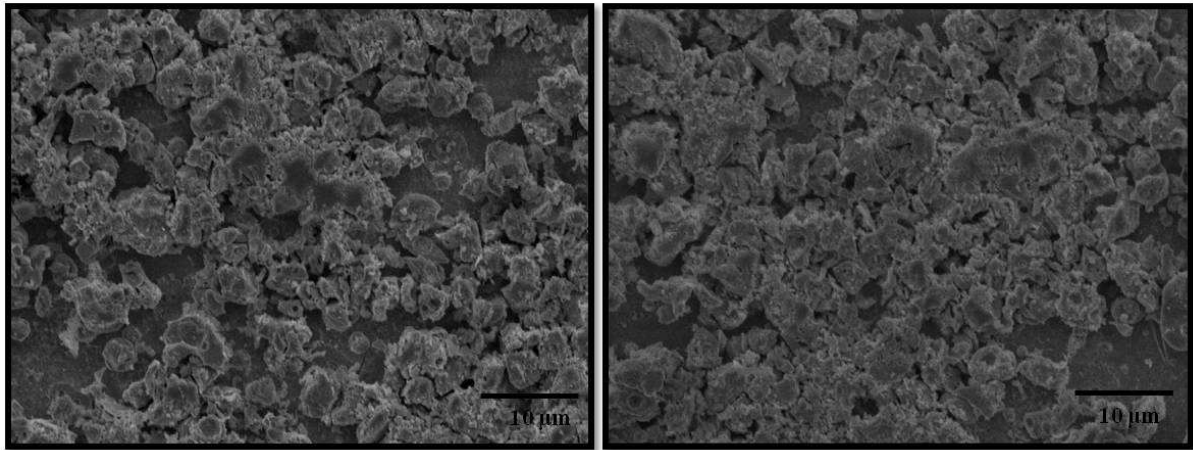


Fig. V-8. FEG-SEM pictures of region II formed during a microscratch test up to 500 mN.

Fig. V-9 shows the surface of the scratch corresponding to region III. This surface presents a high level of compaction with some residual porosity being detected between the compacted fragments. The densification level is, however, lower than that observed in the scratches in Fig. V-3d produced at much higher load. In this region, there is a decrease in depth with the increasing force, that probably corresponds to the build-up of material at the end of the scratch that sometimes occurs.

Image analysis performed on images of this surfaces allow estimating an areal fraction of solid material that increases from about 40 % in the initial surface to about 65 % in region II and about 90 % in region III.

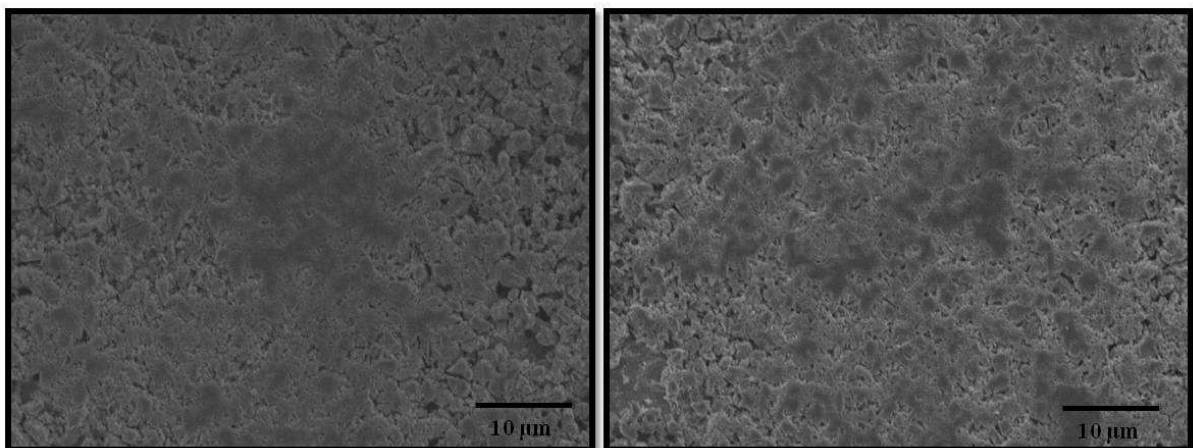


Fig. V-9. FEG-SEM pictures of the region III formed during a microscratch test up to 500 mN.

The mechanism of mechanical deformation of the coral structure under loading is illustrated in the schematics presented in Fig. V-10.

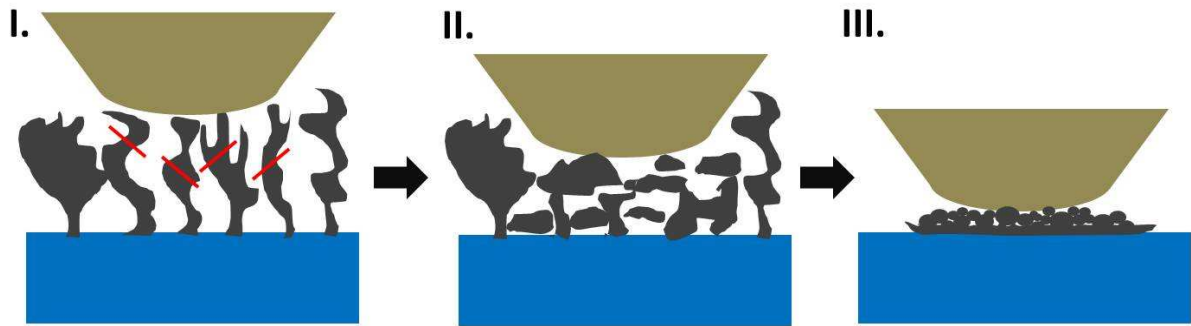


Fig. V-10. The mechanical deformation of the coral microstructure under loading

Fig. V-11 presents a cross sectional view of a compacted layer in a fractured sample of a scratch produced up to 50 N. A layer of fully dense material with a thickness of about 2 μm detached from the sample most probably due to the propagation of subsurface cracks developed in the coating (visible) parallel to the surface. This indicates that the fracture mechanism of the material after compaction has a cohesive nature instead of the adhesive nature that could be expected for this type of material.

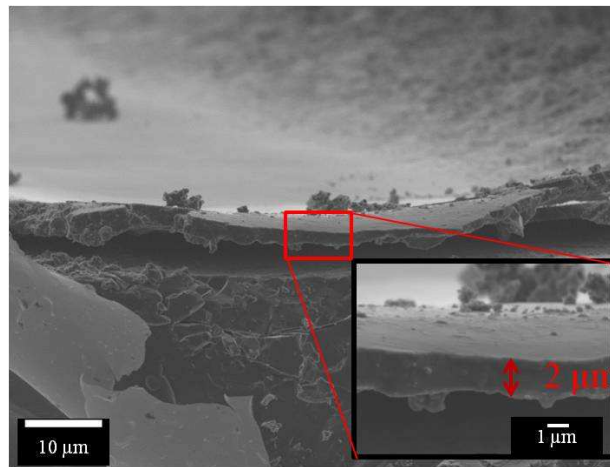


Fig. V-11. Cross-section of a fractured compact layer in a sample with a scratch up to 50 N.

The coral microstructure behaves in a particular mode under the load during scratching. The microstructure is significantly open and consists of corals growth from a substrate, similar to pillars but with a relatively high degree of nanoporosity. Under loading, each coral acts like an isolated column. The stresses are most probably concentrated on the existing pores generating cracks. When the stress reaches a critical value they propagate through the coral up to its free surface causing its fracture. Cracks in one coral have very little probability of propagating into the next one since there is little connection between them.

V.4.2. Instrumented microindentation tests

To qualitatively evaluate the mechanical properties of the coatings structure static indentation tests were carried out in a wide range of loads corresponding to the different regions detected previously in the scratch tests.

V.4.2.1. Indentation tests at 500 mN

Indentation is a technique similar to scratch testing performed with a tip that is limited to displacements in the z-direction. Ultramicroindentation tests were performed using Berkovich tip with a maximum load of 500 mN. Fig. V-12 shows one of the loading/unloading curves and the residual indentation left on the sample surface after unloading. Similarly to what was observed in the scratch tests it is possible to detect several regions in the loading curve with different slopes, though the transitions are much less obvious. The values extracted for the transitions are presented in Table V-2. Though the transitions between the different regions do not occur for the same levels of load, these regions have the same origin as in the scratch test. The differences are however predictable in view of the different indenter geometries being used in both tests that result in different contact area functions and stress distributions. This is especially significant in the lower load region, where the discrepancy is higher.

Table V-2. Values of depth and force for three regions during ultramicroindentation with a maximum load of 500 mN

Region	Depth (μm)	Force (mN)
I	0 – 7.4	0 – 78
II	7.4 – 8.7	78 – 230
III	8.7 – 9.4	230 – 500

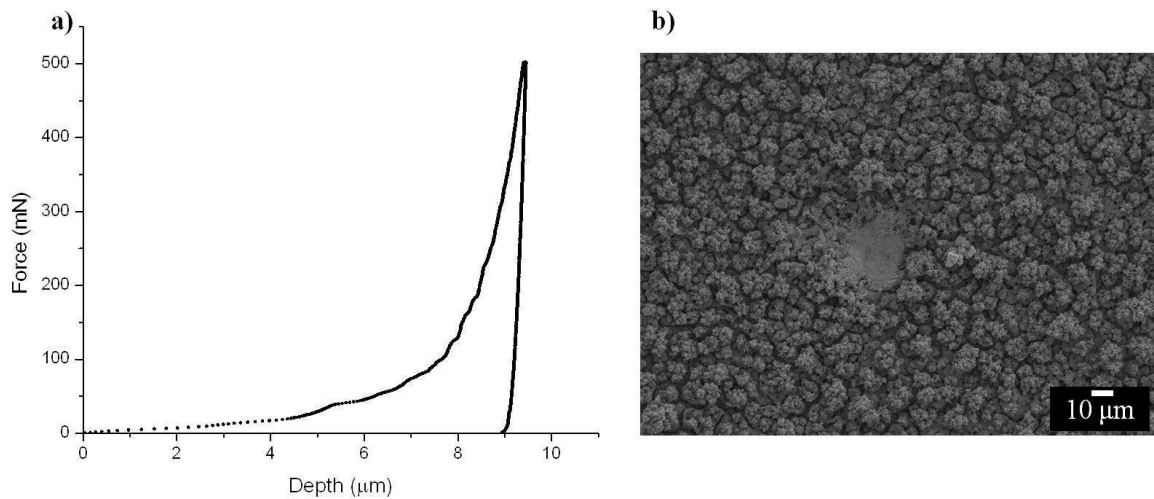


Fig. V-12. Loading-unloading curve for CGO-LSCF coral coating with a maximum loading force of 500 mN using a Berkovich tip a), and the indentation left on the sample surface.

A Young's modulus of 18.4 ± 1.3 GPa and a hardness value of 99.2 ± 8.5 MPa have been obtained from these tests. These values are significantly lower than those obtained by Li et al. [5] for a CGO-LSCF composite with 98 % of the theoretical density produced by pressing and sintering of CGO and LSCF powders (135 GPa and 8.9 GPa, respectively). This difference may be due, on one hand, to the lower density of the compacted CGO-LSCF structure, on the other hand, to the fact that the current structures were heat treated at 900 °C while those of Li et al. [5] were sintered at a higher temperature for longer time.

Indentation tests performed with loads of 500 mN showed a compacting mechanism of the coral microstructure confirming the results obtained previously in the scratch tests. To assess the properties of the coral structured coating itself indentation tests were carried out at much lower loads, corresponding to values in regions I and II identified previously. This approach allowed also a finer determination of the transitions between the different regions and the corresponding material behavior. The results obtained in the various tests performed at loads from 2 to 40 mN are presented and discussed as follows.

V.4.2.2. Indentation tests at low loads: 2 – 40 mN

The further indentation tests were done with reduced loads in order to investigate the first stages of coral cracking corresponding to region I and the eventual transition to region II. With this purpose, indentation tests were done with maximum forces up to 2, 5, 10, 20, 30 and 40 mN. Fig. V-13 presents the indentation curves obtained at maximum forces from 2 to 40 mN.

The load-displacement curves in Fig. V-13 confirm the transitions between the different regions found in the scratch tests. It is clear that the curves at loads up to 20 mN correspond to indentations of the coating in region I. The curves at very low loads present serration with plateaus that correspond to interaction of the tip with individual or only a few corals. The plateaus correspond to the collapsing of the coral structure by fracturing of the solid phase. When the indenter contacts the material the crack generated progressively propagates through the coral causing a large displacement at relatively constant load. In the curves corresponding to 30 mN and 40 mN it is already clear the transition from region I to region II occurring at loads of 15 and 20 mN, respectively, in accordance with the results of the scratch tests.

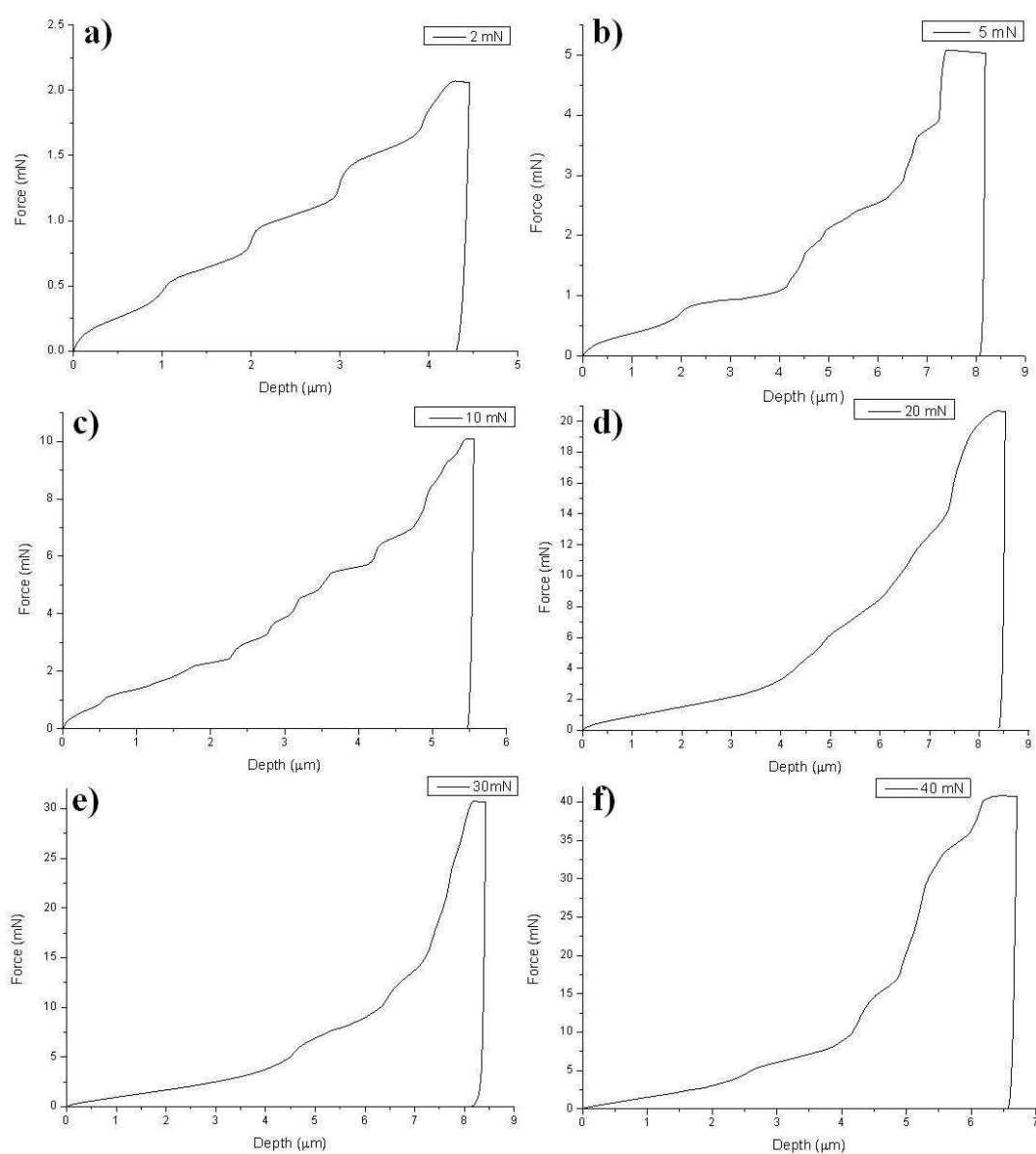


Fig. V-13. Loading/unloading curve for CGO-LSCF coral microstructure with a maximum force of a) 2 mN, b) 5 mN, c) 10mN, d) 20 mN, e) 30 mN and f) 40 mN.

The values of hardness and Young's modulus determined in these tests are presented in Table V-3 as a function of the maximum load used. The values increase significantly with the load. Nevertheless, one must be aware that tests done at the extremely low values of maximum force have a significant influence of factors like the surface conditions (humidity, adsorbed species), indenter geometry defects, etc, which contribution to the overall result are very high. Another factor contributing to the high variability of results is the low scale of the contact that occurs at this level of forces. This contact is almost at individual level and the contact area geometry may change. Besides, at very low forces each indentation corresponds almost to a different material thickness and density. Therefore, the values of the Young's modulus and hardness obtained from the lower load curves should be taken with appropriate care (Table V-3).

Table V-3. Hardness (H) and Young's modulus (E) obtained from indentation tests with maximum forces from 2 - 500 mN

Max. Load (mN)	H (MPa)	E (GPa)
2	2.1 ± 0.8	1.1 ± 0.3
5	2.8 ± 1.3	2.7 ± 0.6
10	6.6 ± 2.3	5.1 ± 1.0
20	6.7 ± 0.5	6.6 ± 0.6
30	12.8 ± 2.7	8.8 ± 1.4
40	19.5 ± 4.7	11 ± 2
500	99.2 ± 8.5	18.4 ± 1.3

G. Pecanac [6] investigated the mechanical properties of pure CGO and LSCF using 3-point bending tests and found a linear relation between the Young's modulus of CGO with porosity. The value for dense CGO was about 192 GPa and decreased to about 50 GPa for the material with 40 % porosity. A similar trend was found for pure LSCF which value of Young's modulus decreased from 48 GPa for the dense material to 16 GPa for the material with 46 % porosity.

Given the fact that the coatings developed in the present study are CGO-LSCF composites the values obtained in the present study using indentation methods are well compatible with those measured by G. Pecanac [6] using macrotechniques. On the other hand, since in the deposition process the last material to be deposited is pure LSCF, it is not surprising that the

values of Young's modulus measured with lower loads that affect a thinner layer of material, are closer to those of LSCF than those measured at higher loads that affect a higher thickness of material where the fraction of CGO is higher. Thus, in the present material a variation of properties along the depth may be expected, on one hand, due to the variations in composition of the coating and, on the other hand, due to the variations in porosity (material density) that occur during indentation.

V.4.3. Calculation of the contact pressure

According to Hertz theory, the elastic contact between a sphere and a plane (Fig. V-14) under a normal force (F), the area of contact (A) is given by:

$$A = \pi a^2 = \pi \left(\frac{3}{4} \frac{FR}{E_r} \right)^{2/3} \quad (\text{Eq. V-1})$$

where R is radius of curvature of the sphere, a the radius of the contact area and E_r the reduced Young's modulus defined by Eq. I-20 (Chapter I).

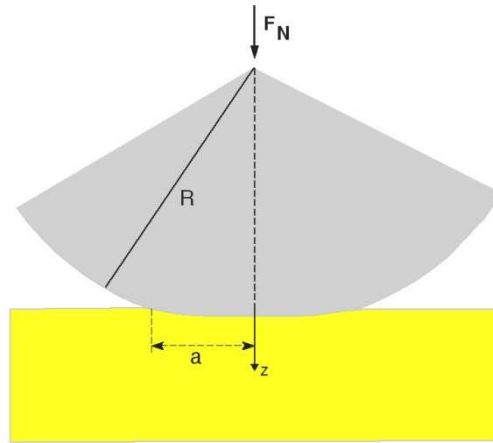


Fig. V-14. The sketch of the elastic contact between a sphere and a plane.

The average compressive stress is then given by:

$$P_0 = \frac{2}{3} \left(\frac{6FE_r^2}{\pi^3 R^2} \right)^{1/3} \quad (\text{Eq. V-2})$$

In the case of a discontinuous material, as occurs in the present structure, the load is distributed among the coral surfaces in contact with the tip and the real contact pressure is given by:

$$P_r = \frac{F}{A_r} \quad (\text{Eq. V-3})$$

where A_r is the real area of contact between the tip and the corals.

Since $A_r < A$, the real average pressure (P_r) could be significantly higher than P_0 and may be determined by (Eq. V-4):

$$P_r = \frac{F}{A_r} = \frac{P_0}{f} \quad (\text{Eq. V-4})$$

where $f = A_r/A$.

This method was used to estimate the real contact pressure evolution along the scratches performed up to 500 mN.

The evolution of the contact pressure as a function of the applied load is presented in Fig. V-15. Both the nominal (P_0) and the real (P_r) contact pressure curves are presented. The real contact pressure variation has been determined using Eq. V-4 by considering the real contact area estimated from the different levels of compaction in each region that were determined by image analysis in section V-4.1.

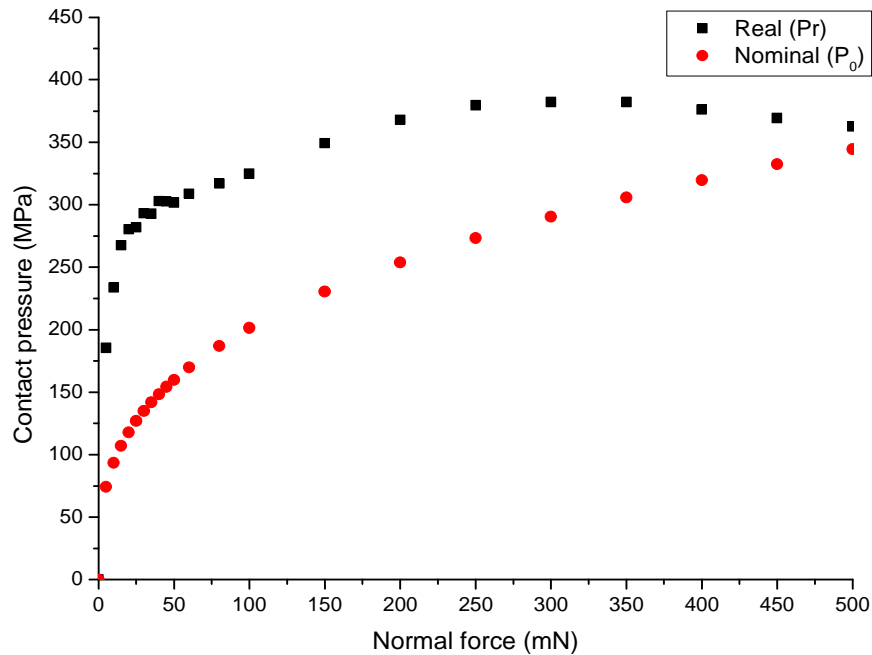


Fig. V-15. Variation of the real and nominal contact pressures as a function of the normal force applied during loading up to 500 mN.

From this it is possible to express the transitions of Table V-1 in terms of contact pressure instead of normal force (Table V-4).

Table V-4. Contact pressure values corresponding to the transitions between the three regions detected during scratching with progressive loading from 0 to 500 mN

Region	Transition Force (mN)	Nominal contact pressure (MPa)	Real contact pressure (MPa)
I	10 - 20	100 ± 15	250 ± 20
II	250 - 300	280 ± 12	380 ± 10
III	500	344 ± 13	362 ± 10

It is well known (Tabor's relation [7]) that, during indentation, the mean pressure between the indenter and the specimen (hardness H) is directly proportional to the material's yield stress in compression (σ_y), and can be expressed as $H \approx 3 \sigma_y$. Therefore, from indentation tests, at least an estimate of the material's yield stress in compression may be obtained.

Using this criterion and considering that material yield occurs in the transition between regions I and II, a value of 83 MPa is obtained for the yield stress. Since the fracture of the corals starts in region I, considering that this fracture occurs right after yielding, as is typical of materials with very narrow plastic regime, one may consider that the fracture strength of the coating developed in the present study is close to this value.

This value is only slightly higher than that obtained by Huang et al. [8] for sintered LSCF (70 MPa) and by Pecanac [6] for sintered CGO (60 MPa). However, the yield stress value obtained in the present study is significantly lower than that calculated from the hardness value (8.9 GPa) obtained by Li et al. [5] using Tabor's criterion (≈ 3000 MPa).

At first, one could attribute this discrepancy to the fact that the samples of Li et al. were sintered at temperatures higher than the materials developed in the present study. However, the same applies to the samples in the studies of Huang et al. [8] and Pecanac [6] where the results obtained are closer to the ones in the present study.

V.4.4. Comparison with powder pressing

The coral microstructure is a unique structure especially in solid oxide fuel cells technology. It is hard to find accurate equivalent for this structure to make sufficient data comparison. However, it was possible to find similar cracking behavior under applied load [9]–[12]. The mechanism presented in this study for the mechanical behavior of the material under loading based on a 3-stage model that involves fracture of single corals followed by compaction is similar to the mechanism observed during compaction of powder materials. The characteristic steps observed during powder pressing are usually named [12]:

- i) Particles reorientation: first short step with no influence on densification
- ii) Particles plastic deformation: flattening of the particles and creating a contact between them
- iii) Impinging of particles: final step that creates a material that is harder and more resistant

Chen et al. [9] and Poquillon et al. [10] used powders with morphologies that could be somehow related to the coral microstructure. The coral structure deposited by ESD is built of CGO and LSCF particles. Each coral should be considered as a cluster of agglomerated particles. During loading, the corals firstly crack at the top or near the interface with the substrate since at the upper coating part there is a small contact with the indenter, thus a very high contact pressure is produced. Secondly, the corals and respective fragments are fractured into small particles (powdering) filling up the empty spaces on the coating. The small particles (powder) start compacting into an increasingly denser layer. This mechanism that occurs during both the scratch and the indentation tests of the coral microstructure is equivalent to what occurs during the densification process of a powder.

V.5. Conclusions

This work has allowed studying the mechanical behavior of the CGO-LSCF coating with a coral microstructure under compressive forces applied during scratch and ultramicroindentation tests. It was found that the material does not behave like a typical brittle coating that fractures and detaches from the substrate during the tests. Instead, the deformation behavior during loading involves a three-stage regime. In the initial stage of contact, at low nominal stresses (0-100 MPa), individual corals start to fracture and the structure starts to disintegrate. As the stress increases up to 280 MPa the material enters a stage of compaction of the fragments into an increasingly denser layer. In the final stage, the material may reach an almost fully dense layer, which density may vary from 95 to 100 % depending of the maximum load applied. At a nominal contact pressure of 344 MPa a 95 % of the material was obtained dense. In the last stage, the material behaves like a compact solid. The material pile-up in front of the tip what may occur even during scratching. This mechanism of corals cracking and densification is similar to that observed in the densification of powders. The mechanical properties (hardness and Young's modulus) of the coating in the different stages of deformation were determined by ultramicroindentation tests at loads in the different regimes. The values of hardness and Young's modulus increase with the decrease in

the porosity level that occurs during testing due to densification. Hardness increases from about 2 to 99 MPa, while the Young's modulus varies in the range 1-18 GPa as the levels of porosity decrease from 60 to about 5 %. Calculations of the real contact pressure during loading have allowed estimating a yield stress of 83 MPa that can be considered as a low limit for the materials fracture strength. The properties determined in the present study show the same order of values measured by other authors using macroscale testing methods and the trends found with porosity levels are similar. This shows that microscale testing methods like indentation and scratching may be used to evaluate the mechanical properties of this type of materials. The material behavior under loading is understood and the tests are carried out within the boundaries of transitions that occur.

Acknowledgments

We would like to thank for IDS-FunMat in the framework of the European Programme 'Erasmus Mundus II 2009-2013' for the PhD grant. Special thanks go to Rudy Ghisleni (from Laboratory of Mechanics of Materials and Nanostructures in EMPA Thun) for support in the scratch tests.

V.6. References

- [1] S. Meille, M. Lombardi, J. Chevalier, and L. Montanaro, “Mechanical properties of porous ceramics in compression: On the transition between elastic, brittle, and cellular behavior,” *J. Eur. Ceram. Soc.*, vol. 32, no. 15, pp. 3959–3967, 2012.
- [2] J. Sar, F. Charlot, A. Almeida, L. Dessemond, and E. Djurado, “Coral Microstructure of Graded CGO/LSCF Oxygen Electrode by Electrostatic Spray Deposition for Energy (IT-SOFC, SOEC),” *Fuel Cells*, vol. 14, no. 3, pp. 357–363, 2014.
- [3] Wayne S. Rasband US National Institutes of Health, Bethesda, Maryland, USA
- [4] “[http://imagej.nih.gov/ij/.](http://imagej.nih.gov/ij/)”
- [5] N. Li, A. Verma, A. Smirnova, and P. Singh, “Measurement of Mechanical properties of LSCF - GDC Composite SOFC Cathode,” *Am. Ceram. Soc. Meet.*, 2010.
- [6] G. Pećanac, “Thermo-mechanical investigations and predictions for oxygen transport membranes materials,” PhD Thesis, Westfälischen Technischen Hochschule Aachen, 2013.
- [7] A. C. Fischer-Cripps, *Nanoindentation (Mechanical Engineering Series)*, Third Edit. Springer, pp. 8-9, 2011.
- [8] B. X. Huang, J. Malzbender, R. W. Steinbrech, and L. Singheiser, “Mechanical properties of $\text{La}_{0.58}\text{Sr}_{0.4}\text{Co}_{0.2}\text{Fe}_{0.8}\text{O}_{3-\delta}$ membranes,” *Solid State Ionics*, vol. 180, no. 2–3, pp. 241–245, 2009.
- [9] W. Chen, Y. Yamamoto, W. H. Peter, M. B. Clark, S. D. Nunn, J. O. Kiggans, T. R. Muth, C. A. Blue, J. C. Williams, and K. Akhtar, “The investigation of die-pressing and sintering behavior of ITP CP-Ti and Ti-6Al-4V powders,” *J. Alloys Compd.*, vol. 541, pp. 440–447, 2012.
- [10] D. Poquillon, J. Lemaitre, P. Tailhades, and J. Lacaze, “Cold compaction of iron powders — relations between powder morphology and mechanical properties Part I: Powder preparation and compaction,” *Powder Technol.*, vol. 126, pp. 65–74, 2002.

- [11] W. Chen, Y. Yamamoto, and W. H. Peter, “Investigation of Pressing and Sintering Processes of CP-Ti Powder Made by Armstrong Process,” *Key Eng. Mater.*, vol. 436, pp. 123–130, 2010.
- [12] H. F. Fischmeister and E. Arzt, “Densification of Powders by Particle Deformation,” *Powder Metall.*, vol. 26, no. 2, pp. 82–88, 1983.

VI. Durability test on coral CGO-LSCF with LSCF current collector working in SOFC and SOEC modes

Durability test on coral CGO-LSCF with LSCF current collector working in SOFC and SOEC modes

Jaroslav Sar^{1,2}, Josef Schefold³, Annabelle Brisse³, Elisabeth Djurado^{1,2*}

¹ Univ. Grenoble Alpes, LEPMI, F-38000 Grenoble, France;

² CNRS, LEPMI, F-38000 Grenoble, France;

³ European Institute for Energy Research (EIFER), D-76131 Karlsruhe, Germany

* *Elisabeth.Djurado@lepmi.grenoble-inp.com*

VI.1. Abstract

This work presents 790 h durability test performed on solid oxide cells (both SOFC and SOEC). An innovative CGO-LSCF oxygen electrode with coral microstructure was deposited on SOFC anode supported with 8YSZ electrolyte. An initial cell voltage was found 817 mV at 773 °C under synthetic air on the oxygen electrode side and pure hydrogen (500 mL.min⁻¹) on the hydrogen electrode side under 0.5 A.cm⁻² current density in SOFC. An initial cell voltage in SOEC was 1200 mV at 773 °C under synthetic air on the oxygen electrode side and mixture of steam – hydrogen (80 % - 20 %) on the hydrogen electrode side under -0.75 and -0.5 A.cm⁻² current density. The cell resistance was increasing during the durability test. The increase at high frequency range was mainly responsible for an increase in the total cell resistance. This frequency range was associated with the blocking effect on the oxygen electrode/electrolyte interface. U-j curves showed reversibility of the current loading from -0.75 to 0.5 A.cm⁻². Post-mortem SEM observations showed cracks in 8YSZ electrolyte, the lack of CGO barrier diffusion layer and the detachment of the oxygen electrode from the substrate.

Keywords: CGO, LSCF, oxygen electrode, SOFC, SOEC, durability, degradation.

VI.2. Introduction

The great interest in high temperature solid oxide cells (SOC) comes from its reversible operation in solid oxide fuel cell (SOFC) and solid oxide electrolysis cell (SOEC). In SOFC,

the electricity is produced directly from electrochemical reaction between gaseous hydrogen and oxygen. In SOEC (inversely to first), hydrogen or syngas is produced by splitting H₂O or a mixture of H₂O with CO₂. Commercialization of SOFC is troubled by the material and fabrication costs. However, the continuously extending lifetime of the cell stack is reaching the acceptable value of 50000 h or around 6 years [1]. The current research in the domain of SOFC and SOEC is to increase durability and performances. The main cell degradation problems are reported to come from: grain coarsening [2], particle smoothing/coarsening [3], [4], kinetic demixing and formation of Kirkendall voids or micropores [5], [6]. Furthermore, the cell stability and performances are diminished by phase instability [7], interfacial segregation [8]–[10], evaporation [1], [11], accumulation of impurities at active zones [12], [13], interdiffusion [14], delamination and the microstructure degradation of the electrolyte/oxygen electrode interface [15]–[19].

Comparison of voltage degradation rates is difficult to realize due to different experimental conditions. There are no standardized test conditions and test features. In addition, the cell itself can also vary by the used materials, the design, the area, and the thickness. Thus a particular comparison between the fuel cell and the electrolysis mode of operation is required. The current density (*j*) flow in the circuit depends of the operating mode and is generally described as positive in the fuel-cell mode and negative in the electrolysis mode. Cathode and anode reverse their role depending of the working mode. To unify terms, the hydrogen electrode is the electrode on which fuel is consumed (SOFC) or produced (SOEC) and the oxygen electrode is the electrode on which oxygen is produced (SOEC) or consumed (SOFC). Cells based on Ni-YSZ hydrogen electrode, 8YSZ electrolyte and LSCF oxygen electrode were tested in fuel cell and electrolysis modes. Under fuel cell operation conditions, such cells achieved a voltage degradation rate of 0.9 – 1.5 %·1000 h⁻¹ at 750 °C under 0.5 A·cm⁻² over long test duration between 2000 and 5000 h. [20], [21]. Voltage degradation rates in the electrolysis mode were noticed to be higher than in the SOFC mode. Low voltage degradation value as 3.2 %·kh⁻¹ was found for metal supported cell with an area of 12.5 cm² under -0.3 A·cm⁻² at 800 °C during 2000 h [22]. Voltage degradation rates are reported to start from 5 %·kh⁻¹ and to stabilize at the final stage of the test at 2 %·kh⁻¹ by Hauch et al. [13] for 16.5 cm² anode supported cell under current density of -0.5 A·cm⁻² at 850 °C during 600 – 700 h. Also similar degradation rate of 3 %·kh⁻¹ was found in 1000 h long test on 45 cm² cell [23]. Schefold et al. [24] reported the initial low degradation of 2.5 %·kh⁻¹ up to 5600 h (even 1.7 %·kh⁻¹ between 2000 h and 5600 h) and a total degradation of 3.8 %·kh⁻¹ for 9000 h durability test for 45 cm² anode supported cell at 780 °C and -1 A·cm⁻² current density.

This work presents durability tests on the full cell working in the SOFC and SOEC modes. These durability tests were performed as a final part of PhD project after successful fabrication of CGO-LSCF oxygen electrode (Chapter II), electrochemical tests by Impedance Spectroscopy (Chapter III), microstructural (Chapter IV) and mechanical (Chapter V) analysis of coral microstructure. Impedance spectroscopy was used to investigate the cell kinetics. The ohmic resistance, the electrochemical and gas polarization resistance were de-convoluted and confronted with the post-mortem microstructural and chemical analysis.

VI.3. Experimental

VI.3.1. Oxygen electrode preparation

A circular anode-supported SOFC with an area of 45 cm² was from Forschungszentrum Jülich on which the up-scaled oxygen electrode was deposited by ESD in LEPMI. On 1.5 mm thick Ni/YSZ substrate a 8 μm thick Ni/YSZ cermet served as the hydrogen electrode. 8 mol.% yttria-stabilized zirconia (8YSZ) was used as a dense electrolyte with a thickness of 10 μm. Processing details of Ni/YSZ electrode with 8YSZ electrolyte can be found elsewhere [25], [26]. The oxygen electrode was made of coral functional layer (CFL) deposited by electrostatic spray deposition (ESD) and current collector layer (CCL) printed by screen-printing. A homogeneous composition of Ce_{0.9}Gd_{0.1}O_{2-δ} and La_{0.6}Sr_{0.4}Co_{0.2}Fe_{0.8}O_{3-δ} (CGO-LSCF) as CFL and CGO as barrier diffusion layer was deposited prior printing LSCF as CCL. The parameters for ESD were chosen to create highly porous microstructure called coral microstructure [27] adjusted to the large scale of the substrate. As a first part of deposition, a dense and thin CGO barrier diffusion layer was deposited by ESD for 45 min (see Chapter II) [28]. The next step was the deposition of CGO and LSCF with 1:1 molar ratio for 405 min. The last step was coating of pure LSCF for 90 min. An x-y moving substrate holder was used during to cover the full surface and guarantee good homogeneity in the coating thickness. A precise description of CGO-LSCF composite production was presented in [28]. A post-annealing treatment was performed at 900 °C for 2 h in air to ensure the crystallization. LSCF CCL was screen-printed onto sintered coral microstructure in two cycles. The sample was kept for 1 h drying at 60 °C between printings. After that, the sample was heated up to 600 °C with a rate of 0.5 °C.min⁻¹ to burn out the binder and then sintered at 900 °C for 2 h with a heating/cooling rate of 3 °C.min⁻¹.

VI.3.2. Durability test in the SOFC and the SOEC modes

The durability test and other electrochemical tests were performed in SOFC test bench from ECN (The Netherlands) adapted for both SOFC and SOEC testing at EIFER. The experimental setup with the cell is presented in Fig. VI-1.

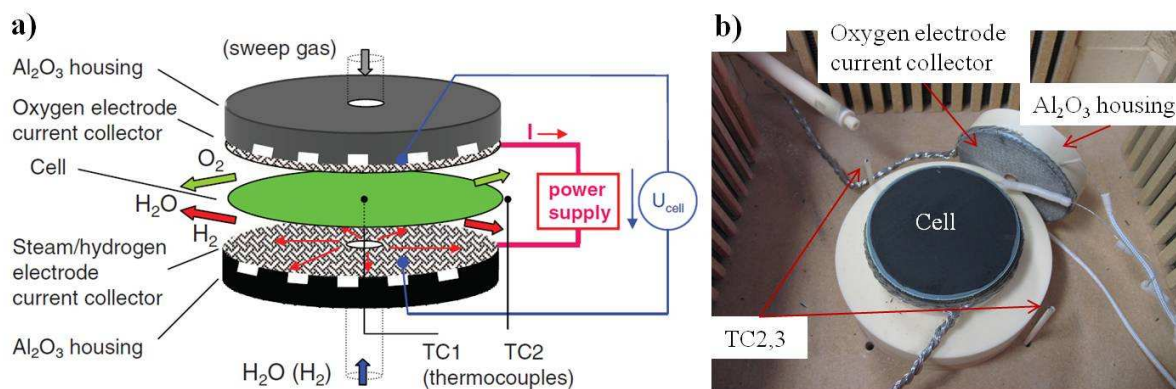


Fig. VI-1. The test bench, a) schema of the experimental test setup, b) mounted cell.

The cell was placed in between two alumina plates which served at the same time as gas distributors. Pt-grids were used to provide current collecting for the electrodes. The cell voltage was measured with Pt sense wires welded to the grids. Moreover, 2 kg weight load was used to ensure a good grid-electrode contact. The sweep gas was synthetic air (O_2 and N_2) on the oxygen electrode side. The total gas flow was kept stable of $1500 \text{ mL}\cdot\text{min}^{-1}$. The hydrogen electrode was supported in H_2 , N_2 and H_2O . The exact gas flows were varying with the experiments (see Result section). Steam was produced from de-ionized water preheated by upstream tubing. In addition, external heating was guaranteed by a ceramic heating element. One should keep in mind that the setup was operating in open housing, H_2 was burnt out at the rim of the cell. This may increase the cell temperature if the gases flow is not adapted. Three thermocouples were set in the setup, one in the cell center (corresponding to the cell temperature) and the two lasts on the cell edges. The electrometer of Solartron 1287 potentiostat was used to measure the cell voltage. The overvoltage protection was used to cut the current density in case of steam lack. The impedance spectroscopy spectra were measured using Solartron potentiostat/galvanostat frequency analyzer (SI 1255) within frequency range of 0.1 Hz to 40 kHz. The frequency limit for IS measurements was about 10 kHz due to an electromagnetic coupling between the current and the voltage sensing cables at the cell and shunt. It affected the measurement of low impedances in the range of $\text{m}\Omega$ [29]. A maximum AC current density of the frequency analyzer was $50 \text{ m}\Omega\cdot\text{cm}^{-2}$. Details about the setup and about the testing can be found elsewhere [24], [30], [31].

VI.3.3. Post-mortem microstructure observations

Energy dispersive X-ray spectroscopy and FEG-SEM were used to observe changes in the cell microstructure and the compositional fluctuation. The cell was embedded and infiltrated with epoxy resin. After one day of resin curing, the cell was cut in small pieces in order to observe cross section of the cell components. Finally, the cell was polished to achieve flat surface.

VI.4. Results and discussion

The cell was tested for the total time of 790 h. The cell was working in SOFC mode for more than 350 h and more than 430 h in SOEC mode. Current densities and temperatures during durability test are listed in (Fig. VI-2). Firstly, the cell operated in SOFC mode under 0.5 A.cm^{-2} load with a H_2 gas flow of 500 mL.min^{-1} at the hydrogen electrode and with a mixture of $300 \text{ mL.min}^{-1} \text{ O}_2$ and $1200 \text{ mL.min}^{-1} \text{ N}_2$ (synthetic air) at the oxygen electrode for 125 h. The oxygen electrode was fed with the same gases for all the experiments in fuel cell and electrolysis mode. The cell was operating in SOEC under conditions listed in Table VI-1. Under electrolysis mode, it was noticed that the cell voltage increased from 1090 mV to 1187 mV by changing the $|j|$ from 0.5 to 0.75 A.cm^{-2} .

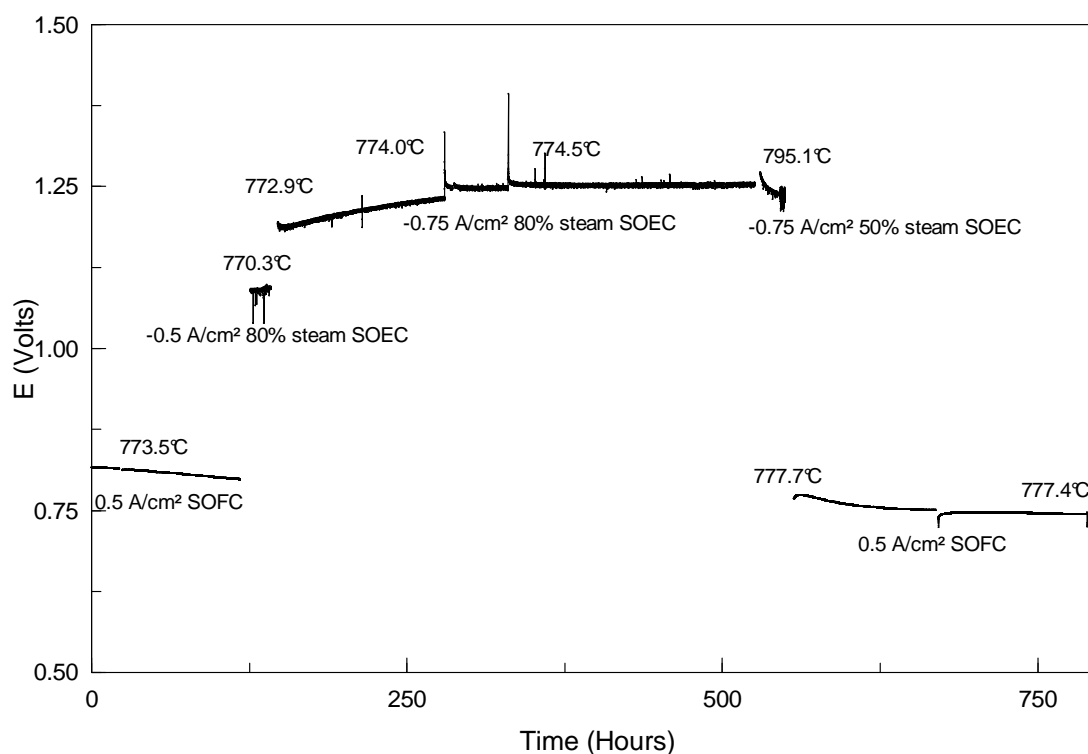


Fig. VI-2. The cell voltage changes during durability test of 790h for the cell working in SOFC and SOEC.

Furthermore, high current density provided the Joule heating to the cell due to ohmic losses in the cabling in the cell housing. Finally, the cell was operating back in SOFC mode under initial conditions. OCV for SOFC conditions was 1.041 V at around 774 °C under pure hydrogen and 0.871 V at around 770 °C and 80 vol.% steam to H₂ ratio at the H₂ electrode side. At this point, it should be kept in mind that other researchers skip the first few hundred hours of the cell operation since the cell is not fully stable in thermo-chemical conditions. This work shows the complete cell voltage evolution just after reduction of NiO to metallic Ni.

Table VI-1. Cell conditions operating in SOEC mode.

Time (h)	Load (A.cm ⁻²)	Gases on hydrogen electrode		H ₂ O – H ₂ (%)
		H ₂ (mL.min ⁻¹)	H ₂ O (g.h ⁻¹)	
16	-0.5	146	28	80 – 20
388	-0.75	146	28	80 – 20
20	-0.75	582	28	50 – 50

VI.4.1. SOFC mode

VI.4.1.1. Cell voltage degradation

The cell was operating in SOFC mode at the beginning (first 125 h) of the durability test and after the SOEC mode. The initial cell voltage was 817 mV under 0.5 A.cm⁻². The cell voltage degradation rate was found from the slope of the linear fit to the cell voltage data. The total potential degradation during time for SOFC was 116 mV.kh⁻¹ (14.3 %.kh⁻¹ in relation to the initial potential value). However, variations of the degradation were scanned. The highest degradation was at the beginning of the test of 166 mV.kh⁻¹ (20.4 %). When the cell was switched back to SOFC after operating in electrolysis, the cell degradation was stabilized from 127 mV.kh⁻¹ (15.5 %) to 50 mV.kh⁻¹ (6.2 %). The detailed cell voltage degradation is presented in Fig. VI-3.

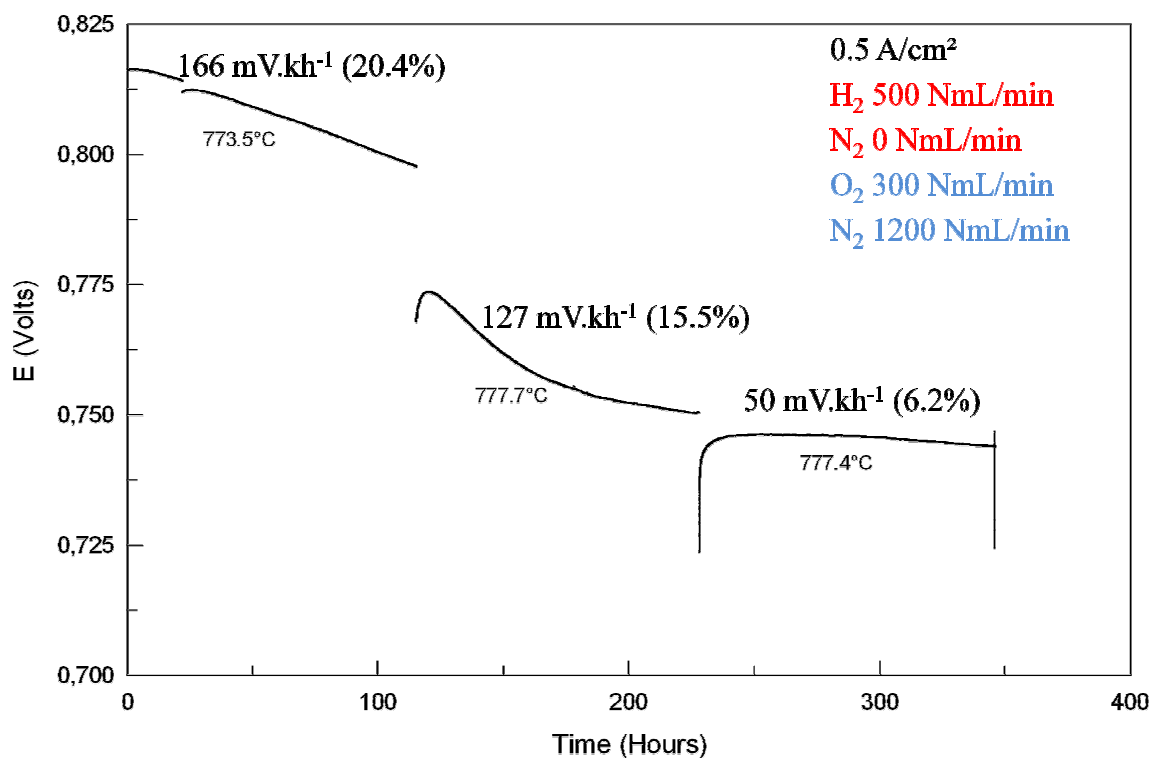


Fig. VI-3. The cell voltage changes during durability test of the cell working in the SOFC mode.

VI.4.1.2. Cell resistance

The impedance spectroscopy was performed regularly in order to see the evolution of cell resistance (Fig. VI-4). The cell was under 0.5 A.cm^{-2} current density with applied 500 mL.min^{-1} of H_2 on the hydrogen electrode side and air on the oxygen electrode side. The cell resistance was increasing with time, even after operating in the SOEC mode. The moment of switching from SOFC to SOEC mode is indicated by a vertical line in Fig. VI-4. The initial cell area specific resistance was $378 \text{ m}\Omega.\text{cm}^2$ and increased by almost 35 % to a final value of $508 \text{ m}\Omega.\text{cm}^2$. The impedance data were fitted by using equivalent element circuit consisted of three constant phase elements (CPE). Contributions with characteristic capacitances and frequencies were described as a low frequency range (LF) ascribed to the mass transfer, a medium frequency range (MF) typical of charge transfer and a high frequency range (HF) responsible for the blocking effect of the oxygen transfer on the oxygen electrode/electrolyte interface. The graph in Fig. VI-5 shows the changes of each contribution with time. The low and medium frequency contributions remained stable over the duration of the test. The small measured LF and MF resistances evolution were negligible in comparison with the large HF one. The high frequency part significantly increased and was mainly responsible for the growth of the cell resistance. HF contribution increased by 78 % from the initial value to the

final one of $296 \text{ m}\Omega\cdot\text{cm}^2$. The explanation of this phenomenon came from the delamination of the oxygen electrode and creation of horizontal voids on the electrode/electrolyte interface. Frequencies of each contribution were described by apex frequencies which ranged $1.22 - 1.51 \text{ Hz}$, $117 - 174 \text{ Hz}$ and $2.28 - 28.9 \text{ kHz}$ for LF, MF and HF, respectively. In the same time corresponding capacitances were $1.25 - 1.49 \text{ F}\cdot\text{cm}^{-2}$, $0.012 - 0.021 \text{ F}\cdot\text{cm}^{-2}$ and $2.36 \times 10^{-5} - 1.66 \times 10^{-4} \text{ F}\cdot\text{cm}^{-2}$ for LF, MF and HF, respectively. Small differences in capacitances and apex frequencies indicated that three elements were correctly fitted. Moreover, capacitances and apex frequencies were stable during the operation time (Fig. VI-6 and Fig. VI-7).

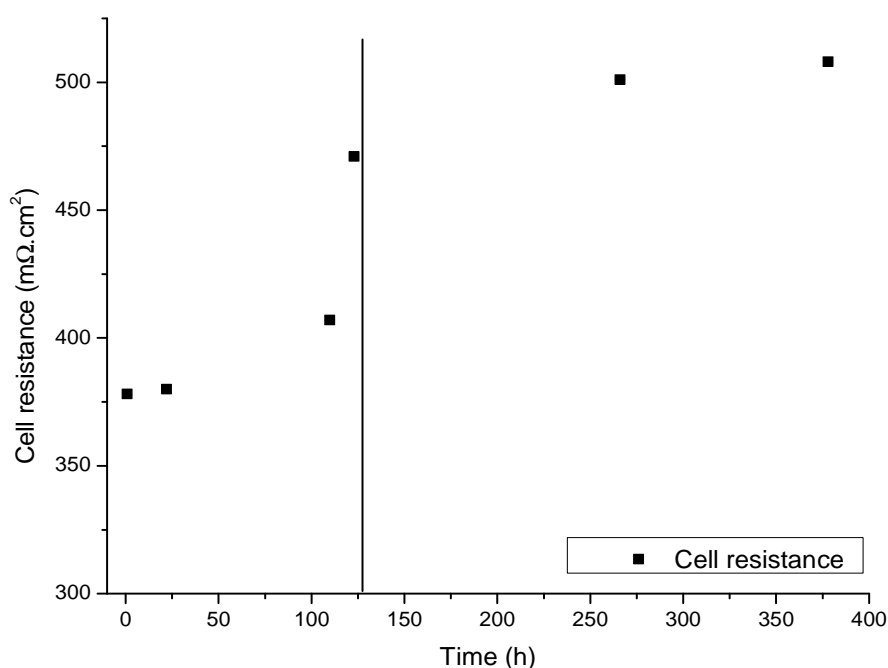


Fig. VI-4. Evolution of cell resistance operating in the SOFC mode versus time at $0.5 \text{ A}\cdot\text{cm}^{-2}$ current load. Vertical line indicates the moment of switching to SOEC mode.

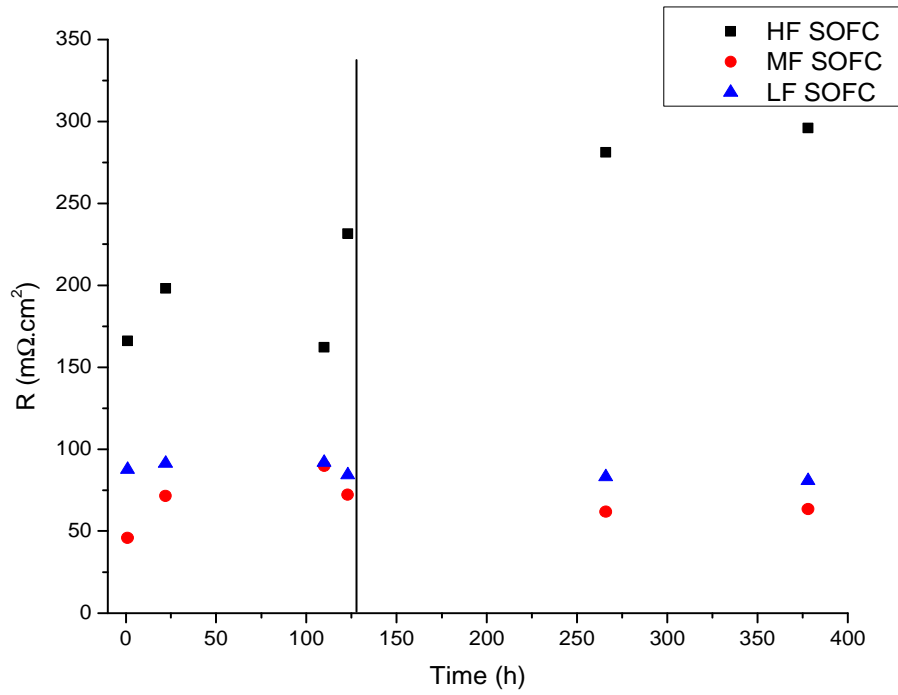


Fig. VI-5. Evolution of the resistance for high frequency, medium frequency and low frequency elements versus operating time in the SOFC mode. Vertical line indicates the moment of switching to SOEC mode.

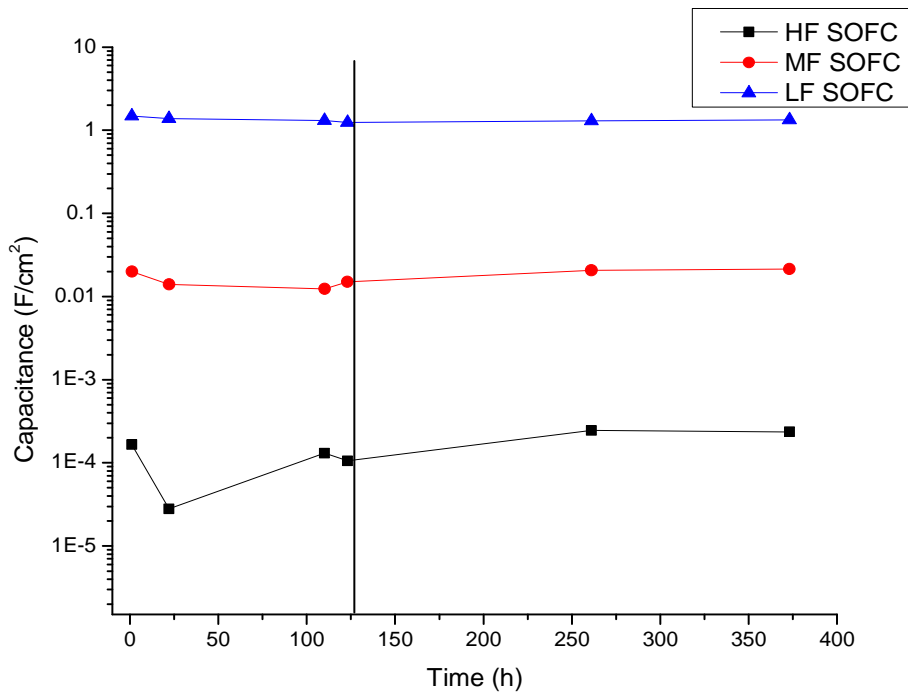


Fig. VI-6. Capacitances for LF, MF and HF contributions versus operating time in the SOFC mode. Vertical line indicates the moment of switching to SOEC mode.

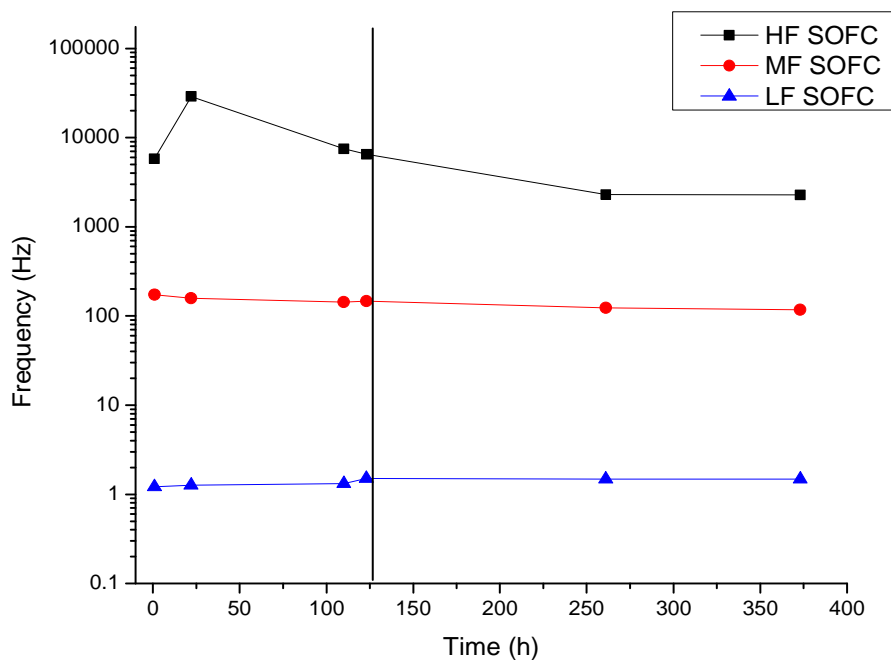


Fig. VI-7. Apex Frequencies for LF, MF and HF contributions versus operating time in the SOFC mode. Vertical line indicates the moment of switching to SOEC mode.

VI.4.1.3. Influence of O₂ gas flow change

The behavior of electrodes is difficult to determine due to the superposition of the impedance responses. One solution to separate the electrodes contributions was to change gas flows on each electrode side and perform impedance spectroscopy analysis. The contribution of the oxygen electrode was investigated by changing the oxygen and the nitrogen gas flows on the oxygen electrode side. The total gas flow was kept stable at 1500 mL.min⁻¹. The oxygen flow was varied from 150, 300, 500 and 1000 mL.min⁻¹, the rest of the gas was compensated by N₂ to achieve the total flow. During the test, the cell was under the current density of 0.5 A.cm⁻². When the oxygen gas content was increased, the cell voltage was increased and the cell resistance was decreased. Changes of the cell resistance and the cell voltage are described in Table VI-2. Moreover, the change of oxygen gas flow had no influence on the cell temperature itself. A small increase of the cell temperature was recorded for an oxygen gas flow of 1000 mL.min⁻¹ due to the burning of hydrogen at edges of the cell resulted from the open housing. The R_{LF} was decreased when the oxygen gas flow was increased. This is in good agreement with the typical behavior of the oxygen electrode while changing the oxygen partial pressure as previously reported for LSCF oxygen electrodes [32]–[34].

Table VI-2. Changes of the cell resistance and the cell voltage by varying the oxygen gas flow.

O_2 (mL.min ⁻¹)	150	300	500	1000
R (mΩ.cm²)	603	501	479	451
Cell voltage (mV)	698	750	769	792

Three contributions were selected from fitted impedance spectra. The significant increased of the cell resistance was noticed at the low frequency range responsible for mass transfer. Furthermore, capacitances and apex frequencies did not show main changes versus different oxygen flows suggesting the absence of additional contributions (Fig. VI-8 and Fig. VI-9).

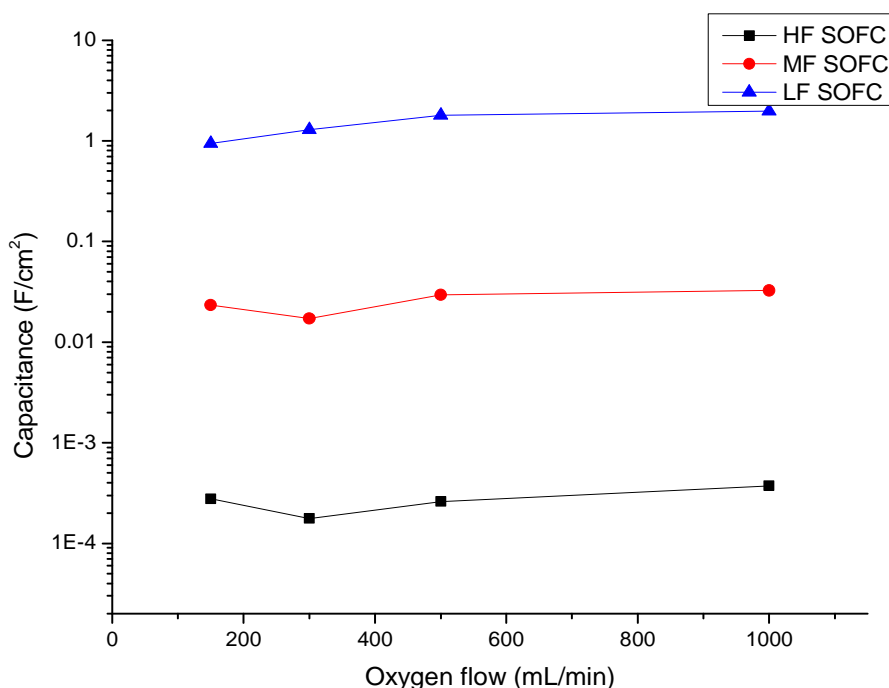


Fig. VI-8. Capacitances for LF, MF and HF contributions in different oxygen flows on the oxygen electrode side in the SOFC.

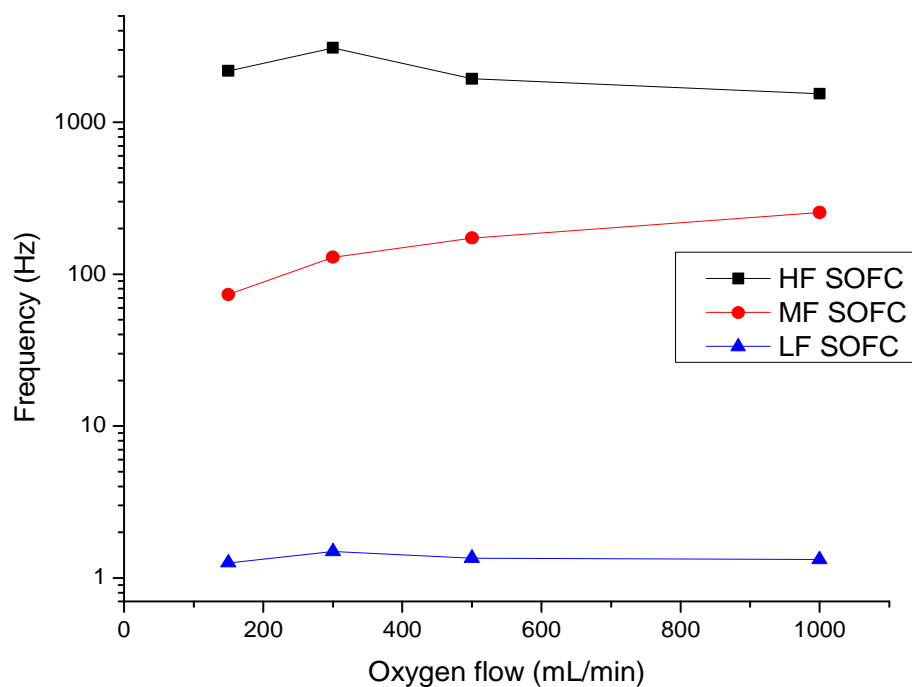


Fig. VI-9. Apex frequencies for LF, MF and HF contributions in different oxygen flows on the oxygen electrode side in the SOFC.

VI.4.1.4. Influence of H₂ gas flow change

The hydrogen electrode was investigated by changing the hydrogen gas flow. The hydrogen gas flow was varied from 250, 500 to 1000 mL.min⁻¹ under current density of 0.5 A.cm⁻². If the hydrogen gas flow was lower than 500 mL.min⁻¹, it was compensated by N₂. In the case of higher flow than 500 mL.min⁻¹ pure hydrogen was applied. It is worth to mention that by changing the hydrogen gas flow, the cell temperature was meaningfully changed. The hydrogen was applied on the cell center but still a large part of the flow went to cell edges where was burned out heating even more the cell. Impedance measurements were quickly performed to avoid longtime waiting for the temperature stabilization. In such case the cell was not in isothermal conditions but still stable to do the impedance without points with frequencies below 10⁻¹ Hz. Similar to changes of the oxygen gas flow, the cell resistance and the cell voltage were decreased when hydrogen content was increased on the hydrogen electrode side. Fig. VI-10 shows changes in capacitances for LF, MF and HF ranges. Changes in capacitances can be explained by not stable thermal conditions. Moreover, the shift of the theta peak to higher frequency was registered for higher hydrogen gas flow at LF range (Fig. VI-11).

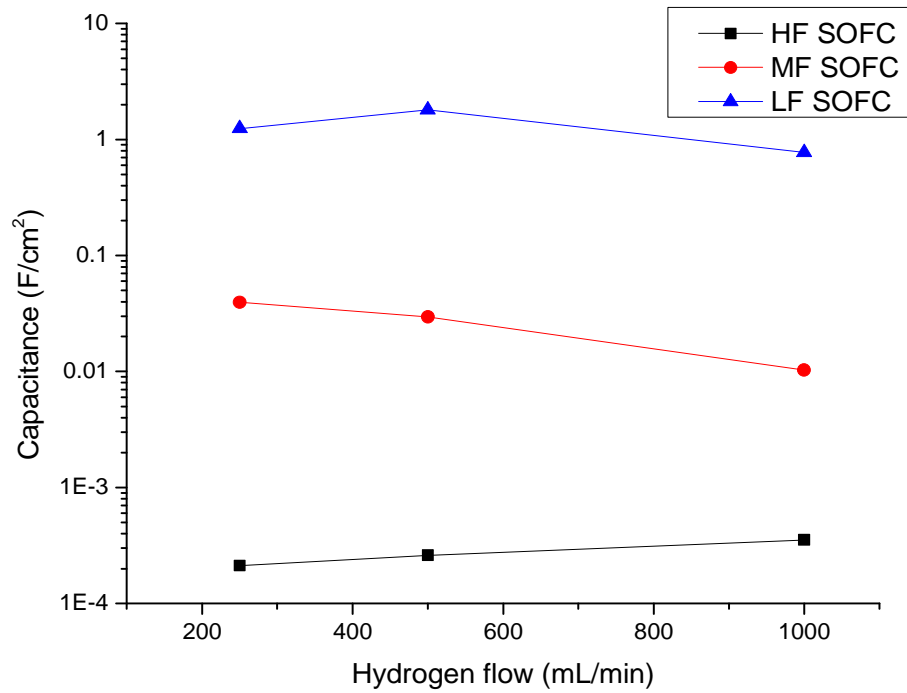


Fig. VI-10. Capacitances for LF, MF and HF contributions in different hydrogen flows on the hydrogen electrode side in the SOFC mode.

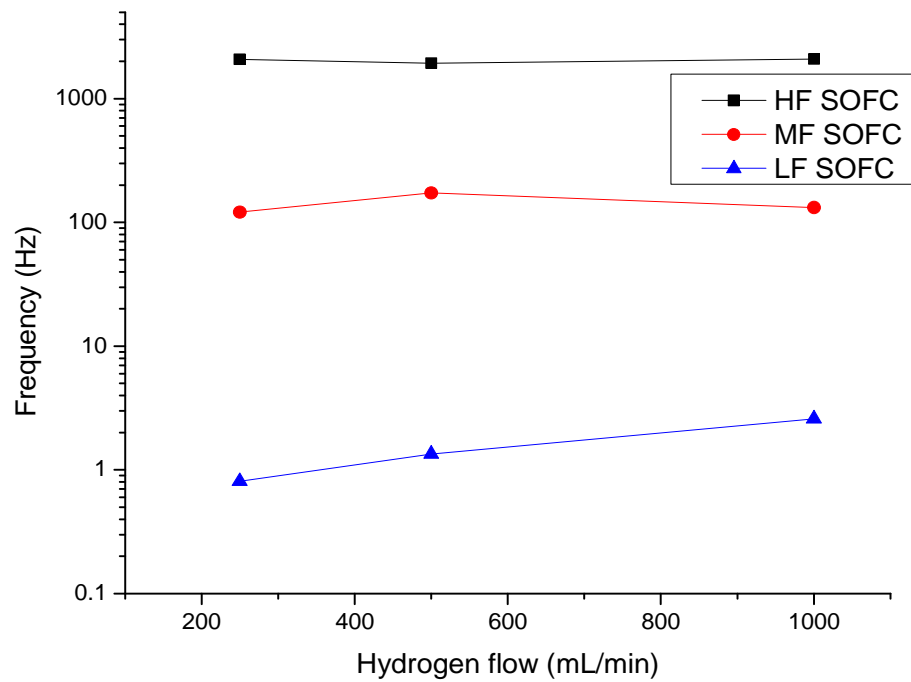


Fig. VI-11. Apex frequencies for LF, MF and HF contributions in different hydrogen flows on the hydrogen electrode side in the SOFC mode.

VI.4.2. SOEC mode

VI.4.2.1. Cell voltage degradation

Fig. VI-12 presents the cell voltage changes during time operating in the SOEC mode under -0.75 A.cm^{-2} with 80 % steam on the hydrogen electrode side and synthetic air on the oxygen electrode side. The cell was switched to the SOEC mode after almost 125 h working in the SOFC mode and after next 400 h switched back. The initial cell voltage was 1200 mV at 773 °C. Pulses of the cell voltage were caused by perturbations in the steam supply (resulted in change of the voltage of 5 – 9 mV). The voltage degradation rate was calculated as a slope from the linear fit to the cell voltage changes in the time. The cell voltage was increasing with time. The total cell voltage degradation was 130 mV.kh^{-1} that was corresponding to the drop of the initial SOEC cell voltage of 10.8 \%.kh^{-1} . However, at the beginning of the operation the cell voltage degradation was as high as 353 mV.kh^{-1} (29.7 \%.kh^{-1}) for a longer time than 127 h. Then, the cell voltage was stabilized to a very low value of 2 mV.kh^{-1} (0.2 \%.kh^{-1}) and stayed stable for the rest of the operation. It is worth to mention that the cell voltage degradation rate became so low after the cell voltage peak. The punctual increase in the cell voltage was caused by temporarily lack of steam. In such case the cell was swept only by pure hydrogen on the hydrogen electrode side. This event decreased the high degradation rate. The same event happened at 177 h.

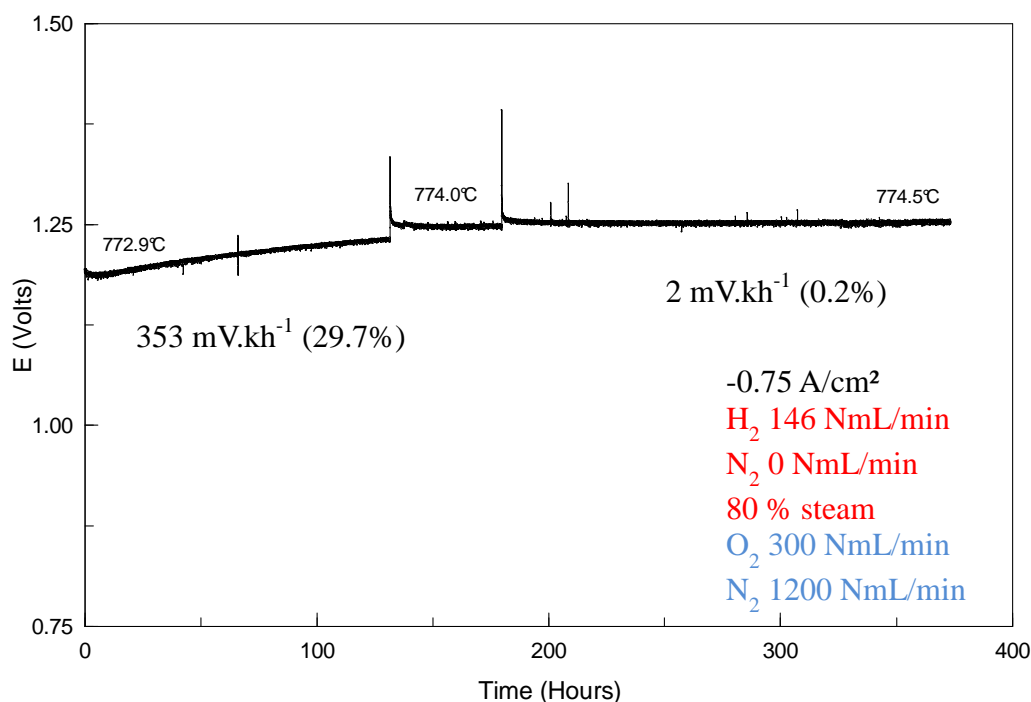


Fig. VI-12. The cell voltage during durability test of the cell working in the SOEC mode.

VI.4.2.2. Cell resistance

The durability test in the SOEC mode was performed under -0.75 A.cm^{-2} , the electrodes were supplied by air on the oxygen electrode side and 80 % H_2O on the hydrogen electrode side. Similarly to durability test in the SOFC mode, the cell resistance was increasing with the operating time presented in Fig. VI-13. There can be several reasons for increasing cell resistance: decreasing of the ionic conductivity in the electrolyte, decreasing of the electronic conductivity in the electrodes, electrodes deactivation and delamination, and formation of low conductive layers in the electrodes [35]. The cell resistance at the beginning of the electrolysis mode was $465 \text{ m}\Omega.\text{cm}^{-2}$ and increased by 26 % to the final value of $588 \text{ m}\Omega.\text{cm}^{-2}$. According to the principle, the ohmic resistances in SOFC and SOEC modes remain equal. However, the cell resistance is higher in electrolysis due to higher electrodes polarization resistances. Indeed, higher steam content requires higher activation polarization of the hydrogen electrode [22]. The equivalent circuit for impedance spectra fit was consisted of constant phase elements similar as in the SOFC mode. Contributions were characterized by mass transfer (LF), charge transfer (MF) and blocking effect on the oxygen electrode/electrolyte interface (HF). Fig. VI-14 shows changes in R_{LF} , R_{MF} and R_{HF} during the operating time. The HF resistance was the main contribution of the cell resistance and showed the highest growth over time. An increase of R_{HF} was also observed by Tietz et al. [35] in a cell working for 9000 h in electrolysis. The post-mortem SEM analysis showed a loss in granular contact area and pore formation on the oxygen electrode/electrolyte interface. Moreover, an increase of the contribution above 300 Hz was clarified by the compositional fluctuation and the morphological changes in the oxygen electrode providing a loss of catalytic activity.

A small increase of R_{LF} was noticed while R_{MF} was decreased. Capacitances and apex frequencies calculated for each contribution were stable excepted for the capacitance at MF which was increased (Fig. VI-15 and Fig. VI-16). Capacitances were found equal to $1.01 - 1.42 \text{ F.cm}^{-2}$, $0.027 - 0.225 \text{ F.cm}^{-2}$ and $4.68 \times 10^{-4} - 1.30 \times 10^{-3} \text{ F.cm}^{-2}$ for LF, MF and HF contributions, respectively. Apex frequencies were varied from 1.41 to 1.52 Hz, 42.8 to 97.6 Hz and 884 to 1130 Hz for LF, MF and HF contributions, respectively.

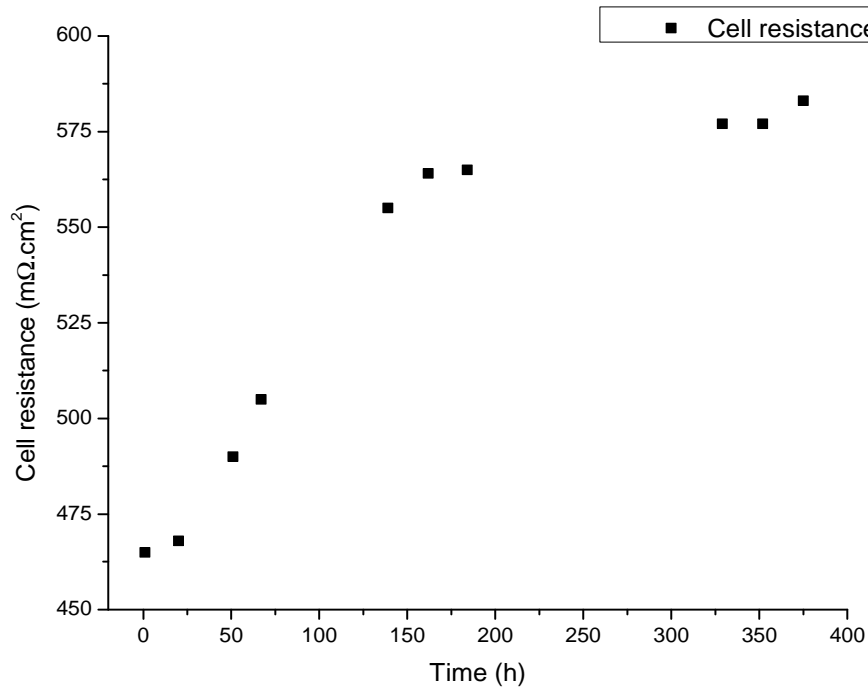


Fig. VI-13. Evolution of cell resistance operating in the SOEC mode in time.

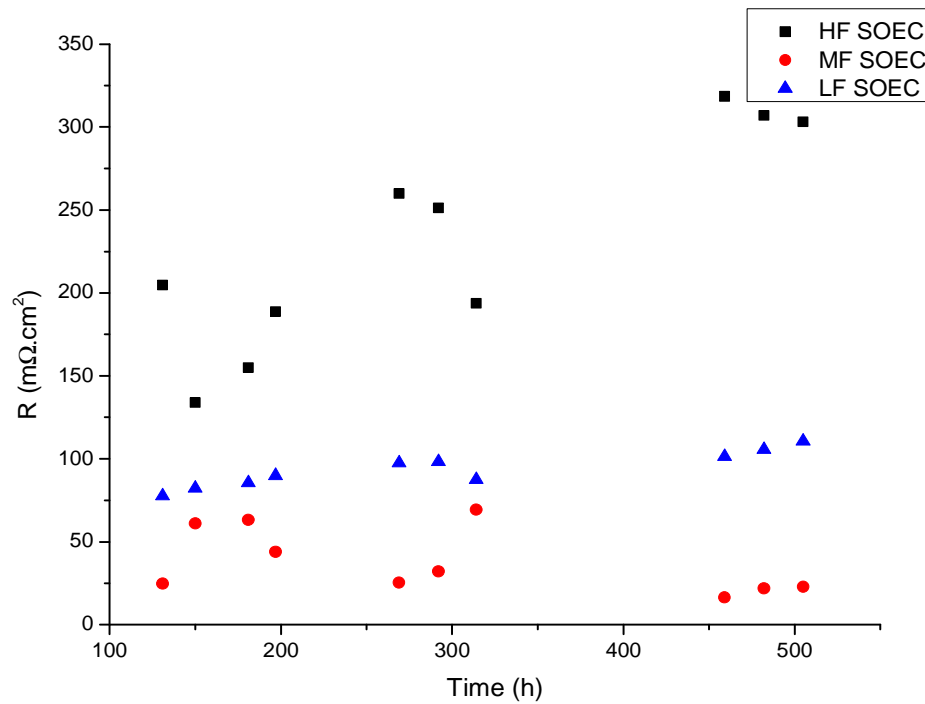


Fig. VI-14. Evolution of the resistance for high frequency, medium frequency and low frequency elements versus operating time in the SOFC mode.

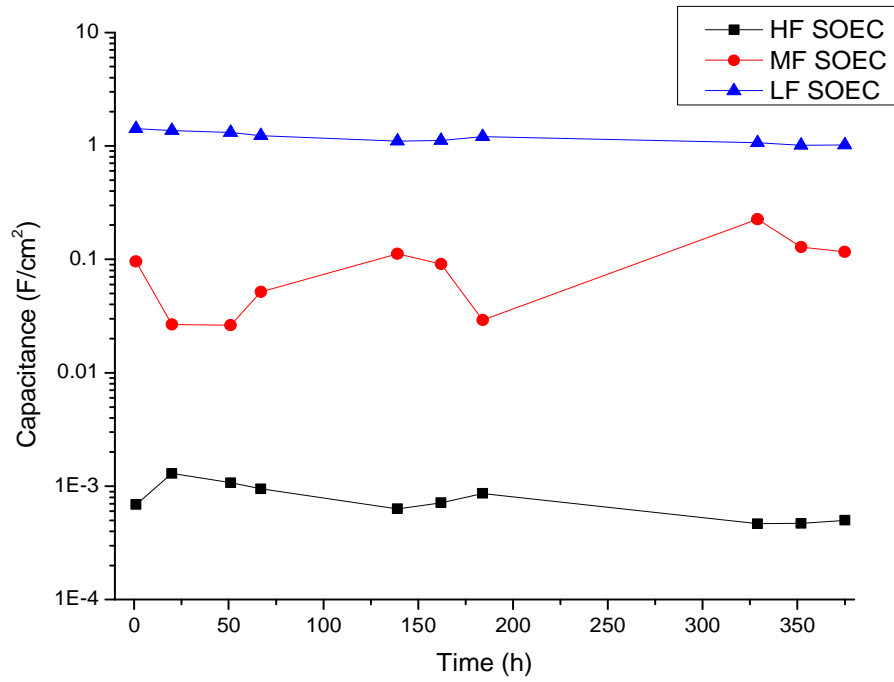


Fig. VI-15. Capacitances for LF, MF and HF contributions versus operating time in the SOEC mode.

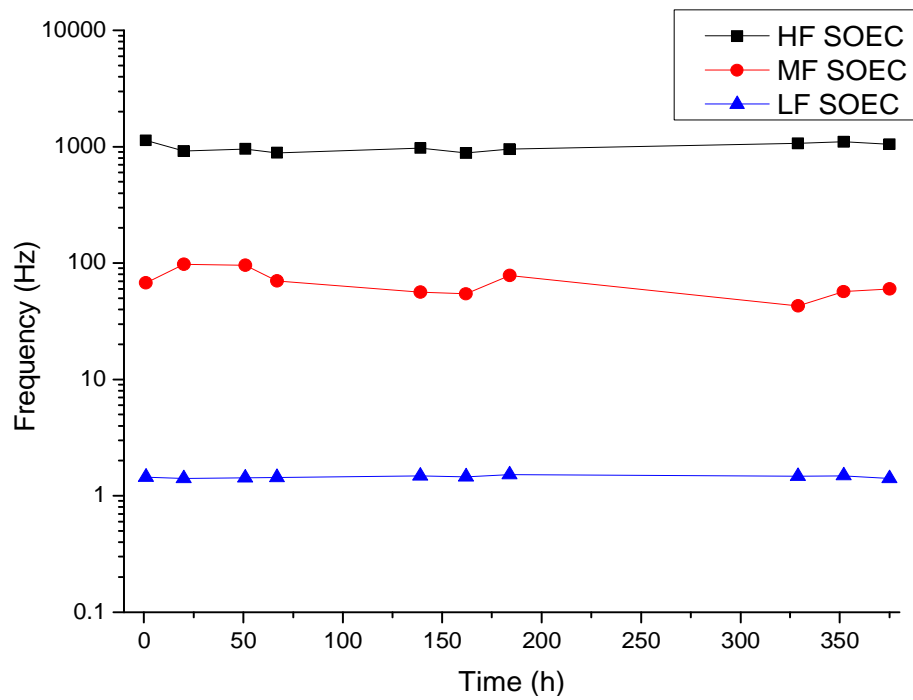


Fig. VI-16. Apex frequencies for LF, MF and HF contributions versus operating time in the SOEC mode.

VI.4.2.3. Influence of O₂ gas flow change

During the durability test the influence of different oxygen partial pressure on the cell was investigated. The oxygen gas flow on the oxygen electrode side was changed from 0, 150, 300 to 500 mL.min⁻¹. The rest of the gas flow was compensated by N₂ to achieve a stable gas flow of 1500 mL.min⁻¹. The current density was -0.75 A.cm⁻². Table VI-3 shows the changes in the cell resistance and the cell voltage by changing the oxygen gas flow. The cell resistance was decreased when the O₂ flow was increased. The same tendency was noticed for the cell voltage with an exception for 300 mL.min⁻¹ when the cell voltage was reached a minimum value of 1253 mV. The cell temperature was constant. Capacitances (Fig. VI-17) and apex frequencies (Fig. VI-18) remained stable by varying the oxygen gas flow leading to no effect on the contributions.

Table VI-3. Changes of the cell resistance and the cell voltage by varying the oxygen gas flow.

O ₂ mL.min ⁻¹	0	150	300	500
R (mΩ.cm ²)	648	603	583	575
Cell voltage (mV)	1288	1263	1253	1258

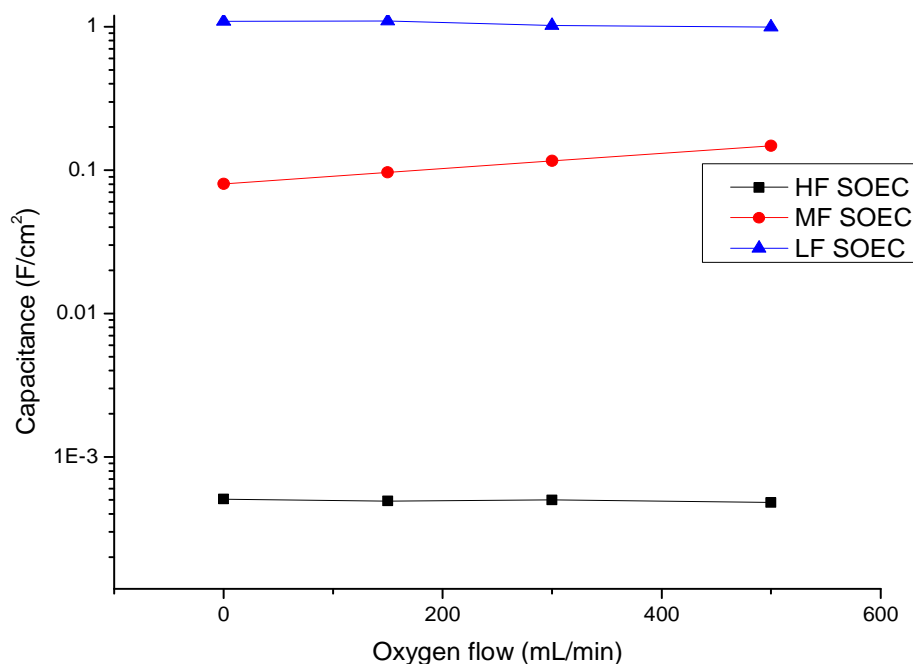


Fig. VI-17. Capacitances for LF, MF and HF contributions in different oxygen flows on the oxygen electrode side in the SOEC mode.

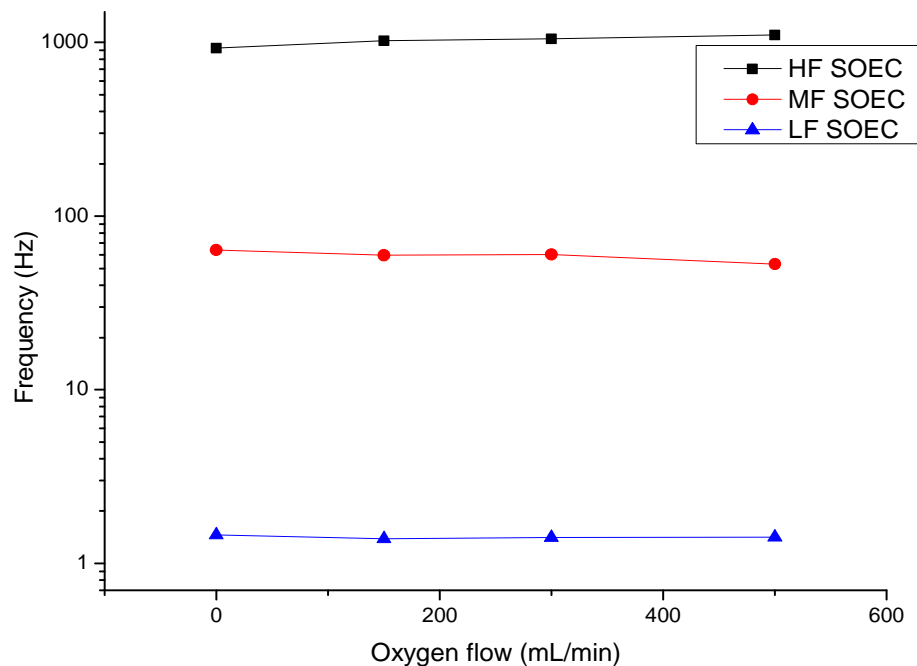


Fig. VI-18. Apex frequencies for LF, MF and HF contributions in different oxygen flows on the oxygen electrode side in the SOEC mode.

VI.4.2.4. Influence of H₂ gas flow change

The influence of H₂ gas flow change applied on the hydrogen electrode side was investigated at the end of the SOEC durability test. It was decided to do it as a last test because the change of the flow had great effect on the cell temperature thus the cell voltage and resistance. After such change the cell needed long time to stabilize in new conditions. Moreover, the H₂ – H₂O ratio was changed requiring an adjustment of the temperature of the evaporator. It was decided to keep water supplied at the same level of 28 g.h⁻¹ and modify only the hydrogen gas flow to get 50 or 80 % steam to hydrogen ratio providing less difficulties for the evaporator stabilization. In such case the total gas flow was different. The cell was under -0.75 A.cm⁻² current density. Variations in the cell resistance, voltage and temperature while changing H₂ – H₂O ratio are presented in Table VI-4. While increasing the hydrogen content the cell resistance was decreasing and the cell voltage was increased. Even an elevated temperature on 21 °C did not compensate the increasing cell voltage. As a result, there was less H₂O applied to the cell and the reaction of water splitting was moderated. Moreover, one could notice the same trend in the apex frequency for LF contribution. The apex frequency shifted to higher value from 1.42 Hz to 2.69 Hz by lowering the H₂O – H₂ ratio.

Table VI-4. Changes of the cell resistance, voltage and temperature versus varied the H₂ – H₂O ratio.

H ₂ – H ₂ O (mL.min ⁻¹ – %)	146 – 80% steam	582 – 50% steam
R (mΩ cm²)	583	544
Voltage (mV)	1253	1273
T (°C)	774	795

VI.4.3. Current voltage behavior

The reversible U-j curves for the cell are shown in Fig. VI-19 and the cell conditions in Table VI-5. The cell was measured in 50 and 80 % of H₂O on hydrogen electrode side and air composition on oxygen electrode side. The general U-j scan was done on 07/04/2014 at the current density range of -0.75 – 0.50 A.cm⁻² and the same gas conditions in all current density range. A clear reversibility of the current loading was scanned for the SOFC and the SOEC modes.

Table VI-5. The cell operating conditions during U-j scans.

Day	T _{start} (°C)	Mode	H ₂ O (g.h ⁻¹)	H ₂ (mL.min ⁻¹)	H ₂ O - H ₂ (%)
02/04/2014	774	SOFC	-	500	-
03/04/2014	773	SOFC	-	500	-
07/04/2014	773	SOFC	24	500	50 - 50
		SOEC	24	500	50 - 50
08/04/2014	770	SOEC	28	146	80 - 20
14/04/2014	773	SOEC	28	146	80 - 20
25/04/2014	794	SOFC	-	500	-
		SOEC	28	582	50 - 50

The slope (ASR) was varied from 339 to 550 mΩ.cm². The highest ASR value of 550 mΩ.cm² was found for a scan performed on 14/04/2014, corresponding to a short event (less than 10 sec) where the cell was not supported in steam. As a result, the voltage drastically raised up to 2.07 V and temperature up to 776 °C. After the event, the cell recovered the stability. The lowest ASR value of 339 mΩ.cm² was obtained for a scan registered on 25/04/2014, such value is explained by a higher operating temperature – due to the burning of an increased quantity of hydrogen. The differences in slope originated from the operating temperature, gas flows (especially on the hydrogen electrode side) and also from the

day of the measurement. The cell voltage was degraded during the durability test that raised the U-j curve slope. In SOEC current density range ($-0.75 - 0 \text{ A.cm}^{-2}$), there is a critical current density point (-0.4 A.cm^{-2}) below which the cell voltage was found lower for higher steam content, this behavior is reversed above this critical point. Moreover, higher ASR values were found for higher steam content. The cell voltage was recorded to be higher in current density range from 0 to 0.5 A.cm^{-2} , when hydrogen gas flow was increased on the hydrogen electrode side.

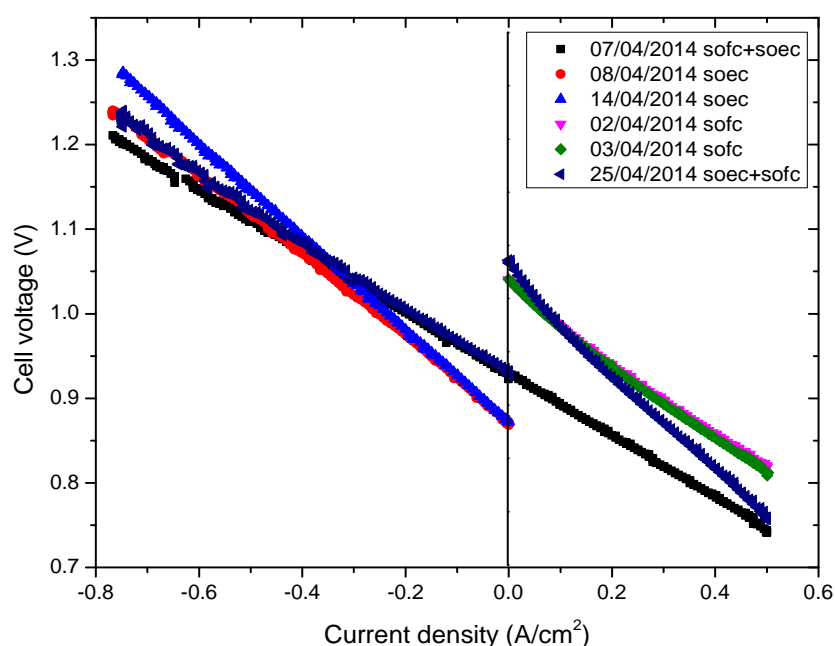


Fig. VI-19. U-j behavior of the cell operating in the SOFC and the SOEC modes for different days and conditions. Detailed conditions are described in Table VI-5.

VI.4.4. Post-mortem microstructural observations

Fig. VI-20 shows the polished cross section of the cell microstructure after durability test in the SOFC and SOEC modes. The thickness of CGO-LSCF corals was around $20 \mu\text{m}$. However, a large part of corals was infiltrated by LSCF current collector. The total thickness of the oxygen electrode was around $60 \mu\text{m}$. The oxygen electrode layer was not continuous with places in which the layer was cracked giving the access to deeper part of the electrode even up to $20 \mu\text{m}$ in depth. These cracks were created during drying of the CCL just after printing or sintering before the durability test. The coral functional layer, the part of corals free of LSCF current collector, had varying thickness from $0 - 9 \mu\text{m}$ depending on the spot. The CGO barrier diffusion is not visible at low magnification picture. The high magnification pictures showed that CGO barrier diffusion layer was ranged between $200 - 500 \text{ nm}$ (Fig. VI-

21). There were also some places where CGO barrier diffusion layer was not presented. The reason of this absence is not clear.

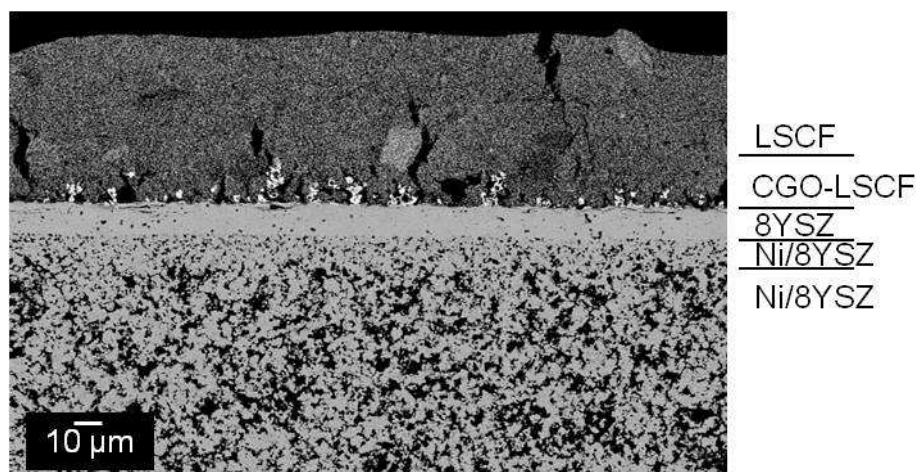


Fig. VI-20. Microstructure of the cell after durability test. The cell consisted of LSCF-current collector layer, coral CGO-LSCF with CGO barrier diffusion layer, 8YSZ electrolyte, Ni/8YSZ hydrogen electrode and Ni/8YSZ substrate.

One explanation could be that during the ESD deposition, the substrate surface was not fully and/or not properly covered due to a certain roughness. Another explanation could be that during the test, the CGO layer cracked and then it was easier to remove it from the substrate during the cell preparation for microscopy analysis. A vertical gap was found on the electrolyte/oxygen electrode (Fig. VI-21b). The gap was also noticed for a reference sample which was not operating but the intensity of the gap and its length was lower. It can indicate that the contact between the electrolyte and the oxygen electrode could give rise to the mechanical and thermal stress from very beginning of the cell durability test and could affect the polarization resistance value.

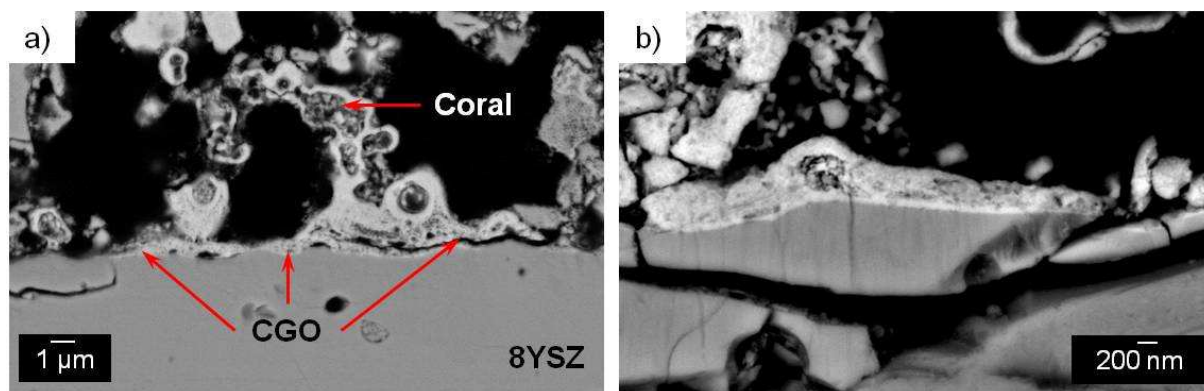


Fig. VI-21. Image of the interface between the CGO barrier diffusion layer and the 8YSZ electrolyte.

The 8YSZ electrolyte was cracked after the durability test (Fig. VI-22). A comparison of the electrolyte before and after the test showed that in both cases the electrolyte was cracked. It was explained by the cell preparation for SEM. The resin infiltrating the cell protected it from detachment of particles and layers, but also provided mechanical stresses during the curing. The electrolyte seemed to be more fragile and easier cracked during the resin curing after 790 h of the cell operation. A similar behavior was found by Tietz et al. [35]

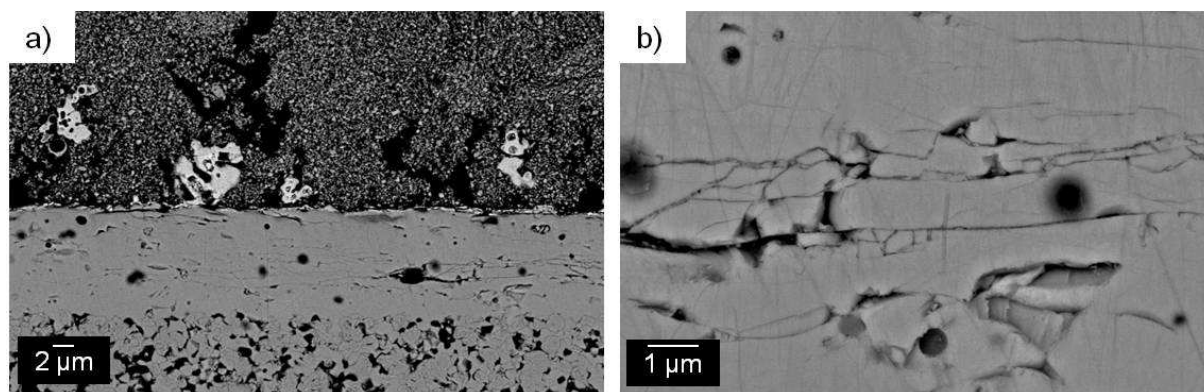


Fig. VI-22. Image of the 8YSZ electrolyte a) at 2 kx magnification, and b) at 10 kx magnification.

The EDS line profile performed on the distance of 85 μm contain all cell components (Fig. VI-23). The analysis was done starting from the oxygen electrode and finishing on the hydrogen electrode. The Zr element was removed from the graph due to much higher intensity of this element (Fig. VI-23a). La, Sr, Co and Fe drastically drop on the interface between corals and CGO barrier diffusion layer, while Ce and Gd are only presented in the line distance related to the CGO barrier diffusion layer thickness. Yttrium could be visible in the 8YSZ electrolyte and also in the Ni/8YSZ. It is important to remember that the cell is mostly consisted of porous layers which give rise to a lot of noises. Sr was detected in the 8YSZ electrolyte and in the hydrogen electrode. This phenomenon occurred due to superposition of Zr ($L_1 = 1.792 \text{ eV}$) with Sr ($L_{\alpha 1} = 1.805 \text{ eV}$, $L_{\alpha 2} = 1.807 \text{ eV}$). No secondary phases were detected.

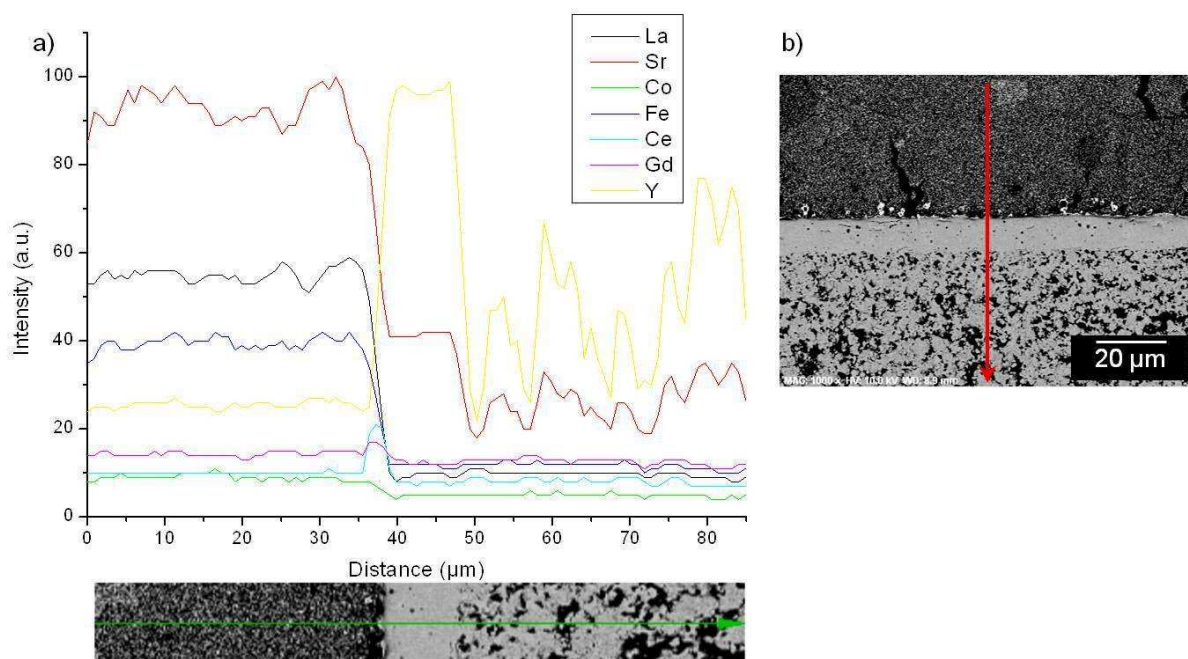


Fig. VI-23. EDS line profile performed along the cell cross section starting from the top to the bottom, a) elements intensity along the profile line, b) SEM image of the investigated area.

VI.4.5. Discussion

As it was previously mentioned, a comparison of electrochemical properties of this cell based on CGO/LSCF oxygen electrode, 45 cm^2 in active area, with other ones reported in the literature is challenging due to different test conditions and cell features. The initial cell voltage was found 817 mV for SOFC mode at $773 \text{ }^\circ\text{C}$, in synthetic air on the oxygen electrode side and pure H_2 on the hydrogen electrode side, under 0.5 A.cm^{-2} current density. The initial cell voltage was recorded 1200 mV for SOEC modes at $773 \text{ }^\circ\text{C}$, in synthetic air on the oxygen electrode side and in a mixture 80 : 20 % of steam, H_2 on the hydrogen electrode side, under -0.75 A.cm^{-2} current density. Such cell voltages were in agreement with those previously reported [20]-[24], [36]-[39].

The total cell voltage degradation was found to be equal to 14.3 \%.kh^{-1} after 350 h for the cell operating in SOFC mode. Then it was decreased to 6.2 \%.kh^{-1} at the last 100 h of the durability test. Typical degradation rates for longer durability tests have been found in the range from 0.2 to 1.4 \%.kh^{-1} [20], [36]-[40]. Those values are much lower than the one presented in this work. However, Gemmen et al. [37] have reported a continuous decrease of the average degradation value during the test. The initial degradation as high as 23 \%.kh^{-1} decreased to 5 \%.kh^{-1} during first 1000 h, and was decreasing during entire durability test (6000 h) to a final value of 1.4 \%.kh^{-1} . This PhD work represents only one tenth of the

durability test from Gemmen et al. [37]. So it is difficult to predict the behavior of our cell up to 6000 h since different degradation processes can occur.

The total cell voltage degradation for SOEC mode was found $10.8 \text{ \%} \cdot \text{kh}^{-1}$, for the cell working at $773 \text{ }^\circ\text{C}$ under $-0.75 \text{ A} \cdot \text{cm}^{-2}$. Such value is much higher than those reported in the literature [13], [21]-[24]. However, one should keep in mind that after the high initial degradation ($29.7 \text{ \%} \cdot \text{kh}^{-1}$, first 130 h), it was stabilized at $0.2 \text{ \%} \cdot \text{kh}^{-1}$ for 300 h of the remaining time. Such low value is lower than those from most of works even than those with lower current density load. Moreover, it can be compared with the degradation rate of $2 \text{ \%} \cdot \text{kh}^{-1}$ recorded at higher temperature of $850 \text{ }^\circ\text{C}$, under lower current density of $-0.5 \text{ A} \cdot \text{cm}^{-2}$ and during 1300 h [13]. Other durability test at $850 \text{ }^\circ\text{C}$ for the total time of 1000 h under $-0.5 \text{ A} \cdot \text{cm}^{-2}$ current density has shown the cell voltage degradation of $3 \text{ \%} \cdot \text{kh}^{-1}$ [23].

The high initial degradation in SOEC was also observed for other cells [13], [22], [24]. The degradation of $2.5 \text{ \%} \cdot \text{kh}^{-1}$ at $780 \text{ }^\circ\text{C}$ was observed during the first 1000 h by Schefold et al. [24] for the cell under $-1 \text{ A} \cdot \text{cm}^{-2}$, then stabilized at $1.7 \text{ \%} \cdot \text{kh}^{-1}$ from 2000 to 5600 h. Additionally, in the literature, one reports that in some cases the high initial degradation is not taken into account and the durability test starts after an initial time explaining that during this time the cell was not under stable thermo-chemical conditions. As an example, Schiller et al. [22] started the durability test after 396 h of operation and the strongest change in overall polarization was observed after 400 h. The durability test presented in this work was started just after reduction of the hydrogen electrode. Based on this durability test, it is hard to estimate a long stability of the cell with a coral microstructure. Nevertheless the final degradation rate of $0.2 \text{ \%} \cdot \text{kh}^{-1}$ classifies the cell as a potential material for further analysis.

The high voltage degradation of this work was a result which can be interpreted mainly as an increase of the polarization resistance. The impedance spectroscopy has shown that the largest influence on the polarization resistance originated from an increase of the resistance at high frequency range that was regarded as a blocking effect on the electrode/electrolyte interface. The proof of this phenomenon comes from the microstructural observations by SEM.

Microstructural observations performed after the durability test have shown that the 8YSZ electrolyte was cracked with a lack of CGO barrier diffusion layer in some parts on the oxygen electrode/electrolyte interface. Consequently a detachment of the oxygen electrode from the electrolyte was deduced. The same phenomena were often observed [22], [35], [40]. Despite the fact that CGO layer was found discontinuous, the presence of secondary phases was not detected. Tietz et al. [35] have found a large formation of SrZrO_3 on the 8YSZ/CGO interface in places in which CGO barrier diffusion layer was interrupted, after 9000 h

operating in SOEC mode. The absence of secondary phases in tested cell may be due to still sufficient dense CGO buffer layer in between LSCF and YSZ and/or too short operation time to create SrZrO_3 . By the limited time and availability of the test bench, the total durability test was finished after 790 h but the positive point is that the cell withstood and was improved with time.

VI.5. Conclusions

The durability test of an anode supported cell, 45 cm^2 in the electrode active area was performed using an innovative CGO-LSCF oxygen electrode with a coral microstructure, operating in the SOFC and the SOEC modes. A total duration of the test was 790 h, more than 350 h operating in the SOFC mode and more than 430 h operating in the SOEC mode. The main results are as the following:

- An initial $U_{\text{cell}} = 817 \text{ mV}$ at $773 \text{ }^\circ\text{C}$ under synthetic air ($1500 \text{ mL}\cdot\text{min}^{-1}$) on the oxygen electrode side and $500 \text{ mL}/\text{min}$ pure H_2 on the hydrogen electrode side in the SOFC mode under $0.5 \text{ A}\cdot\text{cm}^{-2}$ current density,
- An initial $U_{\text{cell}} = 1200 \text{ mV}$ at $773 \text{ }^\circ\text{C}$ with applied air ($1500 \text{ mL}\cdot\text{min}^{-1}$) on the oxygen electrode side and a mixture of $\text{H}_2\text{O} - \text{H}_2$ to give a ratio of 80 % - 20 % ($24 \text{ g}\cdot\text{h}^{-1}$ water – $500 \text{ mL}/\text{min}$ hydrogen) on the hydrogen electrode side in the SOEC mode under $0.75 \text{ A}\cdot\text{cm}^{-2}$ current density,
- A total cell voltage degradation of $116 \text{ mV}\cdot\text{kh}^{-1}$ ($14.3 \text{ \%}\cdot\text{kh}^{-1}$), $166 \text{ mV}\cdot\text{kh}^{-1}$ ($20.4 \text{ \%}\cdot\text{kh}^{-1}$) up to 115 h, and $50 \text{ mV}\cdot\text{kh}^{-1}$ ($6.2 \text{ \%}\cdot\text{kh}^{-1}$) in the last 100 h, in the SOFC mode,
- A total cell voltage degradation of $130 \text{ mV}\cdot\text{kh}^{-1}$ ($10.8 \text{ \%}\cdot\text{kh}^{-1}$), $353 \text{ mV}\cdot\text{kh}^{-1}$ ($29.7 \text{ \%}\cdot\text{kh}^{-1}$) up to 127 h, and $2 \text{ mV}\cdot\text{kh}^{-1}$ ($0.2 \text{ \%}\cdot\text{kh}^{-1}$) in the remaining time, in the SOEC mode,

The increase of the cell resistance during the test was explained by the main increase of HF contribution responsible for the blocking element on the oxygen electrode/electrolyte interface. Finally, U-j curves showed reversibility of the current loading for fuel-cell and electrolysis. During SOEC operation, there were two events characterized by a peak in the cell voltage blocking the steam gas supply. Consequently, the cell was in an electronic conducting mode. Post-mortem observations have showed cracks in 8YSZ electrolyte, a lack of the CGO barrier diffusion layer in some parts at the CGO/8YSZ interface and a detachment

of the oxygen electrode from the electrolyte. These observations confirmed that the greatest increase of the cell resistance was due to increase of the resistance at HF range.

VI.6. References

- [1] R. Knibbe, A. Hauch, J. Hjelm, S. D. Ebbesen, and M. Mogensen, “Durability of Solid Oxide Cells,” *Green*, vol. 1, pp. 141–169, 2011.
- [2] J. Sehested, J. A. P. Gelten, and S. Helveg, “Sintering of nickel catalysts: Effects of time , atmosphere , temperature , nickel-carrier interactions , and dopants,” *Appl. Catalysis A Gen.*, vol. 309, pp. 237–246, 2006.
- [3] D. Simwonis, F. Tietz, and D. Stover, “Nickel coarsening in annealed Ni / 8YSZ anode substrates for solid oxide fuel cells,” *Solid State Ionics*, vol. 132, pp. 241–251, 2000.
- [4] P. Tanasini, M. Cannarozzo, P. Costamagna, A. Faes, J. Van Herle, and C. Comninellis, “Experimental and Theoretical Investigation of Degradation Mechanisms by Particle Coarsening in SOFC Electrodes,” *Fuel Cells*, vol. 5, pp. 740–752, 2009.
- [5] M. Martin, “Electrotransport and demixing in oxides,” *Solid State Ionics*, vol. 136–137, pp. 331–337, 2000.
- [6] M. Kuznecov, P. Otschik, P. Obenaus, K. Eichler, and W. Schaffrath, “Diffusion controlled oxygen transport and stability at the perovskite / electrolyte interface,” *Solid State Ionics*, vol. 157, pp. 371–378, 2003.
- [7] H. Yokokawa, N. Sakai, T. Kawada, and M. Dokiya, “Thermodynamic stabilities of perovskite oxides for electrodes and other electrochemical materials,” *Solid State Ionics*, vol. 52, pp. 43–56, 1992.
- [8] S. B. Desu and D. A. Payne, “Interfacial segregation in perovskites: I, theory,” *J. Am. Ceram. Soc.*, vol. 73, no. 11, pp. 3391–3397, 1990.
- [9] S. B. Desu and D. A. Payne, “Interfacial segregation in perovskites: II, experimental evidence,” *J. Am. Ceram. Soc.*, vol. 73, no. 11, pp. 3398–3406, 1990.
- [10] S. B. Desu and D. A. Payne, “Interfacial segregation in perovskites: III, microstructure and electrical properties,” *J. Am. Ceram. Soc.*, vol. 73, no. 11, pp. 3407–3415, 1990.

- [11] F. Chauveau, J. Mougín, J. M. Bassat, F. Mauvy, and J. C. Grenier, “A new anode material for solid oxide electrolyser: The neodymium nickelate $\text{Nd}_2\text{NiO}_{4+\delta}$,” *J. Power Sources*, vol. 195, no. 3, pp. 744–749, 2010.
- [12] A. Hauch, H. Jensen, J. B. Bilde-Sørensen, and M. Mogensen, “Silica Segregation in the Ni / YSZ Electrode,” *J. Electrochem. Soc.*, vol. 154, no. 7, pp. A619–A626, 2007.
- [13] A. Hauch, S. D. Ebbesen, S. H. Jensen, and M. Mogensen, “Solid Oxide Electrolysis Cells: Microstructure and Degradation of the Ni/Yttria-Stabilized Zirconia Electrode,” *J. Electrochem. Soc.*, vol. 155, no. 11, pp. B1184–B1193, 2008.
- [14] S. Uhlenbruck, T. Moskalewicz, N. Jordan, H.-J. Penkalla, and H. P. Buchkremer, “Element interdiffusion at electrolyte–cathode interfaces in ceramic high-temperature fuel cells,” *Solid State Ionics*, vol. 180, no. 4–5, pp. 418–423, 2009.
- [15] A. Hauch, S. H. Jensen, S. Ramousse, and M. Mogensen, “Performance and Durability of Solid Oxide Electrolysis Cells,” *J. Electrochem. Soc.*, vol. 153, no. 9, pp. A1741–A1747, 2006.
- [16] A. Hauch, S. D. Ebbesen, S. H. Jensen, and M. Mogensen, “Highly efficient high temperature electrolysis,” *J. Mater. Chem.*, vol. 18, no. 20, pp. 2331–2340, 2008.
- [17] J. S. Herring, J. O'Brien, C. Stoots, G. Hawkes, J. Hartvigsen, and M. Shahnam, “Progress in high-temperature electrolysis for hydrogen production using planar SOFC technology,” *Int. J. Hydrogen Energy*, vol. 32, no. 4, pp. 440–450, 2007.
- [18] A. V. Virkar, “Mechanism of oxygen electrode delamination in solid oxide electrolyzer cells,” *Int. J. Hydrogen Energy*, vol. 35, no. 18, pp. 9527–9543, 2010.
- [19] J. R. Mawdsley, J. David Carter, A. Jeremy Kropf, B. Yildiz, and V. a. Maroni, “Post-test evaluation of oxygen electrodes from solid oxide electrolysis stacks,” *Int. J. Hydrogen Energy*, vol. 34, no. 9, pp. 4198–4207, 2009.
- [20] F. Tietz, V. A. C. Haanappel, A. Mai, J. Mertens, and D. Stöver, “Performance of LSCF cathodes in cell tests,” *J. Power Sources*, vol. 156, pp. 20–22, 2006.

- [21] F. Tietz, Q. Fu, V. A. C. Haanappel, A. Mai, N. H. Menzler, and S. Uhlenbruck, “Materials Development for Advanced Planar Solid Oxide Fuel Cells,” *Int. J. Appl. Ceram. Technol.*, vol. 4, no. 5, pp. 436–445, 2007.
- [22] G. Schiller, A. Ansar, M. Lang, and O. Patz, “High temperature water electrolysis using metal supported solid oxide electrolyser cells (SOEC),” *J. Appl. Electrochem.*, vol. 39, no. 2, pp. 293–301, 2009.
- [23] “6th Framework Program of the European Union, EIFER result within the Hi2H2 research project,” (www.hi2h2.com). .
- [24] J. Schefold, A. Brisse, and F. Tietz, “Nine Thousand Hours of Operation of a Solid Oxide Cell in Steam Electrolysis Mode,” *J. Electrochem. Soc.*, vol. 159, no. 2, pp. A137–A144, 2012.
- [25] A. Mai, V. Haanappel, S. Uhlenbruck, F. Tietz, and D. Stover, “Ferrite-based perovskites as cathode materials for anode-supported solid oxide fuel cells. Part I. Variation of composition,” *Solid State Ionics*, vol. 176, no. 15–16, pp. 1341–1350, 2005.
- [26] C. Tropartz, J. Mertens, and F. Tietz, “Various Lanthanum Ferrite-Based Cathode Materials With Ni and Cu Substitution for Anode-Supported Solid Oxide Fuel Cells,” *J. Fuel Cell Sci. Technol.*, vol. 7, p. 0610171, 2010.
- [27] D. Marinha, C. Rossignol, and E. Djurado, “Influence of electrospaying parameters on the microstructure of $\text{La}_{0.6}\text{Sr}_{0.4}\text{Co}_{0.2}\text{Fe}_{0.8}\text{O}_{3-\delta}$ films for SOFCs,” *J. Solid State Chem.*, vol. 182, no. 7, pp. 1742–1748, 2009.
- [28] J. Sar, F. Charlot, A. Almeida, L. Dessemond, and E. Djurado, “Coral Microstructure of Graded CGO/LSCF Oxygen Electrode by Electrostatic Spray Deposition for Energy (IT-SOFC, SOEC),” *Fuel Cells*, vol. 14, no. 3, pp. 357–363, 2014.
- [29] J. Schefold, A. Brisse, and M. Zahid, “Electronic Conduction of Ytria-Stabilized Zirconia Electrolyte in Solid Oxide Cells Operated in High Temperature Water Electrolysis,” *J. Electrochem. Soc.*, vol. 156, no. 8, pp. B897–B904, 2009.

- [30] A. Brisse, J. Schefold, and M. Zahid, “High temperature water electrolysis in solid oxide cells,” *Int. J. Hydrogen Energy*, vol. 33, no. 20, pp. 5375–5382, 2008.
- [31] J. Schefold, A. Brisse, and M. Zahid, “Non-Ionic Conduction Phenomena in Yttria stabilised Zirconia Electrolyte in SOFC Operated in the Electrolysis Mode,” *ECS Trans.*, vol. 25, no. 2, pp. 1021–1028, 2009.
- [32] A. Esquirol, J. Kilner, and N. Brandon, “Oxygen transport in $\text{La}_{0.6}\text{Sr}_{0.4}\text{Co}_{0.2}\text{Fe}_{0.8}\text{O}_{3-\delta}$ / $\text{Ce}_{0.8}\text{Ge}_{0.2}\text{O}_{2-x}$ composite cathode for IT-SOFCs,” *Solid State Ionics*, vol. 175, pp. 63–67, 2004.
- [33] N. Grundbaum, L. Dessemond, J. Fouletier, F. Prado, and A. Caneiro, “Electrode reaction of $\text{Sr}_{1-x}\text{La}_x\text{Co}_{0.8}\text{Fe}_{0.2}\text{O}_{3-\delta}$ with $x = 0.1$ and 0.6 on $\text{Ce}_{0.9}\text{Gd}_{0.1}\text{O}_{1.95}$ at $600 \leq T \leq 800$ °C,” *Solid State Ionics*, vol. 177, pp. 907–913, 2006.
- [34] D. Marinha, L. Dessemond, and E. Djurado, “Electrochemical investigation of oxygen reduction reaction on $\text{La}_{0.6}\text{Sr}_{0.4}\text{Co}_{0.2}\text{Fe}_{0.8}\text{O}_{3-\delta}$ cathodes deposited by Electrostatic Spray Deposition,” *J. Power Sources*, vol. 197, pp. 80–87, 2011.
- [35] F. Tietz, D. Sebold, A. Brisse, and J. Schefold, “Degradation phenomena in a solid oxide electrolysis cell after 9000 h of operation,” *J. Power Sources*, vol. 223, pp. 129–135, 2013.
- [36] H. J. Ko, J. Myung, J.-H. Lee, S.-H. Hyun, and J. S. Chung, “Synthesis and evaluation of $(\text{La}_{0.6}\text{Sr}_{0.4})(\text{Co}_{0.2}\text{Fe}_{0.8})\text{O}_3$ (LSCF)– $\text{Y}_{0.08}\text{Zr}_{0.92}\text{O}_{1.96}$ (YSZ)– $\text{Gd}_{0.1}\text{Ce}_{0.9}\text{O}_{2-\delta}$ (GDC) dual composite SOFC cathodes for high performance and durability,” *Int. J. Hydrogen Energy*, vol. 37, no. 22, pp. 17209–17216, 2012.
- [37] R. S. Gemmen, M. C. Williams, and K. Gerdes, “Degradation measurement and analysis for cells and stacks,” *J. Power Sources*, vol. 184, no. 1, pp. 251–259, 2008.
- [38] G. Digiuseppe and L. Sun, “Electrochemical performance of a solid oxide fuel cell with an LSCF cathode under different oxygen concentrations,” *Int. J. Hydrogen Energy*, vol. 36, no. 8, pp. 5076–5087, 2011.
- [39] O. Yamamoto, “Solid oxide fuel cells: fundamental aspects and prospects,” *Electrochim. Acta*, vol. 45, pp. 2423–2435, 2000.

- [40] Q. Fang, L. Blum, P. Batfalsky, N. H. Menzler, U. Packbier, and D. Stolten, “Durability test and degradation behavior of a 2.5 kW SOFC stack with internal reforming of LNG,” *Int. J. Hydrogen Energy*, vol. 38, no. 36, pp. 16344–16353, 2013.

General conclusions and prospect

General conclusions

This project has been focused on the fabrication by electro-spraying, physico-chemical and electrochemical characterizations of original alternative homogeneous and continuous graded electrodes encompassing mechanical testing techniques in order to improve durability of solid oxide fuel cells (SOFCs) and solid oxide electrolyser cells (SOECs) operating at 700 °C and 850 °C respectively in air.

The first objective of this work was to design new surface architectures and microstructures of an advanced oxygen electrode based on a composite of CGO and LSCF with graded and homogeneous compositions. The main advantage of a composite is to sum up the high ionic conductivity of CGO with the electrical properties of the mixed ionic-electronic conducting (MIEC) LSCF material in one electrode volume. The two different composites with a variable composition were able to be produced using ESD. The continuous gradient in composition was achieved by the use of two precursors solutions with varied flow rates. The mechanism of ESD film formation and the resulting microstructure depend mainly on the size of the droplets impacting the hot substrate.

First, an optimization of the ESD parameters, by varying technical parameters (nozzle-to-substrate distance, the precursor solution flow rate and the substrate temperature) and by varying the physico-chemical parameters of the precursor solution (surface tension, viscosity, boiling point and conductivity) has been performed in order to deposit highly porous CGO-LSCF microstructure. In this regard, large nozzle-to-substrate distance, low precursor solution flow rate, high substrate temperature, relatively low surface tension and viscosity, high boiling point are required with high conductivity values of the solution of about $50 \mu\text{S}\cdot\text{cm}^{-1}$. The size of the spread droplets in the high potential field was decreased due to solvents evaporation and decomposition. Dried and small droplets were attracted by the already deposited material creating corals. The CGO-LSCF coral microstructure is characterized by widely open morphology with two scale porosities: nano-scale porosity on the coral surface and micro-porous as a space between corals. Indeed, the microstructure of a MIEC electrode is directly related to its performance as a larger surface area facilitates the ORR by increasing the number of active sites. As the first step of deposition, a dense and thin layer of CGO was deposited to serve as a barrier diffusion layer to separate LSCF from YSZ components and avoid reaction between them. The energy dispersive X-ray spectroscopy analysis proved the graded composition, the electrode is rich in CGO close to YSZ substrate and rich in LSCF at

the surface. As-deposited coatings were found amorphous and a sintering at 900 °C for 2 h in air was found sufficient to reach the crystallization of the electrodes with the presence of the cubic LSCF perovskite and cubic CGO phases with no secondary phases. Grain size of 50 nm was obtained and the coating thickness was ranging from 20 to 30 μm.

Two batches, the graded and the homogeneous coral CGO-LSCF coatings were considered as functional layers for electrochemical impedance spectroscopy in two configurations: using single corals as oxygen electrode with platinum grid and using additional 45 μm thick LSCF layer as a current collector screen-printed on the coral microstructure with the Pt grid. The role of LSCF current collector is to improve the contact between the CGO-LSCF electrode and the grid, and improve the pathway for electrons. The electrode resistances were evaluated at OCV between 450 and 700 °C in air. Moreover, two isothermal tests were performed at 600 °C for 200 h and at 800 °C for 12 h. The polarization resistance for sample without current collector was found 65.2 Ω.cm² at 600 °C that was much higher than for samples with additional LSCF layer which was 1.3 Ω.cm² at 600 °C. The electrochemical performances were constant during durability tests performed at 600 °C for 200 h, proving the stability of the electrode. A dense and thin CGO barrier diffusion layer stopped La and Sr ions migration and avoid the formation of insulating phases on LSCF/YSZ interface. Even for sample with LSCF current collector layer, the electrode polarization resistance remained larger than that for a pure LSCF coral microstructure. The interpretation of this phenomena was based on the fact that the distribution of CGO phase could surround and trap some part of LSCF phase thus making it electrochemically inactive. In such way, both ionic and electronic pathways are cut at some point. No significant difference in polarization resistances between graded and homogeneous composition was found.

The electrochemical properties of such CGO-LSCF electrodes have to be related to a careful investigation of the electrode microstructure. Highly porous morphology with high surface area have led to an improvement of the ORR and consequently to a reduced electrode resistance.

In this order, FIB-SEM and X-ray nanotomography were used to create a three-dimensional model of CGO-LSCF composite. FIB-SEM has proved a good adhesion of the CGO-LSCF coating on the YSZ substrate and has shown that corals are hollow. A more specific analysis was possible to achieve by X-ray nanotomography. The deposition of highly porous coatings on dense YSZ caused difficulties for tomography. Indeed, the different X-ray absorption rates for YSZ and CGO-LSCF coatings have led to the creation of inevitable artifacts which required advanced image processing. Based on radiographs, two data volumes were chosen

from the data stack to calculate the microstructural parameters such as open, closed porosity, surface area, percolation path and tortuosity. The influence of threshold value on the parameters was also investigated. The evaluated parameters were different in comparison to the most common electrode presented in the literature. The total porosity in range of 67 – 87 vol.% placed such oxygen electrode as an unique specimen. Comparison of the microstructure parameters to other electrodes is challenging. The parameters were also used to calculate electrode polarization from ALS model. Modeled R_{pol} value was coherent with the value achieved from impedance spectroscopy for single coral microstructure giving an evidence that microstructural parameters were correctly estimated.

In parallel to the electrochemical properties, the mechanical strength remains an important issue for the durability of the oxygen electrode. Stresses in the cell may be provided during the manufacturing and then should be amplified during operation by oxygen activity gradients, redox cycling, external mechanical load and not homogeneous distribution of the temperature. From one side, the existing mechanical properties of the cell components are originated mainly from the nature of the bulk material and in minority from the form as materials are present in the cell components. On the other side, many researchers use thermo-electrochemical and finite element analysis to model the probability of the mechanical failure for the single cell as well for the stack. In this work, the mechanical behavior of CGO-LSCF coral microstructure was investigated by scratch test and ultramicroindentation. The indentation using atomic force microscope was not adapted because the height of the corals was too high for the tip to be measured. The breaking mechanism of corals was fully new and ran in three steps: particles reorientation, particles plastic deformation and impinge of particles. This mechanism was found for both scratch and ultramicroindentation tests. The similar compaction behavior was found for a powder compaction during pressing. At the first step during tests, the contact pressure was high at the beginning of loading during scratch and indentation tests due to low concentration of material at the top part of coral microstructure.

Finally, the durability test in SOFC and SOEC modes was performed on anode supported SOFC cell at larger scale of a electrode active area of 45 cm^2 . A homogeneous CGO-LSCF oxygen electrode with an active area of 45 cm^2 was deposited on Ni-YSZ cermet with $10 \mu\text{m}$ thick YSZ electrolyte. A CGO barrier diffusion layer was introduced between YSZ and LSCF as a first step of the deposition. The total durability test was as long as 790 h, more than 350 h operating in SOFC and more 430 h in SOEC. The initial cell voltage degradation in SOFC mode was 166 mV.kh^{-1} (20.4 \%.kh^{-1}) during 115 h, and stabilized to 50 mV.kh^{-1} (6.2 \%.kh^{-1}) in the last 100 h, giving a total cell voltage degradation of 116 mV.kh^{-1} (14.3 \%.kh^{-1}). For

SOEC mode, the cell voltage degradation was 353 mV.kh^{-1} (29.7 \%.kh^{-1}) at first 127 h after this time the cell voltage stabilized at 2 mV.kh^{-1} (0.2 \%.kh^{-1}) of the remaining time. This gave a total cell degradation of 130 mV.kh^{-1} (10.8 \%.kh^{-1}). The cell resistance was increasing during operation. The main increase of R_{cell} was noticed at the high frequency range. The contribution linked to this range was responsible for the blocking effect on the oxygen electrode/electrolyte interface. The current-voltage scans performed during analysis indicated reversibility of the current loading for fuel-cell and electrolysis. The significant change in low frequency resistance was noticed when hydrogen gas flow was modified at the oxygen electrode side during SOFC and SOEC mode. The post-mortem SEM observations showed cracks in the electrolyte layer, lack of CGO barrier diffusion layer in some part on YSZ electrolyte, and detachment of the oxygen electrode from the substrate.

To conclude, this positive international work is very fruitful since complementary investigations in different domains and different countries have brought new experiences. At the same time it is quite difficult to manage this huge work into deep understanding in only three years.

Prospect

The main disadvantage of this CGO-LSCF "tree" like morphology or 3D coral-like microstructure is that the electronic and ionic percolation paths are not continuous mainly due to the distribution of nanoscale grains in the electrode volume. One possible extension of this work could be to perform a long-term sintering of the coral microstructure at high temperature for example at 900, 1000 and 1100 °C for several hours in air. The sintering step would be expected to increase the size of the CGO and LSCF phase particles and the density of the oxygen electrode. Consequently, a larger percolation path and better mechanical and electrochemical properties should be expected.

In such a way, it would be possible to distinguish composite phases in X-ray nanotomography whose resolution limit is 25 nm. The coral microstructure would gain new gas channels by shrinkage of the coral.

A proposal for an alternative microstructure for the electrode could be an electrode built from large columns as a next possible morphology which could be obtained by electrostatic spray deposition. The space between columns would serve as gas channels distributing oxygen to the active zones. The electrical performances are also very dependent on the roughness of the electrode surface and consequently on the contact with the current collector. Since the surface

of columnar microstructure is much flatter than the surface of the corals, a much better current collection would be expected.

The particular link between microstructural, mechanical and electrochemical properties could give better description of the CGO-LSCF corals and interest of using it as an oxygen electrode for SOFC and SOEC. The first approach was done in this work however, it did not fill-up the topic.

Finally, the complexity of the coral microstructure is high since the quantity of matter is low. Microstructural, mechanical and electrochemical characterizations and comparison of achieved results with literature were challenging in these conditions. Moreover as a consequence, the difference in the electrical properties of gradient and homogeneous compositions of CGO-LSCF electrodes could not be discriminated.

Since there is little control of the influence of post-mortem characterizations on the degradation of the components in solid oxide cells, it would be worth to propose *in situ* or *operando* experiments in order to understand the electrochemistry of the solid oxide cell operation. Structural properties of the materials and strains at the electrodes/electrolyte and electrode/environment interfaces could be extracted using Raman spectroscopy simultaneously coupling with impedance spectroscopy to get electrical properties in a controlled atmosphere versus time. These processes have to be clearly understood at the atomic scale if optimized, high performance, low cost solid oxide cells are to be produced.

RESUME (FR)

Motivations

L'augmentation de la demande en énergie et l'épuisement des combustibles fossiles, nous poussent à trouver de nouvelles solutions. En effet, l'énergie provient majoritairement de l'utilisation du pétrole, du charbon et du gaz naturel. Récemment, l'administration américaine de l'énergie (the US. Energy Information Administration) a montré que la demande en énergie devrait augmenter de 56 % dans les trente prochaines années (Fig. 1) [1]. Cette forte croissance est essentiellement due au développement des pays émergents comme la Chine, l'Inde et le Brésil. Dans un futur proche, la production d'énergie se concentrera de plus en plus sur des sources d'énergie alternatives. Leur production devra se faire de façon propre, c'est-à-dire sans émission de gaz nocifs pour l'homme et l'environnement, et leur coût de production devra rester compétitif pour pouvoir rivaliser avec les sources d'énergie traditionnelles. Une des solutions envisagée, pour la production de chaleur et d'électricité, est l'utilisation des piles à combustible ainsi que des électrolyseurs à oxydes solides [2] (SOFC et SOEC).

L'un des problèmes majeurs limitant le développement des piles à combustibles et des électrolyseurs est l'utilisation à haute température, de l'ordre de 1000 °C. Cette haute température entraîne l'utilisation de matériaux coûteux et conduit également à la réactivité entre les différents composants, diminuant la durée de vie des systèmes. La diminution de la température de fonctionnement aux environs de 800 °C permettrait de réduire ces phénomènes (IT-SOFC) [3]. Cependant, cette diminution conduit à l'augmentation de la chute ohmique de l'électrolyte et des surtensions d'électrodes, réduisant les performances. Un autre verrou technologique pour le développement des électrolyseurs à haute température est le décollement de l'électrode à oxygène lors du fonctionnement [4]-[6]. Pour pallier cette faiblesse mécanique, de nouvelles électrodes doivent être développées ainsi que l'évaluation fine des interfaces électrodes / électrolytes.

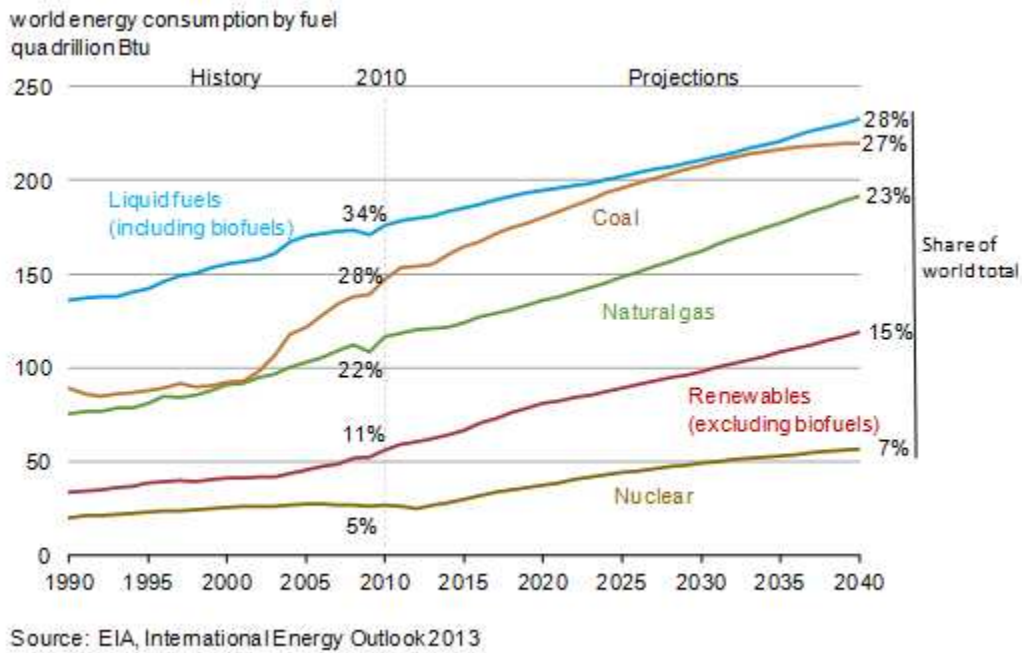


Fig. 1 Consommation énergétique mondiale en quadrillion British thermal unit (10^{24} Btu) [1].

Ce travail a été effectué au sein de l'école doctorale internationale « Matériaux fonctionnels pour l'énergie, la technologie de l'information et la santé » (IDS-FunMat) financé par le programme ERASMUS MUNDUS II (2009-2013) de l'Union Européenne, référencé 2011-08 (EM). L'école IDS-FunMat offre des bourses pour des projets de doctorat en science des matériaux fonctionnels, réalisés en co-tutelle entre deux universités d'un consortium de neuf institutions participantes et d'un partenaire industriel. Les neuf institutions du consortium issues de cinq pays sont :

- l'Université de Louvain et de Liège, Belgique
- l'Université de Waterloo, Canada
- l'Université Bordeaux 1, Grenoble INP, l'Université de Caen Basse-Normandie et l'Université Pierre et Marie Curie, France
- Technische Universität Darmstadt, Allemagne
- Instituto Superior Technico, Portugal

Le projet est intitulé « Interfaces et durabilité d'électrodes innovantes pour l'énergie (piles à combustible et électrolyseurs solides). Il a été réalisé au sein du Laboratoire d'Electrochimie et de Physico-Chimie des Matériaux et des Interfaces (LEPMI, UMR 5279, Grenoble) sous la direction du Pr Elisabeth DJURADO (Grenoble INP), et au sein de l'Instituto de Ciencia e Engenharia de Materiais e superficial (IST-ICEMS, Lisboa, Portugal) sous la direction du

Pr Amélia ALMEIDA (Instituto Superior Technico) et en collaboration avec l'Institut Européen de recherche sur l'énergie (EIFER, Karlsruhe, Allemagne) sous la responsabilité du Dr Annabelle BRISSE.

Objectifs

L'objectif de ce travail a été de réaliser une électrode à oxygène composite, à base de $\text{Ce}_{0,9}\text{Gd}_{0,1}\text{O}_{1,95}$ (CGO) et de $\text{La}_{0,6}\text{Sr}_{0,4}\text{Co}_{0,2}\text{Fe}_{0,8}\text{O}_{3-\delta}$ (LSCF), mince et poreuse déposée sur $(\text{ZrO}_2)_{0,92}(\text{Y}_2\text{O}_3)_{0,08}$ (YSZ), par atomisation électrostatique (Electrostatic Spray Deposition, ESD). Cette électrode permettra d'améliorer la durabilité des piles à combustible à oxyde solide fonctionnant à température intermédiaire (IT-SOFC), et des électrolyseurs à oxydes solides (SOEC). Une couche barrière, fine et mince, de CGO a été insérée entre l'électrode (CGO-LSCF) et l'électrolyte (YSZ), pour limiter la réaction chimique entre LSCF et YSZ.

En dehors des techniques de caractérisation classiques (microscopie électronique à balayage – field emission gun (MEB-FEG), analyse dispersive en énergie (EDS), diffraction des rayons X (DRX)) utilisées pour l'analyse de la microstructure d'un film, une attention particulière sera portée à l'utilisation de la nanotomographie des rayons X à l'ESRF Grenoble (European Synchrotron Radiation Facility) et de la reconstruction 3D par microscopie FIB-MEB (Focus Ion Beam) en collaboration avec le laboratoire SIMaP (Grenoble INP).

L'influence de la composition de l'électrode composite CGO-LSCF, de composition homogène ou à gradient en épaisseur, sur la résistance de polarisation de l'électrode, sera analysée par spectroscopie d'impédance (SI) en configuration demi-cellule. Egalement, l'intérêt de l'insertion de la couche barrière de CGO sera étudié par spectroscopie d'impédance lors d'essais de durabilité. Ces différentes analyses ont été réalisées au sein du laboratoire LEPMI. Les propriétés mécaniques de l'électrode composite, basées sur des mesures d'indentation et de scratch test, ont été déterminées au sein de l'institut ICEMS. Enfin, les performances de l'électrode composite CGO-LSCF, du surface de 45 cm^2 , en configuration mono-cellule seront étudiées à la fois en mode SOFC et SOEC au sein de l'institut EIFER.

Ce travail résume les résultats obtenus au cours de trois années de thèse réalisées au sein de deux institutions académiques (France et Portugal) et d'un partenaire industriel (EIfER, Allemagne), selon un calendrier présenté dans le tableau 1.

Tableau 1. Programme de mobilité au cours de la thèse

Année de thèse	Dates	Durée	Lieu
2011-2012	10/2011-06/2012	9 mois	LEPMI, Grenoble
	07/2012-09/2012	3 mois	ICEMS, Lisbon
2012-2013	10/2012-06/2013	9 mois	LEPMI, Grenoble
	07/2013-09/2013	3 mois	ICEMS, Lisbon
2013-2014	10/2013-11/2013	2 mois	ICEMS, Lisbon
	12/2013	1 mois	LEPMI, Grenoble
	01/2014-06/2014	6 mois	EDF-EIfER, Karlsruhe
	07/2014-09/2014	3 mois	LEPMI, Grenoble

Chapitre I

Structure de la thèse de doctorat

Le premier chapitre de cette thèse présente le contexte global de cette étude. Après une présentation du principe de fonctionnement des piles à combustible et des électrolyseurs à oxydes solides, ainsi que les différents types de matériaux utilisés, les spécificités liées à l'électrode à oxygène sont décrites. Ensuite, une description non exhaustive des techniques expérimentales, utilisées dans ce travail, est présentée. Les cinq chapitres suivants sont écrits sous forme d'articles scientifiques. Chaque chapitre contient un résumé, une introduction, une partie expérimentale, les résultats et une conclusion.

Le second chapitre est consacré à l'élaboration d'une électrode à oxygène composite poreuse et mince, pour IT-SOFC et SOEC, par atomisation électrostatique. Les propriétés physico-chimiques de cette couche poreuse, appelée « corail », ont été déterminées par diffraction des rayons X et par microscopie électronique à balayage.

L'étude des propriétés électrochimiques des électrodes composite CGO-LSCF, de composition homogène ou à gradient en épaisseur sera présentée dans le troisième chapitre. Deux configurations ont été étudiées pour mettre en évidence l'importance du collectage de courant. La première configuration comporte le substrat d'électrolyte (YSZ), la couche barrière de CGO, la couche corail CGO-LSCF et une grille de platine comme collecteur de courant. Pour la deuxième configuration, une couche de LSCF, déposée par sérigraphie est intercalée entre la couche corail et le collecteur de courant. Ensuite, l'étude de durabilité de l'électrode à oxygène a été réalisée à 600 °C pendant 200 h.

Le quatrième chapitre traite de l'extraction des paramètres microstructuraux, de la couche poreuse dite corail, à partir d'un modèle 3D obtenu par nanotomographie des rayons X. Ces paramètres ont ensuite permis de calculer la résistance de polarisation de cette électrode, calcul basé sur le modèle Adler-Lane-Steele (ALS model).

Le comportement mécanique de l'électrode corail, sous chargement, sera traité dans le cinquième chapitre. Des essais de micro-ultra indentation et de scratch test ont permis de déterminer les propriétés mécaniques de cette électrode poreuse, telles que le module de Young ainsi que la dureté.

Le sixième chapitre est consacré au test de durabilité des monocellules, dans les deux modes de fonctionnement, pile à combustible et électrolyse. Des observations post-mortem ont été menées pour déterminer les mécanismes de dégradation des monocellules.

Enfin, une conclusion générale a permis de résumer ces travaux de thèse et de donner quelques perspectives.

Les travaux présentés dans le chapitre II ont été présentés sous la forme d'une communication par affiche lors de la 5th International Conference on Fundamental & Development of Fuel Cells (FDFC 2013) qui ont eu lieu du 16 au 18 Avril 2013, à Karlsruhe en Allemagne. Ces travaux furent récompensés par le prix du meilleur poster dans la catégorie Fuel Cells and Electrolysers Materials. Le proceeding a été ensuite sélectionné pour être publié dans le journal Fuel Cells - From Fundamentals to Systems, publié par Wiley-VCH. Les travaux du chapitre III ont été présentés sous forme d'une communication orale lors du 15th Topical Meeting de The International Society of Electrochemistry qui a eu lieu du 27 au

30 Avril 2014 aux Chutes du Niagara, Canada. Les travaux des chapitres trois à six ont été ou seront soumis dans des revues avec comité de lecture.

Piles à combustible à oxyde solide (SOFC)

La pile à combustible à oxyde solide est un générateur électrochimique permettant la conversion directe de l'énergie chimique en énergie électrique et thermique. La conversion de l'énergie des réactions chimiques se fait par circulation d'un gaz combustible, dans le compartiment anodique, et d'un gaz comburant dans le compartiment cathodique. L'étanchéité entre ces deux compartiments est assurée par un électrolyte solide. Celui-ci doit être un bon conducteur par les ions oxygène et doit être également isolant électronique. Les ions oxygène sont formés par réduction de l'oxygène de l'air, côté cathodique. Puis ils traversent l'électrolyte solide via les lacunes d'oxygène dans le réseau cristallin et rejoignent l'anode, où l'hydrogène est oxydé pour former de l'eau avec libération d'électrons. Ces derniers sont collectés à l'anode et alimentent un circuit électrique extérieur et participent ensuite à la réduction de l'oxygène de l'air à la cathode (Fig. 2). En conclusion, la réaction globale engendre la production d'énergie électrique et thermique ainsi que la formation de vapeur d'eau, à partir de l'oxygène de l'air et d'hydrogène gazeux. La température de fonctionnement d'une SOFC est généralement comprise entre 800 et 1000 °C. Cette température élevée est nécessaire à l'activation énergétique des processus de transport de charge et catalytique, requis pour que les matériaux utilisés atteignent les valeurs souhaitées. Des températures de fonctionnement plus basses, jusqu'à 600 °C, permettraient de diminuer les contraintes thermomécaniques et d'augmenter la stabilité chimique entre les composants du système, diminuant ainsi les coûts d'exploitation et de maintenance. Dans les deux cas (haute et basse température), cette température de fonctionnement permet l'utilisation de différents types de combustibles, tels que l'hydrogène pur ou des hydrocarbures par reformage interne, en s'affranchissant de l'utilisation de catalyseurs onéreux. L'avantage principal des SOFCs par rapport aux autres types de piles à combustible réside dans l'utilisation d'un électrolyte solide. L'utilisation d'un électrolyte solide permet de s'affranchir des problèmes liés à la corrosion sèche et aux fuites. Le rendement des SOFCs est supérieur aux autres types de piles et peut atteindre 80 % [7]-[10]. En effet, la chaleur produite pendant le fonctionnement peut être utilisée pour la cogénération par combinaison avec une turbine à gaz.

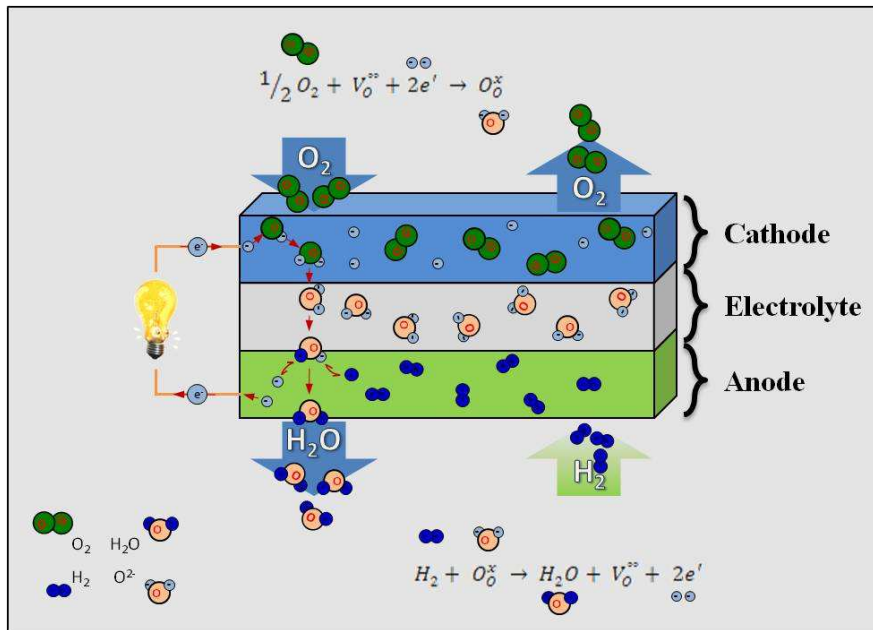


Fig. 2 Représentation schématique d'une SOFC [11].

Il existe plusieurs types de configurations pour les SOFCs qui peuvent être classées principalement en quatre catégories : la configuration tubulaire, planaire, monolithique et monochambre [12]-[13]. La configuration planaire est une configuration plus récente, elle permettrait l'utilisation de température de fonctionnement vers 600 °C, ceci est engendré par l'utilisation de composant de faible épaisseur. La différenciation des différents types de géométrie planaire se fait par l'élément assurant le support mécanique, électrolyte, anode, cathode ou métal support. La pile à combustible est constituée d'un assemblage de monocellules montées en série et/ou en parallèle en utilisant des plaques bipolaires (interconnecteurs), suivant la puissance envisagée du système final. Cet assemblage est appelé « stack ». La figure 3 montre une configuration planaire avec une mise en forme circulaire des éléments. Le combustible arrive par le centre de la monocellule et l'air provient de l'extérieur, les plaques d'interconnexions jouent le rôle de joint d'étanchéité. L'un des problèmes majeurs qui limite le développement des piles à combustible à oxyde solide est le coût encore trop élevé des matériaux constitutifs et des méthodes de fabrication.

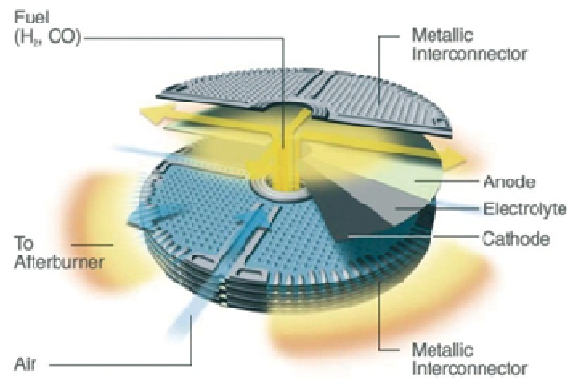
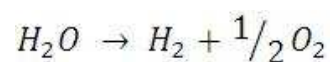


Fig. 3 Assemblage de cellules dans la configuration planaire Hexis [14].

Electrolyseur à oxydes solides (SOEC)

L'utilisation de l'hydrogène comme vecteur énergétique à grande échelle fait partie du contexte actuel de développement de l'énergie propre. La technologie de l'électrolyse à haute température permet la production massive d'hydrogène, sans émission de gaz carbonés. Le combustible le plus efficace utilisable dans les piles à combustible reste l'hydrogène. En effet, l'énergie chimique atteinte pour un kilogramme d'hydrogène est de 39,4 kWh, ce qui est trois fois plus élevé que celle obtenue à partir d'autres combustibles (13,1 kWh pour les hydrocarbures liquides). La technologie des électrolyseurs à oxydes solides (SOECs) est directement issue des développements de la pile à combustible SOFC. Cependant, son principe de fonctionnement est diamétralement opposé à celui des piles, utilisant le procédé d'électrolyse de l'eau pour créer de l'hydrogène et de l'oxygène. Les SOECs sont constitués donc d'une électrode à oxygène (anode), d'une électrode à hydrogène et vapeur d'eau (cathode) séparées par un électrolyte [15]-[16]. Les ions oxygène sont formés par réduction de l'eau côté cathodique. Les ions oxygène traversent l'électrolyte solide via les lacunes d'oxygène et rejoignent l'anode. L'hydrogène est produit côté cathodique. Ensuite, les ions oxygène sont oxydés pour former du dioxygène côté anodique (Fig. 4). L'électrolyse de l'eau est donc la réaction de dissociation de la molécule d'eau soumise à un courant électrique, suivant la réaction globale:



avec une enthalpie de dissociation de l'eau : $\Delta H = 285 \text{ kJ.mol}^{-1}$

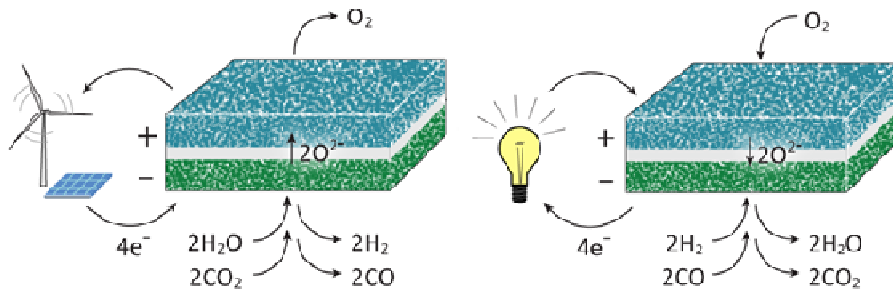


Fig. 4 Cellule à oxyde solide fonctionnent en tant qu'électrolyseur (gauche) et en tant que pile à combustible (droite).

La température de fonctionnement des électrolyseurs est généralement autour de 800°C , afin d'assurer une conductivité suffisante de l'électrolyte. La réaction d'électrolyse de l'eau est une réaction endothermique. Plus la température de fonctionnement est élevée, plus la réaction est endothermique (Fig. 5). Cette perte de chaleur peut être compensée par la chaleur produite, par effet Joule, lors du passage du courant électrique à travers la cellule. Le potentiel thermique pour lequel la chaleur nécessaire au maintien de la température de la cellule est compensée par la chaleur produite, par effet Joule, est nommé potentiel thermoneutre. Cela permettrait également de diminuer le coût de production de l'hydrogène.

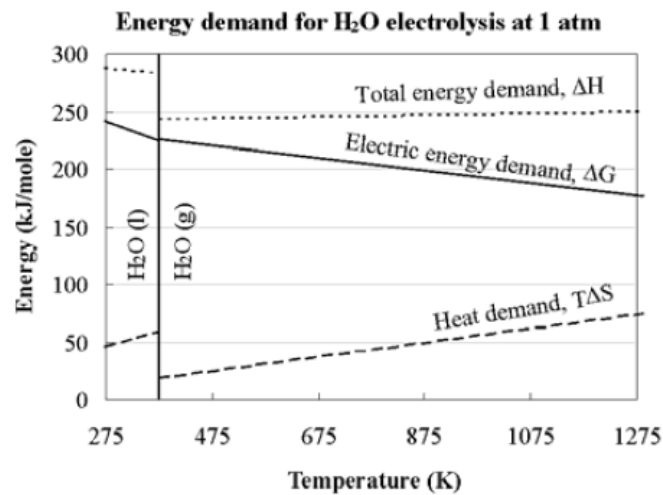


Fig. 5 Propriétés thermodynamiques de H₂O pour une pression de 1 atm [17].

Electrode composite CGO-LSCF

L'objectif de cette partie est de réaliser une électrode à oxygène composite à microstructure et à composition contrôlée, pour IT-SOFCs et SOECs. L'électrolyte composite

est basé sur l'utilisation d'un conducteur mixte (ionique et électronique, MIEC), LSCF, et d'un conducteur ionique, CGO. L'ajout de CGO au sein d'une électrode de LSCF présente plusieurs avantages. Tout d'abord, l'introduction de CGO permet d'augmenter la conductivité ionique de l'électrode composite, car CGO possède une conductivité ionique élevée. Le transport de l'oxygène d'un matériau peut être illustré par deux mécanismes : la diffusion au sein du matériau est décrite par le coefficient de diffusion (D^*) et l'échange à la surface décrit par le coefficient d'échange de surface (k). Le coefficient D^* détermine la capacité du matériau à transporter les ions oxygène. Le coefficient k caractérise les propriétés électrocatalytiques du matériau, c'est-à-dire la capacité du matériau à réduire l'oxygène à la surface du matériau.

Tableau 2 Coefficients d'échange de surface (k) et de diffusion (D^*) pour CGO, LSCF et YSZ.

Matériaux	k (cm.s^{-1})	D^* ($\text{cm}^2.\text{s}^{-1}$)	Température ($^{\circ}\text{C}$)	Po_2 (mbar)	Réf
CGO	8×10^{-8}	1×10^{-6}	900	200	[18]
LSCF	$5,51 \times 10^{-6}$	$4,18 \times 10^{-8}$	800	880	[19]
YSZ	3×10^{-6}	1×10^{-7}	900	200	[20]

CGO est caractérisé par un coefficient de diffusion de l'oxygène (D^*) élevé et par un coefficient d'échange de surface (k) faible par rapport à LSCF et YSZ (Tableau 2). Esquirol et al. [18] ont montré qu'une électrode composite CGO-LSCF possède un coefficient D^* supérieur et un coefficient k semblable à une électrode de LSCF (Fig. 6).

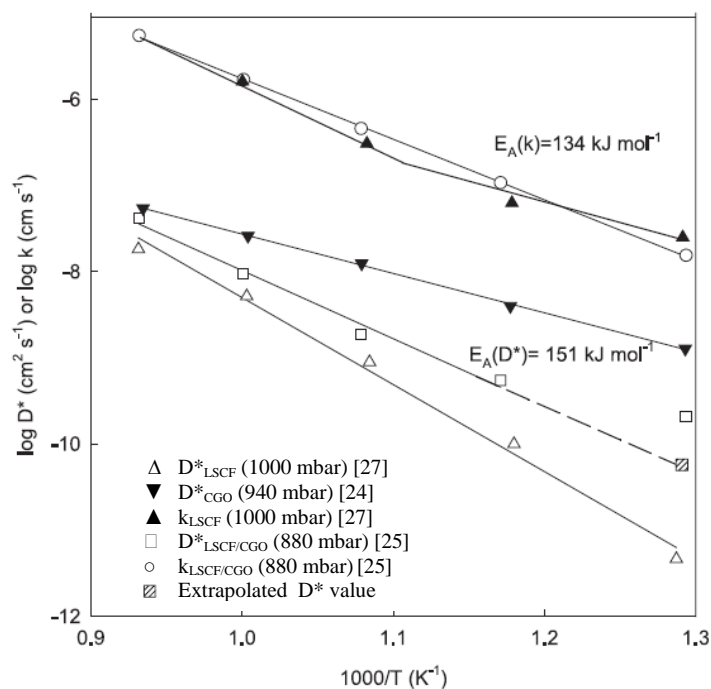


Fig. 6 Diagramme d'Arrhenius des coefficients de diffusion (D^*) et d'échange de surface (k) pour LSCF, CGO et pour un composite CGO-LSCF [19].

Une électrode composite CGO-LSCF possède donc des propriétés électrochimiques plus importantes que pour une électrode de LSCF. Les propriétés électrochimiques du composite CGO-LSCF ont déjà été étudiées en fonction du pourcentage massique de CGO, de 20 à 70 % [21]-[24]. La résistance de polarisation (R_{pol}) d'une telle électrode a été obtenue pour des valeurs allant de 0,17 à 0,60 $\Omega \cdot \text{cm}^2$ à 600 °C, avec un électrolyte de CGO [21]-[23]. Des résistances de polarisation de 0,33 et 1,00 $\Omega \cdot \text{cm}^2$ à 600 °C ont été mesurées sur un électrolyte de YSZ [22], [24]. Des valeurs de R_{pol} de 0,19 $\Omega \cdot \text{cm}^2$ à 600 °C, ont été obtenues sur un électrolyte de YSZ avec une couche barrière mince de CGO intercalée entre l'électrode et l'électrolyte, pour éviter la réaction entre LSCF et YSZ [22]. Ces résistances de polarisation de l'électrode composite CGO-LSCF sont six fois plus faibles que celles obtenues pour une électrode de LSM (conducteur électronique), utilisée comme électrode à oxygène. La composition optimale entre CGO et LSCF est encore controversée. Différentes études ont montré des valeurs de R_{pol} les plus faibles pour des compositions différentes de CGO et de LSCF, comme par exemple pour 60/40 %m. [21], 50/50 %m. [22], [24] ou bien 30/70 %m. [23]. Cependant, une résistance de polarisation quatre fois plus faible a été obtenue avec une composition de 36 %m. en CGO [23]. Néanmoins, la distribution de chaque phase au sein du composite n'est pas été prise en compte, ce qui peut avoir un effet prédominant sur les propriétés. Une mauvaise conception, en termes de microstructure, de composition ou de

distribution de phase, peut entraîner des propriétés électrocatalytiques, thermomécaniques et une stabilité chimique médiocres. Pour obtenir les propriétés les plus élevées, la région proche de l'électrolyte doit être riche en CGO, permettant un transfert ionique à l'électrolyte élevé. Dans le même temps, la partie supérieure de l'électrode doit être riche en LSCF, offrant une activité électrocatalytique à la surface importante. Après la réduction de l'oxygène, dans la partie supérieure de l'électrode, sa diffusion au travers de l'électrode devrait être accélérée par la présence de CGO. Sur cette base, nous avons supposé qu'une électrode composite CGO-LSCF à gradient de composition combinerait les propriétés de conduction ionique de CGO et les propriétés électrocatalytiques de LSCF. Ceci devrait être effectué tout en conservant une porosité importante de l'électrode, facilitant la pénétration de l'oxygène gazeux. L'utilisation d'une électrode composite nanostructurée semble être une solution prometteuse. De nombreux travaux mentionnent l'utilisation d'électrode composite CGO-LSCF, mais aucun ne mentionne l'utilisation d'une électrode composite à gradient de composition.

Chapitre II

Le chapitre II décrit la réalisation d'une électrode à oxygène composite à base de $\text{Ce}_{0,9}\text{Gd}_{0,1}\text{O}_{1,95}$ (CGO) et de $\text{La}_{0,6}\text{Sr}_{0,4}\text{Co}_{0,2}\text{Fe}_{0,8}\text{O}_{3-\delta}$ (LSCF) poreuse et mince, sur un substrat de $(\text{ZrO}_2)_{0,92}(\text{Y}_2\text{O}_3)_{0,08}$ (YSZ), par atomisation électrostatique (ESD Electrostatic Spray Deposition). La réalisation de cette électrode composite a pour objectifs d'améliorer les performances et la durabilité des SOFCs et des SOECs. Une électrode composite CGO-LSCF poreuse, à microstructure « corail », homogène et à gradient de composition a été obtenue avec succès. La microstructure de l'électrode composite a été mise en évidence par microscopie électronique à balayage et par tomographie. Le profil de composition de l'électrode à gradient, riche en CGO proche de l'électrolyte et riche en LSCF à la surface, a été étudié par analyse dispersive en énergie (EDS). Après un traitement thermique à 900 °C pendant 2 h, les diffractogrammes réalisés par diffraction des rayons X, montrent uniquement la présence de deux phases cristallines, correspondant aux structures cubiques de CGO et de LSCF.

Chapitre III

Les performances électrochimiques des électrodes composites CGO-LSCF, homogène et à gradient de composition, ont été étudiées avec et sans une couche de LSCF, déposée par sérigraphie, jouant le rôle de collecteur de courant. Les diagrammes d'impédance ont été enregistrés sous air, de 450 à 700 °C et à l'abandon ($I_{DC} = 0$ A). Des mesures de durabilité ont été effectuées à 600 °C pendant 200 h puis à 800 °C pendant 12 h. Une couche de CGO a été intercalée entre l'électrolyte YSZ et l'électrode composite CGO-LSCF pour prévenir de la réactivité entre ces deux composants. Aucune augmentation significative de la résistance de polarisation de l'électrode composite n'a été mise en évidence lors des mesures de durabilité. L'ajout de la couche de LSCF, collectrice de courant, a permis une diminution de la résistance de polarisation de 1,5 ordre de grandeur.

Chapitre IV

La microstructure de l'électrode joue également un rôle important dans les performances des SOFCs et SOECs. La nanotomographie par rayons X, avec une taille de voxel de 25 nm, a été utilisée pour déterminer la microstructure de l'électrode composite CGO-LSCF. Les données extraites après un traitement d'images ont permis la réalisation d'un modèle 3D de cette microstructure. Deux volumes d'électrodes ont été sélectionnés, à partir du modèle 3D, pour calculer les paramètres microstructuraux, tels que la porosité, la surface spécifique, les chemins de percolation et la tortuosité. L'influence des valeurs de seuils d'image appliquées au calcul des paramètres a été étudiée. La comparaison de ces paramètres avec les données précédemment reportées a montré des différences significatives. La porosité de l'électrode composite CGO-LSCF varie entre 67 et 87 % vol. Un tel niveau de porosité rend cette microstructure unique. L'extraction des paramètres microstructuraux a permis de calculer la résistance de polarisation de l'électrode à l'aide du modèle ALS (Adler-Lane-Steele). La résistance de polarisation calculée est en accord avec les données expérimentales.

Chapitre V

Le comportement mécanique de l'électrode CGO-LSCF, à microstructure corail, a été étudié par ultra-microindentation et par scratch test. Au lieu d'une fracturation et d'un décollement de la couche, comportement typique d'un matériau fragile sous chargement, les coraux se brisent en trois étapes sous charge. Tout d'abord, la partie supérieure des coraux se brisent et tombent à la surface. Puis, l'électrode se densifie et enfin, le matériau est presque totalement compacté. Le même mécanisme de rupture a été identifié pour les deux essais. Les paramètres mécaniques, tels que la dureté (H) et le module de Young (E) ont été déterminés dans chacun des trois régimes. Durant le chargement, la porosité de l'électrode passe de 60 à 5 % vol. La valeur des paramètres mécaniques augmente lorsque la porosité de l'électrode diminue durant les essais mécaniques.

Chapitre VI

Le chapitre VI présente un essai de durabilité d'une durée d'environ 790 h, de la monocellule travaillant dans les deux modes de fonctionnement SOFC et SOEC. La monocellule est composée d'une électrode à hydrogène support de Ni-YSZ, d'un électrolyte de YSZ, d'une couche barrière de CGO et d'une électrode à oxygène composite CGO-LSCF. La tension initiale de la cellule est de 817 mV à 773 °C sous air synthétique du côté de l'électrode à oxygène, et sous hydrogène pur du côté de l'électrode à hydrogène, (500 mL.min⁻¹), sous une densité de courant de 0,5 A.cm⁻² en mode SOFC. La tension initiale de la cellule est de 1200 mV à 773 °C, en mode SOEC, sous air synthétique et sous un mélange vapeur d'eau/hydrogène (80:20) sous une densité de courant de -0,75 et -0,5 A.cm⁻². La résistance de la monocellule a augmenté lors de l'essai de durabilité. Cette dégradation est principalement liée à l'augmentation de la partie haute fréquence de la résistance. Cette plage de fréquence est associée à un effet de blocage au niveau de l'interface électrode/électrolyte. Des analyses post-mortem ont montré la présence de fissures au sein de l'électrolyte YSZ, et de la couche barrière de CGO.

Conclusions générales

Le premier objectif de ce travail fut la conception d'une électrode à oxygène à microstructure innovante, élaborée par atomisation électrostatique. L'électrode est basée sur la réalisation d'une électrode composite, de composition homogène ou à gradient en épaisseur, entre CGO et LSCF. Le principal avantage dans la réalisation d'une électrode composite CGO-LSCF réside dans la combinaison des propriétés de conduction ionique élevée de CGO et de conduction mixte (ionique et électronique) de LSCF, au sein du volume de l'électrode. Une couche barrière dense de CGO a été déposée au préalable entre le substrat de YSZ et l'électrode CGO-LSCF, afin d'éviter la réactivité entre LSCF et YSZ. L'électrode composite obtenue possède une microstructure très poreuse dite corail, donc une surface active très élevée. Cette microstructure corail est caractérisée par une mésoporosité au sein des coraux et d'une macroporosité entre les coraux. La réalisation d'une électrode à conduction mixte possédant une surface active élevée permet d'augmenter les performances électrochimiques de celle-ci. En effet, les performances électrochimiques sont directement liées aux nombres de sites actifs, c'est-à-dire à la surface de l'électrode en contact avec la phase gazeuse. Après un traitement thermique à 900 °C pendant 2 h, les diffractogrammes X montrent la présence de seulement deux phases cristallines, correspondant aux structures cubiques de CGO et de LSCF. L'épaisseur de l'électrode est comprise entre 20 et 30 μm et la taille des grains est d'environ 50 nm. L'obtention d'une électrode composite à gradient de composition a été confirmée par analyse dispersive en énergie. L'électrode est riche en CGO à proximité de l'interface avec YSZ et elle est riche en LSCF à sa surface. Le gradient de composition a été obtenu en modifiant les débits des deux solutions de précurseurs, à base de CGO et de LSCF, lors du processus de dépôt.

Les propriétés électrochimiques de l'électrode composite CGO-LSCF, à microstructure corail, ont été déterminées par spectroscopie d'impédance, de 450 à 700 °C sous air à l'abandon. Les spectres d'impédance ont été enregistrés en configuration à 3 et à 2 électrodes. Pour la moitié des échantillons, une couche de LSCF, de 45 μm d'épaisseur, a été déposée par sérigraphie sur l'électrode composite CGO-LSCF. Le rôle de cette couche LSCF est d'améliorer le contact entre l'électrode et le collecteur de courant, la grille de platine, c'est-à-dire d'améliorer le transfert des électrons entre les deux composants. La résistance de polarisation pour les échantillons sans ajout de la couche de LSCF est de 65,2 $\Omega\cdot\text{cm}^2$ à 600 °C. L'ajout de cette couche de LSCF permet de diminuer la valeur de la résistance de

polarisation à $1,3 \Omega \cdot \text{cm}^2$ à $600 \text{ }^\circ\text{C}$. Des essais de durabilité, effectués à $600 \text{ }^\circ\text{C}$ pendant 200 h et à $800 \text{ }^\circ\text{C}$ pendant 12 h, sous air à l'abandon, ont montrés la stabilité thermique de cette électrode composite. La couche barrière dense et mince de CGO, intercalée entre YSZ et CGO-LSCF, a permis d'éviter la migration des ions Sr^{2+} et ainsi la formation de phases isolantes à l'interface avec l'électrolyte. Aucune différence significative des résistances de polarisation n'a été déterminée entre l'électrode composite de composition homogène et à gradient. Les performances électrochimiques de la couche composite CGO-LSCF, malgré l'ajout de la couche fine et dense de LSCF, restent inférieures à celles obtenues pour une électrode pure de LSCF ayant la même microstructure. Ceci pourrait s'expliquer par une distribution hétérogène des phases CGO et LSCF au sein de l'électrode composite. Des grains de LSCF pourraient être entourés par des grains de CGO, rendant les grains LSCF électrochimiquement inactifs sous air.

Des analyses microstructurales par FIB-MEB et par nanotomographie des rayons X ont permis de réaliser un modèle 3D de l'électrode composite CGO-LSCF. Les analyses FIB-MEB ont montré une bonne adhérence du revêtement CGO-LSCF sur l'électrolyte YSZ. La différence de porosité et de taux d'absorption des rayons X entre YSZ et l'électrode CGO-LSCF ont conduit à l'obtention d'artéfacts et ont donc nécessité un traitement d'images avancé. Deux volumes d'électrodes ont été sélectionnés, à partir du modèle 3D, pour calculer les paramètres microstructuraux, tels que la porosité ouverte et fermée, la surface spécifique, les chemins de percolation et la tortuosité. L'influence des valeurs de seuils d'images appliquées sur le calcul des paramètres a été étudiée. La porosité de l'électrode est de l'ordre de 67 à 87 % vol. Un tel niveau de porosité rend cette microstructure unique. Les paramètres ont également été utilisés pour calculer la résistance de polarisation de cette électrode à l'aide du modèle ALS. Ces valeurs sont cohérentes avec les valeurs expérimentales, ce qui confirme que les paramètres microstructuraux ont été extraits correctement.

Les propriétés mécaniques de l'électrode à oxygène demeurent un problème important pour la longévité des monocellules. L'électrode à oxygène doit supporter de fortes contraintes mécaniques de sources variées. Les contraintes mécaniques peuvent être liées au processus de dépôt, au processus de conduction de l'oxygène, aux cycles redox, au gradient de température et aux contraintes mécaniques externes. Les propriétés mécaniques des composants au sein des monocellules sont le plus souvent extraites de matériaux sous forme massive, ce qui n'est pas représentatif des conditions réelles. De plus, la modélisation de probabilité de défaillance

mécanique de la monocellule ou du stack est réalisée par analyse thermo-électrochimique et par élément fini. Dans ce travail, le comportement mécanique de l'électrode composite CGO-LSCF, à microstructure corail, a été étudié par ultra-microindentation et par scratch test, sur l'électrode CGO-LSCF déposée sur le substrat de YSZ. La technique d'indentation utilisant la microscopie à force atomique ne fut pas adaptée, car la topologie de surface est trop importante pour la pointe. Le mécanisme de rupture des coraux est un mécanisme en trois étapes, réorientation des particules, déformation plastique et densification. Le même mécanisme de rupture a été identifié pour les deux techniques.

L'essai de durabilité a été réalisé pendant 790 h, 350 h de fonctionnement en mode SOFC et 430 h en mode SOEC. L'électrode composite CGO-LSCF, de 45 cm^2 de surface, a été déposée sur un cermet support de Ni-YSZ avec un électrolyte de YSZ de $10 \mu\text{m}$ d'épaisseur. Une couche barrière dense et mince de CGO a été intercalée entre l'électrode CGO-LSCF et l'électrolyte. La dégradation de la tension de la monocellule initiale en mode SOFC, a été de 166 mV.kh^{-1} ($20,4 \text{ \%.kh}^{-1}$) pendant 115 h, puis elle s'est stabilisée à 50 mV.kh^{-1} ($6,2 \text{ \%.kh}^{-1}$) pendant 100 h. La dégradation de la tension de la monocellule a été donc de 116 mV.kh^{-1} ($14,3 \text{ \%.kh}^{-1}$). En mode SOEC, la dégradation de la monocellule initiale a été de 353 mV.kh^{-1} ($29,7 \text{ \%.kh}^{-1}$) pendant 127 h, ensuite elle s'est stabilisée à 2 mV.kh^{-1} ($0,2 \text{ \%.kh}^{-1}$). La dégradation, en mode SOEC, a été donc de 130 mV.kh^{-1} ($10,8 \text{ \%.kh}^{-1}$). La résistance de la monocellule augmente au cours du fonctionnement. Cette augmentation est principalement liée à la dégradation de la partie haute fréquence de la résistance de la monocellule. Cette dégradation peut être liée à un effet de blocage au niveau de l'interface entre l'électrode à oxygène et l'électrolyte. Les analyses courant-tension ont montré la réversibilité des modes pile à combustible et électrolyseur. Une variation de la résistance de la partie basse fréquence a été observée lorsque le débit d'hydrogène a été modifié lors du passage du mode SOFC et SOEC, au niveau de l'électrode à oxygène. Les analyses post-mortem ont montré la présence de fissures au sein de l'électrolyte, la discontinuité de la couche barrière de CGO et le décollement de l'électrode à oxygène. Les analyses n'ont pas montré la présence de phases isolantes du type SrZrO_3 ou $\text{La}_2\text{Zr}_2\text{O}_7$, issues de la réactivité entre LSCF et YSZ.

Perspectives

Le principal inconvénient de cette électrode composite CGO-LSCF, à microstructure dite corail, est que la répartition des grains de taille nanométrique ne permet pas d'avoir des chemins de percolation électroniques et ioniques suffisants, au sein du volume de l'électrode. Un traitement thermique, par exemple, à 900, 1000 et à 1100 °C pendant plusieurs heures permettrait d'augmenter la taille des particules des phases de CGO et LSCF et la densité de l'électrode, ce qui devrait permettre une amélioration des chemins de percolation. Après ce traitement thermique, des chemins de percolation plus larges, de meilleures propriétés mécaniques et électrochimiques doivent être attendues. De plus, cela permettrait de distinguer les phases par nanotomographie des rayons X, dont la limite de résolution est de 25 nm.

La compréhension des mécanismes de dégradation de la monocellule lors du fonctionnement reste un enjeu important, pour améliorer la durabilité des systèmes électrochimiques. Des études *in situ* ou *in operando*, par exemple coupler la spectroscopie d'impédance et la spectroscopie Raman, permettrait d'obtenir des informations microstructurales, au niveau des différentes interfaces, lors du fonctionnement de la monocellule.

L'utilisation d'une électrode à microstructure colonnaire permettrait une amélioration de l'interface électrode/collecteur de courant. En effet, comme pour la microstructure corail, elle est caractérisée par une mésoporosité au sein des colonnes et d'une macroporosité entre les colonnes. Ceci doit permettre une bonne diffusion des gaz au sein de la cathode favorisant le transport de matière en phase gazeuse au sein de l'électrode. De plus, la surface de ce type d'électrode est beaucoup plus lisse que la surface de celle de l'électrode corail, ce qui entraîne un meilleur contact avec le collecteur de courant.

Références

- [1] EIA. International Energy Outlook (IEO 2013), 2013.
- [2] D. Marinha, L. Dessemond, and E. Djurado, “Comprehensive Review of Current Developments in IT-SOFCs,” *Curr. Inorg. Chem.*, vol. 3, no. 1, pp. 2–22, 2013.
- [3] J. A. Kilner and M. Burriel, “Materials for Intermediate-Temperature Solid-Oxide Fuel Cells,” *Annu. Rev. Mater. Res.*, vol. 44, pp. 365–393, 2014.
- [4] A. Hauch, S. H. Jensen, S. Ramousse, and M. Mogensen, “Performance and Durability of Solid Oxide Electrolysis Cells,” *J. Electrochem. Soc.*, vol. 153, no. 9, pp. A1741–A1747, 2006.
- [5] J. S. Herring, J. O'Brien, C. Stoots, G. Hawkes, J. Hartvigsen, and M. Shahnam, “Progress in high-temperature electrolysis for hydrogen production using planar SOFC technology,” *Int. J. Hydrogen Energy*, vol. 32, no. 4, pp. 440–450, 2007.
- [6] A. V. Virkar, “Mechanism of oxygen electrode delamination in solid oxide electrolyzer cells,” *Int. J. Hydrogen Energy*, vol. 35, no. 18, pp. 9527–9543, 2010.
- [7] S. Park, J. M. Vohs, and R. J. Gorte, “Direct oxidation of hydrocarbons in a solid-oxide fuel cell,” *Nature*, vol. 404, pp. 265–267, 2000.
- [8] K. Eguchi, H. Kojo, T. Takeguchi, R. Kikuchi, and K. Sasaki, “Fuel flexibility in power generation by solid oxide fuel cells,” *Solid State Ionics*, vol. 152–153, pp. 411–416, 2002.
- [9] S. C. Singhal, “Solid oxide fuel cells for stationary, mobile, and military applications,” *Solid State Ionics*, vol. 152–153, pp. 405–410, 2002.
- [10] O. Yamamoto, “Solid oxide fuel cells: fundamental aspects and prospects,” *Electrochim. Acta*, vol. 45, pp. 2423–2435, 2000.

- [11] G. Constantin, "Interfaces et durabilité d'un cœur de pile à combustible à oxyde solide fonctionnant à température intermédiaire," PhD Thesis, Grenoble INP, 2012.
- [12] T. Hibino, H. Tsunekawa, S. Tanimoto, and M. Sano, "Improvement of a Single-Chamber Solid-Oxide Fuel Cell and Evaluation of New Cell Designs," *J. Electrochem. Soc.*, vol. 147, no. 4, pp. 1338–1343, 2000.
- [13] N. Minh, "Solid oxide fuel cell technology – features and applications," *Solid State Ionics*, vol. 174, no. 1–4, pp. 271–277, 2004.
- [14] Hexis Ltd., "http://www.hexis.com/downloads/HEXIS_Zellstapel_e.jpg,".
- [15] A. Züttel, A. Borgschulte, and L. Schlapbach, *Hydrogen as a future energy carrier*. Weinheim: Wiley-VHC Verlag GmbH & Co., 2008.
- [16] M. A. Laguna-Bercero, "Recent advances in high temperature electrolysis using solid oxide fuel cells: A review," *J. Power Sources*, vol. 203, pp. 4–16, 2012.
- [17] W. Donitz and E. Erdle, "High-temperature electrolysis of water vapor-status of development and perspectives for application," *Int. J. Hydrogen Energy*, vol. 10, no. 5, pp. 291–295, 1985.
- [18] P. S. Manning, J. D. Sirman, and J. A. Kilner, "Oxygen self-diffusion electrolytes and surface exchange studies of oxide having the fluorite structure," *Solid State Ionics*, vol. 93, pp. 125–132, 1997.
- [19] A. Esquirol, J. Kilner, and N. Brandon, "Oxygen transport in $\text{La}_{0.6}\text{Sr}_{0.4}\text{Co}_{0.2}\text{Fe}_{0.8}\text{O}_{3-\delta}$ / $\text{Ce}_{0.8}\text{Ge}_{0.2}\text{O}_{2-x}$ composite cathode for IT-SOFCs," *Solid State Ionics*, vol. 175, pp. 63–67, 2004.
- [20] P. S. Manning, J. D. Sirman, R. A. De Souza, and J. A. Kilner, "The kinetics of oxygen transport in 9.5 mol % single crystal yttria stabilised zirconia," *Solid State Ionics*, vol. 100, pp. 1–10, 1997.

- [21] Y. Leng, S. Chan, and Q. Liu, "Development of LSCF–GDC composite cathodes for low-temperature solid oxide fuel cells with thin film GDC electrolyte," *Int. J. Hydrogen Energy*, vol. 33, no. 14, pp. 3808–3817, 2008.
- [22] W. Wang and M. Mogensen, "High-performance lanthanum-ferrite-based cathode for SOFC," *Solid State Ionics*, vol. 176, no. 5–6, pp. 457–462, 2005.
- [23] V. Dusastre and J. A. Kilner, "Optimisation of composite cathodes for intermediate temperature SOFC applications," *Solid State Ionics*, vol. 126, pp. 163–174, 1999.
- [24] E. P. Murray, M. J. Sever, and S. A. Barnett, "Electrochemical performance of (La,Sr)(Co,Fe)O₃–(Ce,Gd)O₃ composite cathodes," *Solid State Ionics*, vol. 148, pp. 27–34, 2002.

Interfaces and durability of advanced electrodes for energy (IT-SOFC and SOEC)

The objective of this PhD thesis is to fabricate advanced oxygen electrode based on $\text{Ce}_{0.9}\text{Gd}_{0.1}\text{O}_{1.95}$ (CGO) and $\text{La}_{0.6}\text{Sr}_{0.4}\text{Co}_{0.2}\text{Fe}_{0.8}\text{O}_{3-\delta}$ (LSCF) with graded and homogeneous composition onto yttria-stabilized zirconia (YSZ = 8 mol. % Y_2O_3 -doped ZrO_2) electrolyte using electrostatic spray deposition. A thin and dense layer of CGO was inserted between LSCF and YSZ to serve as a barrier diffusion layer. The novel microstructure with high porosity and large surface area is expected to improve the electrochemical performances. The electrical behavior of the electrode was investigated by impedance spectroscopy versus temperature in air. A detailed microstructural description was performed by 3D reconstructed model from FIB-SEM and X-ray nanotomography and related to electrical properties. The mechanical analysis was performed by microscratch and ultramicroindentation tests. Finally, durability tests were performed on the electrode with 45 cm^2 oxygen active area, up to 800 h at around $770 \text{ }^\circ\text{C}$, in full cell SOFC and SOEC configurations operating respectively in H_2 and H_2/water mixture.

Keywords: SOFC, SOEC, LSCF, CGO, coral microstructure, ESD, EIS, X-ray nanotomography, 3D reconstruction, ultra-microindentation.

Interfaces et durabilité des électrodes de pointe pour l'énergie (PAC et EHT)

L'objectif de cette thèse concerne l'élaboration, par atomisation électrostatique, d'une électrode à oxygène à architecture innovante, basée sur un composite $\text{Ce}_{0.9}\text{Gd}_{0.1}\text{O}_{1.95}$ (CGO) - $\text{La}_{0.6}\text{Sr}_{0.4}\text{Co}_{0.2}\text{Fe}_{0.8}\text{O}_{3-\delta}$ (LSCF) possédant un gradient de composition ou une composition homogène. Cette électrode a été déposée sur un substrat de zircone yttrée (YSZ = 8 % mol. Y_2O_3 - ZrO_2) sur laquelle, a été intercalée au préalable une couche barrière mince et dense de CGO. Cette électrode possède une microstructure innovante, à porosité élevée permettant d'obtenir une grande surface active qui devrait conduire à l'amélioration des performances électrochimiques. Le comportement électrique de l'électrode a été étudié par spectroscopie d'impédance en fonction de la température et sous air. Une description microstructurale détaillée a été effectuée à l'aide d'un modèle de reconstruction 3D obtenu par MEB équipé d'une sonde ionique focalisée et par nanotomographie X. Ces propriétés microstructurales ont été reliées aux propriétés électriques. Les propriétés mécaniques et tribologiques de cette électrode composite ont été déterminées par des tests de microscratch et ultramicroindentation. Finalement, des tests de durabilité ont été effectués sur une électrode de grande taille possédant une surface active de 45 cm^2 jusqu'à 800 h à environ $770 \text{ }^\circ\text{C}$, dans une cellule complète de configurations PAC et fonctionnant respectivement sous H_2 et un mélange $\text{H}_2/\text{H}_2\text{O}$.

Mots clés: PAC, EHT, LSCF, CGO, microstructure de type « corail », atomisation électrostatique, spectroscopie d'impédance, nanotomographie des rayons X, reconstruction 3D, ultra-microindentation.